

**Efficient analysis algorithms for  
Gravitational Waves  
and  
Cosmology**

OFFICIAL TITLE:

Gravitational Waves from Inspiring Binaries and Cosmological Ramifications

BY  
**Sanjit Mitra**

A THESIS FOR THE DEGREE OF

**Doctor of Philosophy**  
( in Physics )

SUBMITTED TO THE  
University of Pune

SUPERVISOR: **Prof. Sanjeev Dhurandhar**  
CO-SUPERVISOR: **Prof. Tarun Souradeep**

**Inter-University Centre for Astronomy and Astrophysics**  
Post Bag 4, Ganeshkhind, Pune 411 007, INDIA

**DECEMBER 2006**



# Dedicated to Nature

of which I am a part



# Contents

<b>Dedication</b>	<b>iii</b>
<b>Acknowledgment</b>	<b>xiii</b>
<b>List of Publications</b>	<b>xv</b>
<b>Declaration</b>	<b>xvii</b>
<b>Abstract</b>	<b>xix</b>
<b>1 Introduction</b>	<b>1</b>
1.1 Basics . . . . .	1
1.1.1 Gravitational Waves (GW) . . . . .	1
1.1.2 Cosmic Microwave Background (CMB) . . . . .	2
1.2 Search for GW from Inspiring Binaries: Chebyshev Interpolation . . . . .	3
1.3 Search for GW Background: Radiometer Analysis . . . . .	5
1.4 Deconvolution of Sky-Maps . . . . .	5
1.5 Non-circular Beam Correction to CMB Power Spectrum . . . . .	6
1.6 Organization of the Thesis . . . . .	7
<b>2 Introduction to Gravitational Waves (GW)</b>	<b>9</b>
2.1 Gravitational Waves . . . . .	10
2.1.1 General Relativity: Einstein's Equation . . . . .	10
2.1.2 Weak field limit: Linearized Theory . . . . .	10
2.1.3 Plane Polarized Monochromatic Gravitational Waves . . . . .	14
2.2 Detection . . . . .	14
2.3 Sources and Analysis Strategies . . . . .	18
2.4 Summary and Conclusion . . . . .	20

<b>3</b>	<b>Search for GW from Inspiring Binaries: Chebyshev Interpolation</b>	<b>21</b>
3.1	Chirp Signal . . . . .	23
3.2	Dense Search . . . . .	25
3.2.1	Matched Filtering . . . . .	25
3.2.2	Template placement . . . . .	26
3.2.3	Choice of parameter . . . . .	29
3.3	Efficient Search Algorithms . . . . .	30
3.4	Interpolated Search . . . . .	32
3.4.1	Interpolation of the Wiener filter output . . . . .	32
3.4.2	Search strategy . . . . .	36
3.4.3	Template placement . . . . .	38
3.5	Comparison between Dense and Interpolated search: ROC curves . . . . .	42
3.6	Summary and Conclusion . . . . .	44
<b>4</b>	<b>Search for GW Background (GWB): Radiometer Analysis</b>	<b>49</b>
4.1	Stochastic Gravitational Wave Background (GWB) . . . . .	50
4.2	Sources of GWB . . . . .	54
4.3	Detection of GWB: Radiometer Analysis . . . . .	56
4.3.1	Cross-correlation statistic . . . . .	57
4.3.2	Correlation between GW Strains . . . . .	62
4.3.3	Detector Noise . . . . .	64
4.3.4	Optimal Filter . . . . .	65
4.3.5	Observed Point Estimate and SNR . . . . .	69
4.3.6	Summary . . . . .	71
4.4	Applications . . . . .	73
4.4.1	All-sky isotropic background . . . . .	74
4.4.2	Directed Search . . . . .	76
4.5	Summary and Conclusion . . . . .	79
<b>5</b>	<b>Introduction to the Cosmic Microwave Background (CMB)</b>	<b>81</b>
5.1	Origin . . . . .	82
5.2	CMB Anisotropy . . . . .	84
5.3	Angular Power Spectrum: Cosmic Variance . . . . .	86
5.4	Experiments . . . . .	89
5.5	Summary and Conclusion . . . . .	90

<b>6</b>	<b>Beams and Deconvolution in CMB and GWB Mapmaking: Analysis and Formalism</b>	<b>91</b>
6.1	Beam Function . . . . .	92
6.2	Observed CMB Data . . . . .	92
6.3	Observed (Directed) GW Radiometer Point Estimate . . . . .	95
6.4	Maximum Likelihood (ML) skymap Estimation . . . . .	101
6.5	ML Estimation of CMB Anisotropy Map . . . . .	103
6.6	ML Estimation of GWB Anisotropy . . . . .	104
6.6.1	Basic Analysis of Skymap . . . . .	104
6.6.2	Extensions of the simple MapMaking . . . . .	105
6.6.3	Multipole moments from the directed search . . . . .	107
6.6.4	Multipole moments from isotropic all-sky search . . . . .	108
6.7	Summary and Conclusions . . . . .	111
<b>7</b>	<b>Numerical Implementation of ML Mapmaking for GWB</b>	<b>113</b>
7.1	Preparation of Simulated Data . . . . .	114
7.2	Preparation of the “Dirty” Maps . . . . .	116
7.3	Computation of the Beam Matrix . . . . .	117
7.4	Deconvolution: The “Clean” Maps . . . . .	120
7.5	Results and Comparisons . . . . .	123
7.6	Summary and Conclusion . . . . .	125
<b>8</b>	<b>Non-circular Beam Correction to CMB Power Spectrum: Perturbative Analysis</b>	<b>127</b>
8.1	Pseudo- $C_l$ Approach to Non-circular Beam Correction . . . . .	128
8.2	Window functions of CMB experiments: a brief primer . . . . .	131
8.2.1	Window function for circular beams . . . . .	133
8.2.2	Window function for non-circular beams . . . . .	134
8.3	Bias Matrix . . . . .	138
8.3.1	Circular Symmetric Beam . . . . .	140
8.3.2	Non-circular Beam . . . . .	141
8.4	Error-Covariance Matrix . . . . .	148
8.4.1	Circular Beam . . . . .	151
8.4.2	Non-circular Beam . . . . .	151
8.5	Discussion and Conclusion . . . . .	155

<b>9 Non-circular Beam Correction to CMB Power Spectrum:</b>	
<b>Complete Analysis Framework</b>	<b>159</b>
9.1 Analytical Framework . . . . .	160
9.1.1 Bias in the pseudo- $C_l$ estimator . . . . .	160
9.1.2 Evaluation of the Bias Matrix . . . . .	162
9.1.3 Checking different limits . . . . .	166
9.2 Implementation . . . . .	167
9.3 Discussions and Conclusion . . . . .	171
<b>10 Conclusion</b>	<b>173</b>
<b>A Properties of the Chebyshev Polynomials</b>	<b>177</b>
<b>B Directed GW Radiometer Beam: Stationary Phase Approximation</b>	<b>179</b>
B.1 Beam Pattern: SPA Trajectory . . . . .	180
B.1.1 The case of small $\Delta\Omega$ . . . . .	181
B.1.2 General SPA solution . . . . .	183
B.2 Evaluation of the Beam Function on SPA trajectory . . . . .	184
<b>C Cosmic Variance</b>	<b>187</b>
<b>D Elliptical Gaussian fit to the WMAP beam maps</b>	<b>189</b>
<b>E Derivations for perturbative analysis of beam correction to pseudo-<math>C_l</math> estimator</b>	<b>195</b>
<b>F Derivations for general analysis of beam correction to pseudo-<math>C_l</math> estimator</b>	<b>201</b>
F.1 Useful formulae . . . . .	201
F.2 Expansion of Wigner-D Function . . . . .	202
F.3 Evaluation of $J_{nm''mm'}^{ll'}$ using sinusoidal expansion of Wigner- $d$ . . . . .	205
F.4 Evaluation of $J_{nm''mm'}^{ll'}$ using Clebsch-Gordon series and sinusoidal expansion of Wigner- $d$ . . . . .	207
F.5 The full sky and circular beam limit . . . . .	209
F.6 The circular beam limit with cut sky . . . . .	211
F.7 The full sky limit with non-circular beam . . . . .	213
<b>G Fast computation of non-circular beam correction to CMB power spectrum</b>	<b>215</b>

# List of Tables

3.1	Comparison between dense and interpolated search . . . . .	44
8.1	Definition of parameters that quantify non-circularity . . . . .	138
B.1	Coordinate of the LIGO detectors . . . . .	182
D.1	Ellipticities of WMAP beams . . . . .	193



# List of Figures

2.1	Effect of GW on matter: Detection scheme . . . . .	15
2.2	GW Detectors . . . . .	16
2.3	LIGO-I sensitivity curves . . . . .	17
3.1	Illustration of Matched Filtering . . . . .	27
3.2	Ambiguity function . . . . .	30
3.3	Illustration of Interpolated Search . . . . .	37
3.4	Variation of bias with no. of interpolated search templates . . . . .	40
3.5	Variation of Match with signal location . . . . .	41
3.6	Comparison: False Alarm & False Dismissal probability . . . . .	45
3.7	Comparison: ROC Curves . . . . .	46
4.1	Inflationary GWB spectra and detectability using the advanced LIGO detectors . . . . .	55
4.2	GWB spectra and detectability landscape . . . . .	56
4.3	Time independent overlap reduction function . . . . .	75
4.4	Geometry of an elementary radiometer . . . . .	77
4.5	A test sky map made using the GWB radiometer . . . . .	78
5.1	Evolution of anisotropies in the universe . . . . .	83
5.2	Observed CMB frequency spectrum by COBE FIRAS . . . . .	84
5.3	WMAP CMB anisotropy sky . . . . .	85
5.4	Observed CMB Power Spectrum . . . . .	88
5.5	CMB Experiments . . . . .	89
6.1	WMAP image planes . . . . .	94
6.2	Numerical and Theoretical GW radiometer beam patterns . . . . .	97
6.3	Contour plots of GW radiometer beam patterns . . . . .	98

7.1	A typical GW radiometer Beam Matrix . . . . .	120
7.2	Deconvolved (simulated) GWB skymaps . . . . .	126
8.1	Illustration of beam rotation . . . . .	134
8.2	WMAP Q1 Beam . . . . .	135
8.3	Bias matrix without beam rotation . . . . .	145
8.4	Characteristics of the bias matrix elements (no beam rotation) . . . . .	146
8.5	Effect of beam rotation on bias matrix . . . . .	147
8.6	$C_l$ estimation error due to non-circular beams . . . . .	149
8.7	$C_l$ estimation error published in the WMAP 3yr results [96] . . . . .	150
8.8	Covariance of $C_l$ 's due to beam non-circularity . . . . .	154
9.1	The original Kp2 mask . . . . .	170
9.2	Comparison of mask transforms . . . . .	170
A.1	Plots of the first few orders of Chebyshev polynomials . . . . .	178
B.1	Cone traced out by a radiometer baseline . . . . .	180
B.2	Beam functions in flat latitude-longitude grid . . . . .	181
D.1	Profile of WMAP Q-beam fitted using IRAF . . . . .	190
D.2	IRAF estimated parameters characterizing WMAP beams . . . . .	191

# Acknowledgment

Over the past five years, the research I have carried out would not have been possible without the help of people from IUCAA, the LIGO Scientific Collaboration (LSC) and many others from scientific and nonscientific communities. This thesis is too short to acknowledge all of them, still, I would not miss this opportunity to thank few of the special ones.

I whole heartedly thank my supervisors Prof. Sanjeev Dhurandhar and Prof. Tarun Souradeep for offering me the opportunity to work with them. The care and guidance they have provided me during my Ph.D. has played a crucial role to shape my career as a researcher. I am deeply obliged to Dr. Albert Lazzarini for his support and encouragement during my visit to Caltech. It would not have been possible to finish the thesis in time without his constant supervision. I would thank Prof. Lee Samuel Finn, Dr. Vuk Mandic, Dr. Sukanta Bose, the stochastic group of the LSC and the other members of the LSC for being my collaborators.

My academic work and social activities were greatly benefitted by the help that I got from Prof. J. V. Narlikar, Prof. N. K. Dadhich, Prof. T. Padmanabhan, Prof. A. K. Kembhavi, Prof. S. Tandon, Prof. V. Sahni, Dr. R. Misra, Dr. S. Ravindranath, Dr. S. Engineer, Dr. V. Chellathurai, Ms. S. Ponrathnam, Ms. N. Bawdekar and every other member of IUCAA. I also remember all my past teachers on this occasion, who have equally supported me in the respective stages of my life.

During my stay at IUCAA, it has been a pleasure to be in the constant company of IUCAAns, specially Anand<sup>0</sup>-da, Atul, Rita, Samir, Subharthi-da, Arnab-da, Sudipta, Somu, Susmita, Nirupam, Gauranga, Minu, Arman, Ghazal, Abhishek, Tirtho-da, Sushan-di, Tapan, Himan, Amir, Hum Chand for every little thing. Beyond the world of IUCAA, I fondly remember Rasiya, Aditya, Tapu, Debjani, Manoj, Shweta, Anindya, Rajarshi and all my friends in Kolkata, where my home is.

Finally and very importantly, I could not have gone anywhere in life but for the constant presence of my parents, uncle, brother, Shamin and all the family members.



## List of Publications

1. T. Souradeep, S. Mitra, A. S. Sengupta, S. Ray, and R. Saha, "CMB power spectrum estimation with the non-circular beam", in *Proceedings of the "Fundamental Physics With CMB workshop" March 23-25, 2006, New Astron. Rev.*, vol. 50, p. 1030. 2006. [astro-ph/0608505](#).
2. S. Mitra, S. V. Dhurandhar, and L. S. Finn, "Improving the efficiency of the detection of gravitational wave signals from inspiraling compact binaries: Chebyshev interpolation", *Phys. Rev.* **D72** (2005) 102001, [gr-qc/0507011](#).
3. S. Mitra, A. S. Sengupta, and T. Souradeep, "CMB power spectrum estimation using noncircular beams", *Phys. Rev.* **D70** (2004) 103002, [astro-ph/0405406](#).
4. S. Mitra, S. Dhurandhar, T. Souradeep, A. Lazzarini, V. Mandic, and S. Bose, "Gravitational wave radiometry: Deconvolution of the GWB sky map". In preparation, 2006.
5. S. Mitra, A. S. Sengupta, S. Ray, R. Saha, and T. Souradeep, "CMB power spectrum estimation with the non-circular beam". In preparation, 2006.
6. **LIGO Scientific** Collaboration, B. Abbott *et al.*, "Searching for a stochastic background of gravitational waves with LIGO", [astro-ph/0608606](#).
7. **LIGO Scientific** Collaboration, B. Abbott *et al.*, "Coherent searches for periodic gravitational waves from unknown isolated sources and scorpius x-1: results from the second LIGO science run", [gr-qc/0605028](#).
8. **LIGO Scientific** Collaboration, B. Abbott *et al.*, "Joint LIGO and tama300 search for gravitational waves from inspiralling neutron star binaries", *Phys. Rev.* **D73** (2006) [gr-qc/0512078](#).

9. **LIGO Scientific** Collaboration, B. Abbott *et al.*, "Search for gravitational wave bursts in LIGO's third science run", *Class. Quant. Grav.* **23** (2006) S29, [gr-qc/0511146](#).
10. **LIGO Scientific** Collaboration, B. Abbott *et al.*, "Search for gravitational waves from binary black hole inspirals in LIGO data", *Phys. Rev.* **D73** (2006) 062001, [gr-qc/0509129](#).
11. **LIGO Scientific** Collaboration, B. Abbott *et al.*, "First all-sky upper limits from LIGO on the strength of periodic gravitational waves using the hough transform", *Phys. Rev.* **D72** (2005) 102004, [gr-qc/0508065](#).
12. **LIGO Scientific** Collaboration, B. Abbott *et al.*, "Upper limits on a stochastic background of gravitational waves", *Phys. Rev. Lett.* **95** (2005) 221101, [astro-ph/0507254](#).
13. T. K. Das, J. K. Pendharkar, and S. Mitra, "Multitransonic black hole accretion disks with isothermal standing shocks", *Astrophys. J.* **592** (2003) 1078, [astro-ph/0301189](#).

**Certificate of the Guides**

CERTIFIED that the work incorporated in the thesis “**Gravitational Waves from Inspirling Binaries and Cosmological Ramifications**” submitted by Mr. **Sanjit Mitra** was carried out by the candidate under our supervision/ guidance. Such material as has been obtained from other sources has been duly acknowledged in the thesis.

Prof. Sanjeev Dhurandhar  
(Thesis Supervisor)

Prof. Tarun Souradeep  
(Thesis Co-supervisor)

**Declaration by the Candidate**

I declare that the thesis entitled “**Gravitational Waves from Inspirling Binaries and Cosmological Ramifications**” submitted by me for the degree of Doctor of Philosophy is the record of work carried out by me during the period from **December 2003 to December 2006** under the guidance of **Prof. Sanjeev Dhurandhar & Prof. Tarun Souradeep** and has not formed the basis for the award of any degree, diploma, associateship, fellowship, titles in this or any other University or other institution of Higher learning.

I further declare that the material obtained from other sources has been duly acknowledged in the thesis.

Date:

Place:

Sanjit Mitra



# Abstract

The past five years have ushered in a new era of observational astronomy. Ground based gravitational wave (GW) detectors - LIGO, TAMA and GEO - have started taking science quality data. Space based cosmic microwave background (CMB) experiments - WMAP - has produced a true image of the CMB temperature anisotropy sky and also has mapped the CMB polarization sky. Efficiently extracting maximum amount of science out of these data rich experiments pose challenges to the modern analysis techniques. Few of the issues regarding efficient analysis of data have been addressed in my thesis.

Detection of GW from inspiraling binaries is perhaps the most important experimental goal in experimental general relativity for the next few years. However, extracting the true GW strain signal from much stronger random detector noise is quite challenging. Current analysis strategy relies on matched filtering techniques which is computationally expensive. We have developed an interpolation scheme for efficient implementation of matched filtering based analysis algorithms. We use numerical simulations to show that this new method reduces computational cost, thereby increasing the volume the parameter space that can be searched with the available computing resources.

Measurement of the anisotropy of the CMB and the gravitational wave background (GWB) are equally important challenges in experimental cosmology to probe the history of the early universe. Usually the imaged skymaps are convolved with the instrumental beam functions - also known as the point spread functions (PSF). Unbiased estimation of the anisotropies of these backgrounds requires development of smart analysis strategies. We have analytically formulated and numerically implemented complete analysis frameworks to account for the effects of beam functions in the analysis of CMB and GWB.

The thesis has been organized as follows:

- **Chapter 1** provides an overall introduction and motivation on the works presented in this thesis.
- **Chapter 2** provides an introduction to Gravitational Waves (GW) and its sources, detectors and data analysis, essentially mentioning the features important for the detection of GW.
- The Chebyshev interpolated search algorithm for efficient detection of GW from inspiraling binaries and the results are presented in **Chapter 3**.
- A brief introduction to stochastic Gravitational Wave Background (GWB) and a detailed review of the general radiometer analysis for the detection of GWB has been presented in **Chapter 4**.
- Brief introduction to the theory and experiments of Cosmic Microwave Background (CMB) and its anisotropy, emphasizing points which are relevant to the work presented in this thesis, is provided in **Chapter 5**.
- The analytical formulation of beams and deconvolution in CMB and GWB analysis is presented in **Chapter 6**.
- Implementation of radiometer deconvolution algorithm and application to GWB skymaps obtained from simulated detector outputs is presented in **Chapter 7**.
- The leading order correction to CMB power spectrum due to non-circular beams is estimated using a perturbative analysis in **Chapter 8**.
- General analysis framework for the pseudo- $C_l$  approach to correct for non-circular beams including the effect of incomplete sky coverage is developed in **Chapter 9**.
- The summary of the main results obtained in this thesis and future directions are mentioned in **Chapter 10**.

# Chapter 1

## Introduction

In the past few decades, astronomy, in particular, cosmology has emerged into a precision science. A host of instruments have come up with advanced measurement techniques. These instruments produce large volumes of data and extracting maximum amount of science out of these data is one of the primary goals of modern astronomy and astrophysics.

My thesis concerns with two very important areas of modern astronomy and cosmology - the analysis of data from gravitational wave and cosmic microwave background detectors. Though these detectors work differently, we shall see that the data analysis challenges possess many common attributes.

The overall introduction and motivation of this thesis is provided in this chapter. The discussions presented here will be brief; more detailed material can be found in the subsequent chapters.

### 1.1 Basics

#### 1.1.1 Gravitational Waves (GW)

General theory of relativity (GR) has so far been the unchallenged theory of gravity. Unlike Newtonian theory of gravity, in GR, the effect of gravity does not affect instantaneously - gravitational information travels at the speed of light and the information is carried by the gravitational waves. In the weak field approximation, GW can be considered as an external field over a background space-time - ripples in space-time. GW are massless excitations, hence have two polarizations, + and  $\times$ .

GW interact weakly with matter, which makes them extremely difficult to detect. However, on a positive note, being weakly interacting with matter, GW can

travel large distances without getting absorbed or distorted. Detection of GW is, therefore, not only important to test GR, but promise a whole new possibility of GW astronomy. When gravitational waves are incident on a local coordinate system defined by a set of test masses, the light travel time between two points changes. This principle is exploited for detecting GW. The GW strain is proportional to the distance between particles, so long detectors are desired to improve the sensitivity.

Several detectors are under construction all over the world and proposed. The detectors are either bar detectors (ALLEGRO, EXPLORER, NAUTILUS) sensitive to high (kHz) frequencies or interferometric detectors (LIGO, TAMA, GEO, VIRGO, LISA) at lower (mHz to few hundred Hz) frequencies. Since different sources have different frequency spectrum, each detector is most sensitive to a specific class of sources. The LIGO detectors, currently the most sensitive ones, TAMA and GEO have started taking science quality data, which are being used to put upper limits on important astrophysical quantities. Besides terrestrial GW detectors, there are proposals to build interferometric space antennas.

GW are generated by massive bodies with varying moment of inertia. There are different sources of GW, with different frequency spectra. The sources have been classified into three major types depending on the time scales and characteristics:

1. Burst (inspiraling binaries, supernovae)
2. Stochastic (unmodeled sources, characterized by statistical expectations)
3. Continuous (pulsars)

The data analysis challenges and, therefore, strategies are different for each type of source. In this thesis we have considered an efficient strategy to extract the inspiral waveform from a compact binary system (category 1). Secondly, we analyze and implement targeted search for the stochastic GW background (category 2).

### **1.1.2 Cosmic Microwave Background (CMB)**

The Big Bang theory is the currently accepted working model of the universe. According to the big bang model, the universe was a very hot plasma in its early stages. The photons were tightly coupled to the plasma in thermal equilibrium - attaining a black body distribution. As the universe expanded, the plasma recombined to neutral state where photons could then travel freely. This epoch of recombination is known as the last scattering surface. Photons from the last scattering surface, received continuously from all directions, constitute the relic background. Due to the

expansion of the universe, the photon density has decreased and due to cosmological redshift the wavelengths of the photons have increased. So the temperature of the background has decreased - currently at 2.7K, which corresponds to microwave radiation. Thus the relic electro-magnetic radiation background of the hot early universe is called the cosmic microwave background (CMB).

The early universe was highly homogenous and isotropic. This fact is reflected in the high degree of isotropy of CMB. However, the early universe also had small inhomogeneities, which have grown to form the presently observed structures, like galaxies. These signatures are also present in CMB as  $\mu\text{K}$  fluctuations. CMB anisotropy is an extremely important probe of the early universe. Gaussian and statistically isotropic CMB anisotropy can be completely characterized by its angular power spectrum.

Since the first detection by COBE satellite of CMB anisotropy in 1992, a host of terrestrial, balloon borne and space based experiments to measure CMB anisotropy have been performed, commissioned and being proposed. The earth based experiments include interferometric detectors (e.g., CBI, DASI), scanning detectors (e.g., ACBAR), balloon borne detectors (e.g., BOOMERang, Archeops) and the space based detectors include COBE and WMAP. Another spaced based mission, the Planck surveyor, is planned in 2007. CMB observations have been used to precisely constrain cosmological models and parameters. CMB research has taken the leading role in entering the era of precision cosmology. The precision of the experiments, however, demands unbiased analysis of data. Unbiased estimation of the CMB power spectrum by removing systematic effects is one of the broad concerns of this thesis.

## 1.2 Search for GW from Inspiring Binaries: Chebyshev Interpolation

GW interact weakly with matter, which makes them very difficult to detect. Though the most advanced technologies of microscopic measurements are being used in the gravitational wave experiments, the detector outputs will be dominated by noise. However, the sources of gravitational waves, which are expected to be detected with the modern detectors, have been theoretically modeled. This knowledge can be used to extract signal from noisy data. This is the only possible way of detection of gravitational waves using the detectors which are currently operating or coming up in the near future.

If the phase of the expected signal is precisely modeled, matched filtering is optimal. In the current analysis methodology, a theoretically modeled signal (template) is correlated with data for different sets of parameters that densely cover the physically permitted parameter space and detection will be claimed if the correlation exceeds a pre-assigned threshold. The reason for such a dense coverage of parameter space is to minimize the chance that a real signal, near the detection threshold, will be missed by the parameter space sampling.

The current analysis is computationally expensive. Efforts are being made to develop efficient search algorithms which would allow search over a larger volume of parameter space with greater number of parameters. For small variations in the parameters, the filter responses are strongly correlated, which is the case for a dense search. This is the result of over sampling. The efficiency of search using matched filtering can be improved by optimally sampling the parameter space and then reconstructing the likelihood (or the match) function. We have investigated the use of Chebyshev interpolation for reducing the number of templates that must be evaluated *without sacrificing the efficiency of the search*. Additionally, rather than focus on the “loss” of signal-to-noise associated with the finite number of filters in the template bank, we evaluated the Receiver Operating Characteristic, or ROC, as a measure of the efficiency of a search technique. The ROC relates the false alarm probability to the false dismissal probability of an analysis, which are the quantities that bear most directly on the effectiveness of an analysis scheme.

The time-dependent signature of GW from compact inspiraling binaries is well-characterized function of a relatively small number of parameters, which makes them very promising sources for the ground and space based interferometric detectors. As a demonstration we compared the present “dense sampling” analysis methodology with the “interpolation” methodology using Chebyshev polynomials, restricted to one dimension of the multi-dimensional analysis problem for inspiraling binaries by plotting the ROC curves. We found that the interpolated search can be arranged to have the same false alarm and false dismissal probabilities as the dense sampling strategy using 25% fewer templates. Generalized to the full seven dimensional parameter space that characterizes the signal associated with an eccentric binary system of spinning neutron stars or black holes it suggests an order of magnitude increase in computational efficiency. A reduction in the number of templates evaluations translates directly into an increase in the size of the parameter space that can be analyzed and, thus, the science that can be accomplished with the data.

### 1.3 Search for GW Background: Radiometer Analysis

The stochastic GW background arises from unresolved astrophysical sources and is predicted from the physics of the early universe. The measurement of the GW background (GWB) can probe the inhomogeneities of the nearby universe and important phenomena, like inflation, in the early universe.

By definition, stochastic signals are characterized by expectation values. The best strategy to detect GWB is to correlate the outputs of different detectors that have independent noise. The correlation between noise streams will tend to cancel on time integration, but the common GW signal will add. This principle can be used to measure the sky averaged strength of the GWB, as well as, to make a sky map. The sky map is made by introducing a phase shift between the detector outputs that accounts for the delay between two detectors in receiving a signal from a certain direction. Signals from a target direction is coherently added and signals from other direction tend to cancel out. This method is similar to the earth rotation image synthesis used in interferometric radio astronomy, hence we name this analysis as GW radiometer. Extending primary work on GW radiometry for special cases of GWB, we have developed a general GW radiometer analysis strategy, which can be applied to a broad range of GWB models.

### 1.4 Deconvolution of Sky-Maps

The observed sky maps of the GWB and CMB are both convolved with a beam (or a point spread function) - the image of a point source is not a point source, it is a pattern of finite size. The estimation of the true skymap requires correction of the observed "dirty" maps to eliminate the effects of the antenna pattern functions.

Unlike CMB experiments, the beam function of a GW radiometer has a highly asymmetric pattern. The beam patterns also depend on the sky position. Our first goal was to understand the beam pattern of the radiometer search. We used stationary phase approximation (SPA) to analytically explain the beam patterns which matched very well with the numerically obtained ones.

The next step was to remove the effect of beam function from the dirty maps. Several deconvolution algorithms exist in literature. Because of the broad similarity between the convolution equations of GWB and CMB, we followed a method that has been successfully applied in CMB analysis - the maximum likelihood (ML) sky map estimation. We have developed the deconvolution algorithm for GWB

sky-maps based on the statistical and numerical methods suggested by the CMB analysts. The method was numerically implemented and injected test maps were recovered with a fairly good accuracy.

## 1.5 Non-circular Beam Correction to CMB Power Spectrum

The measurements of the angular power spectrum of the Cosmic Microwave Background (CMB) anisotropy has proven crucial to the emergence of cosmology as a precision science in recent years. In this remarkable data rich period, the limitations to precision now arise from the inability to account for finer systematic effects in data analysis.

The optimal analysis to account for the effect of the beam function, a full maximum likelihood (ML) analysis, is computationally prohibitive because of high resolutions of CMB experiments. Currently sub-optimal pseudo- $C_l$  analysis seems to be the only feasible way. The pseudo- $C_l$  estimator is defined as the power spectrum of the observed CMB anisotropy sky map obtained from the time ordered data assuming a circularly symmetric experimental beam of infinite resolution. The correction due to the non-circular experimental beam of finite resolution is applied to the pseudo- $C_l$  estimator in order to get the unbiased estimate of the true angular power spectrum.

The non-circularity of the experimental beam has become progressively important as CMB experiments strive to attain higher angular resolution and sensitivity. We have developed a complete analysis framework to study the effects of a non-circular beam on the CMB power spectrum estimation. First we find the leading order correction due to non-circular beam alone. Next, we present a general analytic framework to find the bias on CMB power spectrum due to the non-circular beams, where we include the effect of incomplete sky coverage in analytical calculations that was considered only numerically in the previous analysis. We also suggest apodized (azimuthally smoothed) masks, which reduce the computation required to implement our analysis and still mask pixels strongly contaminated by our galaxy and point sources. We consider a mildly non-circular beam, which allows us to perform a perturbative analysis. We compute the bias in the pseudo- $C_l$  power spectrum estimator and then construct an unbiased estimator using the bias matrix. The covariance matrix of the unbiased estimator is computed for smooth, non-circular beams. Quantitative results are shown for CMB maps made by a *hypothetical* experiment with a non-circular beam comparable to our fits to the WMAP

beam maps described in an appendix and uses a *toy* scan strategy. We find that significant effects on CMB power spectrum can arise due to non-circular beam on multipoles comparable to, and beyond, the inverse average beam-width where the pseudo- $C_l$  approach may be the method of choice due to computational limitations of analyzing the large datasets from current and near future CMB experiments. Recently WMAP team have corrected for the non-circular beam effect in their 3 year results. The estimated effect is in good agreement with the prediction of our method for a WMAP-like beam.

## 1.6 Organization of the Thesis

The thesis has been organized as follows: Chapter 2 provides an introduction to GW and its sources, detectors and data analysis, essentially mentioning the features important for the detection of GW. The Chebyshev interpolated search algorithm for efficient detection of GW from inspiraling binaries and the results are presented in chapter 3. A brief introduction to stochastic GWB and a detailed review of the general GW radiometer analysis for the detection of GWB has been presented in chapter 4. A brief introduction to the theory and experiments of CMB, emphasizing points which are relevant to the work presented in this thesis, is described in chapter 5. The analytical formulation of beams and deconvolution in CMB and GWB analysis is presented in chapter 6. Implementation of radiometer deconvolution algorithm and application to GWB skymaps obtained from simulated detector outputs is presented in chapter 7. General pseudo- $C_l$  approach to correct for non-circular beams is described in the next two chapters - leading order correction is estimated using a perturbative analysis in chapter 8 and the general analysis framework including the effect of incomplete sky coverage is developed in chapter 9. The summary of the main results obtained in this thesis and the future directions are mentioned in chapter 10.



## Chapter 2

# Introduction to Gravitational Waves (GW)

The General theory of Relativity (GR) predicts the existence of Gravitational Waves (GW). GR has so far been the unchallenged theory of gravitation. It provides a geometrical interpretation of gravity by incorporating special theory of relativity and Newton's law of gravitation. Unlike Newton's theory, gravitational interaction is not instantaneous, gravitational information travels at the speed of light and, analogous to electromagnetic waves in case of electrodynamics, this information is carried by Gravitational Waves.

Although it was possible to detect GW through the observations of Hulse-Taylor binary pulsars, the direct detection of GW has not been possible so far. Several ground based interferometric GW observatories, namely TAMA, LIGO, GEO, are already generating science quality data and the Virgo detector is in the commissioning stage. The LIGO is presently the most sensitive GW detector, it is operating at the initial design sensitivity for the past one year. The space based observatories, LISA and DECIGO, are flying within a decade. Detection of GW will undoubtedly be an exciting development in experimental general relativity - it is not only important to test general relativity, but it promises a whole new astronomy inaccessible to the electromagnetic regime.

GW are generated by different types of sources, e.g., coalescing compact binary stars, rotating neutron stars and primordial density fluctuations near the big bang. Different analysis strategies are used to search for different kind of sources.

In this chapter, I briefly mention some parts of the basic theory of gravitational waves and their sources, detection and data analysis. Only those parts are consid-

ered here which are relevant to the work done in this thesis. For further details see standard references, e.g., [1,2,3,4,5,6,7] and references therein.

## 2.1 Gravitational Waves

### 2.1.1 General Relativity: Einstein's Equation

Albert Einstein, almost single handedly, formulated the relativistic theory of gravity, the General theory of Relativity (GR) in the year 1915. GR, being a relativistic theory, incorporates the maximum information propagation speed - the velocity of light in vacuum. The gravitational information also travels at this speed and the information is carried by gravitational waves.

Instead of treating gravity like other forces in nature, Einstein gave a geometric interpretation to gravity - the curvature and dynamics of space-time are controlled by the distribution and kinematics of energy ( $\equiv$  mass). This relation is formally expressed by the famous Einstein's equation (without the cosmological constant)

$$G_{\mu\nu} = \frac{8\pi G}{c^4} T_{\mu\nu}, \quad (2.1)$$

where  $G$  is the universal constant of Gravitation,  $c$  is the maximum velocity of information propagation (which is same as the velocity of light in vacuum),  $G_{\mu\nu}$  is the curvature tensor and  $T_{\mu\nu}$  is the energy-momentum tensor. Formal definitions of these quantities can be found in any standard text on GR, e.g., [2]. The indices of the four vectors/tensors run from 0 to 3, where 0 corresponds to the time-like component and 1, 2, 3 correspond to the three space-like components. The metric of space-time  $g_{\mu\nu}$  can be obtained by solving Einstein's equation. The energy momentum tensor determines the metric and the metric, in turn, determines the dynamics of the energy-momentum tensor - this makes Einstein's equation highly nonlinear, and hence difficult to solve exactly except in very few special cases.

### 2.1.2 Weak field limit: Linearized Theory

Solving Einstein's equation becomes manageable in the weak field limit, where the curvature of space-time, measured by the Riemann-Christoffel curvature tensor  $R_{\mu\nu\alpha\beta}$ , can be regarded as "small",  $R_{\mu\nu\alpha\beta} \rightarrow 0$ . In flat space-time there exists a coordinate system where the metric is Minkowski type,  $\eta_{\mu\nu}$ , where  $\eta_{\mu\nu}$  is a diagonal matrix with diagonal elements  $(-1, 1, 1, 1)$ . Similarly, far away from massive bodies,

where gravity is weak, there exists a coordinate system where the metric is perturbed Minkowski<sup>1</sup> [4]

$$g_{\mu\nu} = \eta_{\mu\nu} + h_{\mu\nu}, \quad (2.2)$$

with  $|h_{\mu\nu}| \ll 1$  over the whole nearly flat volume of space-time. The metric perturbations  $h_{\mu\nu}$  transform like a tensor under Lorentz boosts  $\Lambda_{\beta}^{\alpha}$ ,

$$h'_{\mu\nu} = \Lambda_{\mu}^{\alpha} \Lambda_{\nu}^{\beta} h_{\alpha\beta}, \quad (2.3)$$

preserving the form of the metric given by eqn (2.2). This convenient fact gives us the freedom to treat metric perturbations as a separate tensor field propagating over a background space-time with constant metric coefficients. This is the key strategy to understand gravitational interaction in a perturbative way.

The metric perturbations satisfy two sets of Gauge conditions which are utilized to obtain mathematical simplicity.

#### Lorentz/harmonic gauge:

Under a coordinate transformation of the form

$$x^{\mu} \rightarrow x^{\mu} + \xi^{\mu}(x^{\nu}), \text{ such that, } |\xi_{,\nu}^{\mu}| \ll 1, \quad (2.4)$$

the metric preserves the form given by eqn (2.2) if the perturbations are transformed using the formula

$$h_{\mu\nu} \rightarrow h_{\mu\nu} - \xi_{\nu,\mu} - \xi_{\mu,\nu}. \quad (2.5)$$

The above Gauge freedom allows us to choose a coordinate system where the *trace reversed* metric perturbations,

$$\bar{h}_{\mu\nu} := h_{\mu\nu} - \frac{1}{2}\eta_{\mu\nu}h^{\alpha}_{\alpha}, \quad (2.6)$$

are *divergenceless*,

$$\bar{h}_{\mu\nu}{}^{,\nu} = 0. \quad (2.7)$$

With these *four* coordinate conditions, Einstein's equation in free space takes the form of a wave equation

$$\square \bar{h}_{\mu\nu} = 0. \quad (2.8)$$

---

<sup>1</sup>It is also possible to consider a curved space-time as the background, which is routinely done for studying metric perturbations in the early universe or close to a black hole

This equation is quite similar to the Maxwell's equation in vacuum in electrodynamics and, analogous to electromagnetic radiation, solutions to this equation describe the propagation of Gravitational Waves (GW). This form clearly suggests that *GW travel at the velocity of light and the amplitude of a spherical wavefront is inversely proportional to the radial distance.*

The general solution to the gravitational wave equation [eqn (2.8)] can be formally written as

$$\bar{h}_{\mu\nu} = \bar{h}_{\mu\nu}(k^\alpha x_\alpha), \text{ such that } k^0 := \omega = |\mathbf{k}|, \quad (2.9)$$

where  $\mathbf{k} \equiv k^a$ ,  $a = 1, 2, 3$ . The Lorentz gauge condition, eqn (2.7), then implies

$$\bar{h}_{\mu\nu} k^\nu = 0, \quad (2.10)$$

that is, the wave solutions are orthogonal to the propagation 4-vector  $k^\mu$ .

### Transverse-Traceless (TT) Gauge:

The Lorentz gauge condition is preserved under coordinate transformations of the form

$$x^\mu \rightarrow x^\mu + \xi^\mu(x^\nu), \text{ such that, } \square \xi^\mu = 0. \quad (2.11)$$

These *four* gauge conditions can be used to minimize the number of non-vanishing  $h_{\mu\nu}$  to (twice) the number of degrees of freedom. Usually the gauge is chosen such that the metric perturbations have the following properties:

1. *Traceless*, that is,

$$\bar{h}^\alpha_\alpha = 0. \quad (2.12)$$

Obviously, this condition implies  $\bar{h}_{\mu\nu} = h_{\mu\nu}$ .

2. Orthogonal to a chosen time like vector  $U^\mu$

$$h_{\mu\nu} U^\mu = 0. \quad (2.13)$$

Usually one chooses  $U^\mu = \delta_0^\mu$ , so that, all the timelike components of the metric perturbations vanish,  $h_{\mu 0} = h_{0\mu} = 0$ .

These coordinate conditions (in Lorentz gauge) make GW *transverse* to the propagation direction [6], as explained below.

Imposing the above *eight* gauge conditions and choosing  $U^\mu = \delta_0^\mu$  one can see that the metric perturbations can be completely parameterized by *two* independent polarization amplitudes  $h_+(x^\mu)$  and  $h_\times(x^\mu)$ :

$$h_{\mu\nu} = h_+ e_{\mu\nu}^+ + h_\times e_{\mu\nu}^\times, \quad (2.14)$$

where  $\mathbf{e}^+ \equiv e_{\mu\nu}^+$  and  $\mathbf{e}^\times \equiv e_{\mu\nu}^\times$  are the polarization 4-tensors:

$$\mathbf{e}^+ := \begin{pmatrix} 0 & 0 & 0 & 0 \\ 0 & 1 & 0 & 0 \\ 0 & 0 & 1 & 0 \\ 0 & 0 & 0 & 0 \end{pmatrix}; \quad \mathbf{e}^\times := \begin{pmatrix} 0 & 0 & 0 & 0 \\ 0 & 0 & 1 & 0 \\ 0 & -1 & 0 & 0 \\ 0 & 0 & 0 & 0 \end{pmatrix}. \quad (2.15)$$

Since, with the above choice of coordinates  $h_{\mu 0} = h_{0\mu} = 0$ , we may represent the metric perturbations only by the 3-tensor

$$h_{ab} = h_+ e_{ab}^+ + h_\times e_{ab}^\times, \quad a, b = 1, 2, 3, \quad (2.16)$$

where the polarization tensors  $e_{ab}^{+, \times}$  are now 3-tensors - the first row and the first column from the 4-tensors in the definitions given in eqn (2.15) have been removed. One can now write the transversality condition, eqn (2.10), in terms of the quantities dependent only on the three spatial indices:

$$h_{ab} k^b = 0, \quad a, b = 1, 2, 3, \quad (2.17)$$

where the 3-vector  $\mathbf{k} \equiv k^a$ ,  $a = 1, 2, 3$  is the wave propagation direction. Thus, in the TT gauge, gravitational waves are orthogonal to the direction of propagation.

Note that in the TT gauge when gravitational waves fall on free particles the coordinates of the particles do not change. However, the metric perturbations do change the light travel time delay between two points. This is a coordinate independent quantity and, therefore, this fact is exploited in the gravitational wave detectors. In any coordinate system, gravitational waves appear as propagating waves of varying tidal forces. The expression for these variations can be computed from the geodesic deviation equation [2].

### 2.1.3 Plane Polarized Monochromatic Gravitational Waves

The plane polarized monochromatic solution to the GW equation [eqn (2.8)] is given by  $h_{\mu\nu}(k^\alpha x_\alpha) = A_{\mu\nu} \exp(ik^\alpha x_\alpha)$ , where  $A_{\mu\nu}$  are coordinate independent quantities. In the TT gauge this solution can be equivalently expressed by choosing the polarization modes ( $A = +, \times$ ) in eqn (2.16) as  $h_A(x^\mu) = \tilde{h}_A(f, \hat{\Omega}) \exp[2\pi i f(t - \hat{\Omega} \cdot \mathbf{x}/c)]$ , where  $f = k^0/(2\pi)$  is the frequency of the monochromatic wave, the unit 3-vector  $\hat{\Omega} := \mathbf{k}/|\mathbf{k}|$  is the direction of propagation,  $t = x_0/c$  is time,  $\mathbf{x} \equiv x_i$ ,  $i = 1, 2, 3$  is the 3-vector for spatial coordinates and  $\tilde{h}_A(f, \hat{\Omega})$  is the amplitude of a plane wave propagating in the direction  $\hat{\Omega}$  with frequency  $f$ . The importance of the plane wave solution is quite obvious - waves from distance sources can be regarded as the superposition of plane monochromatic waves.

When a plane polarized monochromatic GW is normally incident on a circular ring of particles the ring gets sheared as shown in figure 2.1, taken from the gallery “LISA images” [8]. The direction of shear is different for different polarizations. Figure 2.1 illustrates that the polarizations of GW are at an angle of  $45^\circ$ , as expected for a spin 2 field. The figure also outlines how this phenomenon is exploited in the interferometric GW detectors.

## 2.2 Detection

Gravitational waves were indirectly detected by R. A. Hulse and J. H. Taylor in the year 1974. They measured the decrease in orbital period with time of the double pulsar system PSR B1913+16 [9], which precisely matched (within 0.2% after 30 years of observation [10]) the theoretically expected variation due to the radiation of GW by the binary system. Hulse and Taylor got the Nobel prize for Physics in the year 1993 for this remarkable discovery.

Direct detection of gravitational waves is perhaps the most important challenge in experimental general relativity of recent times. Detection of GW is not only important as a highly convincing test of GR, but it promises a whole new astronomy inaccessible to the electromagnetic regime.

The main principle of detection is to measure the (coordinate independent) variation of light travel time between different points when GW is incident on a detector. Since the variation of light travel time between two points is proportional to the distance between the points, longer detectors are preferred for better sensitivity. Two kinds of detectors are currently being used for the detection of GW:

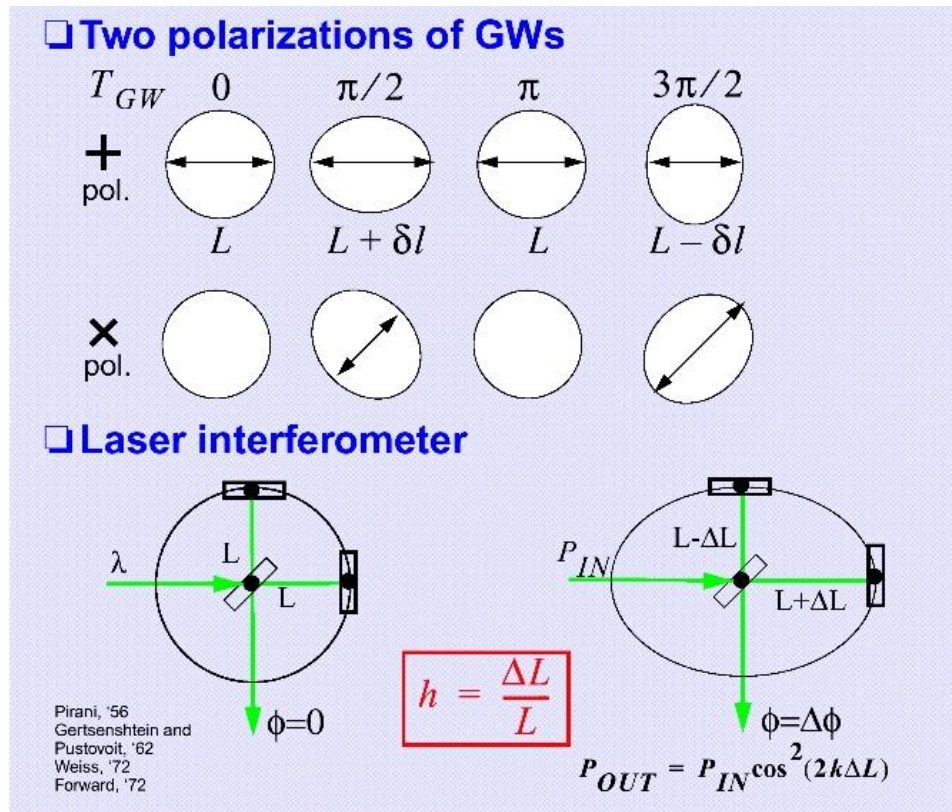


Figure 2.1: **Effect of GW on matter: Detection scheme.** When a plane polarized monochromatic GW is incident normally on a ring of particles, the ring gets sheared and the direction of shear is dependent on the polarization of the wave as shown in the top panel titled "Two polarizations of GWs". The angle between the two polarizations is  $45^\circ$ , as expected for a spin 2 field. The bottom panel illustrates how this effect is exploited in the (Michelson) interferometric GW detectors. This figure is taken from the gallery "LISA images" [8].

- **Resonant bar detectors:** As the name suggests, a detector of this kind is essentially a bar of heavy material. GW, while passing through the bar, excite the near characteristic (resonant) frequency modes of the bar and these excitations are read using sophisticated coupled oscillators.

The resonant bar detector made by Weber around 1968 is the first ever GW detector, though the claim of GW detection [11] using this detector could not be verified by the scientific community. The present cryogenically cooled bar detectors are much more advanced; many of them in different countries are currently operating e.g., ALLEGRO (USA) [12], NAUTILUS (Italy) [13], AURIGA (Italy) [14], EXPLORER (Switzerland) [15]. Bar detectors are sensitive

to high frequencies ( $\sim$  kHz), so core collapse supernovae are the most promising sources for these detectors. These detectors, in combination to other bar or interferometric detectors, are being used to put upper limit on a stochastic background. Different omnidirectional shapes, e.g., spherical and “truncated icosahedral”, for this kind of detectors are also being built. The examples are MiniGRAIL (Netherlands) [16] and TIGA (USA) [17]. The image of the ALLEGRO bar detector at Luisiana State University, is shown in the left panel of figure 2.2 (image taken from “ALLEGRO Archive Photos” [18]).



Figure 2.2: **GW Detectors.** The left panel shows the ALLEGRO bar detector at Luisiana, US (image taken from “ALLEGRO Archive Photos” [18]). The right panel shows an aerial view of the LIGO detector at Hanford, US. This instrument, in fact, hosts two detectors of 4km and 2km arms (image taken from “LIGO Press & Media Kit: LIGO photos” [19]).

- **Interferometric detectors:** These detectors are very long (kilometer arm for ground based and thousands to millions kilometer for space based) power-recycled Michelson’s inferometers. As illustrated in the previous section, when GW fall on a long Michelson interferometer, the light travel times in different arms change, which result in a fringe shift in the output port of the interferometer. Extracting true GW strain signal from the time series of fringe shifts is the most promising way of detecting GW.

As many as six ground based inteferometric detectors in different countries are either currently operating or in the commissioning stages, they are: two LIGO (USA) detectors [20,21] - at Livingston (LLO) and at Hanford (LHO), TAMA (Japan) [22,23], GEO (Germany + UK) [24,25], Virgo (France + Italy) [26,27] and AIGO of ACIGA (Australia) [28,29]. The TAMA team is also

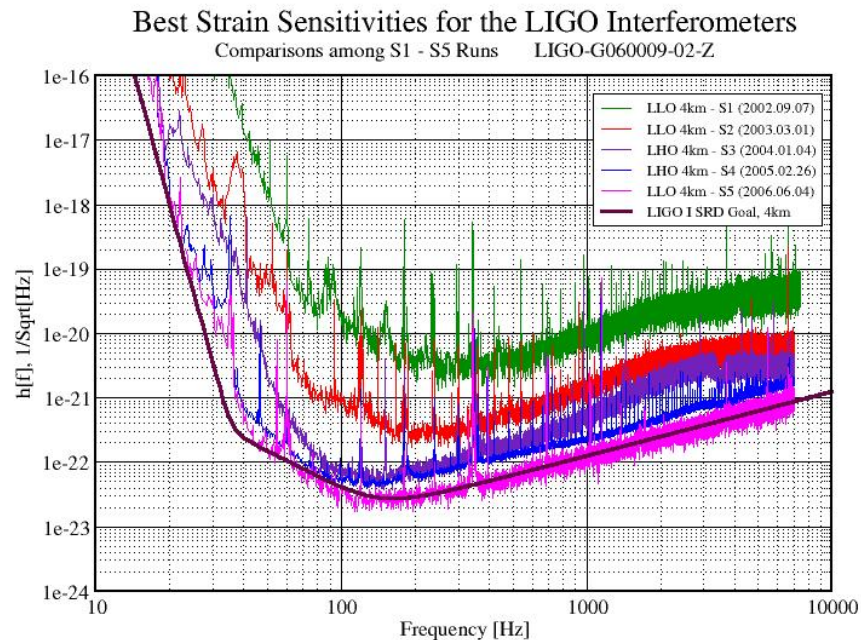


Figure 2.3: **LIGO-I sensitivity curves.** The noise Power Spectral Densities (PSDs) of the LIGO detectors are overlaid on the goal sensitivity of the first generation LIGO detector. LIGO has reached the goal sensitivity in the fifth science run (S5), which is on for the last one year. Image taken from the “[LIGO Sensitivity](#)” website [32].

making a cryogenically cooled ground based interferometric detector LCGT (Japan) [30,31].

An aerial view of the LIGO detector at Hanford, USA is shown in the right panel of figure 2.2 (image taken from “[LIGO Press & Media Kit: LIGO photos](#)” [19]). The ground based interferometric detectors are most sensitive near few 100 Hz; coalescing stellar mass inspiraling binaries are the most promising sources for the interferometric detectors. The sensitivity curves, the plot of square root of noise Power Spectral Density (PSD) with frequency, of the LIGO detectors for different science runs are overlaid on the sensitivity goal in figure 2.3, taken from the “[LIGO Sensitivity](#)” website [32]. The LIGO detectors are operating at the first stage (LIGO-I) goal sensitivity for the last one year. The advanced LIGO sensitivity is targeted within the next few years.

Two space based interferometric detectors, LISA (ESA + NASA) [33,34,35] and DECIGO (Japan) [36], each consisting of three satellites forming a triangular

configuration with huge arm-lengths ( $5 \times 10^6$  km for LISA and  $10^5$  km for DECIGO), are also expected within a decade. It is much easier in space to isolate the low frequency noise, as no seismic vibration is present there. (However, due to the variation of distances between the spacecrafts, the cancellation of laser frequency noise will require post-processing of detector outputs using Time Delay Interferometry [37].) LISA and DECIGO will operate in a low frequency range (milli-Hertz and deci-Hertz respectively) and hence they are expected to receive very high energy from high mass binary systems, which emit at low frequencies. These satellites are also important for putting better upper limits on the stochastic background. A space based observatory, the Big Bang Observer (BBO) [38, 39], consisting of multiple satellites, is being planned as part of NASA's Beyond Einstein program [40]; it is expected to precisely measure the cosmological GWB originated during inflation in the very early universe.

The GW event rate is proportional to the observed volume of space and the amplitude of GW is inversely proportional to the distance. Therefore, the probability of GW detection increases as the cube of sensitivity. Advanced LIGO will undergo about an order of magnitude improvement in sensitivity as compared to the LIGO-I detectors; which means that the advanced LIGO detector is thousand times more likely to detect a GW event, while the event rate for LIGO-I is just one in few years. Thus, the possibility of detection of GW in the next few years is very high.

### 2.3 Sources and Analysis Strategies

Different kinds of sources generate GW with different frequency spectra. The analysis strategies also depend on the kind of sources one is trying to detect. The three broad classification of sources and their detection strategies are listed below.

1. **Burst:** Compact inspiraling binaries in the last few cycles before coalescence and supernova core collapse release highly energetic GW in very short time. They are called burst sources.

The GW signals from inspiraling binaries have been precisely modeled using Post-Newtonian approximations [41], hence matched filtering can be used for extracting the true GW signal buried inside strong detector noise. Therefore, the coalescing compact binaries, in particular, the stellar mass binaries which emit in the sensitive frequency band of the ground based interferometric

detectors, are the most promising candidates for the detection of GW. More details on the detection strategy of these sources can be found in chapter 3.

On the other hand, the sources like supernovae are unmodeled high frequency ( $\sim 1$  kHz) sources. The analysis strategy to detect such sources makes use of excess power statistics technique.

2. **Stochastic:** Unmodeled and unresolved sources of astrophysical and cosmological origin constitute a stochastic GW Background (GWB). The cosmological background is analogous to the Cosmic Microwave Background (CMB) and the astrophysical background is analogous to the galactic foreground observed while making CMB skymaps. The detection of cosmological GWB will be a direct probe of inflation and some other important phenomena in the early universe.

Since the stochastic signals are unmodeled and characterized by their statistical expectation values. The best strategy to detect stochastic sources (or put upper limits) is by correlating outputs of two detectors (which can be of different types - bar and interferometric, say) - forming a GW radiometer. The GW radiometer analysis can be tuned to measure the all sky averaged power of the stochastic background, as well as, to make a sky map of the GWB anisotropy.

The stochastic background is of major interest in this thesis. A more detailed introduction to the stochastic sources and the complete radiometer analysis are presented in chapter 4, chapter 6 and chapter 7.

3. **Continuous:** Sources which emit GW continuously over the full observation time of a detector without significant change in the characteristics are called continuous sources. Asymmetric pulsars and inspiraling binaries, which are not in the final few cycles before coalescence, are the examples of such sources.

The locations, and also the phase evolutions, of many radio pulsars are quite precisely known from electromagnetic astronomy. So a targeted search, by correlating signals from two detectors with a time dependent phase factor that accounts for the light travel time delay between two detectors, is the best strategy for the detection of GW from known radio pulsars. Search for unknown pulsars is computationally costly, as the parameter space (which includes position coordinates) is quite big. The Einstein@Home project [42], in a similar line as the SETI@home project [43], offers a nice solution to utilize idle computational resources to search for unknown pulsars.

## 2.4 Summary and Conclusion

Gravitational wave research is reaching new dimensions as the current detectors are producing science quality data and many ground and space based detectors are coming up. Brief introduction to the theory, detection, sources and data analysis of gravitational waves were presented in this chapter.

General theory of Relativity (GR) predicts Gravitational Waves (GW). In the weak field limit GW can be treated as an independent tensor field propagating over a constant (flat) background. GW travel at the speed of light and follows many other properties similar to the electromagnetic waves, except for polarizations - GW are spin 2 excitations, so the polarization axes are at an angle  $45^\circ$ .

GW change the light travel time between different points, which is exploited in the GW detectors. Two kinds of detectors are currently being used - bar detectors and interferometric detector. The ground based interferometric detector, LIGO, is operating at its first stage goal sensitivity for the last one year. Many more ground based and two space based detectors are coming up within a decade.

Different kinds of sources emit GW, which can be classified in three major classes - burst, stochastic and continuous. The analysis strategies for different sources are also different. Compact inspiraling binaries in the last few cycles before coalescence are theoretically well modeled sources, hence matched filtering can be used for these sources. Therefore, the stellar mass compact binaries, which emit in the sensitive bands of the ground based interferometric detectors, are the most promising sources for the detection of GW. data analysis strategies for detecting GW signal from inspiraling binaries and stochastic background are principal goals of this thesis.

The existence of GW has been indirectly established by Hulse and Taylor from the observations of the binary pulsar B1913+16. However, the direct detection of GW is still awaited. Worldwide efforts are being made to detect GW not only to perform a crucial test of GR, they promises a whole new astronomy inaccessible to the conventional electromagnetic regime. The advanced detectors, scheduled to come up in the next few years, are expected to have a very high probability of detection of GW. The detection of GW will be an extremely important achievement in experimental GR. The main goal of this thesis is the development of analysis techniques which can efficiently extract GW signals from the output of the modern gravitational wave detectors.

## Chapter 3

# Search for GW from Inspiring Binaries: Chebyshev Interpolation

Gravitational waves interact weakly with matter, which makes it very difficult to detect. Though the most advanced technologies of microscopic measurements are being used in the gravitational wave experiments, the detector outputs will be dominated by noise. However, the sources of gravitational waves, which are expected to be detected with the modern detectors, have been theoretically modeled. This knowledge can be used to extract signal from noisy data. This is the only possible way of detection of gravitational waves using the detectors which are currently operating or coming up in the near future.

Inspiring compact-object binary systems are promising gravitational wave sources for ground and space-based detectors. The time-dependent signature of these sources is well-characterized function of a relatively small number of parameters; thus, the favored analysis technique makes use of matched filtering and maximum likelihood methods. As the parameters that characterize the source model vary, so do the templates against which the detector data are compared in the matched filter.

Current analysis methodology samples a bank of filters whose parameter values are chosen so that the correlation between successive samples from successive filters in the bank is 97%. Correspondingly, the additional information available with each successive template evaluation is, in a real sense, only 3% of that already provided by the nearby templates. The reason for such a dense coverage of parameter space is to minimize the chance that a real signal, near the detection threshold, will be missed by the parameter space sampling.

The current analysis is computationally costly. Efforts are being made to develop efficient search algorithms which would allow search over a larger volume of parameter space with greater number of parameters. For small variations in the parameters, the filter responses are closely correlated. The efficiency of search for inspiraling binaries can be improved by reconstructing the likelihood (or the match) function using sample values of the match function over the parameter space. We have investigated the use of Chebyshev interpolation for reducing the number of templates that must be evaluated to obtain the same analysis sensitivity [44]. Additionally, rather than focus on the “loss” of signal-to-noise associated with the finite number of filters in the template bank, we evaluated the Receiver Operating Characteristic, or ROC, as a measure of the effectiveness of an analysis technique. The ROC relates the false alarm probability to the false dismissal probability of an analysis, which are the quantities that bear most directly on the effectiveness of an analysis scheme.

As a demonstration we compared the present “dense sampling” analysis methodology with the “interpolation” methodology using Chebyshev polynomials, restricted to one dimension of the multi-dimensional analysis problem by plotting the ROC curves. We found that the interpolated search can be arranged to have the same false alarm and false dismissal probabilities as the dense sampling strategy using 25% fewer templates. Generalized to the two dimensional space used in the computationally-limited current analyses this suggests a factor of two increase in computational efficiency; generalized to the full seven dimensional parameter space that characterizes the signal associated with an eccentric binary system of spinning neutron stars or black holes it suggests an order of magnitude increase in computational efficiency. Since the computational cost of the analysis is driven almost exclusively by the matched filter evaluations, a reduction in the number of templates evaluations translates directly into an increase in computational efficiency; additionally, since the computational cost of the analysis is large, the increased efficiency translates also into an increase in the size of the parameter space that can be analyzed and, thus, the science that can be accomplished with the data.

In this chapter, I first give a brief introduction to (Newtonian) Chirp signals. I summarize the current analysis technique to search for inspiraling binaries based on matched filtering. Then I mention about the ongoing efforts to develop efficient search technique. Rest of the chapter is devoted to the method developed by us using Chebyshev interpolation and illustrate its efficiency in comparison to the dense search.

### 3.1 Chirp Signal

Inspiring compact binaries of stellar mass neutron stars or black holes are among the most important gravitational wave sources accessible to the current generation of ground-based interferometric gravitational wave detectors [45, 46, 47, 48]. They are also very “clean” systems, in the sense that the gravitational wave signal arising from the inspiral depends only on general relativity (eg., the structure of the binary components is unimportant) and can be calculated to great accuracy by the well-understood techniques of post-Newtonian perturbation theory [49, 50, 41].

The gravitational wave signature of inspiraling binary systems depends on a set of 15 parameters that characterize the system (i.e., component masses, orbital energy and angular momentum at a given epoch, component spins, orientation relative to detector line of sight). The signal from inspiraling binaries vary most rapidly, however, along the axis spanned by the so called “Chirp mass”:

$$\mathcal{M} := \mu^{3/5} M^{2/5}, \quad (3.1)$$

where  $M$  is the system’s total mass and  $\mu$  its reduced mass. For reasons that will be elaborated later, in this work we would only consider the Chirp mass parameter.

The strain response of an interferometric detector due to gravitational waves incident from an inspiraling binary neutron star system, to quadrupolar approximation, can be written as

$$h(t|t_a, \tau_0) = h_0 [\pi f(t - t_a - \tau_0) \mathcal{M}]^{2/3} \cos \Phi(t - t_a - \tau_0), \quad (3.2a)$$

where

$$f(t|t_a, \tau_0) := \frac{1}{\pi \mathcal{M}} \left( \frac{5}{256} \frac{\mathcal{M}}{\tau_0 + t_a - t} \right)^{3/8}, \quad (3.2b)$$

$$\Phi(t|t_a, \tau_0) := \Phi_a + 2\pi \int_t^{t_a + \tau_0} dt f(t|t_a, \tau_0) \quad (3.2c)$$

for  $t < t_a + \tau_0$ . Here  $t_a$  is the moment when the instantaneous wave frequency is equal to  $f_a$  and  $\tau_0$  is the elapsed time from that moment until (in this approximation) the system coalesces, which is directly related to the system’s chirp mass  $\mathcal{M}$ :

$$\tau_0 = \frac{5}{256\pi f_a} \frac{1}{(\pi \mathcal{M} f_a)^{5/3}}. \quad (3.3)$$

A typical signal is shown in the top panel of figure (3.1). The amplitude as well as frequency of the GW signal from inspiraling binaries increase with time, hence they are often called “Chirp”. The waveform formula given above is calculated using the quadrupolar approximation and Newton’s law of gravitation, the signal is thus called Newtonian Chirp. Its shape depends only on the Chirp mass parameter.

Chirp signals have been modeled to a very high degree of accuracy using the post-Newtonian<sup>1</sup> (PN) approximation of order 3.5 — the error in phase variation is less than one in every few thousands cycles, which is the typical number of cycles while the frequency of the wave is in the sensitive bands of the modern ground based detectors. However, like the Newtonian waveforms, very precise Chirp waveforms are also highly sensitive to the Chirp mass as compared to other physical parameters characterizing the compact binary. In this work we are interested in studying the relative performances of different search algorithms. We use a one dimensional parameter space to compare the performances of two methods, which, we believe, can be extrapolated to higher dimensions. It is quite obvious that, for a one dimensional analysis, we should consider only the most important intrinsic parameter, the Chirp mass, and the Newtonian Chirp waveform, as its shape is entirely determined by the Chirp mass. This explanation will be repeated in the context of computational cost in the next section.

The elapsed time to coalescence  $\tau_0$  is a useful surrogate for the chirp mass  $\mathcal{M}$ : templates equispaced in  $\tau_0$  have constant cross-correlation, independent of  $\tau_0$ . Choosing  $f_a$  equal to 40 Hz, which is commonly taken as the lower-edge of the LIGO detector bandwidth at design sensitivity [51],  $\tau_0$  ranges from approximately 43 s for a binary system consisting of two  $1 M_\odot$  compact objects to 0.15 s for a binary consisting of two  $30 M_\odot$  black holes.

It will soon become clear that working in the frequency domain is quite convenient. For neutron star binaries in the LIGO or Virgo band the Fourier transform can be evaluated to an excellent approximation using the stationary phase approximation [52]:

$$\tilde{h}(f) = \mathcal{N} f^{-7/6} \exp \{i [-\Phi_a - \pi/4 + \Psi(f|t_a, \tau_0)]\}, \quad (3.4a)$$

---

<sup>1</sup>Post-Newtonian approximation is a perturbative analysis, where Einstein’s equations are expanded as a power series in relative velocity  $v$  [using  $c = 1$ ] of the binary components. The order of approximation is defined as the highest power of  $v^2$  used in the expansion.

where

$$\Phi_a = \Phi(t_a|t_a, \tau_0), \quad (3.4b)$$

$$\Psi(f|t_a, \tau_0) = 2\pi f t_a + f_a \tau_0 \frac{6\pi}{5} \left(\frac{f}{f_a}\right)^{-5/3}. \quad (3.4c)$$

The factor  $\mathcal{N}$  is a constant amplitude.

## 3.2 Dense Search

As mentioned in the last section, gravitational waves from inspiraling binaries can be accurately modeled using general relativity and they are independent of the structure of the binary components. Because of these reasons matched filtering and maximum likelihood techniques are well-suited for the detection and characterization of the signal from these systems [53, 52]. An implementation based on these methods is currently used in the analysis of data from the LIGO and GEO detectors (cf. [54, 55, 56, 57]).

### 3.2.1 Matched Filtering

The above (conventional) search begins with the construction of theoretically modeled waveforms or “templates” for discrete points  $\lambda_k$  on the parameter space  $\lambda$ . [Technically, this process is also called “placement of a template bank over the parameter space”]. The data is then “matched filtered” using the theoretically constructed template bank [58]. For the purpose of the present work we have  $\lambda = \{\tau_0, t_a, \Phi_a\}$  — the chirp mass parameter, the time of arrival and the initial phase. However, as we shall see, it may not be necessary to construct template banks over all the parameters; some parameters can be searched for using sophisticated mathematical tools, like FFT, consuming very little computation time as described in [54].

The strain output generated by a gravitational wave detector is a time series of real numbers. The Wiener (matched) filter output is the scalar product between the data  $g(t)$  and the template  $h(t)$ . It is convenient to work in the frequency domain, as the statistical properties of detector noise can be easily characterized by a frequency power spectrum. Following the Neumann-Pearson approach of Maximum Likelihood estimation, it can be shown that (cf. [59]) for GW signal from inspiraling binaries the signal-to-noise ratio (SNR) is maximized if we define the

scalar product with an inverse noise weight as

$$\langle g, h \rangle = 4 \int_0^\infty df \Re \left[ \frac{\widetilde{g}(f) \widetilde{h}^*(f)}{S_n(f)} \right], \quad (3.5)$$

where  $\widetilde{g}(f)$ ,  $\widetilde{h}(f)$  are the Fourier transforms of  $g(t)$ ,  $h(t)$  respectively and  $S_n(f)$  is the one sided power spectral density of detector noise. The basic steps for matched filtering can then be listed as below:

1. Evaluate the Wiener filter output  $W(\mathbf{d}|S_n, \lambda_k)$  at each of the template locations  $\lambda_k$ ;
2. Determine the template  $\lambda_j$  whose Wiener filter output is greatest;
3. If the filter output at  $\lambda_j$  exceeds the given threshold, report an event with the parameters  $\lambda_j$ .

An illustration matched filtering is provided in figure 3.1. A typical chirp signal (top panel), is injected in comparatively stronger noise (middle). The data is then correlated with the templates. In this case the templates are also chirp signals of same shape but with different time of arrivals. The cross correlation value is plotted against the time of arrival. One can see that, when the time of arrival of the templates matches that of the injected signal, a very high correlation value is observed.

### 3.2.2 Template placement

To choose the template locations we use the match function. Denoting by  $h(t|\lambda)$  the signal characterized by  $\lambda$  the match  $\Gamma(\lambda_j, \lambda_k)$  is

$$\Gamma(\lambda_j, \lambda_k) = \frac{\langle h(t|\lambda_j), h(t, \lambda_k) \rangle}{\sqrt{\langle h(t|\lambda_j), h(t, \lambda_j) \rangle \langle h(t|\lambda_k), h(t, \lambda_k) \rangle}}. \quad (3.6)$$

By construction  $|\Gamma| \leq 1$ . The templates locations are chosen so that consecutive templates in any of the directions  $\lambda_j$  have an overlap  $\Gamma_0$ , referred to as the “minimum match” (MM).

It is also important to distinguish between the nature of the parameters that characterize the template. Changes in some parameters, like  $\tau_0$ , change the *shape* of the Chirp waveform: we term such parameters *dynamical* parameters ( $\mu_k$ ). On the



Figure 3.1: **Illustration of Matched Filtering.** Top: Typical “Chirp” signal due to Newtonian compact binaries. Middle: The above signal is injected into comparatively strong detector like noise. Bottom: Matched filtering is done over time of arrival and high correlation is seen when the time of arrival matches the injection time of arrival.

other hand, parameters, such as  $t_a$  or  $\Phi_a$ , translate the waveform, but do not alter its shape: we term these *kinematical* parameters<sup>2</sup>. Maximization of the Wiener filter output over the kinematical parameters can be performed in a computationally efficient manner as shown in the literature [54]. It is not required to search for the parameters phase  $\Phi_a$  and time of arrival  $t_a$  of the signal by binning those parameters and computing the Wiener filter output for each bin. Computation of Wiener filter outputs  $W(\mathbf{d}|S_n, \boldsymbol{\mu}_k, t_a, 0)$  and  $W(\mathbf{d}|S_n, \boldsymbol{\mu}_k, t_a, \pi/2)$  for two orthogonal phase components  $\Phi_a = 0, \pi/2$  can be combined together using the formula

$$W(\mathbf{d}|S_n, \boldsymbol{\mu}_k, t_a) = \sqrt{W(\mathbf{d}|S_n, \boldsymbol{\mu}_k, t_a, 0)^2 + W(\mathbf{d}|S_n, \boldsymbol{\mu}_k, t_a, \pi/2)^2} \quad (3.7)$$

to maximize the match over the phase  $\Phi_a$ . The estimate for the signal phase is given by

$$\Phi_a = \tan^{-1} \left[ \frac{W(\mathbf{d}|S_n, \boldsymbol{\mu}_k, t_a, \pi/2)}{W(\mathbf{d}|S_n, \boldsymbol{\mu}_k, t_a, 0)} \right]. \quad (3.8)$$

Also, the Wiener filter outputs for all the time of arrival parameter bins can be calculated at once using fast fourier transform (FFT) technique effectively using the same amount of computation as required to calculate for just one bin. Therefore, while designing efficient search algorithms, dynamical (intrinsic) parameters are our main concern.

To identify an incident signal using a matched filter requires the application of a fair sampling of filter templates, each defined by a unique choice of the parameters associated with the physical system. Current implementations of matched filtering used in the analysis of gravitational wave detector data involves a very dense sampling of the two-dimensional parameter subspace corresponding to the binary component masses (intrinsic parameter space) and assuming zero eccentricity orbits and no body spins. The rationale for choosing a subspace is that the computational cost of a full parameter space search is high and that many systems are believed to be adequately represented by this subspace. Even for this two dimensional subspace the minimum computational cost for a matched filter search over component masses in the range  $0.2 M_\odot < m_1 \leq m_2 < 30 M_\odot$  in the LIGO detector band is several hundred GFlops/s [56]. When significant body spin is allowed the computational cost grows by several orders of magnitude [60]. The templates are spaced so closely that the correlation between templates at neighboring points in the subspace - the minimal

<sup>2</sup>In the literature, dynamical and kinematical parameters are also known as intrinsic and extrinsic parameters respectively. Unlike the dynamical parameters, the kinematical parameters can be handled quickly and easily in the filtering algorithms.

match - is 97% [56,55]. We refer to this as the “dense” search strategy. The rationale underlying the dense search strategy is to reduce the probability that a weak signal, characterized by parameters that fall between those sampled, will be missed by the sampling<sup>3</sup>.

Here we are interested in understanding the performance of the different search strategies. The current analysis focuses on a two-dimensional parameter space spanned by the masses of the individual binary components. However, the templates vary most rapidly with the chirp mass. The linear density of templates needed by the dense search in the direction  $\partial_{\mathcal{M}}$  is approximately 100 times the linear density needed in the orthogonal direction. Because of this, for the comparison of efficiencies we perform here, we focus attention on the number of template evaluations needed for binaries with equal mass components that vary only in  $\mathcal{M}$ . We expect that the ratio of performance, measured as the number of templates required by different search strategies to achieve the same search results, will be the same in the complementary dimension and in the other dimensions that will be introduced in future searches that accommodate component spins and orbital eccentricity.

### 3.2.3 Choice of parameter

There are many different ways of parameterizing the template space. Choosing  $\tau_0$  as a dynamical variable has the advantage that  $\Gamma(\tau_0, \tau'_0)$  depends only on the difference  $\tau_0 - \tau'_0$ ; consequently, in the dense search templates are spaced uniformly in  $\tau_0$  [54,55,56]. To determine that spacing we evaluate

$$\mathcal{H}(\Delta\tau_0) = \Gamma(\tau_0, \tau_0 + \Delta\tau_0), \quad (3.9)$$

where now  $\Gamma$  has been maximized over the kinematical parameters  $t_a$  and  $\phi_a$ . We call  $\mathcal{H}$  the dynamical ambiguity function or simply as the ambiguity function. It quantifies the fractional match between the template at  $\tau_0$  and the signal at  $\tau_0 + \Delta\tau_0$ . Figure 3.2 shows  $\mathcal{H}$  for power spectral density specified in the initial LIGO science requirements [51]. The requirement that  $\mathcal{H}(\Delta\tau_0)$  is equal to a constant for any two consecutive templates determines the spacing  $\Delta\tau_0$  between templates that differ only in  $\tau_0$ . For our example problem, which has just one dynamical parameter, the requirement that  $\mathcal{H}(\Delta\tau_0)$  is 97% (the conventional choice) for neighboring templates

<sup>3</sup>Because the total accessible volume is proportional to the cube of minimum detectable amplitude and it is assumed that the distribution of detectable sources is uniform in the nearby universe, to ensure that *at most* 10% signals are missed due to the mismatch between data and template, the match function should not fall below  $\sqrt[3]{1 - 10\%} \approx 0.97$ .

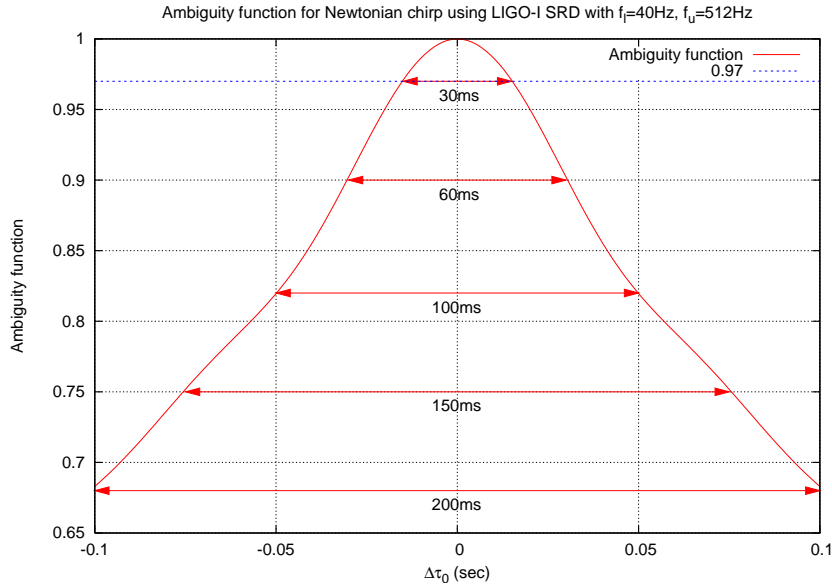


Figure 3.2: **Ambiguity function.** Ambiguity function  $\mathcal{H}$  plotted as a function of  $\Delta\tau_0$ . Horizontal lines are drawn for various matches; the dashed horizontal line is for a 97% match, which corresponds to an inter-template separation of  $\sim 30$  ms.

leads to a template spacing  $\Delta\tau_0$  equal to 30 ms.

### 3.3 Efficient Search Algorithms

Dense search is computationally expensive. It is not possible to search over the whole physically allowed parameter space considering all the parameters with the available computing power. Therefore it is extremely important to design efficient search algorithms. Several efforts are being made by different research groups to develop fast data analysis algorithms for the detection of inspiraling binaries. One of the very promising methods is *hierarchical search* [61, 62]. In the first stage of hierarchy a coarse template bank is used with a lower threshold of detection. In the subsequent stages, the threshold is increased and a finer search is performed around the trigger events in the previous stage.

We have developed another<sup>4</sup> straightforward and practical way of using interpolation to take advantage of the correlation between the matched filter output associated with nearby points in the parameter space to significantly reduce the

<sup>4</sup>Our method can work *with* the hierarchical search, so this is *not* an alternative to the hierarchical scheme, rather, our algorithm can be used to enhance its performance.

number of matched filter evaluations without sacrificing the efficiency with which real signals are recognized.

We are not the first to observe the significance of the high correlation between neighboring templates nor to consider the opportunity for and advantages of interpolation as part of the implementation of matched filtering for the analysis of binary inspiral signals. The significance of the high correlation as an indication that fewer templates should be able to recover signals with the same efficiency, was first made in [55]. Croce et al [63, 64] explored the use of Cardinal interpolation with a truncated series of sinc functions to estimate the value of the matched filter output when the filter used corresponds to the actual parameters that describe the signal. They found a sampling of parameter space that would insure the interpolated estimate would be no less than 97% of the maximum over a two dimensional intrinsic parameter space. Their sampling and interpolation reduced by a factor of 4, compared to the dense search, the number of templates required to search over a *two dimensional* intrinsic parameter space. Here we find that we can achieve an increase in efficiency by a factor of 3.5 for *one dimensional* parameter space, with a simpler template spacing and a simpler and quicker to evaluate interpolation function.

Cardinal interpolation with sinc functions provides perfect reconstruction of a band-limited function from equispaced samples. In the present case, however, the function being interpreted is not band-limited and — in any event — we do not have the infinite number of samples that would be required for perfect reconstruction. As an alternative to cardinal interpolation with a truncated series of sinc functions we consider interpolation using Chebyshev polynomials, which have two important properties: first, they have (very nearly) the minimum maximum error of all polynomial interpolating expressions of fixed degree; and second, they have the practical advantage of being quick and easy to calculate. Few more useful properties of Chebyshev polynomials have been listed in Appendix A

To understand and demonstrate the performance of the interpolated search we evaluate the both the minimum number of templates required to obtain a given detection efficiency using both the (Chebyshev) interpolation and dense strategies. We go further, however, and calculate also the false alarm probability of both search strategies. The relationship between the false alarm and false dismissal probabilities is referred to as the Receiver Operating Characteristic, or ROC. Clearly, given two analysis strategies with the same efficiency, the strategy with the lower false alarm fraction has superior discriminating power. We find that interpolation strategy using Chebyshev interpolation is superior to the dense analysis strategy or

interpolation using the sinc function, from the perspective of either computational efficiency or discriminating ability.

### 3.4 Interpolated Search

As discussed in the previous section, the correlation between the Wiener filter outputs of neighboring templates can be exploited to reduce the number of template evaluations required to search over the full parameter space. The Wiener filter output can be sampled and the full function can be reconstructed using a suitably chosen interpolation scheme. In this section we describe our proposed template placement scheme using Chebyshev interpolation and compare it with other relevant template placement schemes [44].

#### 3.4.1 Interpolation of the Wiener filter output

The Wiener matched filter  $W$ , corresponding to an expected signal characterized by  $\tau$ , is a scalar-valued function of the (vector-valued) instrument data  $\mathbf{d}$ , noise power spectral density  $S_n$ :

$$W(\mathbf{d}|\tau) = W(\tau|S_n, \mathbf{d}). \quad (3.10)$$

In our particular problem  $W(\mathbf{d}|\tau)$  is a continuous function of  $\tau$  and  $\tau$  corresponds to the intrinsic parameters that characterize our binary system model: e.g., binary system component masses, orbital energy and angular momentum, component spins, etc. Given a data set  $\mathbf{d}$  we wish to find an interpolating function  $\tilde{W}(\tau)$  and a set of points  $\tau_k$  in the space of possible signals such that

$$W_k = \tilde{W}(\tau_k) = W(\mathbf{d}|S_n, \tau_k). \quad (3.11)$$

There are, of course, an infinite number of continuous functions  $\tilde{W}(\tau)$  that take on the values  $W_k$  at the  $\tau_k$ : the question is, how do we choose among them?

Focus attention first on the case where  $\tau$  is a scalar  $x$ . One particular choice of interpolant  $\tilde{W}(\mathbf{d}|S_n, x)$ , which is especially important in the context of communication theory, is based on the Whittaker Cardinal function sinc:

$$C(x) = \sum_{k=-\infty}^{\infty} W_k \text{sinc} \frac{x - x_k}{\Delta}, \quad (3.12)$$

where

$$\text{sinc}(x) = \frac{\sin \pi x}{\pi x}, \quad (3.13)$$

$$x_k = x_0 + k\Delta. \quad (3.14)$$

Shannon [65] showed that the Cardinal interpolation  $C(x)$  of  $W(\mathbf{d}|S_n, x)$  is the unique interpolant  $\tilde{W}$  that (i) takes on the values  $W_k$  at the  $x_k$ , (ii) has no singularities, and (iii) and whose spectrum is limited to a bandwidth  $(2\Delta)^{-1}$ . Correspondingly, if  $W(\mathbf{d}|S_n, x)$  is bandlimited in  $x$  and has the values  $W_k$  at the equidistant sampled points  $x_k$  then  $W(\mathbf{d}|S_n, x)$  is equal to  $C(x)$ . In the case where  $\tau$  is multi-dimensional the interpolation can be performed separately on each index: e.g., in the case of two dimensions [i.e.,  $\tau$  equal to  $(\tau_1, \tau_2)$ ]

$$C(\tau) = \sum_{j,k=-\infty}^{\infty} W_{jk} \text{sinc} \frac{\pi}{\Delta_1} (\tau_1 - \tau_{1,j}) \text{sinc} \frac{\pi}{\Delta_2} (\tau_2 - \tau_{2,k}), \quad (3.15)$$

where

$$\tau_{1,j} = \tau_{1,0} + j\Delta_1, \quad (3.16)$$

$$\tau_{2,k} = \tau_{2,0} + k\Delta_2 \quad (3.17)$$

and  $\tau_{1,0}, \tau_{2,0}$  are constants.

Cardinal interpolation using the Cardinal function sinc forms the basis of the interpolation formula used in [63, 64]. If  $W(\mathbf{d}|S_n, \tau)$  is bandlimited and we choose our samples of  $W$  appropriately then we can do no better than using the Cardinal function to interpolate values of  $W$  between the samples. In our problem, however,  $W(\mathbf{d}|S_n, \tau)$  is not bandlimited and we do not have an infinite number of sample points  $W_k$ ; correspondingly, the Cardinal function  $C(\tau)$  is at best an approximation to  $W(\mathbf{d}|S_n, \tau)$ . With that understanding the Cardinal interpolation  $C(\tau)$  is not preferred and we are led to seek other approximations to  $W(\mathbf{d}|S_n, \tau)$  that have favorable properties<sup>5</sup>.

One possibility, chosen from approximation (as opposed to interpolation) theory, is the use of a Chebyshev polynomial expansion to approximate  $W(\mathbf{d}|S_n, \tau)$ . Without loss of generality consider a continuous function  $f(x)$  on  $[-1, 1]$ . The Weier-

<sup>5</sup>In fact, as noted in [13,14], the  $\Gamma$  is *quasi-band-limited*: i.e., there exists a  $B_c$  such the error one makes by undersampling at frequency  $B > B_c$  is proportional to  $\exp[-(B - B_c)]$ . Nevertheless, interpolation with the Cardinal function is still an approximation and, as we are about to see, other interpolating functions can achieve equivalent accuracy at smaller computational costs.

stness Approximation Theorem states that for any  $\epsilon > 0$  we can find a polynomial  $P_n$  of order  $n$  such that

$$\max_{x \in [-1, 1]} |f(x) - P_n(x)| \leq \epsilon. \quad (3.18)$$

The minimax polynomial approximation to  $W(\mathbf{d}|S_n, x)$  is a natural candidate for the interpolation  $\widetilde{W}(x)$ . Unfortunately, finding the minimax polynomial is a very difficult process; nevertheless an excellent *approximation* to the minimax polynomial does exist. Define the error  $E(x|f, P_n)$  associated with the polynomial approximation  $P_n(x)$  by

$$E(x|f, P_n) \equiv f(x) - P_n(x). \quad (3.19)$$

The Chebyshev Equioscillation Theorem [66] states  $P_n^*$  is the minimax polynomial if and only if there exist  $n + 2$  points  $-1 \leq x_0 < x_1 < \dots < x_{n+1} \leq 1$  for which

$$E(x_k|f, P_n^*) = (-1)^k E, \quad (3.20)$$

where

$$|E| \equiv \max_{x \in [-1, 1]} |E(x|f, P_n^*)|. \quad (3.21)$$

As a corollary,  $E(x|f, P_n^*)$  vanishes for  $x \in [-1, 1]$  at  $n + 1$  points  $x'_k$ , with  $x_k < x'_k < x_{k+1}$ . This result, together with the Mean Value Theorem, allows us to write the error term associated with the minimax polynomial  $P_n^*$  as

$$E(x|f, P_n^*) = \frac{f^{(n+1)}(\xi)}{(n+1)!} \prod_{k=0}^n (x - x'_k), \quad (3.22)$$

where  $\xi \in [-1, 1]$ . Correspondingly,

$$|E| \leq \max_{x \in [-1, 1]} \left| \prod_{k=0}^n (x - x'_k) \right| \max_{\xi \in [-1, 1]} \frac{|f^{(n+1)}(\xi)|}{(n+1)!}. \quad (3.23)$$

Focus attention on the order  $n + 1$  polynomial

$$Q_{n+1}^*(x) = \prod_{k=0}^n (x - x'_k). \quad (3.24)$$

This polynomial has leading coefficient unity. A unique property of the Chebyshev polynomial  $T_{n+1}$  is that, of all order  $n + 1$  polynomials  $Q_{n+1}$  with leading coefficient

unity,

$$\max_{x \in [-1,1]} \left| \frac{T_n(x)}{2^{n-1}} \right| \leq \max_{x \in [-1,1]} |Q_{n+1}(x)|. \quad (3.25)$$

Additionally,  $T_{n+1}(x)$  has exactly  $(n + 2)$  extrema on  $[-1, 1]$ , the value of  $|T_{n+1}(x)|$  at these extrema is 1, and the extrema alternate in sign. Correspondingly, if the error term  $E(x|f, P_n^*)$  associated with the minimax polynomial  $P_n^*$  were polynomial — i.e.,  $f^{(n+1)}(\xi)$  were constant in equation 3.22 so that  $E(x|f, P_n^*)$  was equal to  $Q_n^*$  — then by the Equioscillation Theorem  $Q_{n+1}^*$  would be equal to  $T_{n+1}$  and the  $x'_k$  — where the error vanishes — would be the  $n + 1$  roots of  $T_{n+1}$ . This suggests that we find the order  $n$  polynomial  $p_n^*$  such that

$$p_n^*(x'_k) = f(x'_k) \quad \forall k = 0 \dots n \quad (3.26)$$

where, again, the  $x'_k$  are the roots of  $T_{n+1}$ . The polynomial  $p_n^*$  is a *near minimax* polynomial approximation to  $f(x)$ . For this polynomial approximation Powell [67] showed that, as long as  $f(x)$  is continuous on  $[-1, 1]$ ,

$$1 \leq \frac{\epsilon_{\text{cheb}}}{\epsilon_0} \leq \nu_n \equiv 1 + \frac{1}{n+1} \sum_{k=0}^n \tan \left[ \frac{(k+1/2)\pi}{2(n+1)} \right]. \quad (3.27)$$

where

$$\epsilon_0 = \max_{x \in [-1,1]} |E(x|f, P_n^*)|, \quad (3.28)$$

$$\epsilon_{\text{cheb}} = \max_{x \in [-1,1]} |E(x|f, p_n^*)|. \quad (3.29)$$

Powell also showed that  $\nu_n$  grows slowly with  $n$ : in particular,

$$\nu_n \sim \frac{2}{\pi} \log n. \quad (3.30)$$

Somewhat tighter bounds on  $\nu_n$  can be placed when  $f$  is differentiable [68].

As defined above, the near minimax polynomial  $p_n^*$  is the interpolating polynomial that agrees with  $f$  at the  $n + 1$  roots of  $T_{n+1}$ . Alternatively, using several properties of Chebyshev polynomials, the Chebyshev interpolating polynomial can be expressed as a linear combination of Chebyshev polynomials:

$$p_n^*(x) = \sum_{k=0}^n a_k T_k(x) - \frac{1}{2} a_0, \quad (3.31)$$

where

$$a_j = \frac{2}{n+1} \sum_{k=1}^{n+1} f(x'_k) T_j(x'_k), \quad (3.32)$$

where, again, the  $x'_k$  are the  $n+1$  roots of  $T_{n+1}$ .

### 3.4.2 Search strategy

Following the above discussion we are in a position to describe an alternative strategy, which we refer to as the interpolated search strategy.

Here also we first describe the general strategy using the full set of parameters  $\lambda$ . However, as was in the case of dense search, we may not have to place template banks over all the parameters. In the present case, we use interpolated search only for the dynamical parameter<sup>6</sup>, namely the Chirp mass  $\tau_0$ , and maximize over the kinematical parameters, the time of arrival  $t_a$  and the initial phase  $\Phi_a$ , using the fast FFT based method described in [54].

The general scheme is as follows. First, fix the order of the interpolating polynomial. This determines the template locations  $\lambda_k$  on the parameter space  $\lambda$ . Then

1. Evaluate the Wiener filter  $W(\mathbf{d}|S_n, \lambda_k)$  at each of the template locations  $\lambda_k$ ;
2. Form the interpolating polynomial from the  $W(\mathbf{d}|S_n, \lambda_k)$ ;
3. Determine the location  $\lambda'$  where the interpolating polynomial is maximized;
4. Perform a final Wiener filter evaluation at  $\lambda'$ ;
5. If the final evaluation exceeds the given threshold, report an event with the parameters  $\lambda'$ .

We illustrate the interpolated search strategy using Fig. 3.3. In Fig. 3.3 we use 37 interpolating search templates, that is, we sample the ambiguity function at 37 points in the  $\tau_0$  space (the marked points on the dotted curve). We construct the interpolating function (the solid curve) and find its maximum by setting its derivative to zero. In order to avoid local extrema, we first find the approximate location of the peak of the interpolating function and then find the zero of its

<sup>6</sup>Note that, interpolation over kinematical parameters may also improve the performance of the search algorithms [55]. Although this case has not been considered in the work presented here, it is worth exploring the possibility in future efforts to maximize the efficiency to search for the binary inspirals.

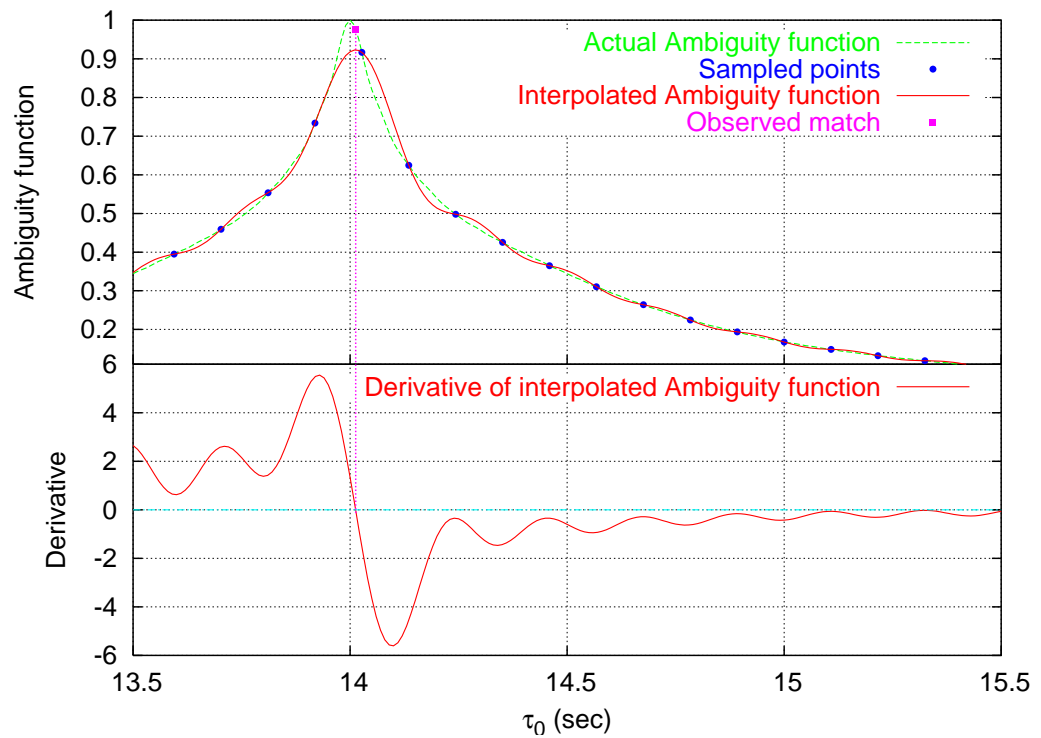


Figure 3.3: **Illustration of Interpolated Search.** This figure demonstrates the interpolated search. The ambiguity function is sampled and reconstructed over the chosen parameter space of  $\tau_0 = 13 - 17$  sec (only a part of the parameter space has been shown in the figure) with the help of the Chebyshev interpolating polynomial. The approximate location of the peak of the interpolating function is first located and the zero of the derivative is obtained by applying successive approximations around the peak. Finally a template is placed at this estimated signal location. Note that by placing a template at the maximum of the interpolating polynomial, the match has improved over the one obtained by simply evaluating the maximum of the interpolating polynomial.

derivative by successive approximation near the region of the peak. One can clearly see that the proper value of the ambiguity function at the maximum of the interpolating function is more than the maximum value of the interpolating function and this is what we gain by placing a template at the maximum of the interpolating function.

### 3.4.3 Template placement

In the dense search templates are equispaced in  $\tau_0$ , with the spacing between adjacent templates — and thus the number of templates — chosen such that the dynamical ambiguity function takes on a specified value. When presented with data an event is signaled when the amplitude at one of these templates exceeds a threshold.

In the interpolated search, on the other hand, the domain  $[\tau_0^{\min}, \tau_0^{\max}]$  is mapped onto  $[-1, 1]$  and the placement and number of templates is chosen to simplify the construction of the Chebyshev interpolating polynomial of the template output over this domain. When presented with data the maximum value of the Chebyshev interpolating polynomial is found and an event is signaled when the amplitude at that location exceeds a threshold.

In the interpolated search our goal is to minimize the order of the interpolating polynomial (and, thus, the number of template evaluations) required for a given accuracy of interpolation. We have some control over this through the choice of mapping from  $[\tau_0^{\min}, \tau_0^{\max}]$  to  $[-1, 1]$ . The linear map

$$\tau' = 2 \frac{\tau_0 - \tau_0^{\min}}{\tau_0^{\max} - \tau_0^{\min}} - 1, \quad (3.33)$$

is the most obvious such mapping. While we have not made an exhaustive search of all possible mappings; however, we have observed that better fits are possible with a lower-order polynomial when we use the mapping

$$\delta = \cos(\tau') = -\cos \left[ \pi \frac{\tau_0 - \tau_0^{\min}}{\tau_0^{\max} - \tau_0^{\min}} \right]. \quad (3.34)$$

Moreover, with this mapping, the roots of the Chebyshev polynomial are equispaced<sup>7</sup> over the parameter range in  $\tau_0$ . Note that the Chebyshev polynomials

<sup>7</sup>This means that the Wiener filter outputs from a conventional dense search can also be used as input to the Chebyshev interpolation scheme to yield a better efficiency by performing negligible

can also be written as  $T_n(x) = \cos[n\theta(x)]$ , where  $x = \cos \theta$ , so in this case  $T_n(\delta) = \cos(n\pi\tau')$ . Since the  $\tau'$  space is sampled uniformly due to the above mapping, Chebyshev interpolation is now equivalent to a type II Discrete Cosine Transform in  $\pi\tau'$ . Equispaced sampling of the parameter space could be beneficial if the signals are distributed uniformly over the  $\tau_0$  space. Nevertheless, for a nonuniform distribution of signals, different transformation could be preferred to give optimum results. Once we have fixed the order  $n$  of the interpolating polynomial, templates are placed at values of  $\delta$  that are roots of the  $T_{n+1}(\delta)$ . This fixes the templates. The coefficients of the interpolating polynomial are found using equation 3.32 and then the interpolating polynomial is constructed using equation 3.31.

It is obvious that minimum number of templates should be used for maximum computational advantage. We choose the order of interpolation  $n$  to be the minimum order that can retain the MM of 97%. This is equivalent of saying that *any* injected signal should be located within the error window where the ambiguity function centered about the injection point is above the MM. So, in our case, the error in locating any signal should be less than 15 ms. To do this, we first inject a normalized signal at a non-special location of the parameter space. The order of interpolation is then varied over a reasonable range of value and the error (bias) in locating the signal is noted for each order. This variation has been plotted in figure 3.4. The minimum order for which the bias is less than 15 ms gives a lower limit to the number of templates to be used. From the figure one can see that the number is 35. We, then, increase the number of templates and find the minimum number for which the maximum match is greater than 97% for *any injection point*. By performing this exercise, we get the minimum order of interpolation required to retain the MM of 97% for the parameter space considered here is 37.

In figure 3.5 we have plotted the match by placing normalized test signals (without noise) at regular intervals of  $\tau_0$ . For each injected signal  $\tau_0$ , we plot the maximum of the interpolating polynomial (dashed curve) and the match obtained by placing a template at the maximum of the interpolating polynomial (solid curve). We see that the match is a (nearly) periodic function of  $\tau_0$ , with the period equal to the template separation. This suggests that the detection probability is also periodic and this fact has been used in carrying out the simulations - the signals are injected within one such "period" in the parameter space. Moreover, one can see that with just  $37 + 1$  interpolated search templates one gets a MM of 0.97, whereas the dense search requires about 133 templates to achieve the same level of MM. This amounts

---

amount of extra computation.

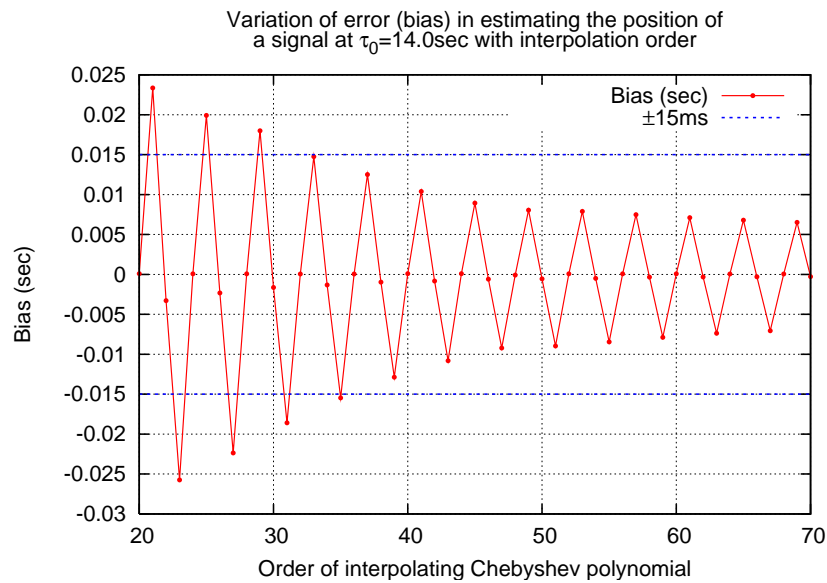


Figure 3.4: **Variation of bias with no. of interpolated search templates.** A normalized test signal (without noise) was injected at a non-special location on the parameter space. The error occurred in locating the signal position (bias) is plotted with the number of templates. This plot gives an indication about the number of templates required to keep the bias less than 15 sec, so that, the minimal match does not fall below 97%. One can see that at least 35 templates are needed to keep the minimal match greater than 97%. See text for the next steps to fix the exact number of templates.

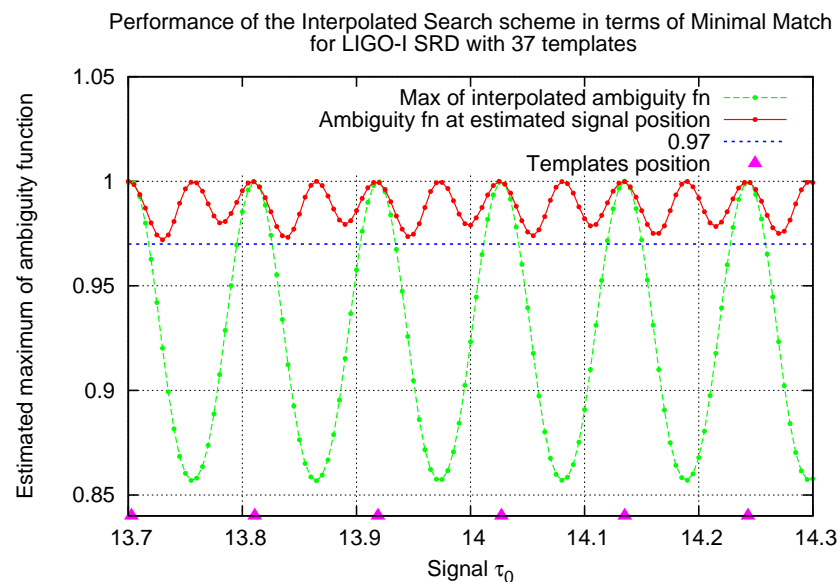


Figure 3.5: **Variation of Match with signal location.** Normalized test signals (without noise) were injected densely at regular intervals along the  $\tau_0$  parameter space. For each injected signal  $\tau_0$ , we plot the maximum of the interpolating polynomial (dashed curve) and the match obtained by placing a template at the maximum of the interpolating polynomial (solid curve) according to the interpolated search strategy. This figure illustrates that the match is a (nearly) periodic function of  $\tau_0$  with the period equal to the template separation. Moreover, with just  $37 + 1$  interpolated search templates the minimal match is 0.97. To maintain the same minimal match 133 templates are needed for the usual dense search.

to a factor of 3.5 over the dense search and this is so for just one dimension. Note that, the gain factor obtained by Croce et al. in [63] is  $\sim 4$  in *two* dimensions, which scales to  $\sim 2$  per dimension. Because the metric (Fisher information matrix) determines the lattice spacing as well as the correlation, they are interdependent. This suggests that the Chebyshev interpolation method can be extended to a parameter space of higher dimensions with about a similar gain factor per dimension.

### 3.5 Comparison between Dense and Interpolated search: ROC curves

In this section we compare the performances of the dense and interpolated search strategies when applied to the problem of identifying the gravitational wave signature of coalescing neutron star systems in the LIGO detectors.

We are interested in two, related, comparisons: first, the relative “sensitivity” of a search carried-out with a fixed number of template evaluations using the dense search strategy and the interpolated search strategy; second, the number of template evaluations required by the interpolated search in order to achieve the same “sensitivity” as the dense search. To give meaning to the “sensitivity” of these two strategies we use the Receiver Operating Characteristic, or ROC.

The ROC is a plot of true positives as a function of the fraction of false positives for a binary classifier system as its discrimination threshold is varied. Both the dense search and the interpolated search are binary classifiers: i.e., they classify an interval of data  $\mathbf{d}$  as including a signal or not including a signal. A true positive is a classification of  $\mathbf{d}$  as including a signal when in fact it does; a false positive is a classification of  $\mathbf{d}$  as including a signal when it does not. In both of the search strategies described here the discrimination threshold is matched filter output that must be exceeded for a data interval to be classified as including a signal. The false positive fraction is also known as the type II, or false alarm, error fraction and is denoted  $\alpha$ . The fraction of true positives is also known as the detection efficiency  $\epsilon$ , which is one minus the type I, or false positive, error fraction (which is denoted  $\beta$ ). At fixed  $\alpha$  a more sensitive search method has a greater  $\epsilon$ . The ROC associated with a search method no better than a toss of a (possibly loaded) coin is given by the diagonal  $\alpha = \epsilon$ .

Using numerical simulations we have evaluated  $\alpha$  and  $\epsilon$  as a function of the detection threshold for both the interpolated search and the dense search, for different numbers of templates (dense search) and different interpolating polynomial

order (interpolated search).

To evaluate the false positive fraction  $\alpha$  we generate a large number of data segments, each  $2^{15}$  samples long, and each consisting of Gaussian noise whose power spectrum (assuming a 1024 Hz sample rate) is that specified as the initial LIGO science requirement [51]. (The Gaussian random numbers are themselves generated using the Mersenne Twister Pseudo Random Number Generator [69] and then filtered in the Fourier domain by scaling the Fourier components by the square root of the PSD.) For the purpose of this comparison we look for signals in the interval  $\tau_0 \in [13 \text{ s}, 17 \text{ s}]$ . Both the dense and interpolated search methods are applied to this data. The ratio of the number of events signaled to the number of data segments examined as a function of the threshold  $\eta$  is  $\alpha$  for that threshold. Approximately 50,000 realizations of detector noise are used to evaluate  $\alpha$ , which gives reliable results for  $\alpha$  greater than approximately  $10^{-3}$ .

To compute  $\epsilon$ , the true positive fraction, we proceed in a similar fashion. Now, however, with each noise instantiation we add a signal, with  $\tau_0$  drawn uniformly and randomly from the interval covered by the search: i.e.,  $\tau_0 \in [13 \text{ s}, 17 \text{ s}]$ . We inject signals of SNR 8. In almost all cases 50,000 realizations of detector noise plus signal are used to evaluate the efficiency, which gives reliable results for efficiencies greater than approximately  $10^{-3}$ . However, for the flat search with 40 templates and the interpolated search with 30 templates, we have used 400,000 realizations. The larger number of realizations in these cases results in smoother curves.

The top panel of Fig. 3.6 shows the variation of  $\alpha$  for both methods using 40 templates: i.e., a 100 ms template spacing for the dense search and an order 39 interpolating polynomial in  $\delta$  (cf. equation 3.34). For any threshold  $\alpha$  is always greater for the dense search than for the interpolated search; similarly, as shown in the center panel of Fig. 3.6, for any given threshold the efficiency  $\epsilon$  is always greater for the interpolated search than for the dense search. Finally, the bottom panel of Fig. 3.6 shows the ROC for a 40 template dense search and an order 39 interpolated search, both of which involve 40 template evaluations to decide if a signal has been detected. Comparing both ROCs it is clear that the interpolated search is more sensitive at any given  $\alpha$  than the dense search. This is always true: i.e., for a fixed number of template evaluations the interpolated search will always have a better efficiency at a given  $\alpha$  than the dense search, though as the number of templates grows large the fractional difference in sensitivity will decrease.

Figure 3.7 and table 3.1 addresses the second of our two questions: the number of templates evaluations required of an interpolated search to have the same sensi-

Table 3.1: **Comparison between dense and interpolated search.** Number of template evaluations required to obtain the same efficiency at a false alarm fraction of  $10^{-3}$  in a dense search and an interpolated search. Note how the interpolated search is computationally more efficient for the same sensitivity.

# templates		$\epsilon$ at $\alpha = 10^{-3}$
Dense	Interp.	
40	31	0.859
50	41	0.890
60	49	0.905
80	64	0.919
100	89	0.924
140	105	0.927
160	115	0.929

tivity as a dense search. Figure 3.7 shows the ROCs for dense searches using 140 and 160 templates, together with the ROCs for interpolated searches using 120 and 100 templates. The interpolated search with an order 120 interpolating polynomial is clearly as sensitive as a dense search with 160 templates, and an interpolating search with an order 100 polynomial is as sensitive as a dense search with 140 templates. Table 3.1 shows similar pairings of the number of templates in a dense search and the number of templates in an interpolating search necessary to achieve the same sensitivity.

### 3.6 Summary and Conclusion

Inspiring binaries are the most promising sources for the currently operating and upcoming gravitational wave detectors. Signals from these detectors will be dominated by instrumental noise. However, the signals from the inspiring binaries can be accurately modeled using (approximate theories of) general relativity and these signals do not depend on their internal structures of the binary components. This makes it possible to detect the signals using matched filtering and maximum likelihood techniques.

The existing data analysis algorithm, that is being used for the analysis of LIGO and GEO data, considers only two mass parameters of the binary and densely places templates over this parameter space so that signals are not missed out if they fall in between two templates. We call this “dense” search. Dense search is computationally expensive and it is extremely difficult with the available computing

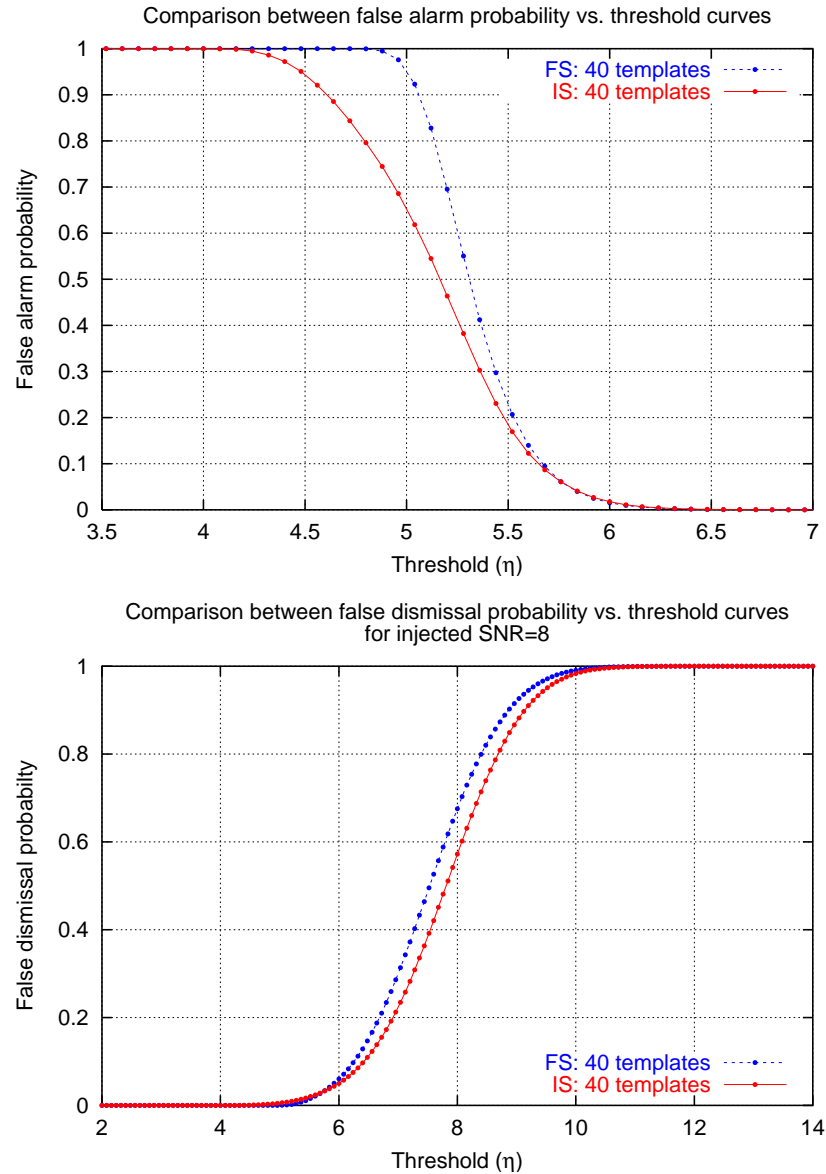


Figure 3.6: **Comparison: False Alarm & False Dismissal probability.** The variation of the false and true positive fractions,  $\alpha$  and  $\epsilon$  with threshold  $\eta$  for the dense and interpolated search methods, each making use of 40 template evaluations. The top panel shows the false positive fraction. Note how the false positive falls much sooner for the interpolated search than for the dense search. The bottom panel shows  $\epsilon$  when a signal of amplitude signal to noise 8 is present in the range  $\tau_0 \in [13 \text{ s}, 17 \text{ s}]$ . Note how the  $\epsilon$  is always greater for the interpolated search than for the dense search. For the same computational cost (determined by the number of template evaluations) the interpolated search will always perform better than the dense search.

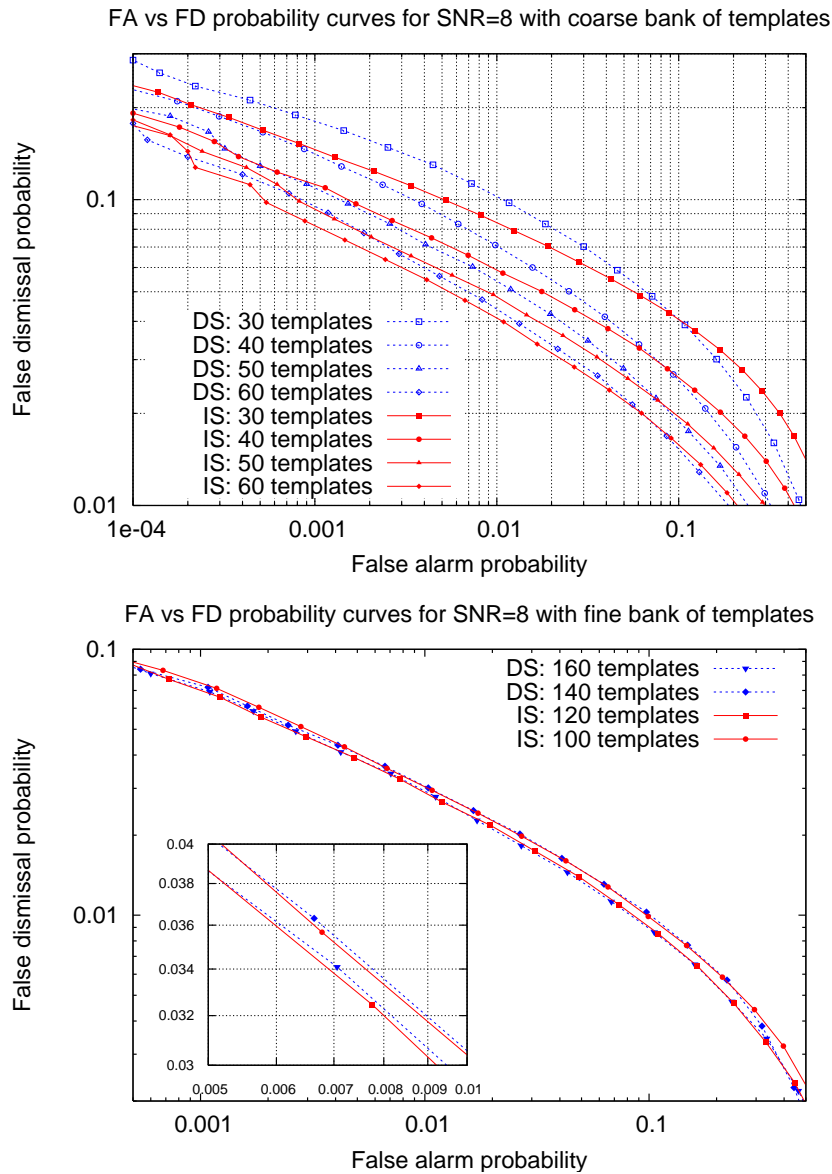


Figure 3.7: **Comparison: ROC Curves.** ROC curves for dense searches (solid curves) and interpolating searches (dashed curves). For a given number of templates, the solid curves are 'lower' - less false dismissal probability for the same false alarm - than the dotted curves in the regime of low false alarm showing that the interpolated search performs better than the dense search for low false alarm. The bottom panel shows analogous plot for high minimal match (fine bank)  $\sim .98$ . Here the performance of the dense search with 160 and 140 templates is comparable to that of the interpolated search with 120 and 100 templates respectively.

resources to search over all the parameters and the full volume of the parameter space using dense search.

We have shown that the use of near-minimax interpolating polynomials to fit the output of matched filters to the filter parameter values can greatly improve the sensitivity of a matched-filter based search for gravitational waves from compact binary inspiral. Since the lattice for dense search and the correlations are dependent on the metric (Fisher information matrix) and *any interpolation* exploits these correlations, we believe that the Chebyshev interpolation method can be extended to a parameter space of higher dimensions with about a similar gain factor per dimension. Using such a polynomial to find the parameters of the signal template leading to the best match we can reduce the computational cost of a search over a two dimensional parameter space by a factor of two compared to the methods currently in use, without any loss of sensitivity or discriminating power. This factor of two becomes a factor of ten when the search is over the seven dimensional parameter space that includes not only the masses but also the spins of the binary components [70]. This savings in computational cost is estimated under the assumption, which we believe well-founded, that we will obtain the same savings when the interpolation is extended to additional dimensions.

Moreover, the scheme we have developed places templates uniformly over the parameter space, like the current dense search. So the Wiener filter outputs of the dense search can be used as input to the Chebyshev interpolation and better efficiency can be achieved by performing negligible amount of extra computation.

Other suggestions have been made for reducing the number of filter evaluations without sacrificing detection efficiency. One promising proposal involves a hierarchical search strategy, wherein a low-threshold trigger generated by the evaluation of the matched filters associated with a much coarser sampling of parameter space followed by (if necessary) a higher threshold evaluation matched filters over a much finer sampling of parameter space [61,71,72,73,62]. The interpolation strategy we describe here can be implemented together with the hierarchical strategies to further improve the computational efficiency of binary inspiral analysis. While the gain in efficiency of the interpolated search over the dense search is approximately constant in the desired false alarm probability, the balance between the coarseness of the grids in the hierarchical steps, the number of hierarchical steps, and the gain in computational efficiency associated with the interpolation is not obvious and requires further study. Nevertheless, since the major contribution to the computational cost of a multi-grid search is thought to arise in the initial stage

of the search, the gain in computational efficiency — and, correspondingly, the size of the parameter space that can be studied with fixed computational resources — could be substantial.

## Chapter 4

# Search for GW Background (GWB): Radiometer Analysis

The universe is expected to have a stochastic Gravitational Wave Background (GWB) of astrophysical and cosmological origin. Incoherent superposition of unmodeled and/or unresolved sources of GW, which are characterized by statistical expectation values, constitute the stochastic GWB. The cosmological GWB component is analogous to the Cosmic Microwave Background (CMB) - a stochastic background of electro-magnetic radiation, whereas the GWB component generated from astrophysical sources, e.g., supernovae, binaries etc., is analogous to the foreground observed in CMB experiments, which will generally be higher in amplitude from the GWB of cosmological origin. Different types of astrophysical and cosmological sources of GWB and their modeled frequency spectra have been listed in section 4.2. Measurement of the strength of the statistically isotropic cosmological GWB will be a direct probe of inflation and some other important phenomena in the early universe.

As the noise streams in different instruments are independent, the cross-correlation between the data from a pair of detectors is the best statistic for the estimation of the strengths of stochastic signals. The cross-correlation statistic can be used to measure the sky averaged strength of the GWB [74,75,76], as well as, to make skymap of the GWB [77,78,79,80,81,82] using the ground and space based detectors. In order to “point” a baseline formed by a pair of detectors at different locations, a time dependent phase delay is introduced in the cross-correlation statistic that accounts for the light travel time delay between the detector sites for a given source direction. As the earth rotates, the phase factor is adjusted in such a way

that the signal from the pointing direction is coherently added, while the signals from other directions wash out. The phase delay, however, is introduced through a filter function, which also takes into account the variation of source power spectral density (PSD) and non-stationary detector noise PSD over different frequency bands. The filter function can be altered to search for different models of stochastic backgrounds.

The method of synthesis imaging using the rotation of the earth is well developed in radio astronomy and CMB analysis. A similar approach is used here, for the first time, to propose a method for mapping the GWB and, hence, the analysis is called “GW radiometer”. The general GW radiometer framework is presented in section 4.3 to search for any model of GWB. Two important “blind” estimations - the search for a isotropic background and to map the GWB sky - have been outlined in section 4.4.

Blind estimations of the upper limits on the strengths of a isotropic GWB and a stochastic point source using a GW radiometer formed by the pair of LIGO observatories at Hanford and Louisiana have already been implemented [83,84,85]. The upper limit on the sky averaged stochastic GWB obtained from the fourth LIGO science run data is currently the best in the frequency range 51 – 150Hz [84].

## 4.1 Stochastic Gravitational Wave Background (GWB)

A gravitational wave in the weak field limit can be treated as an external field over a flat Minkowski background:

$$ds^2 = -c^2 dt^2 + dx^2 + h_{ab}(t, \mathbf{x}) dx^a dx^b \quad (4.1)$$

where the roman indices  $a, b$  run from 1 to 3. In the transverse traceless (TT) gauge the metric perturbations  $\mathbf{h}(t, \mathbf{x}) \equiv h_{ab}(t, \mathbf{x})$  can be expanded in terms of plane waves of the two polarizations  $A = +, \times$

$$\mathbf{h}(t, \mathbf{x}) = \sum_{A=+, \times} \int_{-\infty}^{\infty} df \int_{S^2} d\hat{\Omega} \tilde{h}_A(f, \hat{\Omega}) \mathbf{e}^A(\hat{\Omega}) e^{2\pi i f(t - \hat{\Omega} \cdot \mathbf{x}/c)}, \quad (4.2)$$

where a tilde ( $\tilde{\phantom{x}}$ ) above a variable denotes its Fourier transform, the complex Fourier amplitudes satisfy the relation  $\tilde{h}_A^*(f, \hat{\Omega}) = \tilde{h}_A(-f, \hat{\Omega})$  owing to the reality of  $\mathbf{h}(t, \mathbf{x})$ ,

$\hat{\Omega}$  is a unit vector on the two sphere with spherical polar coordinates  $(\theta, \phi)$

$$\hat{\Omega} = \cos \phi \sin \theta \hat{x} + \sin \phi \sin \theta \hat{y} + \cos \theta \hat{z} \quad (4.3)$$

and the polarizations tensors  $\mathbf{e}^A(\hat{\Omega}) \equiv e^A_{ab}(\hat{\Omega})$  are defined by the following equations

$$\hat{\mathbf{m}}(\hat{\Omega}) := \sin \phi \hat{x} - \cos \phi \hat{y} \quad (4.4a)$$

$$\hat{\mathbf{n}}(\hat{\Omega}) := \cos \phi \cos \theta \hat{x} + \sin \phi \cos \theta \hat{y} - \sin \theta \hat{z} \quad (4.4b)$$

$$\mathbf{e}^+(\hat{\Omega}) := \hat{\mathbf{m}}(\hat{\Omega}) \otimes \hat{\mathbf{m}}(\hat{\Omega}) - \hat{\mathbf{n}}(\hat{\Omega}) \otimes \hat{\mathbf{n}}(\hat{\Omega}) \quad (4.4c)$$

$$\mathbf{e}^\times(\hat{\Omega}) := \hat{\mathbf{m}}(\hat{\Omega}) \otimes \hat{\mathbf{n}}(\hat{\Omega}) + \hat{\mathbf{n}}(\hat{\Omega}) \otimes \hat{\mathbf{m}}(\hat{\Omega}). \quad (4.4d)$$

Stochastic signals can not be modeled as a time series, they are characterized by their expectation values. If we assume a stochastic GWB without any correlation between different polarizations<sup>1</sup>, frequencies and directions<sup>2</sup> we may write

$$\langle \tilde{h}_A^*(f, \hat{\Omega}) \tilde{h}_{A'}(f', \hat{\Omega}') \rangle = \delta_{AA'} \delta(f - f') \delta^2(\hat{\Omega} - \hat{\Omega}') \mathcal{P}^A(\hat{\Omega}) H(f), \quad (4.5)$$

where  $\mathcal{P}^A(\hat{\Omega})$  is proportional to the strength of the GWB in the direction  $\hat{\Omega}$  and  $H(f)$  is the *two sided* GW source Power Spectral Density (PSD).<sup>3</sup> The quantity  $\mathcal{P}^A(\hat{\Omega})$  may be properly interpreted by comparing it with the total GW energy density.

The total GW energy density  $\rho_{\text{GW}}(t, \mathbf{x})$  can be defined as [2,76]

$$\rho_{\text{GW}}(t, \mathbf{x}) = \frac{c^2}{32\pi G} \langle \dot{\mathbf{h}}(t, \mathbf{x}) : \dot{\mathbf{h}}(t, \mathbf{x}) \rangle, \quad (4.6)$$

where a dot ( $\dot{\phantom{x}}$ ) represents derivative with respect time  $t$  and a colon ( $:$ ) represents the matrix contraction operation. For a stochastic background  $\rho_{\text{GW}}(t, \mathbf{x})$  is

<sup>1</sup>It is important to note that, even if the polarizations are independent in certain direction, there can be mixing between polarizations in the other directions due to the rotation of the basis vectors. This complication has not been included in this thesis, because for numerical applications we only consider equal power in both the polarizations where this complexity does not arise. However, it should be straight forward to include this phenomenon in the analysis framework presented here.

<sup>2</sup>The inflationary GWB will have angular correlations over angular scales larger than the angular resolution of the radiometers formed using the ground based detectors. Development of a more general analysis technique to incorporate the angular correlations in GWB is being planned.

<sup>3</sup>In general, we can not separate  $H(f)$  from  $\mathcal{P}^A(\hat{\Omega})$ , because the frequency power spectrum  $H(f)$  could also depend on the direction  $\hat{\Omega}$ . A more general treatment would use

$$\langle \tilde{h}_A(f, \hat{\Omega}) \tilde{h}_{A'}(f', \hat{\Omega}') \rangle = \delta_{AA'} \delta(f - f') \delta^2(\hat{\Omega} - \hat{\Omega}') \mathcal{P}^A(\hat{\Omega}, f),$$

where  $\mathcal{P}^A(\hat{\Omega}, f)$  describes both frequency and angular distribution of GWB power together.

statistically stationary and, in practice, it should not vary significantly over the neighborhood of earth where we can place the detectors. Hence, from now on, we omit the arguments  $(t, \mathbf{x})$  from  $\rho_{\text{GW}}(t, \mathbf{x})$ .

In cosmology, energy density of a component is usually represented by its relative magnitude with respect to the cosmological critical density  $\rho_{\text{crit}}$  required for a flat universe,

$$\rho_{\text{crit}} = \frac{3c^2 H_0^2}{8\pi G}, \quad (4.7)$$

(in the units of energy density) where  $H_0$  is Hubble constant at the current epoch. If the GWB is statistically homogenous and stationary<sup>4</sup>, the energy density of the GWB  $\rho_{\text{GW}}$  is uniform over the whole universe, hence the energy density is better represented by its relative strength  $\Omega_{\text{GW}}$  with respect to the critical density

$$\Omega_{\text{GW}} := \frac{\rho_{\text{GW}}}{\rho_{\text{crit}}}. \quad (4.8)$$

The frequency spectrum of GWB energy density is also a very important physical quantity. The community has adopted the notation  $\Omega_{\text{GW}}(f)$  to represent the *one sided* frequency spectrum, which should not be confused with its all frequency integrated counterpart  $\Omega_{\text{GW}}$ . The frequency spectrum of GWB produced by slow roll inflation, a very important pillar of standard big bang cosmology, is scale invariant, i.e., flat in logarithmic frequency scale. Therefore, conventionally, the GWB spectrum is defined as the energy density per unit logarithmic frequency interval

$$\Omega_{\text{GW}}(f) := \lim_{\delta \ln f \rightarrow 0} \left[ \frac{1}{\rho_{\text{crit}}} \frac{\delta \rho_{\text{GW}}}{\delta \ln f} \right]_f, \quad (4.9)$$

where  $\delta \rho_{\text{GW}}$  is the contribution to the energy density from the infinitesimal logarithmic frequency interval  $\delta \ln f$  at frequency  $f$  (for an alternative but equivalent definition of  $\Omega_{\text{GW}}(f)$  see, e.g., [86]). If we define a cumulative spectrum of energy density  $\rho_{\text{GW}}(f)$  as the *one sided* total energy density contributed by the frequency interval  $[0, f]$ , so that,  $\rho_{\text{GW}}(\infty) \equiv \rho_{\text{GW}}$ , we can express the spectrum as a proper logarithmic derivative:

$$\Omega_{\text{GW}}(f) = \frac{1}{\rho_{\text{crit}}} \frac{d\rho_{\text{GW}}(f)}{d \ln f}. \quad (4.10)$$

If the frequency spectrum  $\Omega_{\text{GW}}(f)$  is integrated over all the (logarithmic) frequen-

---

<sup>4</sup>Though the energy density  $\rho_{\text{GW}}$  is statistically stationary, it can vary over cosmological time scales due to the expansion of the universe.

cies, one gets back the total energy density:

$$\int_{-\infty}^{\infty} \Omega_{\text{GW}}(f) d \ln f = \frac{1}{\rho_{\text{crit}}} \int_{-\infty}^{\infty} \frac{d\rho_{\text{GW}}(f)}{d \ln f} d \ln f = \frac{1}{\rho_{\text{crit}}} [\rho_{\text{GW}}(\infty) - \rho_{\text{GW}}(0)] = \Omega_{\text{GW}}. \quad (4.11)$$

This was a consistency check for the above definition of GWB frequency spectrum.

The quantity  $\mathcal{P}^A(\hat{\Omega})$  can now be interpreted by comparing two sides of eqn (4.6). Substituting eqn (4.2), eqn (4.5) and eqn (4.8) in eqn (4.6) and using the identity  $\mathbf{e}^A : \mathbf{e}^A \equiv e^A_{ab} e^{ab}_A = 2$  one gets

$$\Omega_{\text{GW}} = \frac{2\pi^2}{3H_0^2} \int_{-\infty}^{\infty} df f^2 H(f) \int_{S^2} d\hat{\Omega} [\mathcal{P}^+(\hat{\Omega}) + \mathcal{P}^\times(\hat{\Omega})] \quad (4.12)$$

$$= \frac{4\pi^2}{3H_0^2} \int_{S^2} d\hat{\Omega} [\mathcal{P}^+(\hat{\Omega}) + \mathcal{P}^\times(\hat{\Omega})] \int_0^{\infty} df f^2 H(f). \quad (4.13)$$

Hence, the GW energy density contributed by per unit solid angle of GWB sky is

$$\lim_{|\delta\hat{\Omega}| \rightarrow 0} \frac{\delta\Omega_{\text{GW}}}{\delta\hat{\Omega}} \Big|_{\hat{\Omega}} = \frac{4\pi^2}{3H_0^2} [\mathcal{P}^+(\hat{\Omega}) + \mathcal{P}^\times(\hat{\Omega})] \int_0^{\infty} df f^2 H(f), \quad (4.14)$$

where  $\delta\Omega_{\text{GW}}$  is the part of energy density coming from the infinitesimal solid angle  $\delta\hat{\Omega}$  located at the direction  $\hat{\Omega}$ . Related definition of specific intensity commonly used in astrophysics is given at the end of the section.

One can take a similar approach to establish the relation

$$\Omega_{\text{GW}}(f) = \frac{4\pi^2}{3H_0^2} f^3 H(f) \int_{S^2} d\hat{\Omega} [\mathcal{P}^+(\hat{\Omega}) + \mathcal{P}^\times(\hat{\Omega})]. \quad (4.15)$$

Since, both  $H(f)$  and  $\mathcal{P}^A(\hat{\Omega})$  are unnormalized, we are free to choose *one* additional normalization condition<sup>5</sup>. Using the (polarization independent) normalization

$$\int_{S^2} d\hat{\Omega} [\mathcal{P}^+(\hat{\Omega}) + \mathcal{P}^\times(\hat{\Omega})] = 8\pi, \quad (4.16)$$

one gets the relation between  $\Omega_{\text{GW}}(f)$  and  $H(f)$  as

$$\Omega_{\text{GW}}(f) = \frac{32\pi^3}{3H_0^2} f^3 H(f) \Rightarrow H(f) = \frac{3H_0^2}{32\pi^3} |f|^{-3} \Omega_{\text{GW}}(|f|). \quad (4.17)$$

<sup>5</sup>Note that, the normalization of  $\mathcal{P}^A(\hat{\Omega})$  is not compulsory, it is required only for comparing with the conventionally defined quantity  $\Omega_{\text{GW}}(f)$ . We may not use this condition while constructing filters.

More generally, one can extend eqn (4.14) to derive the expression for GWB energy density per unit logarithmic frequency interval per unit solid angle

$$\Omega_{\text{GW}}(f, \hat{\Omega}) := \lim_{|\delta\hat{\Omega}| \rightarrow 0} \left. \frac{\delta\Omega_{\text{GW}}(f)}{\delta\hat{\Omega}} \right|_{\hat{\Omega}} = \frac{4\pi^2}{3H_0^2} f^3 H(f) [\mathcal{P}^+(\hat{\Omega}) + \mathcal{P}^\times(\hat{\Omega})], \quad (4.18)$$

where  $\delta\Omega_{\text{GW}}(f)$  is the part of frequency spectrum coming from the infinitesimal solid angle  $\delta\hat{\Omega}$  located at the direction  $\hat{\Omega}$ . The above quantity differs by a factor of  $c/f$  from the *specific intensity*, defined as the energy density per unit frequency interval per unit solid angle. Thus the specific intensity<sup>6</sup> of GWB,

$$I_{\text{GW}}(f, \hat{\Omega}) = \frac{4\pi^2 c}{3H_0^2} f^2 H(f) [\mathcal{P}^+(\hat{\Omega}) + \mathcal{P}^\times(\hat{\Omega})], \quad (4.19)$$

provides a complete physical interpretation for  $\mathcal{P}^A(\hat{\Omega})$ .

## 4.2 Sources of GWB

The stochastic gravitational wave background consists of two parts - an highly anisotropic astrophysical background caused by unresolved long and short term sources and a (relatively low) statistically isotropic cosmological background generated in the very early universe. A comprehensive review of the astrophysical and cosmological GWB can be found in [87]. Few points of interest for our analysis are listed below. The wide spectrum of the GWB components and their detectability using the two upcoming advanced LIGO detectors are nicely illustrated in figure 4.1 (Fig 1 of [87]).

The astrophysical GWB can be classified into two main types depending on the nature of the sources:

- **Continuous:** The continuous sources of GW are slowly varying sources whose evolution times are comparable to the observation time, say, one year, e.g., rotating binary (not in the final few minutes before coalescence), deformed neutron star and galactic white dwarfs. The continuous sources create a continuous GWB.
- **Burst:** Burst sources are unmodeled sources whose evolution time is much smaller than the observation time. If the burst sources have a very high event

<sup>6</sup>Note that, we have used  $\rho_{\text{crit}}$  as the unit of energy, to express the specific intensity in the usual unit of energy (e.g., CGS),  $I_{\text{GW}}(f, \hat{\Omega})$  should be multiplied by  $\rho_{\text{crit}}$  in the corresponding units.

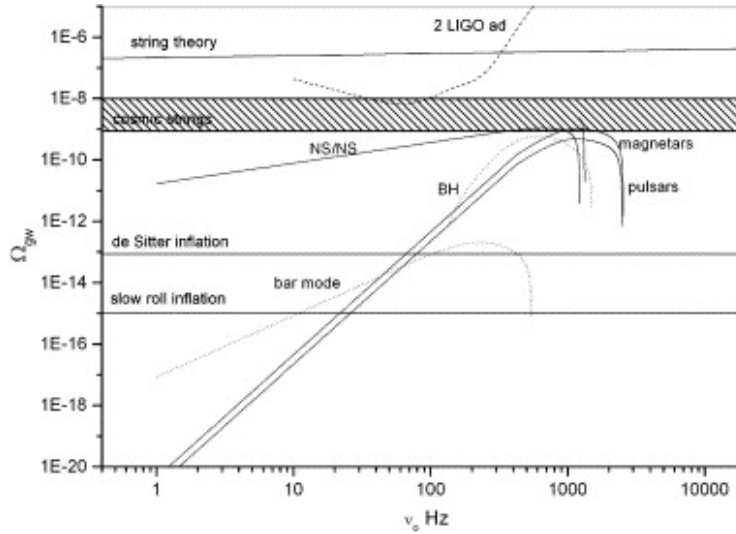


Figure 4.1: **Inflationary GWB spectra and detectability using advanced LIGO detectors.** The figure shows the spectra of different astrophysical and cosmological GWB sources and their detectability using the two upcoming advanced LIGO detectors (Fig 1 of [87]). Though it may not be possible to measure the GWB using the advanced LIGO detectors, putting strong upper limit on the background is of great scientific importance.

rate, so that, effectively there is at least one burst event at any given time over the full observation time, a continuous GWB is produced. If the even rate times event duration (Duty Cycle) is less than one, there are times when there is no burst event. These sources create a non-continuous GWB known as the popcorn noise.

The cosmological GWB is generated by phenomena in the very early universe and hence it can be a direct probe of the universe when its age was comparable to the Planck time  $10^{-43}$ s. The “standard” model of cosmology requires an inflationary phase of the universe to explain the very high degree of homogeneity, isotropy and flatness of the universe. Most of the reasonable models of inflation predict a very broad band scale invariant cosmological GWB, so the detection of the cosmological GWB would be a direct probe of the inflation. Several experiments are being proposed to detect the cosmological GWB at different frequencies. These experiments either aim to probe the GWB directly using the GW detectors or plan to measure cosmological GWB at very low frequencies by probing the B-mode polarization of the cosmic microwave background. The spectrum and detectability of the inflationary GWB is shown in figure 4.2 taken from page 18 of [88]. While the ground based GW

detectors are unlikely to detect the inflationary GWB, the space based GW detectors look quite promising. The upcoming CMB polarization experiments are likely to probe the inflationary GWB at very low frequencies by precise measurement of B-mode polarization anisotropy of the cosmic microwave background.

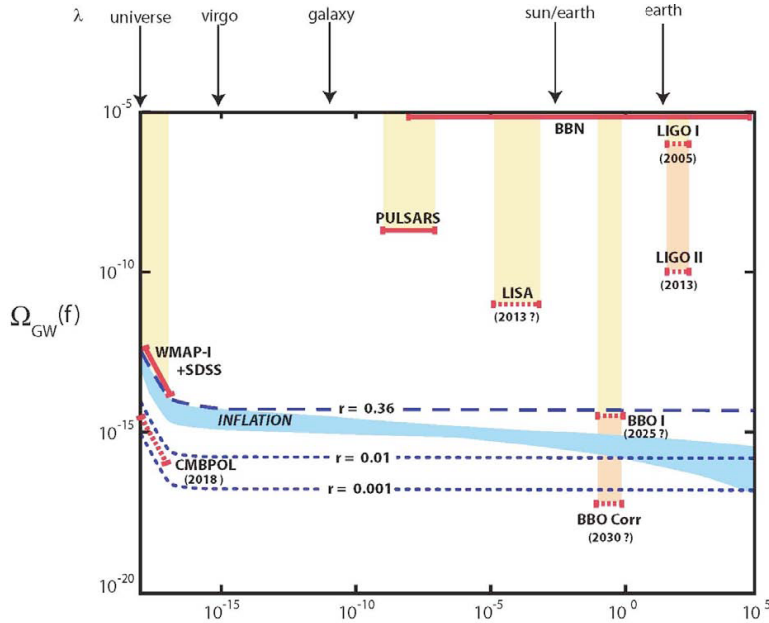


Figure 4.2: **GWB spectra and detectability landscape.** The figure shows the expected levels of cosmological inflationary GWB for different scalar to tensor ratio and their detectability using the currently operational and proposed detectors (Picture taken from page 18 of [88]). While the ground based GW detectors may not detect the cosmological GWB, the proposed space based GW detectors are quite promising. Indirect detection of the inflationary GWB at very low frequencies by precise measurement of B-mode polarization anisotropy of the cosmic microwave background is likely with the CMB polarization experiments coming in the next few decades.

### 4.3 Detection of GWB: Radiometer Analysis

Stochastic signals are characterized by their statistical expectation values. Two different detector have statistically independent noise. The simplest statistics is the two point correlation or equivalently the power spectrum. These facts suggest that the correlation of data from two independent detectors should be the best statistic for detecting and mapping a stochastic GWB. This method has broad similarity

with the earth rotation synthesis imaging used in radio astronomy and CMB experiments, so, following a similar nomenclature, the analysis has been named as “GW radiometer”. The general GW radiometer analysis technique has been presented in this section.

### 4.3.1 Cross-correlation statistic

The time series data  $s_I(t)$  from detector  $I$  consists of two parts - the true GW strain  $h_I(t)$  and noise  $n_I(t)$ :

$$s_I(t) = h_I(t) + n_I(t). \quad (4.20)$$

The true GW strain in the detector  $I$  due to the incident GW  $\mathbf{h}(t, \mathbf{x}(t)) \equiv h_{ab}(t, \mathbf{x}(t))$  is given by the inner product

$$h_I(t) = \mathbf{d}_I(t) : \mathbf{h}(t, \mathbf{x}_I(t)), \quad (4.21)$$

where  $\mathbf{x}_I(t)$  is the location of detector  $I$  and  $\mathbf{d}_I(t)$  is the detector tensor defined in terms of the outer products of the unit vectors along its arms  $\hat{\mathbf{X}}_I(t)$  and  $\hat{\mathbf{Y}}_I(t)$ :

$$\mathbf{d}_I(t) := \frac{1}{2} [\hat{\mathbf{X}}_I(t) \otimes \hat{\mathbf{X}}_I(t) - \hat{\mathbf{Y}}_I(t) \otimes \hat{\mathbf{Y}}_I(t)]. \quad (4.22)$$

Here we are using equatorial coordinate system, whose origin coincides with the centre of the Earth. The axes are defined as follows: For a fixed but arbitrarily chosen time  $t = 0$ , the  $x$ - $y$  axes are in the equatorial plane forming a right handed triad with the  $z$  axis pointing to the north celestial pole and the  $x$ -axis is chosen to be point at the Greenwich meridian. So, the detector locations  $\mathbf{x}_I(t)$ , the vector joining the sites  $\Delta\mathbf{x}(t) := \mathbf{x}_1(t) - \mathbf{x}_2(t)$  and the detector arms  $\hat{\mathbf{X}}_I(t)$ ,  $\hat{\mathbf{Y}}_I(t)$  are all vectors rotating with the earth, their instantaneous value can be obtained by using the Euler rotation formula, e.g.,

$$\Delta\mathbf{x}(t) = \mathbf{R}(-\omega_E t) \cdot \Delta\mathbf{x}(0), \quad (4.23)$$

where  $\omega_E = 2\pi/(1 \text{ sidereal day})$  is the earth’s rotation frequency and  $\mathbf{R}(\phi)$  represents Euler rotation matrix about the earth’s rotation axis ( $z$ -axis) by an angle  $\phi$ :

$$\mathbf{R}(\phi) := \begin{pmatrix} \cos \phi & \sin \phi & 0 \\ -\sin \phi & \cos \phi & 0 \\ 0 & 0 & 1 \end{pmatrix}. \quad (4.24)$$

The detector tensor  $\mathbf{d}_I(t)$  can be obtained by a similarity transform with  $\mathbf{R}(-\omega_E t)$ :

$$\mathbf{d}_I(t) = \mathbf{R}(-\omega_E t) \mathbf{d}_I(0) \mathbf{R}(\omega_E t). \quad (4.25)$$

Statistically, the quantities  $h_I(t)$  are uncorrelated with  $n_J(t)$ ; that is, the four correlations, in the time domain are zero:  $\langle h_I(t)n_J(t') \rangle = 0$ ,  $I, J = 1, 2$ , where  $t, t'$  are any two time instants. We also assume that the noise in the different detectors is uncorrelated; that is,  $\langle n_1(t)n_2(t') \rangle = 0$ . This assumption is not unreasonable when the detectors are widely separated. Thus the only possible correlation we envisage is between  $h_1(t)$  and  $h_2(t')$ . Moreover, a stochastic background is characterized by its statistical expectation values. Therefore, the cross-correlation between detector outputs is used as the statistic. The simplest cross-correlation statistic that could be formed for the observation time  $T$  is

$$\int_{-T/2}^{T/2} dt s_1(t) s_2(t). \quad (4.26)$$

However, the outputs of modern GW detectors are too noisy, one needs to suppress all those frequency bands which have excess noise. So it is necessary to introduce a filter function in the cross-correlation statistic that weigh the product of the signal appropriately. A filter can handle “colored” noise, and, in addition, it provides a complete mathematical framework to search for different models of GWB, including a directed search to map the GWB sky. Also, the detector coordinates and noise power spectra are non-stationary, so the correlation statistic has to be computed over smaller time chunks to simplify filter evaluation. The chunk size is usually chosen much greater than the light travel time delay between the detector sites (few tens of milliseconds for ground based detectors) over which the detector outputs are correlated; but small enough, so that the detector noise spectra and the earth can be regarded as stationary over each chunk. The size of the chunk used in current data analysis varies from 32 to 192 seconds. The “broadening” of the Fourier components,  $\sim \text{few} \times 10^{-2} \text{Hz}$ , due to the finite size of the chunk is much smaller than the size of the frequency band of the stochastic signals we are interested in. The final statistic for the full observation time  $T$  is obtained by linearly combining the cross-correlations over the smaller chunks as a weighted sum.

To incorporate all the above requirements, we construct a more sophisticated statistic using a (possibly direction dependent) filter function  $Q(t; t', t'')$ , which connects sidereal time  $t'$  of one detector’s data to  $t''$  of the other detector’s data to match

the phases of the GW strains in the detectors. In general, the filter is a functional of the source and detectors characteristics, more specifically, the frequency PSDs of the GWB signal, noise in detectors and, also, the angular power distribution of the GWB. However, we do not explicitly show these dependencies in the filter, unless we are using some models for those functions (or parameters) for constructing filters. Optimized filters are constructed for each chunk of size  $\Delta t$  at different sidereal times  $t$ . The general form of the cross-correlation statistic  $S$  for all the  $n = T/\Delta t$  sidereal time bins can then be formally expressed using the following equations:

$$\Delta S(t) := \int_{t-\Delta t/2}^{t+\Delta t/2} dt' \int_{t-\Delta t/2}^{t+\Delta t/2} dt'' s_1(t') s_2(t'') Q(t; t', t''). \quad (4.27)$$

$$S := \sum_{i=1}^n w_i \Delta S(t_i); \quad \sum_{i=1}^n w_i = 1. \quad (4.28)$$

The weight factors  $w_i$  are chosen in such a way that the Signal-to-Noise Ratio (SNR) is maximized. If we choose the filter  $Q(t; t', t'')$ , such that, the expectation of  $\Delta S(t)$  does not vary with time, it is easy to show that, to maximize SNR the weight factors should be inversely proportional to the variance of  $\Delta S(t)$ . The proof is given below:

**Problem:** Let  $\mathbf{x} \equiv x_i$  be a set of independent estimators with mean  $\boldsymbol{\mu} \equiv \mu_i := \langle x_i \rangle$  and variance  $\sigma_i^2 := \langle (x_i - \langle x_i \rangle)^2 \rangle$ . Let us construct an estimator  $X$  as a weighted sum of the estimators  $x_i$ :

$$X := \sum_i w_i x_i; \quad \sum_i w_i = 1. \quad (4.29)$$

The problem is to choose the normalized weight factors  $w_i$ , such that, the signal-to-noise ratio (SNR) of the estimator  $X$  is maximized.

**Solution:** Mean, variance and SNR of the estimator  $X$  are respectively

$$\mu_X := \langle X \rangle = \sum_i w_i \mu_i \quad (4.30)$$

$$\sigma_X^2 := \langle (X - \langle X \rangle)^2 \rangle = \sum_i w_i^2 \sigma_i^2 \quad (4.31)$$

$$\text{SNR}_X := \frac{\mu_X}{\sigma_X} = \frac{\sum_i w_i \mu_i}{\sqrt{\sum_i w_i^2 \sigma_i^2}}. \quad (4.32)$$

The SNR can be expressed as a scalar product in terms of the unit vector

$\hat{\kappa} \equiv \kappa_i := w_i \sigma_i / \sqrt{\sum_i w_i^2 \sigma_i^2}$  and the vector  $\rho \equiv \rho_i := \mu_i \sigma_i^{-1}$ , where  $\rho_i$  is the SNR of  $x_i$ :

$$\text{SNR}_X = \hat{\kappa} \cdot \rho. \quad (4.33)$$

Clearly, the SNR is maximized when  $\hat{\kappa}$  is parallel to  $\rho$ , which happens when we choose  $w_i \propto \mu_i \sigma_i^{-2}$ . Since, by construction,  $\sum_i w_i = 1$ , the Minimum Variance Estimator (MVE) for the present problem is

$$X = \frac{\sum_i x_i \mu_i \sigma_i^{-2}}{\sum_i \mu_i \sigma_i^{-2}}, \quad (4.34)$$

which is a linear combination of all the estimators, with less noisy and/or more “bright” ones getting more weightage. Then the mean, variance and SNR of  $X$  are respectively

$$\mu_X = \frac{\sum_i \mu_i^2 \sigma_i^{-2}}{\sum_i \mu_i \sigma_i^{-2}}; \quad \sigma_X^2 = \frac{\sum_i \mu_i^2 \sigma_i^{-2}}{[\sum_i \mu_i \sigma_i^{-2}]^2}; \quad \text{SNR}_X = \sqrt{\sum_i \mu_i \sigma_i^{-2}}. \quad (4.35)$$

More generally, if the estimators  $x_i$  are correlated, the coefficients  $w_i$  should be chosen as the solution of the set of linear equations

$$\sum_j \sigma_{ij} w_j = \mu_i \sum_j w_j, \quad (4.36)$$

where  $\sigma \equiv \sigma_{ij} := \langle (x_i - \langle x_i \rangle)(x_j - \langle x_j \rangle) \rangle$  is the covariance matrix of  $x_i$ . The MVE in this case is

$$X = \frac{\mathbf{x} \cdot \sigma^{-1} \cdot \boldsymbol{\mu}}{\mathbf{1} \cdot \sigma^{-1} \cdot \boldsymbol{\mu}}, \quad (4.37)$$

where  $\sigma^{-1}$  is the inverse of the covariance matrix and  $\mathbf{1}$  is a vector whose all the components are 1, and its variance and SNR in are given by

$$\mu_X = \frac{\boldsymbol{\mu} \cdot \sigma^{-1} \cdot \boldsymbol{\mu}}{\mathbf{1} \cdot \sigma^{-1} \cdot \boldsymbol{\mu}}; \quad \sigma_X^2 = \frac{\boldsymbol{\mu} \cdot \sigma^{-1} \cdot \boldsymbol{\mu}}{[\mathbf{1} \cdot \sigma^{-1} \cdot \boldsymbol{\mu}]^2}; \quad \text{SNR}_X = \sqrt{\mathbf{1} \cdot \sigma^{-1} \cdot \boldsymbol{\mu}}. \quad (4.38)$$

If all  $x_i$  are unbiased estimators of a quantity  $\mu$ , that is,  $\langle x_i \rangle = \mu$  (which is always possible by defining a new set of estimators  $x'_i := x_i / \mu_i$ ), by construction  $X$  is an unbiased estimator of  $\mu$ :  $\langle X \rangle = \mu$ . The Minimum Variance Unbiased Estimator (MVUE), its variance and its SNR are then

given by

$$X = \frac{\mathbf{x} \cdot \boldsymbol{\sigma}^{-1} \cdot \mathbf{1}}{\text{Tr}(\boldsymbol{\sigma}^{-1})}; \quad \sigma_X^2 = [\text{Tr}(\boldsymbol{\sigma}^{-1})]^{-1}; \quad \text{SNR}_X = \mu \sqrt{\text{Tr}(\boldsymbol{\sigma}^{-1})}. \quad (4.39)$$

Finally, if all  $x_i$  are independent unbiased estimators of a quantity  $\mu$ , that is,  $\langle X \rangle = \mu$  and  $\sigma_{ij} = \sigma_i^2 \delta_{ij}$ , the weight factors should be chosen as  $w_i \propto \sigma_i^{-2}$  and the MVUE, its variance and its SNR are respectively

$$X = \frac{\sum_i x_i \sigma_i^{-2}}{\sum_i \sigma_i^{-2}}; \quad \sigma_X^2 = \left[ \sum_i \sigma_i^{-2} \right]^{-1}; \quad \text{SNR}_X = \mu \sqrt{\sum_i \sigma_i^{-2}}. \quad (4.40)$$

Thus, if  $\Delta S(t)$  is an *independent unbiased estimator* of a time independent quantity with variance  $\sigma_{\Delta S}^2(t)$ , we may construct the unbiased estimator  $S$  for the full observation time as

$$S = \left[ \sum_{i=1}^n \Delta S(t_i) \sigma_{\Delta S}^{-2}(t_i) \right] / \left[ \sum_{i=1}^n \sigma_{\Delta S}^{-2}(t_i) \right]. \quad (4.41)$$

Clearly, the noisy parts of a day (comparatively large  $\sigma_{\Delta S}$ ) get less weightage. Finally, the overall variance and SNR of the statistic  $S$  are respectively

$$\sigma^2 = \left[ \sum_{i=1}^n \sigma_{\Delta S}^{-2}(t_i) \right]^{-1}; \quad \text{SNR} := \frac{\langle \Delta S(t_i) \rangle}{\sigma} = \langle \Delta S(t_i) \rangle \sqrt{\sum_{i=1}^n \sigma_{\Delta S}^{-2}(t_i)}. \quad (4.42)$$

The power spectra of GW and the detector noise are modeled in the frequency domain, therefore it is convenient to formulate the whole analysis in the frequency domain. The (approximate) Fourier transform of a chunk of detector output can be defined as

$$\widetilde{s}_I(t; f) := \int_{t-\Delta t/2}^{t+\Delta t/2} dt' s_I(t') e^{-2\pi i f t'}. \quad (4.43)$$

The Fourier transform in this case itself is a function of time  $t$ ! This is understandable because the time argument  $t$  in the Fourier transform  $\widetilde{s}_I(t; f)$  is essentially an identifier for the chunk. The size of the frequency bands are negligibly increased due to the finite size of the chunk (which would not happen if  $\Delta t \rightarrow \infty$ ), but, as mentioned before, it does not affect the analysis of data from stochastic signals with

much broader frequency bands. Most importantly, by inverse Fourier transform,

$$\int_{-\infty}^{\infty} df \widetilde{s}_I(t; f) e^{2\pi i f t} = \int_{-\infty}^{\infty} df e^{2\pi i f t} \int_{t-\Delta t/2}^{t+\Delta t/2} dt' s_I(t') e^{-2\pi i f t'} = s_I(t), \quad (4.44)$$

one can recover the whole chunk time series  $s_I(t)$ . This justifies the reason for calling the coefficients  $\widetilde{s}_I(t; f)$  as ‘‘Fourier transforms’’. The same convention will be used for several other quantities as well in this analysis.

Assuming that the noise in the detectors are stationary within each chunk, we may write  $Q(t; t', t'') = Q(t; t' - t'')$ , which allows us to expand the filter in terms of its Fourier transform  $\widetilde{Q}(t, f)$  as

$$Q(t; t', t'') = Q(t; t' - t'') = \int_{-\infty}^{\infty} df e^{2\pi i f (t' - t'')} \widetilde{Q}(t, f). \quad (4.45)$$

Substituting the above in eqn (4.27) one gets

$$\Delta S(t) = \int_{t-\Delta t/2}^{t+\Delta t/2} dt' \int_{t-\Delta t/2}^{t+\Delta t/2} dt'' s_1(t') s_2(t'') \int_{-\infty}^{\infty} df e^{2\pi i f (t' - t'')} \widetilde{Q}(t, f). \quad (4.46)$$

Rearranging terms and using the definition of Fourier transforms of the signal it is easy to show that

$$\Delta S(t) = \int_{-\infty}^{\infty} df \widetilde{s}_1^*(t; f) \widetilde{s}_2(t; f) \widetilde{Q}(t, f). \quad (4.47)$$

This form of the statistic (a.k.a. point estimate) will be used in our analysis.

### 4.3.2 Correlation between GW Strains

While constructing the statistic, it was assumed that the true GW strains in the detectors are correlated (but the noise streams are not). The expression for correlation between the GW strains in two detectors will be derived here, which is necessary for the derivation of the optimal filter.

The Fourier transform of a chunk of GW strain in detector  $I$  [from eqn (4.21)] is

$$\widetilde{h}_I(t; f) := \int_{t-\Delta t/2}^{t+\Delta t/2} dt' e^{-2\pi i f t'} h_I(t') = \int_{t-\Delta t/2}^{t+\Delta t/2} dt' e^{-2\pi i f t'} \mathbf{d}_I(t') : \mathbf{h}(t', \mathbf{x}_I(t')). \quad (4.48)$$

The GW strain involves two time scales of different orders - (i) the intrinsic frequency of the wave and (ii) the period of the earth’s rotation over which the detector coordinates and the noise power spectra significantly change. As mentioned earlier,

the chunk size is kept much smaller than the earth's rotation frequency, so that, the detector parameters can be approximated to be stationary over this period. Hence we may consider the quantities  $\mathbf{d}_I(t')$  and  $\mathbf{x}_I(t')$  to be nearly constant in the above integral and replace them by  $\mathbf{d}_I(t)$  and  $\mathbf{x}_I(t)$  respectively, while keeping the high frequency metric perturbation term  $\mathbf{h}(t, \mathbf{x}_I(t))$  untouched. Then by substituting eqn (4.2) in the above formula we get

$$\begin{aligned}\tilde{h}_I(t; f) &= \int_{t-\frac{\Delta t}{2}}^{t+\frac{\Delta t}{2}} dt' \sum_{A=+, \times} \int_{-\infty}^{\infty} df' \int_{S^2} d\hat{\Omega} \mathbf{d}_I(t) : \mathbf{e}^A(\hat{\Omega}) \tilde{h}_A(f', \hat{\Omega}) e^{2\pi i [f't' - f't' - f' \frac{\hat{\Omega} \cdot \mathbf{x}_I(t)}{c}]} \\ &= \sum_{A=+, \times} \int_{S^2} d\hat{\Omega} F_I^A(\hat{\Omega}, t) \int_{-\infty}^{\infty} df' \tilde{h}_A(f', \hat{\Omega}) e^{2\pi i [(f'-f)t - f' \frac{\hat{\Omega} \cdot \mathbf{x}_I(t)}{c}]} \delta_{\Delta t}(f - f'),\end{aligned}\quad (4.49)$$

where  $F_I^A(\hat{\Omega}, t)$  are the antenna pattern functions of detector  $I$ ,

$$F_I^A(\hat{\Omega}, t) := \mathbf{e}^A(\hat{\Omega}) : \mathbf{d}_I(t), \quad (4.50)$$

and  $\delta_{\Delta t}(f)$  is the finite time delta function

$$\delta_{\Delta t}(f) := \int_{-\Delta t/2}^{\Delta t/2} dt e^{-2\pi i f t} = \frac{\sin \pi f \Delta t}{\pi f}. \quad (4.51)$$

The finite time delta function  $\delta_{\Delta t}(f)$  behaves as Dirac delta function  $\delta(f)$  in the limit  $\Delta t \rightarrow \infty$ , but has the property  $\delta_{\Delta t}(0) = \Delta t$ . Hence for large chunk size  $\Delta t$  the Fourier transform of chunk of data from detector  $I$  takes the simple form

$$\tilde{h}_I(t, f) = \int_{S^2} d\hat{\Omega} \left[ F_I^+(\hat{\Omega}, t) \tilde{h}_+(f, \hat{\Omega}) + F_I^\times(\hat{\Omega}, t) \tilde{h}_\times(f, \hat{\Omega}) \right] e^{-2\pi i f \hat{\Omega} \cdot \mathbf{x}_I(t)/c}. \quad (4.52)$$

The expectation of cross-correlation between the Fourier transforms of chunks of detector outputs at time  $t$  can be expressed as [using eqn (4.49) and eqn (4.5)]:

$$\langle \tilde{h}_1^*(t, f) \tilde{h}_2(t, f') \rangle = e^{2\pi i t(f-f')} \int_{-\infty}^{\infty} df'' H(f'') \delta_{\Delta t}(f''-f) \delta_{\Delta t}(f''-f') \gamma_{\mathcal{P}^A}(t, f''), \quad (4.53)$$

in terms of the very important quantity, the *general overlap reduction function*

$$\gamma_{\mathcal{P}^A}(t, f) := \int_{S^2} d\hat{\Omega} \left[ F_1^+(\hat{\Omega}, t) F_2^+(\hat{\Omega}, t) \mathcal{P}^+(\hat{\Omega}) + F_1^\times(\hat{\Omega}, t) F_2^\times(\hat{\Omega}, t) \mathcal{P}^\times(\hat{\Omega}) \right] e^{2\pi i f \hat{\Omega} \cdot \Delta \mathbf{x}(t)/c}, \quad (4.54)$$

where  $\Delta \mathbf{x}(t)$  is the separation vector between the two detectors  $\Delta \mathbf{x}(t) := \mathbf{x}_1(t) - \mathbf{x}_2(t)$ .

In the limit of large chunk size, the above relation takes the neat form

$$\langle \widetilde{h}_1^*(t, f) \widetilde{h}_2(t, f') \rangle = \delta(f - f') H(f) \gamma_{\mathcal{P}^A}(t, f). \quad (4.55)$$

The advantage of expressing  $\langle \widetilde{h}_1^*(t, f) \widetilde{h}_2(t, f) \rangle$  by eqn (4.53) can be readily realized if we put  $f = f'$ . In this case, the correlation diverges in the limit  $\Delta t \rightarrow \infty$ , as evident from eqn (4.55). But, in practice,  $\Delta t$  is finite, and hence, we expect a finite value. Eqn (4.53) lets us compute that finite value of  $\langle \widetilde{h}_1^*(t, f) \widetilde{h}_2(t, f) \rangle$  at  $f = f'$ . We use the large  $\Delta t$  limit and replace one of the finite time delta functions  $\delta_{\Delta t}(f'' - f)$  in the integrand of eqn (4.53) by the Dirac delta function  $\delta(f'' - f)$ , while treating the other  $\delta_{\Delta t}(f'' - f)$  as a normal function and put  $\delta_{\Delta t}(0) = \Delta t$ . We get

$$\langle \widetilde{h}_1^*(t, f) \widetilde{h}_2(t, f) \rangle = \Delta t H(f) \gamma_{\mathcal{P}^A}(t, f). \quad (4.56)$$

This result is important for injecting test signals in the detector output.

### 4.3.3 Detector Noise

The detectors outputs, and so the cross-correlation statistic, are overwhelmed by noise. However, since the noise in the detectors are uncorrelated whereas the true GW strains are correlated, we hope to detect a stochastic background by cross-correlating detector outputs. Though the expected value of the signal is determined by the true GW strain, the noise terms produce fluctuations in the statistic. The properties of detector noise in a finite sized chunk is described here.

The noise time series  $n_I(t)$  in detector  $I$ , and hence its Fourier transform,

$$\widetilde{n}_I(t; f) := \int_{t-\Delta t/2}^{t+\Delta t/2} dt n_I(t) e^{-2\pi i f t}, \quad (4.57)$$

are of zero mean:  $\langle n_I(t) \rangle = 0$ ,  $\langle \widetilde{n}_I(t; f) \rangle = 0$  and uncorrelated with true strain signal and noise of other detectors,

$$\langle \widetilde{n}_1^*(t; f) \widetilde{n}_2(t; f) \rangle = \langle \widetilde{h}_1^*(t; f) \widetilde{n}_2(t; f) \rangle = \langle \widetilde{n}_1^*(t; f) \widetilde{h}_2(t; f) \rangle = 0. \quad (4.58)$$

The chunk size is usually kept few tens of seconds over which detector noise can be regarded as stationary. Which means that  $\langle n_I(t') n_I(t'') \rangle$  is a function of  $t'' - t'$ , provided both  $t', t''$  are in the same chunk centered at time  $t$ . Then, using the fact

that  $n_I(t)$  is a real, we may write

$$\langle n_I(t') n_I(t'') \rangle = \frac{1}{2} \int_{-\infty}^{\infty} df P_I(t; |f|) e^{2\pi i f(t'' - t')}, \quad (4.59)$$

where  $P_I(t; f)$  is the *one sided* noise PSD. This noise PSD also is a function of time  $t$ , because the noise power spectrum usually varies over different chunks.

It is useful to translate the above equation in terms of the Fourier transform of noise. Taking Fourier transforms for both the time variables  $t', t''$ , we get

$$\begin{aligned} & \left\langle \int_{t-\Delta t/2}^{t+\Delta t/2} dt' e^{2\pi i f' t'} n_I(t') \int_{t-\Delta t/2}^{t+\Delta t/2} dt'' e^{-2\pi i f'' t''} n_I(t'') \right\rangle \\ &= \frac{1}{2} \int_{-\infty}^{\infty} df P_I(t; |f|) \int_{t-\Delta t/2}^{t+\Delta t/2} dt' e^{2\pi i (f' - f) t'} \int_{t-\Delta t/2}^{t+\Delta t/2} dt'' e^{-2\pi i (f'' - f) t''}, \quad (4.60) \end{aligned}$$

where we have converted the “one sided” frequency integral  $[0, \infty]$  to a “two sided” frequency integral  $[-\infty, \infty]$ . Then, interchanging dummy variables and introducing the finite time delta functions, we obtain

$$\langle \tilde{n}_I^*(t; f) \tilde{n}_I(t; f') \rangle = \frac{1}{2} \int_{-\infty}^{\infty} df'' P_I(t; |f''|) \delta_{\Delta t}(f'' - f) \delta_{\Delta t}(f'' - f'). \quad (4.61)$$

In the large chunk limit we arrive at the usual formula

$$\langle \tilde{n}_I^*(t; f) \tilde{n}_I(t; f') \rangle = \frac{1}{2} \delta(f - f') P_I(t; |f|). \quad (4.62)$$

The advantage of the expressing  $\langle \tilde{n}_I(t; f) \tilde{n}_I(t; f') \rangle$  using eqn (4.61) becomes evident when we put  $f = f'$ : The regular formula [eqn (4.62)] involving Dirac delta function diverges, which, in practice, is finite. Whereas in eqn (4.61) if we replace one finite time delta function by Dirac delta function and treat the other as a normal function we get

$$\langle |\tilde{n}_I(t; f)|^2 \rangle = \frac{1}{2} \Delta t P_I(t; |f|). \quad (4.63)$$

This formula is very useful for generating simulated noise.

#### 4.3.4 Optimal Filter

As the name suggests, we would like to construct an “optimal” filter to maximize the SNR of the cross-correlation statistic over the small chunks. The optimal filter depends on the theoretical model of the GWB. We shall derive the expression for

filter for the general case and then we shall present the implementation schemes for a couple of special cases.

We start by calculating the SNR of the statistic over small chunks, that is, calculate the ratio of mean and standard deviation of  $\Delta S(t)$  using the correlation properties of signal and noise derived above.

- **Mean:**

The mean of the statistic  $\Delta S(t)$

$$\mu_{\Delta S}(t) := \langle \Delta S(t) \rangle = \int_{-\infty}^{\infty} df \langle \tilde{s}_1^*(t; f) \tilde{s}_2(t; f) \rangle \tilde{Q}(t, f). \quad (4.64)$$

Since the noise satisfies the correlation properties stated in eqn (4.58)

$$\langle \tilde{s}_1^*(t; f) \tilde{s}_2(t; f) \rangle = \langle \tilde{h}_1^*(t; f) \tilde{h}_2(t; f) \rangle. \quad (4.65)$$

Using the above expression, we arrive at the result

$$\mu_{\Delta S}(t) = \Delta t \int_{-\infty}^{\infty} df H(f) \gamma_{\mathcal{P}^A}(t, f) \tilde{Q}(t, f). \quad (4.66)$$

- **Variance:**

True GW strains in the detectors are much smaller than noise, which is more severe for the stochastic signal analysis, where matched filtering can not be used. For the same reason, the cross-correlation statistic over each small chunk will also be strongly dominated by detector noise. We hope to detect a signal by combining all the chunk cross-correlations over the full observation time. Thus, while calculating the variance of  $\Delta S(t)$ , we may neglect the signal terms as compared to the noise terms. Then, the variance of  $\Delta S(t)$  can be written as

$$\begin{aligned} \sigma_{\Delta S}^2(t) &:= \langle (\Delta S(t) - \langle \Delta S(t) \rangle)^2 \rangle & (4.67) \\ &\approx \int_{-\infty}^{\infty} df \int_{-\infty}^{\infty} df' \langle \tilde{n}_1^*(t; f) \tilde{n}_2(t; f) \tilde{n}_1^*(t; f') \tilde{n}_2(t; f') \rangle \tilde{Q}^*(t, f) \tilde{Q}(t, f'), \\ &= \int_{-\infty}^{\infty} df \int_{-\infty}^{\infty} df' \langle \tilde{n}_1^*(t; f) \tilde{n}_1(t; -f') \rangle \langle \tilde{n}_2(t; f) \tilde{n}_2^*(t; -f') \rangle \tilde{Q}^*(t, f) \tilde{Q}(t, f'). \end{aligned}$$

Then substituting eqn (4.61) in the above equation, we obtain

$$\begin{aligned} \sigma_{\Delta S}^2(t) &= \int_{-\infty}^{\infty} df \int_{-\infty}^{\infty} df' \left[ \frac{1}{2} \int_{-\infty}^{\infty} df_1 P_1(t; |f_1|) \delta_{\Delta t}(f_1 - f) \delta_{\Delta t}(f_1 + f') \right] \\ &\quad \times \left[ \frac{1}{2} \int_{-\infty}^{\infty} df_2 P_2(t; |f_2|) \delta_{\Delta t}(f_2 + f') \delta_{\Delta t}(f_2 - f) \right] \tilde{Q}^*(t, f) \tilde{Q}(t, f'). \end{aligned} \quad (4.68)$$

In the above expression if we use large chunk limit and convert *one* finite time delta function to Dirac delta function for each integral (while treating the remaining ones as normal functions and putting  $\delta_{\Delta t}(0) = \Delta t$ ), we reach the final expression

$$\sigma_{\Delta S}^2(t) = \frac{\Delta t}{4} \int_{-\infty}^{\infty} df P_1(t; |f|) P_2(t; |f|) |\tilde{Q}(t, f)|^2. \quad (4.69)$$

The above results can be combined to write the expression for SNR over the small chunks as:

$$\text{SNR}_{\Delta S}(t) := \frac{\mu_{\Delta S}(t)}{\sigma_{\Delta S}(t)} = 2\sqrt{\Delta t} \frac{\int_{-\infty}^{\infty} df H(f) \gamma_{\mathcal{P}^A}(t, f) \tilde{Q}(t, f)}{\sqrt{\int_{-\infty}^{\infty} df P_1(t; |f|) P_2(t; |f|) |\tilde{Q}(t, f)|^2}} \quad (4.70)$$

Since  $P_1(t; |f|) P_2(t; |f|)$  is positive definite, we may introduce the inner product at time  $t$

$$(A, B)_t := \int_{-\infty}^{\infty} df P_1(t; |f|) P_2(t; |f|) \tilde{A}^*(t; f) \tilde{B}(t; f), \quad (4.71)$$

which satisfies all the properties of scalar product in a complex vector space indexed by  $f$ . The vector space is finite for practical purposes as the number of frequency bins used for data analysis is finite. We may also define the norm of a complex function  $A(t; f)$  at time  $t$  to be

$$\|A\| = \sqrt{(A, A)_t}. \quad (4.72)$$

In terms of the “unit” filters  $\hat{Q} := Q/\|Q\|_t$  of this space, such that,  $(\hat{Q}, \hat{Q})_t = 1$ , the SNR can be expressed in an elegant form:

$$\text{SNR}_{\Delta S}(t) = 2\sqrt{\Delta t} \left( \frac{H(f) \gamma_{\mathcal{P}^A}^*(t, f)}{P_1(t; |f|) P_2(t; |f|)}, \hat{Q} \right)_t. \quad (4.73)$$

Clearly,  $\text{SNR}_{\Delta S}(t)$  is the projection of the vector  $2\sqrt{\Delta t} H(f) \gamma_{\mathcal{P}^A}^*(t, f) / [P_1(t; |f|) P_2(t; |f|)]$

on the unit vector  $\hat{Q}$ . So, the SNR is maximized when the “signal” and the “filter” vectors are parallel, which happens when

$$\tilde{Q}(t, f) \propto \tilde{q}(t, f) := \frac{H(f) \gamma_{\mathcal{P}^A}^*(t, f)}{P_1(t; |f|) P_2(t; |f|)}, \quad (4.74)$$

where we call  $\tilde{q}(t, f)$  as the *unnormalized* filter function. From now on,  $q$  will always denote the above “unnormalized” filter for the corresponding filter  $Q$ ; same notation will be used to explicitly show the dependencies.

In practice, we have to choose the filter  $\tilde{Q}(t, f)$  such that the above criteria is satisfied, but we do not have an exact a priori model for  $H(f)$  and  $\mathcal{P}^A(\hat{\Omega})$ , which we are trying to measure! We use different models for  $H(f)$  and  $\mathcal{P}^A(\hat{\Omega})$  to search for different types of backgrounds. These models are used to construct the model dependent overlap reduction function  $\gamma_{\mathcal{P}^A}(t, f)$  and then the filter  $Q_{\mathcal{P}^A, H} \equiv \tilde{Q}_{\mathcal{P}^A, H}(t, f)$  to measure the filter dependent statistic  $\Delta S_Q(t)$  (and  $S_Q$ ). We employ a generic suffix  $Q$  to represent all the parameters  $Q$  depends on. Here  $Q$  represents, in short,  $\mathcal{P}^A, H$ . Thus, to search for a GWB with PSD  $H(f)$  and angular energy density distribution  $\mathcal{P}^A(\hat{\Omega})$ , the optimal filter is given by

$$\tilde{Q}_{\mathcal{P}^A, H}(t, f) = \lambda_Q(t) \tilde{q}_{\mathcal{P}^A, H}(t, f) = \lambda_Q(t) \frac{H(f) \gamma_{\mathcal{P}^A}^*(t, f)}{P_1(t; |f|) P_2(t; |f|)}, \quad (4.75)$$

where  $\lambda_Q(t)$  is a (real) proportionality constant, to be fixed by the normalization condition for the statistic. As discussed before, for each GWB model, we normalize the statistic over small chunks in such a way that they become unbiased estimators of a single (time independent) quantity, that is,

$$\langle \Delta S_Q(t) \rangle = \Delta t \int_{-\infty}^{\infty} df H(f) \gamma_{\mathcal{P}^A}(t, f) \tilde{Q}_{\mathcal{P}^A, H}(t, f) \quad (4.76)$$

should not vary with time  $t$ . In practice, we do not have the exact model for GWB, but the filter is still normalized by setting the mean to be constant when the filter matches the true GWB. We choose

$$\Delta t \int_{-\infty}^{\infty} df H(f) \gamma_{\mathcal{P}^A}(t, f) \tilde{Q}_{\mathcal{P}^A, H}(t, f) = 1 \quad (4.77)$$

$$\Rightarrow \lambda_Q(t) \Delta t \int_{-\infty}^{\infty} df \frac{H^2(f) |\gamma_{\mathcal{P}^A}(t, f)|^2}{P_1(t; |f|) P_2(t; |f|)} = \lambda_Q(t) \Delta t \|q_{\mathcal{P}^A, H}\|_t^2 = 1. \quad (4.78)$$

It is worth noting that the normalization equation can be rewritten in terms of the

scalar product defined in eqn (4.71) as

$$\lambda_Q(t) = \Delta t (Q_{\mathcal{P}^A, H}, Q_{\mathcal{P}^A, H})_t \equiv \Delta t \|Q_{\mathcal{P}^A, H}\|_t^2, \quad (4.79)$$

in other words, the normalization constant is proportional to the square of the norm of the filter. The normalization condition sets [see eqn (4.69) and eqn (4.79)]

$$\sigma_{\Delta S}^2(t) = (\Delta t/4)(Q_{\mathcal{P}^A, H}, Q_{\mathcal{P}^A, H})_t = \lambda_Q(t)/4 = \|q_{\mathcal{P}^A, H}\|_t^{-2}/(4\Delta t). \quad (4.80)$$

This allows us to express the statistic over the full observation time as<sup>7</sup>

$$S_Q = \left[ \Delta t \sum_{i=1}^n \|q_{\mathcal{P}^A, H}\|_{t_i}^2 \right]^{-1} \sum_{i=1}^n \int_{-\infty}^{\infty} df \tilde{s}_1^*(t_i; f) \tilde{s}_2(t_i; f) \tilde{q}_{\mathcal{P}^A, H}(t_i, f), \quad (4.81)$$

which has the overall variance [from eqn (4.42)]

$$\sigma_Q^2 = \frac{1}{4} \left[ \sum_{i=1}^n \lambda_Q^{-1}(t_i) \right]^{-1} = \frac{1}{4} \left[ \Delta t \sum_{i=1}^n \|q_{\mathcal{P}^A, H}\|_{t_i}^2 \right]^{-1}. \quad (4.82)$$

It is quite important to note that the statistic defined above, in practice, is a real quantity. This is because the Fourier transforms of (real) chunk time series data satisfies the relation  $\tilde{s}_1(t; -f) = \tilde{s}_1^*(t; f)$  and  $\tilde{q}_{\mathcal{P}^A, H}(t, -f) = \tilde{q}_{\mathcal{P}^A, H}^*(t, f)$  [as  $\gamma_{\mathcal{P}^A}(t, -f) = \gamma_{\mathcal{P}^A}^*(t, f)$ ] and the range of the integral is spread symmetrically over the positive and negative frequencies.

### 4.3.5 Observed Point Estimate and SNR

The optimal filter requires exact models for the PSD  $H(f)$  and the angular power distributions of the GWB  $\mathcal{P}^A(\hat{\Omega})$ , which are the quantities one wishes to measure. Hence, the models can not be exactly known a priori, hence we can *not* have the “true” filter  $Q_{\text{true}} \equiv Q_{\mathcal{P}_{\text{true}}^A, H_{\text{true}}}$  - filters can only be *suboptimal*. The expected point

<sup>7</sup>The expression for optimal statistic derived here follows the historical route starting from [76] and provides a practical picture. However, the same expression could be derived in a simple mathematically elegant way by defining a scalar product in the  $t \otimes f$  space as

$$(A, B) = \Delta t \sum_{i=1}^n \int_{-\infty}^{\infty} df P_1(t_i; f) P_2(t_i; f) \tilde{A}^*(t_i; f) \tilde{B}(t_i; f)$$

and using the fact that the GW strains of two detectors in different chunks are uncorrelated as the chunk size is much greater than the light travel time delay between the detector sites.

estimate and SNR using an approximate filter is estimated below. The maximum SNR than can be observed if the models were exactly known is also obtained.

Suppose that the true GWB PSD is  $H_{\text{true}}(f)$  and the true angular power distribution is  $\mathcal{P}_{\text{true}}^A(\hat{\Omega})$ , while this background is searched using the corresponding model functions  $H(f)$  and  $\mathcal{P}^A(\hat{\Omega})$ . Then the source term will have the “true” overlap reduction function,

$$\gamma_{\mathcal{P}^A}^{\text{true}}(t, f) \equiv \gamma_{\mathcal{P}_{\text{true}}^A}(t, f) = \sum_{A=+, \times} \int_{S^2} d\hat{\Omega} F_1^A(\hat{\Omega}, t) F_2^A(\hat{\Omega}, t) \mathcal{P}_{\text{true}}^A(\hat{\Omega}) e^{2\pi i f \hat{\Omega} \cdot \Delta \mathbf{x}(t)/c}, \quad (4.83)$$

and the statistic  $S_Q$  over the full observation time will have the following properties:

- **Mean:** [using eqn (4.81), eqn (4.66)]

$$\mu_Q^{\text{obs}} = \left[ \Delta t \sum_{i=1}^n \|q_{\mathcal{P}^A, H}\|_{t_i}^2 \right]^{-1} \Delta t \sum_{i=1}^n (q_{\text{true}, \mathcal{P}^A, H})_{t_i} \quad (4.84)$$

$$= \frac{\Delta t \sum_{i=1}^n \int_{-\infty}^{\infty} df \frac{H(f) \gamma_{\mathcal{P}^A}^*(t_i, f)}{P_1(t_i; |f|) P_2(t_i; |f|)} H_{\text{true}}(f) \gamma_{\mathcal{P}^A}^{\text{true}}(t_i, f)}{\Delta t \sum_{i=1}^n \int_{-\infty}^{\infty} df \frac{H^2(f) |\gamma_{\mathcal{P}^A}(t_i, f)|^2}{P_1(t_i; |f|) P_2(t_i; |f|)}} \quad (4.85)$$

- **SNR:** [using eqn (4.85) and eqn (4.82)]

$$\text{SNR}_Q^{\text{obs}} = \frac{\mu_Q^{\text{obs}}}{\sigma_Q} = 2 \left[ \Delta t \sum_{i=1}^n \|q_{\mathcal{P}^A, H}\|_{t_i}^2 \right]^{-1/2} \Delta t \sum_{i=1}^n (q_{\text{true}, \mathcal{P}^A, H})_{t_i} \quad (4.86)$$

$$= 2 \frac{\Delta t \sum_{i=1}^n \int_{-\infty}^{\infty} df \frac{H(f) \gamma_{\mathcal{P}^A}^*(t_i, f)}{P_1(t_i; |f|) P_2(t_i; |f|)} H_{\text{true}}(f) \gamma_{\mathcal{P}^A}^{\text{true}}(t_i, f)}{\sqrt{\Delta t \sum_{i=1}^n \int_{-\infty}^{\infty} df \frac{H^2(f) |\gamma_{\mathcal{P}^A}(t_i, f)|^2}{P_1(t_i; |f|) P_2(t_i; |f|)}}} \quad (4.87)$$

In the most optimistic case, where the true background is proportional to the modeled background,  $H_{\text{true}}(f) \mathcal{P}_{\text{true}}^A(\hat{\Omega}) = \kappa H(f) \mathcal{P}^A(\hat{\Omega})$ , where  $\kappa$  is the *proportionality*

constant, the expectation of observed point estimate and SNR are respectively

$$\mu_Q = \kappa \frac{\mu_Q^{\text{obs}}}{\sigma_Q} = \left[ \Delta t \sum_{i=1}^n \|q_{\mathcal{P}^A, H}\|_{t_i}^2 \right]^{-1} \Delta t \sum_{i=1}^n (q_{\mathcal{P}^A, H}, q_{\mathcal{P}^A, H})_{t_i} = \kappa \quad (4.88)$$

$$\text{SNR}_Q^{\text{max}} = 2 \kappa \sqrt{\Delta t \sum_{i=1}^n \|q_{\mathcal{P}^A, H}\|_{t_i}^2} = 2 \kappa \sqrt{\Delta t \sum_{i=1}^n \int_{-\infty}^{\infty} df \frac{H^2(f) |\gamma_{\mathcal{P}^A}(t_i, f)|^2}{P_1(t_i; |f) P_2(t_i; |f)}}. \quad (4.89)$$

This is the maximum detectable SNR (depending, of course, on  $\kappa$ ) by a radiometer search. This relation is important to test the algorithm using artificial injections and, more importantly, for putting upper limits on the GWB.

The above discussion shows that the ignorance about the correct model of the sky leads to a loss of SNR. The ratio of the observed signal-to-noise ratio  $\text{SNR}_Q^{\text{obs}}$  with the modeled filter  $Q_{\mathcal{P}^A, H}$  and the signal-to-noise ratio  $\text{SNR}_{\text{true}}$  that could be observed given the true model is given by

$$\epsilon := \frac{\text{SNR}_Q^{\text{obs}}}{\text{SNR}_{\text{true}}} = \frac{\Delta t \sum_{i=1}^n (q_{\text{true}}, q_{\mathcal{P}^A, H})_{t_i}}{\sqrt{\Delta t \sum_{i=1}^n \|q_{\text{true}}\|_{t_i}^2} \sqrt{\Delta t \sum_{i=1}^n \|q_{\mathcal{P}^A, H}\|_{t_i}^2}}, \quad (4.90)$$

which is the ‘‘angle’’ between the truly optimal ( $q_{\text{true}}$ ) and the modeled ( $q_{\mathcal{P}^A, H}$ ) unnormalized optimal filters. The quantity  $\epsilon$  would be a good measure to quantify the necessity of developing more accurate (and possibly more complicated) filters.

### 4.3.6 Summary

To search for a stochastic GWB Fourier transforms of outputs  $\tilde{s}_I(t; f)$  from the detectors  $I = 1, 2$  for each of  $n$  chunks of size  $\Delta t$  are cross-correlated [eqn (4.47)]

$$\Delta S_Q(t) = \int_{-\infty}^{\infty} df \tilde{s}_1^*(t; f) \tilde{s}_2(t; f) \tilde{Q}_{\mathcal{P}^A, H}(t, f)$$

through a filter function [eqn (4.75)]

$$\tilde{Q}_{\mathcal{P}^A, H}(t, f) = \lambda_Q(t) \tilde{q}_{\mathcal{P}^A, H}(t, f) := \lambda_Q(t) \frac{H(f) \gamma_{\mathcal{P}^A}^*(t, f)}{P_1(t; |f) P_2(t; |f)},$$

where  $H(f)$  is the modeled GWB PSD,  $P_I(t; f)$  is the noise PSD of detector  $I$ ,  $\gamma_{\mathcal{P}^A}(t, f)$  is the modeled overlap reduction function,  $\lambda_Q(t)$  is a (real) normalization constant and  $\tilde{q}_{\mathcal{P}^A, H}(t, f)$  is the unnormalized filter function. The modeled overlap reduction function depends on the modeled angular power distribution  $\mathcal{P}^A(\hat{\Omega})$  and the antenna pattern functions  $F_I^A(t, \hat{\Omega})$  of the detectors [eqn (4.54)]

$$\gamma_{\mathcal{P}^A}(t, f) = \int_{S^2} d\hat{\Omega} \left[ F_1^+(\hat{\Omega}, t) F_2^+(\hat{\Omega}, t) \mathcal{P}^+(\hat{\Omega}) + F_1^\times(\hat{\Omega}, t) F_2^\times(\hat{\Omega}, t) \mathcal{P}^\times(\hat{\Omega}) \right] e^{2\pi i f \hat{\Omega} \cdot \Delta \mathbf{x}(t)/c}.$$

The normalization constant is (usually) fixed by the relation [eqn (4.78)]:

$$\lambda_Q(t) \Delta t \int_{-\infty}^{\infty} df \frac{H^2(f) |\gamma_{\mathcal{P}^A}(t, f)|^2}{P_1(t; |f|) P_2(t; |f|)} =: \lambda_Q(t) \Delta t \|q_{\mathcal{P}^A, H}\|_{t_i}^2 = 1.$$

Filter dependent correlations over the short chunks  $\Delta S_Q(t)$  are then combined to get the statistic  $S_Q$  over the full observation time using a linear sum with inverse weightage of noise variance  $\sigma_{\Delta S}^2(t) = \lambda_Q(t)/4$  in the small chunks [eqn (4.41)]:

$$S_Q = \left[ \sum_{i=1}^n \Delta S_Q(t_i) \sigma_{\Delta S}^{-2}(t_i) \right] / \left[ \sum_{i=1}^n \sigma_{\Delta S}^{-2}(t_i) \right],$$

which can also be written as [eqn (4.81)]

$$S_Q = \left[ \Delta t \sum_{i=1}^n \|q_{\mathcal{P}^A, H}\|_{t_i}^2 \right]^{-1} \sum_{i=1}^n \int_{-\infty}^{\infty} df \tilde{s}_1^*(t_i; f) \tilde{s}_2(t_i; f) \tilde{q}_{\mathcal{P}^A, H}(t_i, f).$$

If the modeled and true GWB are proportional,  $H_{\text{true}}(f) \gamma_{\mathcal{P}^A}^{\text{true}}(t_i, f) = \kappa H(f) \gamma_{\mathcal{P}^A}(t_i, f)$ , where  $\kappa$  is the *proportionality constant*, the observed SNR is maximum. The expectation of point estimate [eqn (4.88)] and SNR [eqn (4.89)] in the most favourable case are respectively

$$\mu_Q = \kappa; \quad \text{SNR}_Q^{\text{max}} = 2\kappa \sqrt{\Delta t \sum_{i=1}^n \|q_{\mathcal{P}^A, H}\|_{t_i}^2} = 2\kappa \sqrt{\Delta t \sum_{i=1}^n \int_{-\infty}^{\infty} df \frac{H^2(f) |\gamma_{\mathcal{P}^A}(t_i, f)|^2}{P_1(t_i; |f|) P_2(t_i; |f|)}}.$$

The above results are important for putting upper limits on a certain kind of background. These formulae have been extensively used in this thesis for testing the algorithm with injected signals.

## 4.4 Applications

In the previous section, we established that the “optimal” filter to search for a stochastic GWB with PSD  $H(f)$  and angular power distribution  $\mathcal{P}^A(\hat{\Omega})$  is given by [eqn (4.75)]

$$\tilde{Q}_{\mathcal{P}^A, H}(t, f) = \lambda_Q(t) \frac{H(f) \gamma_{\mathcal{P}^A}^*(t, f)}{P_1(t; |f|) P_2(t; |f|)},$$

where the sky model dependent overlap reduction function [eqn (4.54)]

$$\gamma_{\mathcal{P}^A}(t, f) = \int_{S^2} d\hat{\Omega} \left[ F_1^+(\hat{\Omega}, t) F_2^+(\hat{\Omega}, t) \mathcal{P}^+(\hat{\Omega}) + F_1^\times(\hat{\Omega}, t) F_2^\times(\hat{\Omega}, t) \mathcal{P}^\times(\hat{\Omega}) \right] e^{2\pi i f \hat{\Omega} \cdot \Delta \mathbf{x}(t)/c}.$$

So the optimal search is *an all-sky search for a colored anisotropic background*.

However, a priori, we do not have exact models for  $H(f)$  and  $\mathcal{P}^A(\hat{\Omega})$ . Which means that, we can not perform truly “optimal” search. But, like many other signal analysis methods, we opt for suboptimal methods - knowledge about the GWB sky, available from different theoretical and observational fields of astronomy, will be used to construct  $H(f)$  and  $\mathcal{P}^A(\hat{\Omega})$ , and in turn, the filter.

Approximate models are available for the PSDs  $H(f)$  of different kinds of astrophysical and cosmological GWB, which were shown in figure 4.1 [87]. From the figure one can see that most of these models are linear over a broad logarithmic frequency range. This suggests that the PSDs can be modeled in the sensitive frequency bands (around 100 Hz) of the detectors using power laws of the form

$$H(f) = H_\alpha \left( \frac{f}{100\text{Hz}} \right)^\alpha. \quad (4.91)$$

The popular slow roll inflation model predicts  $\Omega_{\text{GW}}(f) = \text{constant}$ , which corresponds to  $\alpha = -3$ .

Due to the lack of reasonable models for  $\mathcal{P}^A(\hat{\Omega})$ , to search for a GWB in the data from the currently operational detectors (e.g., LIGO), only *blind estimations* have so far been considered. No prior knowledge about the sky has been used in the data analysis - which is why we call it blind estimation. Two possible blind estimations, which have already been implemented in LIGO data analysis, are presented here - 1. the all-sky search for an isotropic background and 2. the directed search to map the GWB sky.

### 4.4.1 All-sky isotropic background

The background produced by the large scale cosmological processes, like inflation in the very early universe, could give rise to a statistically isotropic GWB.<sup>8</sup> This has motivated the search for a isotropic background with equal power in both the polarizations.

To construct filters for the isotropic model with equal power in both the polarizations,  $\mathcal{P}^A(\hat{\Omega}) = 1$ , we need to use the *time independent overlap reduction function*

$$\gamma_{\text{iso}}(f) := \int_{S^2} d\hat{\Omega} \left[ F_1^+(\hat{\Omega}, t) F_2^+(\hat{\Omega}, t) + F_1^\times(\hat{\Omega}, t) F_2^\times(\hat{\Omega}, t) \right] e^{2\pi i f \hat{\Omega} \cdot \Delta \mathbf{x}(t)/c}, \quad (4.92)$$

which can be calculated in a closed form as outlined in appendix-B of [75]. Though the integrand in the above integral contains time dependent quantities, the integral is independent of time because of the following reason: Evaluation of the integral on the right at any non-zero time  $t$  is equivalent of rotating the integration variable  $\hat{\Omega}$  in the arguments of *all* the quantities in the integrand by an azimuthal angle of  $-\omega_E t$  and then evaluating the integral at  $t = 0$  (which is *not*, in general, valid for an anisotropic GWB). Since a two sphere remains invariant under rotation, the integral is independent of time. Moreover, since  $\hat{\Omega} \rightarrow -\hat{\Omega}$  does not change expression inside the square bracket in the integrand,  $\gamma_{\text{iso}}(f)$  is real.

In terms of  $\Omega_{\text{GW}}(f)$ , using eqn (4.17) we may write the isotropic filter as

$$\tilde{Q}_H(t, f) = \frac{3H_0^2}{32\pi^3} \lambda_Q \frac{|f|^{-3} \Omega_{\text{GW}}(|f|) \gamma_{\text{iso}}^*(f)}{P_1(t; |f|) P_2(t; |f|)}. \quad (4.93)$$

Unfortunately, the time independent overlap reduction function becomes nearly zero at frequencies greater than  $\sim 100$  Hz, as shown in figure 4.3 for the LIGO detectors at Hanford and Livingston (note that, our normalization condition is different from the conventional one prescribed in, e.g., [75]). Hence, the cross-correlation statistic does not receive power from the most sensitive bands of the detectors. This problem can be reduced, that is, more power can be acquired from the “sweet spots” of the detectors, by integrating over only a finite patch of the sky instead of the whole sky [89].

If we use  $\Omega_{\text{GW}}(f) = (f/100\text{Hz})^\alpha$  in the filter and the true GWB is isotropic with the spectrum  $\Omega_{\text{GW}}(f) = \Omega_\alpha (f/100\text{Hz})^\alpha$ , then the SNR detected by the isotropic filter

---

<sup>8</sup>Note that, the framework presented in this thesis assumes different directions of the GWB sky are uncorrelated, which may not be a valid assumption for the cosmological GWB.

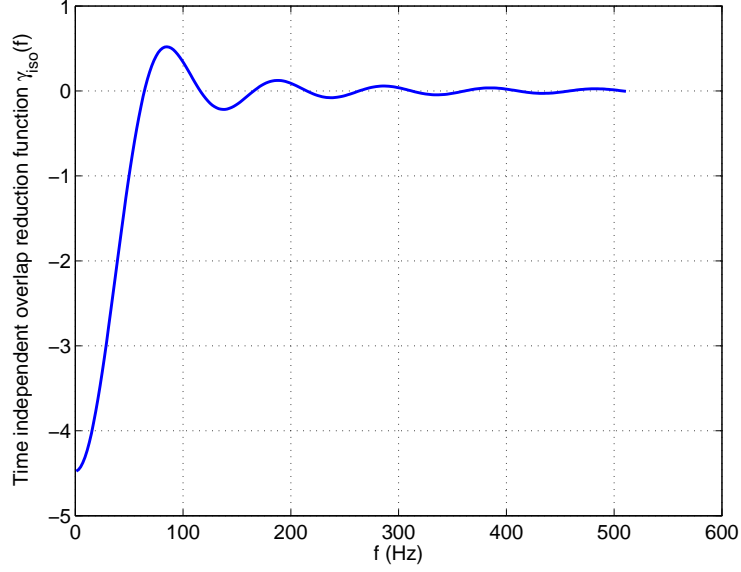


Figure 4.3: **Time independent overlap reduction function.**  $\gamma_{\text{iso}}(f)$  has been plotted for the LIGO Hanford and Livingston detectors. It becomes nearly zero at frequencies greater than  $\sim 100$  Hz, so data from the most sensitive frequency bands of the detectors are effectively left out. Note that, our normalization condition is different from the conventional one prescribed in, e.g., [75].

is maximum. The point estimate and the SNR in that case are respectively [from eqn (4.88) and eqn (4.89)]

$$\mu_\alpha = \Omega_\alpha \quad (4.94)$$

$$\text{SNR}_\alpha^{\text{max}} = \frac{\Omega_\alpha}{100^\alpha} \frac{3H_0^2}{16\pi^3} \sqrt{\Delta t \sum_{i=1}^n \int_{-\infty}^{\infty} df \frac{|f|^{2\alpha-6} |\gamma_{\text{iso}}(f)|^2}{P_1(t_i; |f|) P_2(t_i; |f|)}}. \quad (4.95)$$

In particular, using four months of data from the LIGO Hanford and Livingston detectors at designed sensitivity, a rough estimate of minimum detectable amplitude of a flat GWB spectra,  $\Omega_{\text{GW}}(f) = \Omega_0$ , at the  $1\text{-}\sigma$  level ( $\text{SNR}_0^{\text{max}} = 1$ ) is given by  $\Omega_0 = 3.0 \times 10^{-6} h_{72}^{-2}$ , where  $h_{72}$  is the Hubble constant  $H_0$  at the present epoch in the units of  $72 \text{ km sec}^{-1} \text{ Mpc}^{-1}$ .

The upper limit on  $\Omega_0$  from the 20 days of fourth LIGO science run data is  $6.5 \times 10^{-5} h_{72}^{-2}$  in the frequency range 51 - 150 Hz. This is currently the best upper limit on the isotropic stochastic GWB in that frequency range.

### 4.4.2 Directed Search

The GWB is dominated by nearby anisotropic universe, so the detection of localized sources is more favorable over the all-sky averaged search. Making a skymap of the GWB sky has been a long standing ambition of stochastic GW research. Different analysis methods have been proposed to create skymaps by measuring the first few spherical harmonic multipoles of the sky [77, 78, 80, 81, 82]. A direct approach to the problem is the directed GW radiometer analysis [89, 79]. Here the whole sky is decomposed in a discrete set of pixels and the contribution from each pixel is measured separately by correlating phase shifted detector outputs to generate the whole skymap - a clear application of earth rotation synthesis imaging.

The angular power distribution for only one unit point source on the sky in the direction  $\hat{\Omega}$  with equal power in both the polarizations can be expressed as<sup>9</sup>

$$\mathcal{P}^A(\hat{\Omega}') = \delta(\hat{\Omega}' - \hat{\Omega}). \quad (4.96)$$

The optimal filter for this case is given by

$$\tilde{Q}_{\hat{\Omega}, H}(t, f) = \lambda_{\hat{\Omega}}(t) \frac{H(f) \gamma_{\hat{\Omega}}^*(t, f)}{P_1(t; |f|) P_2(t; |f|)}, \quad (4.97)$$

where  $\lambda_{\hat{\Omega}}(t)$  is the normalization constant and

$$\gamma_{\hat{\Omega}}(t, f) := \left[ F_1^+(\hat{\Omega}, t) F_2^+(\hat{\Omega}, t) + F_1^\times(\hat{\Omega}, t) F_2^\times(\hat{\Omega}, t) \right] e^{2\pi i f \hat{\Omega} \cdot \Delta \mathbf{x}(t)/c} \quad (4.98)$$

is the *direction dependent overlap reduction function*. Unlike the time independent overlap reduction function of the isotropic search, the direction dependent overlap reduction function accepts power from *all* the frequencies.

The working principle of the above filter is evidently similar to the earth rotation image synthesis often used in CMB and radio astronomy to make map of a certain portion or the whole sky. The phase lag between two detectors, separated by a distance  $\Delta \mathbf{x}(t)$ , in receiving a plane wavefront from a certain direction  $\hat{\Omega}$ , as shown in figure 4.4, is accounted for in the filter through the phase factor  $\exp[2\pi i f \hat{\Omega} \cdot \Delta \mathbf{x}(t)/c]$ . As the earth rotates this factor is adjusted, such that, waves from one direction are coherently added, while the effects of the other directions tend to cancel out. Note that, we did not introduce the phase factor by hand, it appeared automatically

<sup>9</sup>Note that, we are *not* normalizing  $\mathcal{P}^A(\hat{\Omega}')$  using eqn (4.16) for constructing filters. However, we need to use proper normalization when we compare the directed search result with the all-sky result using the conventional formula [eqn (4.17)].

through the process of SNR maximization. Though the whole radiometer analysis is based on this principle, the idea is clearly realized in the directed search analysis.

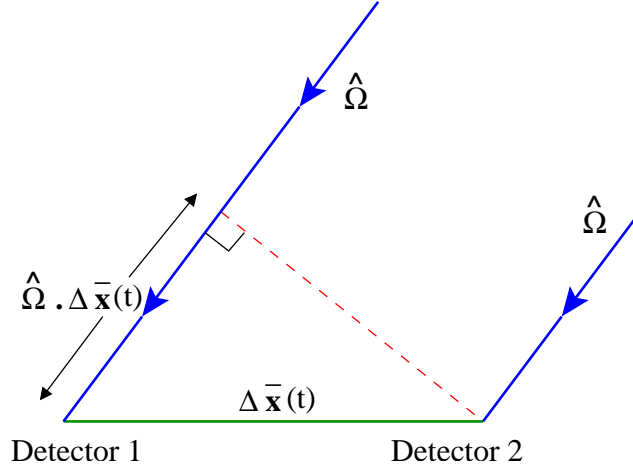


Figure 4.4: **Geometry of an elementary radiometer.**  $\Delta\mathbf{x}(t)$  is the vectorial distance between the two detectors whose magnitude remains constant but its direction changes as the Earth rotates.  $\hat{\Omega}$  is the direction to the source which is fixed in the barycentric frame.

As mentioned above, the directed search filter is constructed by putting a unit point source at the pointing direction,  $\mathcal{P}^A(\hat{\Omega}') = \delta(\hat{\Omega}' - \hat{\Omega})$ . In addition, a power law model is used for the frequency spectrum  $H(f) = (f/100\text{Hz})^\alpha$ . If the true power distribution of the background is proportional to the GWB model used to construct the filters,  $\mathcal{P}_{\text{true}}^A(\hat{\Omega}') H(f) = \delta(\hat{\Omega}' - \hat{\Omega}) \mathcal{P}_{\hat{\Omega}}(f/100\text{Hz})^\alpha$ , the observed point estimate and SNR are maximum, given by [eqn (4.88) and eqn (4.89)]

$$\mu_{\hat{\Omega},\alpha} = \mathcal{P}_{\hat{\Omega}} \quad (4.99)$$

$$\text{SNR}_{\hat{\Omega},\alpha}^{\text{max}} = \frac{2\mathcal{P}_{\hat{\Omega}}}{100^\alpha} \sqrt{\Delta t \sum_{i=1}^n \int_{-\infty}^{\infty} df \frac{f^{2\alpha} |\gamma_{\hat{\Omega}}(t_i, f)|^2}{P_1(t_i; |f|) P_2(t_i; |f|)}}. \quad (4.100)$$

It is expected that, if the filter direction  $\hat{\Omega}$  does not match the true point source direction, say  $\hat{\Omega}_0$ , the observed point estimate and SNR will decrease as the difference between the filter and source directions,  $\hat{\Omega} - \hat{\Omega}_0$ , increases. In fact, only in that case we may hope to make a map of the GWB sky using the directed search analysis. The function that describes the variation of point estimate with  $\hat{\Omega} - \hat{\Omega}_0$  is commonly known in astronomy as the point spread function (PSF) or the beam pattern func-

tion. The observed sky map is convolved with the beam function and it has to be deconvolved in order to estimate the true sky map. This is the most important issue considered in this thesis. Deconvolution of raw skymaps have already been studied in great detail in CMB analysis and radio astronomy. In particular, CMB analysis has broad overlap with GWB map making. So relevant techniques have been adapted from CMB analysis to estimate the true GWB skymaps. Of course, fresh challenges were encountered while implementing the adapted techniques in GWB map making. Last four chapters of this thesis are devoted to address the issues of beams and deconvolution in the context of GWB and CMB analysis.

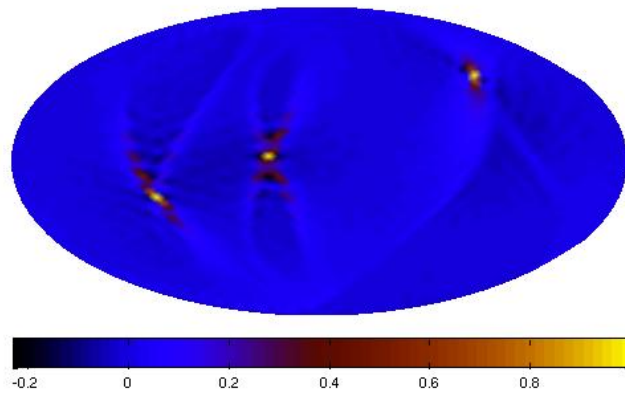


Figure 4.5: **A test sky map made using the GWB radiometer.** Strain in the detectors due to three point sources with flat PSD [ $H(f) = \text{constant}$ ] were injected in white Gaussian noise with upper cutoff frequency  $f_u = 1024$  Hz and the map was made by a GW radiometer formed by two detectors at the LIGO locations - Hanford and Livingston. The point estimates fall off as the pointing direction of the filter moves away of the true sources, which is why one can see three distinct sources in this map. This map demonstrates that, making skymaps with a GW radiometer formed by modern detectors is possible.

A map of the GWB sky made by using a radiometer formed by the two LIGO detectors at Hanford and Livingston from simulated data containing white noise and strain due to three injected point sources with flat PSD [ $H(f) = \text{constant}$ ] is shown in figure (4.5). It shows that, the point estimate indeed falls off when the (filter) “pointing direction” moves away of the true source direction, which is why

the map shows three distinct sources. This exercise demonstrates that it is possible to make sky maps using a GW radiometer. A rough estimate of minimum detectable strength of a stochastic point source at the  $1\text{-}\sigma$  level from four months of LIGO data at the designed sensitivity varies between  $4.0 \times 10^{-50} \text{ Hz}^{-1}$  to  $5.5 \times 10^{-50} \text{ Hz}^{-1}$  for  $\alpha = -3$  [flat  $\Omega_{\text{GW}}(f)$ ] and between  $1.4 \times 10^{-50} \text{ Hz}^{-1}$  to  $1.9 \times 10^{-50} \text{ Hz}^{-1}$  for  $\alpha = 0$  [flat  $H(f)$ ] depending upon the position of the sky.

The directed search analysis has been implemented using 20 days of the fourth science run data of the LIGO detectors [85]. The current upper limits from this analysis on the strength of a point source  $\mathcal{P}_{\hat{\Omega}}$  varies between  $1.2 \times 10^{-48} \text{ Hz}^{-1}$  to  $1.2 \times 10^{-47} \text{ Hz}^{-1}$  for  $\alpha = -3$  [flat  $\Omega_{\text{GW}}(f)$ ] and between  $8.5 \times 10^{-49} \text{ Hz}^{-1}$  to  $6.1 \times 10^{-48} \text{ Hz}^{-1}$  for  $\alpha = 0$  [flat  $H(f)$ ] depending upon the position of the sky. The analysis also puts an upper limit of  $1.20 \times 10^{-4} h_{72}^{-2}$  on the all-sky isotropic point estimate  $\Omega_0$  by combining the point estimates of directed search at each pixels. However, different combinations of the directed search pixel point estimates can provide different estimates for the all-sky averaged result. Since, the true GWB is anisotropic, an optimal combination [e.g., eqn (4.39)] of the directed search pixel point estimates would provide a more accurate estimate of the all-sky averaged GWB - which could even be better than the estimate obtained by using the all-sky isotropic search filter. This issue will be taken up with greater detail in chapter 6.

## 4.5 Summary and Conclusion

A stochastic background of GW from unmodeled and/or unresolved sources of astrophysical and cosmological origin is expected in the universe. These sources can not be modeled as a time series, they are characterized by their expectation values. Conventionally the frequency spectrum is defined as the energy density per unit logarithmic frequency interval. We can also define specific intensity of GWB in terms of the quantity that characterizes the strength of the angular power distribution of GW energy density.

The noise in different detectors are uncorrelated, so the cross-correlation between data from two detectors is the best statistic for the detection of GWB. The correlation is done in the frequency domain through a filter function to put less weight to the noisier frequency bands. Due to non-stationarity of detector noise and (slow) rotation of the earth, the correlations are taken over small chunks of time to simplify the construction of filter functions; the correlations over the smaller chunks are then linearly combined with inverse noise weightage to get the final

statistic over the full observation time.

The filter function can be varied to search for different models of the GWB. A general analysis framework to search for any model of GWB (with no angular correlation) has been presented in this chapter. For any given model of GWB, the optimal filter that maximizes the signal-to-noise ratio (SNR) has been derived. The optimal filter requires true models of the power distribution of GWB, which is not a priori known. Suboptimal filters based on modeled PSD and angular distribution of energy density of GWB have to be used in the analysis. Expressions for the observed SNR using a suboptimal filter due to the presence of an unmodeled anisotropic background and the maximum SNR that could be observed with an exact prior model of the GWB sky have also been derived.

Due to the lack of reasonable models for the angular distribution of GWB, so far only blind estimations have been considered - no prior model of the sky has been used in the analysis, every direction is treated with equal weightage. Two possible blind estimations - upper limit on the all-sky averaged background and upper limit on a stochastic point source - have already been implemented using the fourth science run data of the LIGO detectors at Hanford and Livingston. A skymap of the GWB sky using the directed search analysis has also been prepared. However, it is necessary to deconvolve the observed map in order to estimate the true GWB sky. This is an extremely important issue and will be addressed with great detail in the rest of this thesis. Because of the broad similarity between GWB and CMB true skymap estimation, we adapt techniques from CMB analysis. The next chapter will provide an introduction to theory and experiments of CMB. In the last four chapters we develop and apply deconvolution techniques, specifically designed for the current CMB and GWB analysis.

Finally, we must remember that the implementation of the analysis presented in this thesis focuses only on blind estimations. Better suboptimal filters could be constructed by introducing different models taking inputs from electro-magnetic astronomy. Analysis in the spherical harmonic space may allow us to measure low angular multipoles of the GWB, which can be debiased using the techniques used to account for the non-circular beam corrections presented in [chapter 8](#) and [chapter 9](#). Moreover, inclusion of angular correlation of GWB can also be possible in such analysis. It is also necessary to generalize the analysis by relaxing the assumptions that the frequency power spectrum of the GWB sky is independent of direction and waves of different polarizations are independent. We plan to explore these possibilities in the near future.

## Chapter 5

# Introduction to the Cosmic Microwave Background (CMB)

The Big Bang theory is currently the widely accepted working model of the universe. According to the big bang model, photons were strongly coupled to matter until the last scattering surface, after which, photons could travel freely and, hence, they carry a snapshot of the universe at the last scattering surface. These photons are reaching us from all the direction constituting a background of microwave electromagnetic radiation, commonly known as the Cosmic Microwave Background (CMB).

CMB is isotropic to a very high degree with a temperature of 2.7K. However, the anisotropies in CMB are extremely important for cosmology as they carry the signature of initial density perturbations (including the primordial gravitational waves), which have eventually grown due to gravitational instability to form the structures that are seen in the present universe. If CMB anisotropy is Gaussian and statistically isotropic, as predicted by the well accepted cosmological models, it can be completely specified by its angular power spectrum.

The measurement of CMB anisotropy has played perhaps the most important role in leading cosmology to a precision science. Since COBE's discovery of CMB anisotropy, several ground, space and balloon based experiments have measured CMB anisotropy at different angular scales. However, the precision of the experiments relies on the identification and removal of all the significant systematic effects. Removing the systematic effects from the CMB anisotropy measurement experiments is one of the key issues addressed in this thesis. In this chapter, I briefly mention some of the basic concepts on the origin, measurement and analysis of CMB, which are relevant to the work presented in this thesis.

## 5.1 Origin

The Big Bang theory suggests that the universe has emerged from an extremely dense and hot initial state [90]. So, in the early stages of the universe, photons were strongly coupled to the charged plasma of electrons and baryons. As the universe expanded, the density of photons and electrons decreased, hence the probability of collisions between the photons and the electrons also decreased. The photon-electron scattering rate drastically fell off over a small stretch of time - a period commonly referred to as the Last Scattering Surface (LSS). After LSS photons travelled freely and, hence, the last scattering surface is also called the period of matter-radiation “decoupling”.

During the above decoupling process, the temperature of the universe decreased and free electrons recombined with protons to form neutral hydrogen - a phenomenon commonly known as “recombination” [91]. One would expect that recombination occurred when the temperature of the universe became less than 13.6 eV. However, due to the very high photons to baryons ratio, the high energy tail of photon distribution was enough to ionize neutral hydrogen until the temperature dropped below 0.25 eV [92]. Detailed rate balance equation in the expanding universe predicts that recombination occurred when the temperature of the universe was roughly 3000K.

The decoupled photons, which are traveling freely from the LSS, constitute the Cosmic Microwave Background (CMB). CMB is isotropic to a very high degree - the temperature (in Kelvin) is the same in every direction up to the fifth decimal place<sup>1</sup>. CMB carries signatures of the anisotropies in the universe that existed during the last scatterings. It is also affected by recombination and other fluctuations during its journey from the LSS to the observer. Theory of CMB temperature anisotropy is briefly mentioned in the next section. The timeline of anisotropies in the universe before and after the LSS have been nicely illustrated in cartoon figure `fig:univTimeLine` (taken from WMAP website [93]).

Observations of CMB and its anisotropy is extremely important for constraining cosmological models and parameters, and have, thereby, played the leading role in the transition of cosmology to a precision science.

At the LSS photons were in thermal equilibrium over large scales (possibly due to inflation). Therefore the CMB photons at LSS followed a Planckian distribution.

---

<sup>1</sup>Though the observed CMB has a dipole anisotropy at the  $10^{-3}$  level largely due to the particular velocity of the solar system in the comoving frame and indistinguishable from any intrinsic component, here we are talking about the anisotropy intrinsic to CMB.

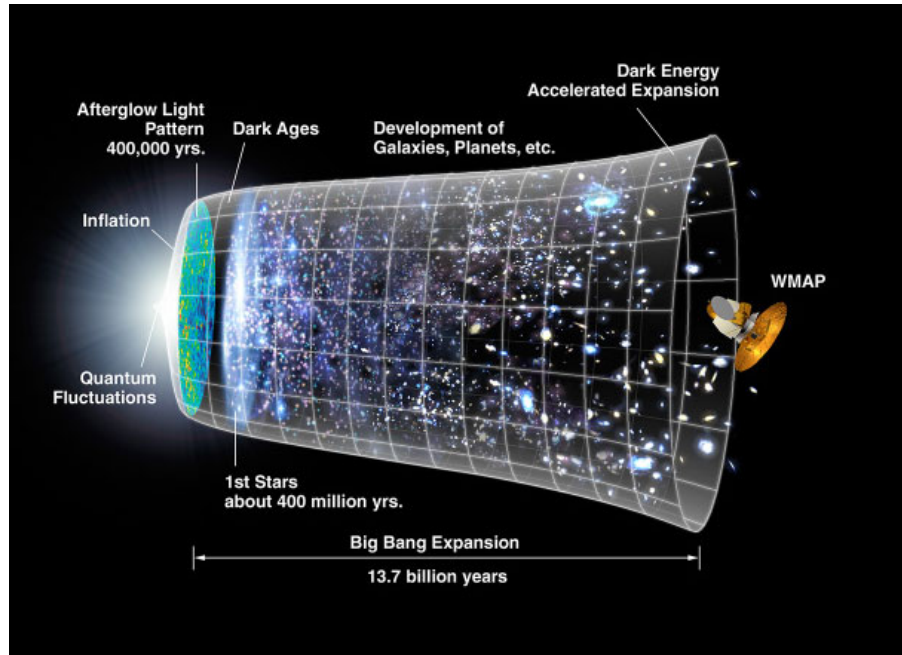


Figure 5.1: **Evolution of anisotropies in the universe.** The timeline of different anisotropies in the universe, including CMB at LSS, has been illustrated in this cartoon. Image taken from the WMAP website [93].

Since the photons travelled freely after LSS, their distribution did not change. This fact was precisely established [94] by the Far Infrared Absolute Spectrophotometer (FIRAS) of the Cosmic Background Explorer (COBE) [95] satellite as shown in figure 5.2 (taken from the COBE website). The plot shows the theoretically expected blackbody spectrum overlaid on the observed CMB frequency spectrum. The error bars in the plot are hidden by the thickness of the line, showing the remarkable match between theory and observation.

The expansion of the universe stretches the wavelengths of the CMB photons and the density of the photons also decrease with the expansion. Therefore, the temperature of the universe is inversely proportional to the scale factor; it can be related to the cosmological redshift through the formula  $T(z) = (1 + z) T_0$ , where  $T_0$  is the observed temperature of the universe at redshift  $z = 0$ , the current epoch. From CMB observations we know that the temperature of the universe today is 2.73K. Comparing this with the recombination temperature ( $\sim 3000\text{K}$ ), one can see that the LSS refers to a redshift of  $z \sim 1100$ . According to the standard cosmological model, redshift of 1100 means  $\sim 4 \times 10^5$  years after the Big Bang. Thus, CMB is a snapshot of the universe when it was about  $4 \times 10^5$  years old.

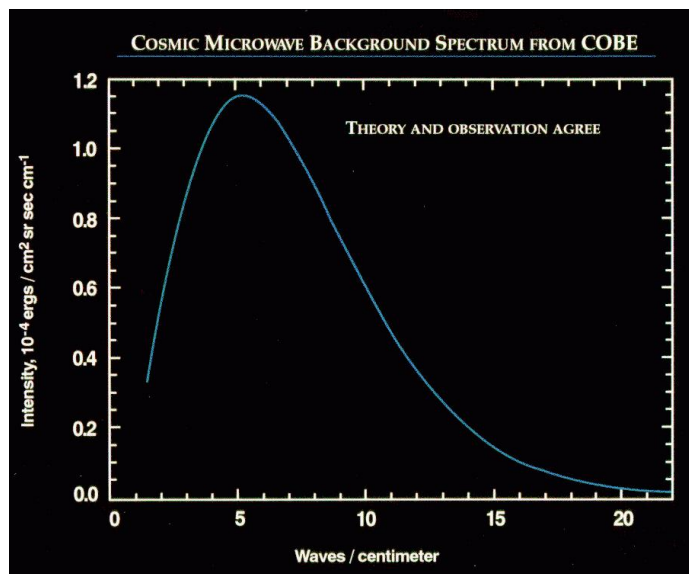


Figure 5.2: **Observed CMB frequency spectrum by COBE FIRAS.** The spectrum matches the blackbody spectrum (Planckian) so remarkably well, that the theoretically expected blackbody curve shown by the solid line, hides the (tiny) error bars in the plot. This image is taken from the COBE website [95].

## 5.2 CMB Anisotropy

The anisotropies in the CMB were originated from the primordial quantum fluctuations in the statistically homogeneous density field. These fluctuations had grown due to the gravitational instability and the corresponding anisotropy in the radiation density is imprinted on CMB as  $10^{-5}$ K fluctuations. The anisotropy of CMB temperature field obtained from the three years' data by the WMAP satellite has been shown in figure 5.3. A polarization skymap has also been made by from that data, which is overlaid on the temperature anisotropy map as solid lines. The image is taken from WMAP [93] press releases. See [96,97,98] for technical details.

These fluctuations are introduced in CMB through two mechanisms of redshift variations: anisotropy in gravitational redshift due to the anisotropy in gravitational potential  $\Phi_{\text{LSS}}(\hat{\mathbf{q}})$  (Sachs-Wolf effect) and anisotropy in the redshift of scattered photons due to the anisotropy in the particular velocity of the LSS  $\mathbf{V}_{\text{LSS}}(\hat{\mathbf{q}})$  in the comoving frame (Doppler effect). The observed anisotropy in CMB is also affected by the thickness of the last scattering surface  $\Delta z_{\text{LSS}} \sim 80$ , which, in turn, is controlled by the process of recombination. The fluctuations at scales smaller than the thickness of the last scattering surface are damped out. In the post-

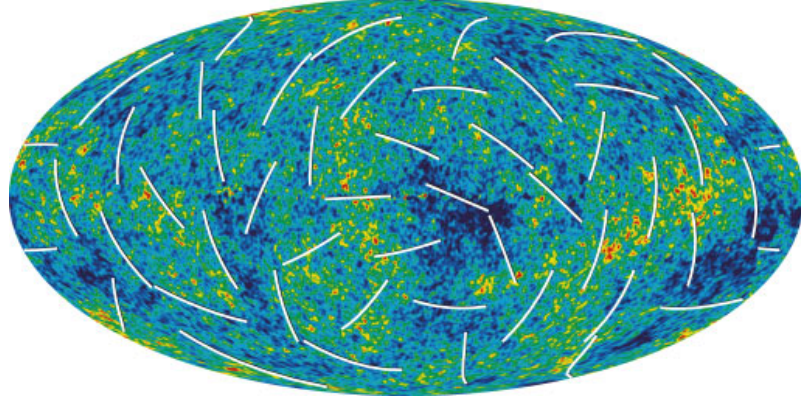


Figure 5.3: **WMAP CMB anisotropy sky.** The  $10^{-5}\text{K}$  level temperature anisotropy skymap obtained from 3-years' data of the WMAP satellite is shown in the figure. The polarization map obtained from that data is also overlaid on the map as solid lines. Image taken from WMAP [93] press releases. See [96, 97, 98] for technical details.

recombination period, while CMB photons travel from the LSS to the observer, they may cross anisotropic potential  $\Phi(t, \hat{\mathbf{q}})$  evolving with time and suffer a net redshift that introduces anisotropy in CMB (integrated Sachs-Wolf effect). Mathematically, we may write the observed CMB anisotropy  $\Delta T(\hat{\mathbf{q}})$  in a direction  $\hat{\mathbf{q}}$  as a fraction of the mean temperature  $T_0$  as [186]

$$\frac{\Delta T(\hat{\mathbf{q}})}{T_0} = \left[ \frac{\hat{\mathbf{q}} \cdot \mathbf{V}_\odot(\hat{\mathbf{q}})}{c} - \frac{\hat{\mathbf{q}} \cdot \mathbf{V}_{\text{LSS}}(\hat{\mathbf{q}})}{c} \right] + \frac{\Phi_{\text{LSS}}(\hat{\mathbf{q}})}{3c^2} + \frac{2}{c^2} \int \frac{\partial}{\partial t} \Phi(t, \hat{\mathbf{q}}) dt, \quad (5.1)$$

where we have also considered the anisotropy introduced due to the particular velocity of the solar system  $\mathbf{V}_\odot(\hat{\mathbf{q}})$  in the comoving cosmological frame.

The angular scale of the fluctuations at the LSS is mostly determined by the competition between the gravitational instability, which tries to increase anisotropy and radiation pressure, which tries to smooth density fluctuations. It can be shown that this competition leads to what is known as the acoustic oscillations and the angular scale over which the patches on the LSS are correlated corresponds to the acoustic horizon at the LSS. The angular size of the acoustic horizon at the LSS as seen from the present epoch in a flat universe is  $\sim 1^\circ$ . We shall explain in the next section that CMB anisotropy is usually characterized by its angular power spectrum. The peaks in the observed CMB power spectrum correspond to different harmonics of the acoustic oscillation, where the first peak corresponds to an angular

size of  $\sim 1^\circ$ .

CMB also contains polarization anisotropy, which is usually classified into two modes, E and B. The large scale anisotropy of B-mode polarization, generated by the tensor perturbation in early universe, can be an important probe of inflation. CMB polarization has not been considered in the works presented in this thesis, see standard references, e.g., [99], for a detailed introduction.

### 5.3 Angular Power Spectrum: Cosmic Variance

If CMB anisotropy is Gaussian, as predicted by well-accepted inflationary Big Bang model, the two point correlation function

$$C(\hat{\mathbf{q}}_1, \hat{\mathbf{q}}_2) := \langle \Delta T(\hat{\mathbf{q}}_1) \Delta T(\hat{\mathbf{q}}_2) \rangle, \quad (5.2)$$

gives a complete description of the statistical properties of the anisotropy field. Further, if CMB anisotropy is *statistically* isotropic, the two point correlation function depends only on the angular separation between two directions,  $C(\hat{\mathbf{q}}_1, \hat{\mathbf{q}}_2) = C(\hat{\mathbf{q}}_1 \cdot \hat{\mathbf{q}}_2)$ , so it is quite convenient to expand it in a Fourier-Legendre series:

$$C(\hat{\mathbf{q}}_1 \cdot \hat{\mathbf{q}}_2) = \sum_{l=0}^{\infty} \frac{2l+1}{4\pi} C_l P_l(\hat{\mathbf{q}}_1 \cdot \hat{\mathbf{q}}_2), \quad (5.3)$$

where  $P_l(x)$  is the Legendre polynomial of order  $l$  and  $C_l$  is the well known angular power spectrum of CMB (anisotropy). The angular power spectrum of CMB ( $C_l$ ) provides a complete description, equivalent to the two-point function, if CMB anisotropy is statistically isotropic and Gaussian. From analysis point of view, however, the angular power spectrum is preferred over the two point correlation function, because the power spectrum estimator  $\tilde{C}_l$  at different multipoles are uncorrelated, at least, in case of a “perfect” CMB experiment which has full sky coverage with circularly symmetric beam. In contrast, the two point correlation functions for different angular separations are correlated.

Thus, the precise measurement of CMB anisotropy essentially means precise measurement of its angular power spectrum, which is one of the key challenges in experimental cosmology. To do so one first measures the spherical harmonic transform of the temperature anisotropy sky (over the 2-sphere):

$$a_{lm} := \int d\Omega_{\hat{\mathbf{q}}} \Delta T(\hat{\mathbf{q}}) Y_{lm}^*(\hat{\mathbf{q}}). \quad (5.4)$$

The statistical isotropy of the temperature anisotropy sky implies that

$$\langle a_{lm}^* a_{l'm'} \rangle = \int d\Omega_{\hat{\mathbf{q}}_1} \int d\Omega_{\hat{\mathbf{q}}_2} C(\hat{\mathbf{q}}_1, \hat{\mathbf{q}}_2) Y_{lm}(\hat{\mathbf{q}}_1) Y_{l'm'}^*(\hat{\mathbf{q}}_2) = C_l \delta_{ll'} \delta_{mm'}, \quad (5.5)$$

where we have made use of the addition theorem for the spherical harmonics [100]

$$\frac{4\pi}{2l+1} \sum_{m=-l}^l Y_{lm}^*(\hat{\mathbf{q}}_1) Y_{lm}(\hat{\mathbf{q}}_2) = P_l(\hat{\mathbf{q}}_1 \cdot \hat{\mathbf{q}}_2) \quad (5.6)$$

and the orthogonality relation of the spherical harmonics

$$\int d\Omega_{\hat{\mathbf{q}}} Y_{lm}^*(\hat{\mathbf{q}}) Y_{l'm'}(\hat{\mathbf{q}}) = \delta_{ll'} \delta_{mm'}. \quad (5.7)$$

Therefore, to measure the CMB angular power spectrum, one can first compute the spherical harmonic transforms  $a_{lm}$  of the temperature anisotropy sky and then, according to the above relation, compute<sup>2</sup>  $|a_{lm}|^2$ , which is an unbiased estimator of  $C_l$ . However, if the temperature anisotropy field is Gaussian, so is  $a_{lm}$ , hence  $|a_{lm}|^2$  is  $\chi^2$  distributed, therefore each measurement of  $|a_{lm}|^2$  will have certain error. Since we have only one CMB sky, one can not reduce this error by taking multiple observations. To reduce the error, we define the estimator for angular power spectrum,  $\tilde{C}_l$ , by averaging over the independent “ $m$ ” modes:

$$\tilde{C}_l := \frac{1}{2l+1} \sum_{m=-l}^l |a_{lm}|^2. \quad (5.8)$$

Even then the estimated angular power spectrum will have certain error, which is independent of the experimental precision. That is, even in an ideal CMB experiment, where we assume that the temperature in a certain direction can be measured with infinite precision, we can *not* measure the angular power spectrum with arbitrary precision. The angular power spectrum estimated from the single realization of the random CMB that can be observed leads to an inevitable uncertainty (akin to sample variance) known as the *cosmic variance*. For statistically isotropic Gaussian

---

<sup>2</sup>In practice,  $a_{lm}$ 's from two different frequency channels, which have independent noise, are cross-correlated to measure  $|a_{lm}|^2$ . This removes the noise bias, that is, makes the product of additive noise terms from  $a_{lm}$  of zero mean and, hence, the estimator of  $C_l$  becomes unbiased.

CMB anisotropy, cosmic variance is given by

$$\text{var}(\tilde{C}_l) = \frac{2}{2l+1} C_l^2. \quad (5.9)$$

The above formula for power spectrum estimator suggests that the “specific” cosmic variance decreases with multipoles. Which is understandable as the number of independent “ $m$ ” modes is more at high multipoles. Detailed derivation of the expression for cosmic variance can be found in appendix C.

The best fit CMB power spectrum obtained from Wilkinson Microwave Anisotropy Probe (WMAP) [93] data compared to other experiments is shown in figure 5.4 (taken from the LAMBDA website [101]). The first peak of the CMB power spec-

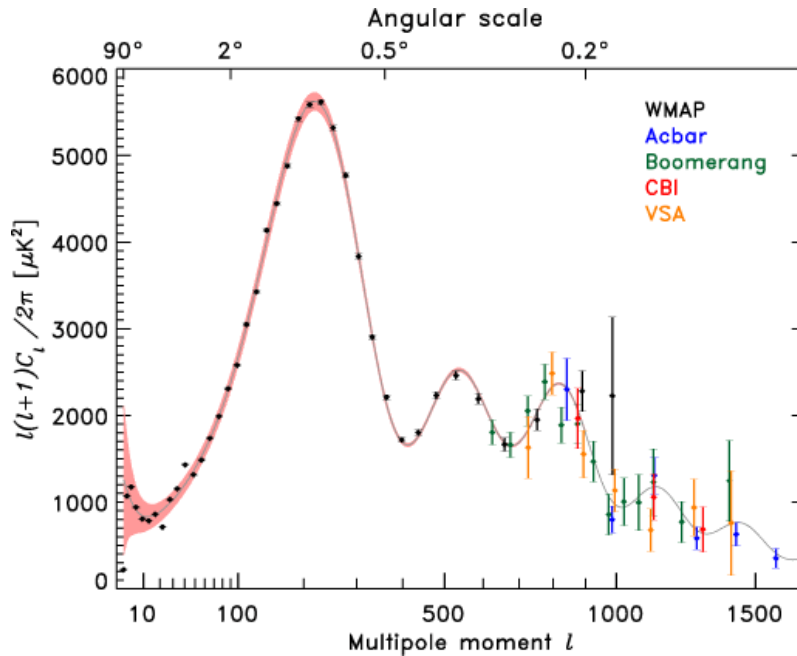


Figure 5.4: **Observed CMB Power Spectrum.** The best fit WMAP 3-year CMB power spectrum is compared with the observed power spectrum from other recent experiments. Note that the errors at the low multipoles and at the high  $C_l$  region around the first peak are cosmic variance dominated, this is the best any CMB experiment can achieve at those multipoles given only one observable universe. Image taken from the LAMBDA website [101].

trum was located with extremely good accuracy by the WMAP experiment. The errors at the low multipoles and the high  $C_l$  region near the first peak are all cosmic variance limited, which is the best any CMB experiment could achieve at those multipoles.

## 5.4 Experiments

CMB was serendipitously discovered by Arno Penzias and Robert Woodrow Wilson at Bell Telephone Laboratory in 1964. This great achievement brought them the 1978 Nobel prize in Physics. Since then a host of CMB experiments have been performed to measure CMB and, more importantly, its anisotropy at different angular scales. COBE's Differential Microwave Radiometer (DMR) [102] detected CMB temperature anisotropy in 1992 [103]; George Smoot and John Mather have received the 2006 Nobel Prize in Physics for this discovery. The ground based experiment DASI (Degree Angular Scale Interferometer) [104] detected CMB polarization anisotropy in 2002 [105]. A map of CMB polarization anisotropy has recently been prepared from WMAP 3-year data [98]. More precise measurements of the polarization anisotropy is expected from the upcoming Planck Surveyor [106] and other future missions, e.g., CMBPol [107]. The measurement of the B-mode polarization anisotropy will be a direct probe of inflation in the early universe.

The CMB anisotropy experiments can be classified into three broad types:

1. Space based (e.g., WMAP, COBE)
2. Balloon borne (e.g., BOOMERanG, MAXIMA)
3. Ground based (e.g., ACBAR, CBI)



Figure 5.5: **CMB Experiments.** Three types of CMB anisotropy measurement experiments - ground based, balloon based and space based, are illustrated in this figure. The left panel shows the space based experiment WMAP [93], the middle panel shows the balloon based experiment BOOMERanG [108] and the right panel shows the ground based interferometer DASI [104]. A list of all the past, ongoing and upcoming CMB experiments can be found in [109, 110].

Examples of the above three kinds of experiments have been shown in figure 5.5. The left panel shows the space based WMAP experiment [93], the middle panel shows the Balloon Observations Of Millimetric Extragalactic Radiation and Geophysics

(BOOMERanG) experiment [108] and the right panel shows the ground based DASI instrument [104]. A list of past, ongoing and future CMB experiments can be found in, e.g., [109, 110]. The timeline of CMB astronomy is listed at [111]. The details of the instrumentation in CMB experiments is beyond the scope of this thesis. Specific details about the instruments, in particular, about the WMAP satellite, will be provided wherever necessary.

## 5.5 Summary and Conclusion

According to the widely accepted working Big bang model of the history of the universe, the universe was a very hot and dense soup of photons and charged plasma. As the universe expanded, its density and temperature of reduced and photons started traveling freely. The electrons and protons also recombined during this time, known as the Last Scattering Surface (LSS). The anisotropies at the LSS are embedded as tiny fluctuations in the CMB. Measurement of these fluctuations are extremely important for constraining cosmological models and parameters and has played a leading role in the transition of cosmology to a precision science.

Standard Big Bang model also predicts that the CMB anisotropy is Gaussian and we observe that the universe is highly isotropic. Because of that, CMB anisotropy is usually characterized by the angular power spectrum, as it provides a complete statistical description of a statistically isotropic Gaussian random field on a 2-sphere. Precise measurement of CMB anisotropy is then equivalent to precise measurement of position and height of the crests and troughs of the CMB power spectrum.

CMB was serendipitously discovered by Penzias and Wilson in 1964 and CMB anisotropy was first detected by COBE in 1992. Since then several space based, balloon borne and ground based experiments have been performed to precisely measure the CMB power spectrum at different scales. The first peak of the CMB temperature power spectrum was precisely determined by the WMAP satellite. Its 3-year data has also provided a CMB polarization anisotropy map, which was first detected by DASI in 2002. Detection of the B-mode polarization due to tensor perturbation in the early universe will be a direct probe of inflation.

The precision of these highly sensitive experiments can be properly utilized if all the significant systematic effects are removed. Study of the systematic effects in CMB experiments, in particular, the WMAP satellite, is one of the major goals of this thesis.

## Chapter 6

# Beams and Deconvolution in CMB and GWB Mapmaking: Analysis and Formalism

The observed skymaps of CMB and GWB are convolved with a beam function, a. k. a., the Point Spread Function (PSF). The observed skymaps need to be deconvolved for the estimation of the true skymaps.

The beam function of a CMB instrument is combined with the scan strategy of the instrument and presented as a mapping matrix. The observed time ordered data is a convolution of the mapping matrix with the true sky map. On the other hand, the (directed) GW radiometer beam patterns are extended, quite asymmetric and vary with sky position. We present an analytical study of the GW radiometer beam involving stationary phase approximation to explain the shape of the beam. Also, unlike CMB map making, the GW radiometer analysis is in a preliminary stage. The definition of beam function and the observed data in CMB and GWB experiments are discussed respectively in section 6.1, section 6.2 and section 6.3.

The observed quantities in both CMB and GWB analysis can be expressed as a linear convolution equation. Because of the broad overlap between the kind of map estimation problem we are addressing in CMB and GWB, it is expected that similar techniques will be applicable to both analyses. CMB map making techniques are quite mature and have been tested for a long time. So, to begin with, we essentially follow the prescription based on maximum likelihood estimation followed in CMB analysis. The analytical details of maximum likelihood map making and its application to CMB and GWB analysis are presented in section 6.4,

section 6.5 and section 6.6 respectively.

Though the analysis that has been used here for GWB map making, was first developed for CMB analysis, it can not be implemented with full strength to make CMB maps using modern high-resolution instruments for the following reason: The CMB beams are mildly non-circular and this systematic effect has to be corrected for high resolution experiments. But incorporating this in a maximum likelihood analysis is computationally prohibitive. A suboptimal analysis to correct for beam anisotropy in CMB analysis has been developed in chapter 8 and chapter 9.

## 6.1 Beam Function

Due to the finite resolution of imaging devices, a point source is mapped to an image of finite size. Similarly when the device is pointed to a certain direction, it receives contributions from the neighboring directions also. The function that describes the image of a point source or the response function of the device for each direction is known as the beam function or the point spread function (PSF) or the kernel. The beam function  $B(\hat{\Omega}, \hat{\Omega}')$  is the observed effect in the direction  $\hat{\Omega}$  due to a unit point source in the direction  $\hat{\Omega}'$ ; it is, in fact, the kernel of the convolution equation. For practical purposes the sky is pixelized and the beam function is represented by a matrix. The beam function (or the matrix) can be interpreted in two ways:

1.  $B(\hat{\Omega}, \hat{\Omega}')$  is the response function for the pointing direction  $\hat{\Omega}$   
(each column of the beam matrix is a response function)
2.  $B(\hat{\Omega}, \hat{\Omega}')$  is the point spread function for the source direction  $\hat{\Omega}'$   
(each row of the beam matrix is a point spread function)

Usually a beam function is maximum along the direction where the device is pointing; it falls off (often rapidly) as the distance between the image point and the pointing direction increases. The size of the beam is quantified by its Full Width at Half Maximum (FWHM). In many imaging devices there are secondary peaks also in the beam functions, which are known as “side lobes”.

## 6.2 Observed CMB Data

Several experiments have been performed to measure CMB anisotropy at different angular scales. Most of the CMB experiments have beams of fairly axisymmetric

shape, which can be approximated by two dimensional Gaussian functions. WMAP analysis is of particular concern in this thesis. We have shown the WMAP beam patterns below and we have fitted WMAP Q-beam in appendix D using the IRAF image processing software. See chapter 8, chapter 9 and appendix D for details.

The goal of the WMAP mission is to make skymaps of CMB anisotropy. The WMAP satellite spins in space and scans the whole sky in this process. At each observation time the horns A and B of the instruments point in two different directions and the difference in temperature detected by the two horns is measured. So, given the scan strategy, the observation time can be mapped to pointing direction of each horn. At any given moment, though each horn points in a certain direction, due to the finite resolution of the instruments, photons are received from its neighboring directions as well. The beam function describes the fractional energy received from each direction corresponding to a certain pointing direction.

In modern astronomical experiments, often an imaging device is capable of creating more than one image of a point source on the focal plane for different parameters, e.g, polarization, frequency bands. Figure 6.1 shows the temperature beam maps of the two horns of the WMAP satellite. Each image plane (side A and B) shows the images of Jupiter (treated as a point source) for 10 frequency channels used for observing CMB anisotropy. Jupiter was observed during different seasons to account for the variation in apparent shape due to different observation angles. The sizes of the WMAP beams vary from  $0.22^\circ$  to  $0.88^\circ$ . The shape of the WMAP beams do *not* vary with sky position, which is a very important property and will be of great use later on.

In a practical application we need to pixelize the sky. Each pixel is given a unique number, so effectively the two dimensional sky can be represented by one pixel index - a skymap can be expressed by a real vector. Thus the combined effect of the scan strategy and the beam function for each horn can be represented by a *mapping matrix*  $\mathbf{M}^{A,B} \equiv M_{ij}^{A,B}$ . Each row of the mapping matrix corresponds to a certain observation time. Elements of each row of the mapping matrix is a beam pattern function for the pointing direction corresponding to that observation time. At every observation time, the instrument measures the difference between the temperature anisotropies between two horn pointing directions; the full observation time generates a vector of *Time Ordered Data* (TOD)  $\mathbf{d}$ . For a differential instrument like WMAP, the mapping matrix  $\mathbf{M} \equiv M_{ij}$ , that convolves the true map to generate

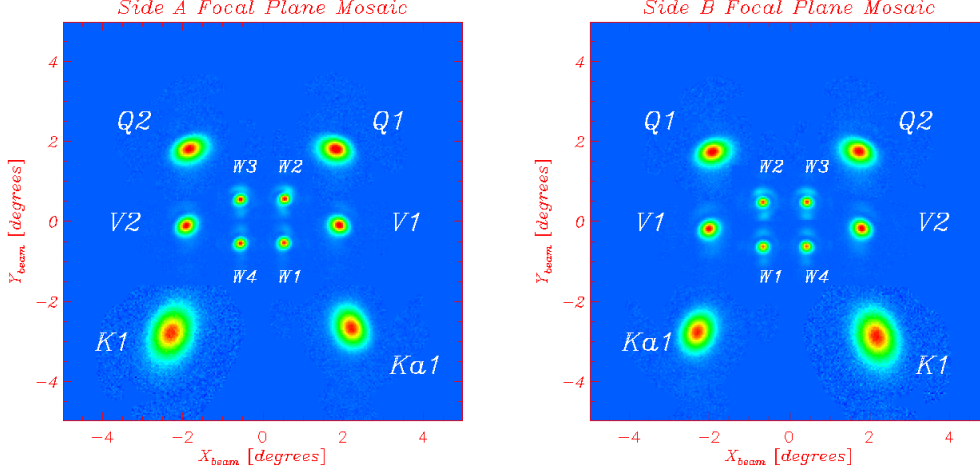


Figure 6.1: **WMAP image planes.** The image of Jupiter (as a point source) in different frequency bands taken by two horns of the WMAP satellite. (Images taken from the [LAMBDA](#) website [101]).

the final output, is the difference between the mapping matrices of two horns [96]

$$\mathbf{M} = \mathbf{M}^A - \mathbf{M}^B. \quad (6.1)$$

For computational simplicity to be explained later, the beam functions of each horn are assumed to be of infinite resolution and circular (axially symmetric about the pointing direction). So one element of each row of the pointing matrices  $\mathbf{M}^{A,B}$  is 1 at the pixel (column) index that corresponds to the pointing direction at the given time (row index). All other elements of the matrices are 0.

Since the true temperature anisotropy map  $\mathbf{t}$  is independent of time, one may write the observed CMB time ordered data as the convolution equation

$$\mathbf{d} = \mathbf{M} \cdot \mathbf{t} + \mathbf{n} \quad (6.2)$$

where  $\mathbf{n}$  is the random instrumental noise. WMAP noise is nearly white zero mean Gaussian, so the noise covariance matrix [96] is given by

$$\mathbf{N} := \langle \mathbf{n} \mathbf{n}^T \rangle = \sigma_0^2 \mathbf{I}, \quad (6.3)$$

where  $\sigma_0^2$  is the variance of each bin of time ordered data and  $\mathbf{I}$  is the identity matrix.

Thus the measured time ordered data  $\mathbf{d}$  from a CMB anisotropy experiment is

a convolution of the true sky  $\mathbf{t}$  with the known mapping matrix  $\mathbf{M}$  and has additive noise  $\mathbf{n}$  of known statistical properties. In the next section we shall see that the output of the GW radiometer can also be expressed in a similar fashion as a linear convolution equation. We then present a general deconvolution method applicable to both CMB and GWB for the estimation of the true anisotropy sky.

### 6.3 Observed (Directed) GW Radiometer Point Estimate

As described in section 4.4.2, it is possible to make a skymap using a directed GW radiometer. The detailed properties of the beam function and convolution equation of the radiometer is presented in this section. From now on we shall only consider the issues of map making using a directed GW radiometer, so the tag “directed” is implied and hence will be omitted.

A GW radiometer is pointed to a direction  $\hat{\Omega}$  by using a direction dependent filter function

$$\tilde{q}_{\hat{\Omega},H}(t, f) = \frac{H(f) \gamma_{\hat{\Omega}}^*(t, f)}{P_1(t; |f|) P_2(t; |f|)}. \quad (6.4)$$

Suppose that there is only one unit *polarized* point source in the sky in the direction  $\hat{\Omega}'$ , that is  $\mathcal{P}_{\text{true}}^A(\hat{\Omega}) = \delta_{AA'} \delta(\hat{\Omega} - \hat{\Omega}')$ . Then the expected point estimate (statistic)  $S_{\hat{\Omega}}$  is maximum when  $\hat{\Omega} = \hat{\Omega}'$  and it falls off as the distance between the pointing direction and the source direction,  $\Delta\Omega := \hat{\Omega} - \hat{\Omega}'$ , increases, when  $\hat{\Omega}$  is close to  $\hat{\Omega}'$ . The expected point estimate  $\langle S_{\hat{\Omega}} \rangle$  in this case is the polarization dependent beam function  $B^A(\hat{\Omega}, \hat{\Omega}')$  for the GW radiometer. Formally, we can express the beam function using eqn (4.88) and eqn (4.98) as

$$\begin{aligned} B^A(\hat{\Omega}, \hat{\Omega}') &= \left[ \Delta t \sum_{i=1}^n \|q_{\hat{\Omega},H}\|_{t_i}^2 \right]^{-1} \Delta t \sum_{i=1}^n \int_{-\infty}^{\infty} df H_{\text{true}}(f) \gamma_{\hat{\Omega}'}^A(t_i, f) \tilde{q}_{\hat{\Omega},H}(t_i, f) \quad (6.5) \\ &= \left[ \Delta t \sum_{i=1}^n \|q_{\hat{\Omega},H}\|_{t_i}^2 \right]^{-1} \Delta t \sum_{i=1}^n \int_{-\infty}^{\infty} df \frac{H_{\text{true}}(f) H(f)}{P_1(t_i; |f|) P_2(t_i; |f|)} \gamma_{\hat{\Omega}'}^A(t_i, f) \gamma_{\hat{\Omega}}^*(t_i, f). \end{aligned} \quad (6.6)$$

Using the polarization and direction dependent overlap reduction function

$$\gamma_{\hat{\Omega}}^A(t, f) := F_1^A(\hat{\Omega}, t) F_2^A(\hat{\Omega}, t) e^{2\pi i f \hat{\Omega} \cdot \Delta \mathbf{x}(t)/c}, \quad (6.7)$$

the shorthands for the combination of the antenna pattern functions

$$\Gamma(\hat{\Omega}, t) := F_1^+(\hat{\Omega}, t)F_2^+(\hat{\Omega}, t) + F_1^\times(\hat{\Omega}, t)F_2^\times(\hat{\Omega}, t) \quad (6.8)$$

and representing the ratio of source and noise PSDs through a single function

$$G(t; f) := \frac{H_{\text{true}}(f)H(f)}{P_1(t; |f|)P_2(t; |f|)} \quad (6.9)$$

the beam function can be expressed in a more compact form

$$B^A(\hat{\Omega}, \hat{\Omega}') = \left[ \Delta t \sum_{i=1}^n \|q_{\hat{\Omega}, H}\|_{t_i}^2 \right]^{-1} \times \Delta t \sum_{i=1}^n \int_{-\infty}^{\infty} df G(t_i; f) F_1^A(\hat{\Omega}', t_i) F_2^A(\hat{\Omega}', t_i) \Gamma(\hat{\Omega}, t_i) e^{-2\pi i f \Delta \Omega \cdot \Delta \mathbf{x}(t_i)/c}. \quad (6.10)$$

If the detector noise PSDs are stationary, the shape of the beam functions for integration over complete day(s) do not depend on the longitude of the pointing direction due to the symmetry about earth's spin axis.

If the injected unit point source is unpolarized, we may use  $\mathcal{P}_{\text{true}}^+(\hat{\Omega}) = \mathcal{P}_{\text{true}}^\times(\hat{\Omega}) = \delta(\hat{\Omega} - \hat{\Omega}')$  and the polarization independent beam functions becomes

$$B(\hat{\Omega}, \hat{\Omega}') = B^+(\hat{\Omega}, \hat{\Omega}') + B^\times(\hat{\Omega}, \hat{\Omega}') \quad (6.11)$$

$$= \left[ \Delta t \sum_{i=1}^n \|q_{\hat{\Omega}, H}\|_{t_i}^2 \right]^{-1} \Delta t \sum_{i=1}^n \int_{-\infty}^{\infty} df G(t_i; f) \Gamma(\hat{\Omega}', t_i) \Gamma(\hat{\Omega}, t_i) e^{-2\pi i f \Delta \Omega \cdot \Delta \mathbf{x}(t_i)/c}. \quad (6.12)$$

From now on we shall assume that the true source PSD is exactly known,  $H_{\text{true}}(f) = H(f)$ , unless otherwise specified (so we omit the subscript "H" from the filter). With this assumption, it is interesting to note that

$$B(\hat{\Omega}, \hat{\Omega}') = \left[ \Delta t \sum_{i=1}^n (q_{\hat{\Omega}}, q_{\hat{\Omega}'}) \right] / \left[ \Delta t \sum_{i=1}^n \|q_{\hat{\Omega}}\|_{t_i}^2 \right], \quad (6.13)$$

which follows the convenient normalization condition  $B(\hat{\Omega}, \hat{\Omega}) = 1$  [see eqn (4.79)].

Typical (polarization independent) beam functions for the baseline formed by the two LIGO detectors at Hanford and Livingston (for white noise PSD with upper cutoff frequency 1024Hz and observation over a full day) are shown in the left panel

of figure 6.2.

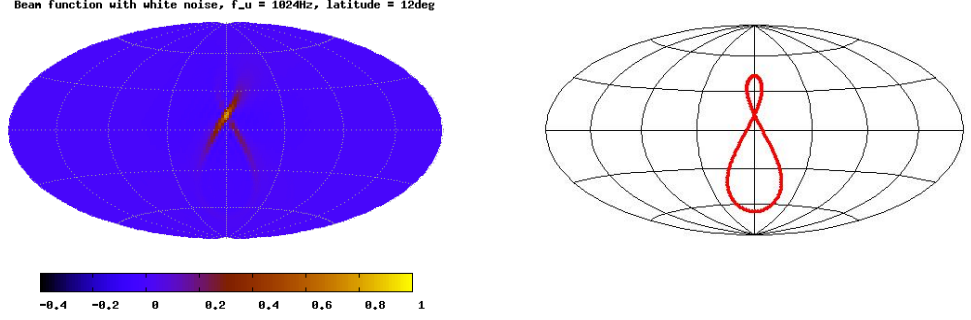


Figure 6.2: **Numerical and Theoretical GW radiometer beam patterns.** The left panel shows a numerical beam patterns for the LIGO Hanford-Livingston baseline pointing at latitude  $12^\circ$  for white noise with an upper cut-off frequency of 1024Hz. The right panel shows the theoretical pattern obtained by stationary phase approximation (SPA). Clearly they are in very good agreement.

The size of the beam of the radiometer using the LIGO Livingston and Hanford detectors can vary between  $\sim 50\text{--}100$  sq. degrees [79] depending on the sky position, the upper cutoff frequency and the source and noise PSDs. Typical contour plots of the beam function including the (negative) side lobes of the LLO-LHO radiometer near latitude  $12^\circ$  for LIGO-I noise PSD and different source PSDs are shown in figure 6.3. The source PSD for the left panel is  $H(f) = \text{constant}$  and for the right panel is  $H(f) \propto f^{-3}$ .

The GW radiometer beams have quite asymmetric shape and they vary with sky position. This compelled us to understand the characteristic of the beam function. In appendix B we have analytically studied the beam pattern using Stationary Phase Approximation (SPA). Where we have used the fact that the functions  $G(t; f)$  and  $\Gamma(\hat{\Omega}, t)$  are slowly varying functions of time, so the integrand constructively contributes when the phase term  $\exp[-2\pi i f \Delta\Omega \cdot \Delta\mathbf{x}(t)/c]$  is stationary. We show that the beam function  $B(\hat{\Omega}, \hat{\Omega}_0)$  for a pointing direction  $\hat{\Omega}_0$  takes significant values when  $\hat{\Omega} - \hat{\Omega}_0$  is parallel to the unit normal  $\hat{\mathbf{n}}_{\text{cone}}(t)$  to the baseline vector  $\Delta\mathbf{x}(t)$  and the cone traced out by the baseline due to earth rotation. Mathematically, the beam pattern stands out along the following trajectory parameterized by sidereal time  $t$ :

$$\hat{\Omega}(t) = \hat{\Omega}_0 - 2[\hat{\Omega}_0 \cdot \hat{\mathbf{n}}_{\text{cone}}(t)]\hat{\mathbf{n}}_{\text{cone}}(t). \quad (6.14)$$

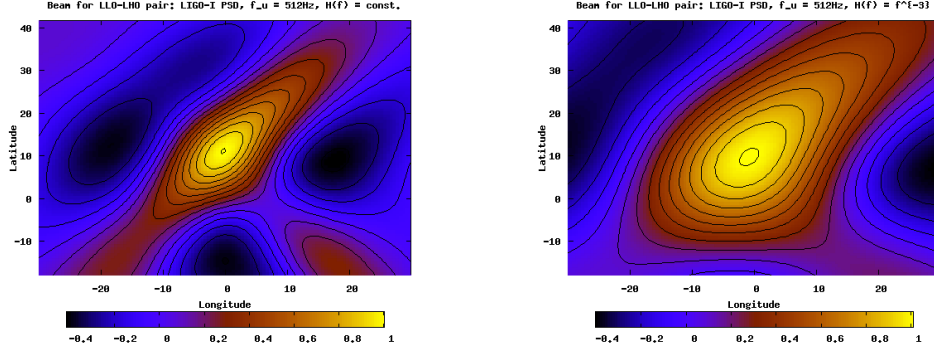


Figure 6.3: **Contour plots of GW radiometer beam patterns.** Approximate size of the beam and the (negative) side lobes for different source PSDs and LIGO detectors with LIGO-I noise PSD are shown in this figure. The left panel shows the beam contours for  $H(f) = \text{constant}$  at latitude  $12^\circ$  and the right panel shows the same for  $H(f) \propto f^{-3}$ . The contours are drawn starting from 1 with an interval of  $-0.1$ . Note that, the beam falls by  $1/e$  in between the 6th and the 7th contour (from the highest value), which can be used to measure the beam size.

The theoretical pattern is shown in the right panel of figure 6.2, which is in very good agreement with the numerical pattern shown in the left panel.

We proceed further and evaluate the (unnormalized) beam function along this trajectory using the formula, again parameterized with time  $t$

$$B(\hat{\Omega}(t), \hat{\Omega}_0) \propto \Gamma(\hat{\Omega}(t); t) \Gamma(\hat{\Omega}_0; t) \frac{\sqrt{f_u} - \sqrt{f_l}}{\omega_E} \sqrt{\frac{8c}{|[\hat{\mathbf{z}} \cdot \Delta \mathbf{x}(t)] [\hat{\mathbf{z}} \cdot (\hat{\Omega}(t) - \hat{\Omega}_0)]|}}, \quad (6.15)$$

where  $f_l$  and  $f_u$  are respectively the lower and upper cutoff frequencies.

The stationary phase analysis also indicates an approximate resolving power of the radiometer. The expression for the phase term  $2\pi i f \Delta \Omega \cdot \Delta \mathbf{x}(t)/c$  suggests that the resolving power of the radiometer is  $\sim c/f_u/\Delta R$ , where  $\lambda$  corresponding to the upper cutoff frequency  $f_u$ . For the LIGO detectors separated by  $\sim 3000\text{km}$  with a upper cut off frequency of  $f_u \sim 1\text{kHz}$  (wavelength  $\sim 300\text{km}$ ). Hence the radiometer resolution should be  $\sim 0.1$  radians, that is,  $\sim 6$  degrees, which is consistent with the numerically obtained beam profiles.

In general, the true sky is a diffuse background of stochastic GW. If the true angular power distribution is described by the polarization dependent function  $\mathcal{P}_{\text{true}}^A(\hat{\Omega})$ , it is straight forward to show using eqn (4.88) that the observed point estimate  $S_{\hat{\Omega}}$  is a convolution of the the true sky  $\mathcal{P}_{\text{true}}^A(\hat{\Omega})$  with the known beam

function  $B^A(\hat{\Omega}, \hat{\Omega}')$  and has additive noise  $n_{\hat{\Omega}}$  of known statistical properties:

$$S_{\hat{\Omega}} = \int_{S^2} d\hat{\Omega}' \left[ B^+(\hat{\Omega}, \hat{\Omega}') \mathcal{P}_{\text{true}}^+(\hat{\Omega}') + B^\times(\hat{\Omega}, \hat{\Omega}') \mathcal{P}_{\text{true}}^\times(\hat{\Omega}') \right] + n_{\hat{\Omega}}. \quad (6.16)$$

Notice the similarity with the CMB time-ordered-data described in the previous section. Our aim is to estimate the true angular power distribution  $\mathcal{P}_{\text{true}}^A(\hat{\Omega})$  from the above integral equation. To be able to do that, we need to study the statistical properties of noise at each pixel.

Unlike CMB, the GW radiometer noise is quite complicated. The noise at different pixel (direction) is related to the detector time stream data through the radiometer analysis, hence, the noise  $n_{\hat{\Omega}}$  at different directions are correlated. The statistical properties of the noise  $n_{\hat{\Omega}}$  are given below.

The noise term in the radiometer signal will have terms containing summations over  $\tilde{n}_I \tilde{n}_J$  and  $\tilde{h}_I \tilde{h}_J$ , where  $I, J = 1, 2$  are the detector indices. All these terms are of zero mean for  $I \neq J$ , but the variance will be highly dominated by the noise-noise term [ $\langle \tilde{n}_I^* \tilde{n}_I \rangle \gg \langle \tilde{h}_I^* \tilde{h}_I \rangle$ ]. Hence, while considering the noise characteristics the other terms are ignored. Moreover, the noises in the detectors are independent, which implies that [112], for  $I \neq J$ ,  $\langle \tilde{n}_I^* \tilde{n}_J \rangle = \langle \tilde{n}_I^* \rangle \langle \tilde{n}_J \rangle$  and  $\langle \tilde{n}_I^* \tilde{n}_I^* \tilde{n}_J \tilde{n}_J \rangle = \langle \tilde{n}_I^* \tilde{n}_I^* \rangle \langle \tilde{n}_J \tilde{n}_J \rangle$ .

- Noise in point estimate:

$$n_{\hat{\Omega}} = \left[ \Delta t \sum_{i=1}^n \|q_{\hat{\Omega}}\|_{t_i}^2 \right]^{-1} \sum_{i=1}^n \int_{-\infty}^{\infty} df \tilde{n}_1^*(t_i; f) \tilde{n}_2(t_i; f) \tilde{q}_{\hat{\Omega}}(t_i, f). \quad (6.17)$$

- Mean of noise:

$$\langle n_{\hat{\Omega}} \rangle = \left[ \Delta t \sum_{i=1}^n \|q_{\hat{\Omega}}\|_{t_i}^2 \right]^{-1} \sum_{i=1}^n \int_{-\infty}^{\infty} df \langle \tilde{n}_1^*(t_i; f) \rangle \langle \tilde{n}_2(t_i; f) \rangle \tilde{q}_{\hat{\Omega}}(t_i, f) = 0. \quad (6.18)$$

- Pixel-to-pixel covariance of observed noise :

$$\begin{aligned}
 \langle n_{\hat{\Omega}_1} n_{\hat{\Omega}_2} \rangle &= \left[ \Delta t \sum_{i=1}^n \|q_{\hat{\Omega}_1}\|_{t_i}^2 \right]^{-1} \left[ \Delta t \sum_{i=1}^n \|q_{\hat{\Omega}_2}\|_{t_i}^2 \right]^{-1} \sum_{i_1=1}^n \sum_{i_2=1}^n \\
 &\quad \int_{-\infty}^{\infty} df_1 \int_{-\infty}^{\infty} df_2 \int_{-\infty}^{\infty} df'_1 \int_{-\infty}^{\infty} df'_2 \delta_{\Delta t}(f_1 - f'_1) \delta_{\Delta t}(f_2 - f'_2) \times \\
 &\quad \langle \tilde{n}_1^*(t_{i_1}; f_1) \tilde{n}_1^*(t_{i_2}; f_2) \rangle \langle \tilde{n}_2(t_{i_1}; f'_1) \tilde{n}_2(t_{i_2}; f'_2) \rangle \tilde{q}_{\hat{\Omega}_1}(t_{i_1}, f'_1) \tilde{q}_{\hat{\Omega}_2}(t_{i_2}, f'_2) \\
 &= \frac{1}{4} \left[ \Delta t \sum_{i=1}^n \|q_{\hat{\Omega}_1}\|_{t_i}^2 \right]^{-1} \left[ \Delta t \sum_{i=1}^n \|q_{\hat{\Omega}_2}\|_{t_i}^2 \right]^{-1} \sum_{i=1}^n \int_{-\infty}^{\infty} df_1 \int_{-\infty}^{\infty} df'_1 \\
 &\quad \delta_{\Delta t}^2(f_1 - f'_1) P_1(t_i, |f_1|) P_2(t_i, |f'_1|) \tilde{q}_{\hat{\Omega}_1}(t_i, f'_1) \tilde{q}_{\hat{\Omega}_2}^*(t_i, f_1) \\
 &= \frac{\Delta t}{4} \left[ \Delta t \sum_{i=1}^n \|q_{\hat{\Omega}_1}\|_{t_i}^2 \right]^{-1} \left[ \Delta t \sum_{i=1}^n \|q_{\hat{\Omega}_2}\|_{t_i}^2 \right]^{-1} \times \\
 &\quad \sum_{i=1}^n \int_{-\infty}^{\infty} df P_1(t_i, |f|) P_2(t_i, |f|) \tilde{q}_{\hat{\Omega}_1}(t_i, f) \tilde{q}_{\hat{\Omega}_2}^*(t_i, f). \quad (6.19)
 \end{aligned}$$

The covariance can be expressed in a convenient form using eqn (6.13)

$$\langle n_{\hat{\Omega}_1} n_{\hat{\Omega}_2} \rangle = \frac{1}{4} \left[ \Delta t \sum_{i=1}^n \|q_{\hat{\Omega}_2}\|_{t_i}^2 \right]^{-1} B(\hat{\Omega}_1, \hat{\Omega}_2) = \frac{1}{4} \frac{\Delta t \sum_{i=1}^n (q_{\hat{\Omega}_1}, q_{\hat{\Omega}_2})}{\Delta t \sum_{i=1}^n \|q_{\hat{\Omega}_1}\|_{t_i}^2 \Delta t \sum_{i=1}^n \|q_{\hat{\Omega}_2}\|_{t_i}^2}. \quad (6.20)$$

- Noise variance [see eqn (4.82)]

$$\langle n_{\hat{\Omega}} n_{\hat{\Omega}} \rangle = \frac{1}{4} \left[ \Delta t \sum_{i=1}^n \|q_{\hat{\Omega}}\|_{t_i}^2 \right]^{-1}. \quad (6.21)$$

The covariance formula gives the same consistent result for  $\hat{\Omega}_1 = \hat{\Omega}_2 = \hat{\Omega}$ .

Moreover, the probability distribution of the noise  $n(\hat{\Omega})$  is normal (so the first and the second moments characterize all the statistical properties). This is ensured by the generalized central limit theorem [113]: If  $X_k$  be mutually independent one dimensional random variables following distributions  $F_k$  with mean 0 and variance  $\sigma_k^2$ , then  $\sum_k X_k$  tend to follow a zero mean normal distribution with variance  $\sum_k \sigma_k^2$ . Since several realizations of the products of Fourier transforms of detector noise  $\tilde{n}_1^*(t; f) \tilde{n}_2(t; f)$  are added [see eqn (6.17)] to generate the noise  $n(\hat{\Omega})$ , the generalized central limit theorem suggests it may be Normal distributed. As a consistency

check, if this argument is used to calculate the variance of  $n(\hat{\Omega})$ , we get the same result as in eqn (6.21).

For practical applications, the sky is pixelized and the true power distribution is usually expanded as a sum of point sources at each pixel,

$$\mathcal{P}_{\text{true}}^A(\hat{\Omega}) = \sum_k \mathcal{P}_k^A \delta(\hat{\Omega} - \hat{\Omega}_k), \quad (6.22)$$

where  $\hat{\Omega}_k$  is the location of pixel  $k$  and  $\mathcal{P}_k^A$  is the strength of pixel  $k$ . Then, we may write the discrete convolution equation as

$$\mathbf{S} = \mathbf{B}^+ \cdot \mathcal{P}^+ + \mathbf{B}^\times \cdot \mathcal{P}^\times + \mathbf{n}, \quad (6.23)$$

where the indices of the vectors and matrices in the above equation refers to the corresponding pixel, more explicitly,  $B_{kk'} \equiv B(\hat{\Omega}_k, \hat{\Omega}_{k'})$ ,  $S_k \equiv S_{\hat{\Omega}_k}$  and  $n_k \equiv n_{\hat{\Omega}_k}$ . The pixel to pixel noise covariance matrix in the observed map  $\mathbf{N} \equiv N_{kk'}$  becomes

$$N_{kk'} := \langle n_k n_{k'} \rangle = \frac{1}{4} \left[ \Delta t \sum_{i=1}^n \|q_{\hat{\Omega}_k}\|_{t_i}^2 \right]^{-1} B_{kk'}. \quad (6.24)$$

The convolution equation for GWB point estimates [eqn (6.23)] is strikingly similar to the convolution equation for the CMB time-ordered-data given by eqn (6.2). Therefore, in effect, the problem of estimation of true GWB anisotropy map from the point estimate at every pixel is identical to the estimation of true CMB anisotropy map from the time-ordered-data. The procedure to estimate the maximum likelihood skymap is described in the next section.

## 6.4 Maximum Likelihood (ML) skymap Estimation

In the last two sections we have established that the CMB and GWB observed map can be expressed by a linear convolution equation of the form

$$\mathbf{d} = \mathbf{K} \cdot \mathbf{t} + \mathbf{n}, \quad (6.25)$$

where our aim is to estimate the true sky vector  $\mathbf{t}$  from the observed data vector  $\mathbf{d}$  using the known *kernel matrix*  $\mathbf{K}$  and the known statistical properties of the Gaussian noise vector  $\mathbf{n}$ . This problem has been addressed in different branches of science using different approaches. Since CMB map making has been developed and

successfully implemented for more than a decade, we opt for the algorithm used for CMB anisotropy map making [114]. This algorithm estimates the Maximum Likelihood (ML) solution from a linear convolution equation with Gaussian noise, which was put together by Borrill [115] as a (publicly available) software package MADCAP [116]. The same algorithm was used to make anisotropy maps using the recently released data from the WMAP satellite [97].

The mathematics is straight forward. If noise follows a multivariate normal distribution, the probability that the data contains the noise vector  $\mathbf{n}$  is given by [112]

$$\mathfrak{P}(\mathbf{n}) = \frac{1}{(2\pi)^{N_d/2}(\det \mathbf{N})^{1/2}} \exp\left[-\frac{1}{2}\mathbf{n}^T \cdot \mathbf{N}^{-1} \cdot \mathbf{n}\right] \quad (6.26)$$

where  $N_d$  is the number of observed data points (number of elements in  $\mathbf{d}$ ),  $\mathbf{N} := \langle \mathbf{n} \mathbf{n}^T \rangle$  is the (symmetric) noise covariance matrix of the *observed* data and  $\det \mathbf{N}$  is the determinant of  $\mathbf{N}$ . Therefore the probability (likelihood) that the data  $\mathbf{d}$  contains the modeled signal  $\mathbf{t}_{\text{mod}}$  is

$$\mathfrak{P}(\mathbf{d}|\mathbf{t}_{\text{mod}}) = (2\pi)^{-N_d/2} \exp\left[-\frac{1}{2}\left((\mathbf{d} - \mathbf{K} \cdot \mathbf{t}_{\text{mod}})^T \cdot \mathbf{N}^{-1} \cdot (\mathbf{d} - \mathbf{K} \cdot \mathbf{t}_{\text{mod}}) + \text{Tr}[\ln \mathbf{N}]\right)\right]. \quad (6.27)$$

The corresponding log-likelihood is

$$\ln[\mathfrak{P}(\mathbf{d}|\mathbf{t}_{\text{mod}})] = -\frac{1}{2}\left((\mathbf{d} - \mathbf{K} \cdot \mathbf{t}_{\text{mod}})^T \cdot \mathbf{N}^{-1} \cdot (\mathbf{d} - \mathbf{K} \cdot \mathbf{t}_{\text{mod}}) + \text{Tr}[\ln \mathbf{N}]\right) + \frac{N_d}{2} \ln(2\pi). \quad (6.28)$$

It can be shown by taking derivative of the above equation with respect to  $\mathbf{t}_{\text{mod}}$  [112] that the (log-)likelihood is maximum when

$$\mathbf{t}_{\text{mod}} = \left(\mathbf{K}^T \mathbf{N}^{-1} \mathbf{K}\right)^{-1} \mathbf{K}^T \mathbf{N}^{-1} \cdot \mathbf{d} =: \hat{\mathbf{t}}, \quad (6.29)$$

which is the maximum likelihood estimate for the given problem. For clarity, we shall use the short hand

$$\mathbf{W} := \left(\mathbf{K}^T \mathbf{N}^{-1} \mathbf{K}\right)^{-1} \mathbf{K}^T \mathbf{N}^{-1}. \quad (6.30)$$

It is important to note that  $\mathbf{W}\mathbf{K} = \mathbf{I}$ , where  $\mathbf{I}$  is the identity matrix. Hence,

$$\hat{\mathbf{t}} = \mathbf{W} \cdot \mathbf{d} = \mathbf{W} \cdot (\mathbf{K} \cdot \mathbf{t} + \mathbf{n}) = \mathbf{t} + \mathbf{W} \cdot \mathbf{n}. \quad (6.31)$$

Since the noise in observed data is of zero mean,  $\langle \mathbf{n} \rangle = 0$ , the above relation suggests

that the ML estimate is *unbiased*:  $\langle \hat{\mathbf{t}} \rangle = \mathbf{t}$ .

The noise in the ML estimate  $\mathbf{n}$  is a convolution of the noise  $\mathbf{n}$  in observed data with the matrix  $\mathbf{W}$ :

$$\mathbf{n} := \hat{\mathbf{t}} - \langle \hat{\mathbf{t}} \rangle = \hat{\mathbf{t}} - \mathbf{t} = \mathbf{W} \cdot \mathbf{n}. \quad (6.32)$$

The noise covariance matrix of the ML estimate is

$$\Sigma := \langle \mathbf{n} \mathbf{n}^T \rangle = \mathbf{W} \langle \mathbf{n} \mathbf{n}^T \rangle \mathbf{W}^T = (\mathbf{K}^T \mathbf{N}^{-1} \mathbf{K})^{-1} \mathbf{K}^T \mathbf{W}^T = (\mathbf{K}^T \mathbf{N}^{-1} \mathbf{K})^{-1}. \quad (6.33)$$

Therefore, to obtain the ML estimate one has to first compute the inverse of the noise covariance matrix  $\Sigma^{-1} = \mathbf{K}^T \mathbf{N}^{-1} \mathbf{K}$ , then invert it to evaluate  $\mathbf{W}$  and, in turn,  $\hat{\mathbf{t}}$ .

## 6.5 ML Estimation of CMB Anisotropy Map

The above mathematics is directly applicable to CMB map making. The ML estimate of the true temperature anisotropy map is given by

$$\hat{\mathbf{t}} = \mathbf{W} \cdot \mathbf{d}; \quad \mathbf{W} = (\mathbf{M}^T \mathbf{N}^{-1} \mathbf{M})^{-1} \mathbf{M}^T \mathbf{N}^{-1}. \quad (6.34)$$

The pixel-to-pixel noise covariance matrix of the estimated map is

$$\Sigma = (\mathbf{M}^T \mathbf{N}^{-1} \mathbf{M})^{-1}. \quad (6.35)$$

However, in practice, the solution  $\hat{\mathbf{t}} = \mathbf{W} \cdot \mathbf{d}$  is too costly to evaluate exactly given the properties of  $\mathbf{M}$  and  $\mathbf{N}^{-1}$  [96]. This is mainly due to very high resolutions of modern CMB experiments and correspondingly large sizes of the matrices. Approximate techniques are adopted for the implementation of the ML analysis. For example, in the map making carried out by the WMAP team, the beams are assumed to be circularly symmetric (about the pointing direction) with infinite resolution for the evaluation of the matrix  $\mathbf{W}$  and the above analysis is then used to estimate the true anisotropy map.<sup>1</sup> Though this assumption is approximately valid for preparing sky maps, it introduces a bias in the skymap and angular power spectrum [117, 118]. This systematic effect is quite significant at high multipoles (low angular scales beyond the beam width), and has to be considered for correct data analysis. Different approaches to deconvolve partial or full skymap for asymmetric beams are being proposed [119, 120]. We have developed a sub-optimal approach to

<sup>1</sup>Similar formalism has been used to make CMB polarization anisotropy map also using the three years of WMAP data [96, 98].

unbias the (pseudo- $C_l$ ) power spectrum estimator, which is presented in chapter 8 and chapter 9. The effect of beam asymmetry has been taken into account in the recent WMAP three years analysis [96] using a similar approach; the results are in very good agreement with our prediction.

## 6.6 ML Estimation of GWB Anisotropy

A straightforward application of ML estimation method described in the previous section to GWB skymap making is presented in this section. While we first present the simplest case of a single baseline interferometry, It is possible to extend the basic analysis to incorporate more complex problems of using multiple baselines and/or making separate maps for each polarization and to measure multipole moments of the GWB sky.

### 6.6.1 Basic Analysis of Skymap

We shall first consider the case of single baseline with equal power in both polarizations,  $\mathcal{P}_+(\hat{\Omega}) = \mathcal{P}_\times(\hat{\Omega})$ . The ML estimate for the GWB sky map is given by

$$\hat{\mathcal{P}} = \mathbf{W} \cdot \mathbf{S}; \quad \mathbf{W} = (\mathbf{B}^T \mathbf{N}^{-1} \mathbf{B})^{-1} \mathbf{B}^T \mathbf{N}^{-1} \quad (6.36)$$

and the pixel-to-pixel noise covariance matrix of the observed map is

$$\boldsymbol{\Sigma} = (\mathbf{B}^T \mathbf{N}^{-1} \mathbf{B})^{-1}. \quad (6.37)$$

Since in this special case the beam matrix is a square matrix, if the inverse of the beam matrix exists the ML estimate takes a simple form

$$\hat{\mathcal{P}} = \mathbf{B}^{-1} \cdot \mathbf{S}. \quad (6.38)$$

However directly inverting the beam matrix is non-trivial and we prefer to solve the following linear algebraic equation to find  $\hat{\mathcal{P}}$ :

$$\mathbf{B} \cdot \hat{\mathcal{P}} = \mathbf{S}. \quad (6.39)$$

This issue will be illustrated in the next section.

It is worth noting that in the case of GWB map making a full blown ML estimate can be implemented because, as compared to the modern CMB experiments, GW

radiometer beam for the ground based detectors is much broader, so the number of pixels (and hence the dimension of the matrices) is numerically tractable.

### 6.6.2 Extensions of the simple MapMaking

The ML analysis to estimate the GWB skymaps can be generalized to address more complex problems of using a network of detectors (multiple baselines) and making separate maps for different polarizations. In each case the form of the expressions for the ML estimate ( $\hat{\mathcal{P}}$ ) and pixel-to-pixel covariance matrix ( $\Sigma$ ) remain the same,

$$\hat{\mathcal{P}} = \Sigma \mathbf{B}^T \mathbf{N}^{-1} \cdot \mathbf{S}; \quad \Sigma^{-1} := \mathbf{B}^T \mathbf{N}^{-1} \mathbf{B}, \quad (6.40)$$

as long as the form of the convolution equation,

$$\mathbf{S} = \mathbf{B} \cdot \mathcal{P} + \mathbf{n}, \quad (6.41)$$

is preserved by redefining different quantities in that equation.

#### Network of Detectors

The description of GWB radiometer beam and its convolution provided in section 6.3 only considered the problem of map making using one baseline (two detectors). However, if we have observed maps (with same pixelization) from different baselines of a network of detectors, we have to incorporate all the baselines by redefining different quantities to get the ML estimate.<sup>2</sup>

Suppose that  $N_b$  baselines have generated skymaps of identical pixelization with  $N_{\text{pix}}$  pixels. Let  $\mathbf{S}^{(i)}$  be the observed map by baseline  $i$ , mapped using the filter “vector”  $\mathbf{q}^{(i)}$ , convolved with beam matrix  $\mathbf{B}^{(i)}$  and contains noise  $\mathbf{n}^{(i)}$ . Then the

<sup>2</sup>Of course, one could also combine the maps from different baselines with suitable pixel dependent weight factors  $\mathbf{w}_i$ ,

$$\mathbf{S} = \sum_i \mathbf{w}_i \cdot \mathbf{S}^{(i)},$$

which may reduce the noise by a factor of  $\sim \sqrt{N_b}$ . But, it would also have issues of combining data from baselines with different beam functions. Further analysis is required to assess which method would be more advantageous.

form of the convolution equation [eqn (6.41)] can be preserved by substituting

$$\mathbf{S} := \begin{pmatrix} \mathbf{S}^{(1)} \\ \mathbf{S}^{(2)} \\ \vdots \\ \mathbf{S}^{(N_b)} \end{pmatrix}; \quad \mathbf{n} := \begin{pmatrix} \mathbf{n}^{(1)} \\ \mathbf{n}^{(2)} \\ \vdots \\ \mathbf{n}^{(N_b)} \end{pmatrix}; \quad \mathbf{B} := \begin{bmatrix} \mathbf{B}^{(1)} \\ \mathbf{B}^{(2)} \\ \vdots \\ \mathbf{B}^{(N_b)} \end{bmatrix}. \quad (6.42)$$

Note that  $\mathbf{S}$ ,  $\mathbf{n}$  are now  $1 \times N_{\text{pix}}N_b$  vectors and  $\mathbf{B}$  is a  $N_{\text{pix}} \times N_{\text{pix}}N_b$  matrix, while  $\mathcal{P}$  (the true GWB sky) remains unchanged. This is similar to CMB experiments where each pixel is visited by the detector several times. In the multi-baseline GW radiometer case each pixel is visited by different baselines, but, unlike CMB, each pixel is visited equal number of times. The noise covariance matrix  $\mathbf{N} := \langle \mathbf{n}\mathbf{n}^T \rangle$  of the raw skymap should also be generalized. Let  $n_{\hat{\Omega}}^{(i)}$  be the noise from the radiometer baseline  $i$  with detectors  $I$  and  $I'$  (and following the same convention for  $j$ ) pointing at  $\hat{\Omega}$ . Then

$$\begin{aligned} \langle n_{\hat{\Omega}_1}^{(i)} n_{\hat{\Omega}_2}^{(j)} \rangle &= \left[ \Delta t \sum_{i_1=1}^n \|q_{\hat{\Omega}_1}^{(i)}\|_{t_{i_1}}^2 \right]^{-1} \left[ \Delta t \sum_{i_2=1}^n \|q_{\hat{\Omega}_1}^{(j)}\|_{t_{i_2}}^2 \right]^{-1} \sum_{i_1=1}^n \sum_{i_2=1}^n \\ &\int_{-\infty}^{\infty} df_1 \int_{-\infty}^{\infty} df_2 \int_{-\infty}^{\infty} df'_1 \int_{-\infty}^{\infty} df'_2 \delta_{\Delta t}(f_1 - f'_1) \delta_{\Delta t}(f_2 - f'_2) \times \\ &\langle \tilde{n}_I^*(t_{i_1}, f_1) \tilde{n}_{I'}^*(t_{i_2}, f_2) \tilde{n}_{I'}(t_{i_1}, f'_1) \tilde{n}_I(t_{i_2}, f'_2) \rangle \tilde{q}_{\hat{\Omega}_1}^{(i)}(t_{i_1}, f'_1) \tilde{q}_{\hat{\Omega}_2}^{(j)}(t_{i_2}, f'_2). \end{aligned} \quad (6.43)$$

If  $i$  and  $j$  denote the same baselines we get back the covariance for single baseline [eqn (6.19)]. However, if  $i$  and  $j$  denote different baselines, at least one pair of the detectors among the two pairs will be different (i.e., either  $I \neq J$  or  $I' \neq J'$ ), so in that case  $\langle n_{\hat{\Omega}_1}^{(i)} n_{\hat{\Omega}_2}^{(j)} \rangle = 0$ . Hence the matrix  $\mathbf{N}$  will be a block diagonal matrix, with diagonal elements  $\mathbf{N}^{(i)} := \langle \mathbf{n}^{(i)} \mathbf{n}^{(i)T} \rangle$  - the covariance matrix of baseline  $i$ .

## Polarization Maps

We may even make skymaps for different polarizations separately by generalizing the definitions of different quantities in the ML analysis. The discrete convolution equation

$$\mathbf{S} = \mathbf{B}_+ \cdot \mathcal{P}_+ + \mathbf{B}_\times \cdot \mathcal{P}_\times + \mathbf{n} \quad (6.44)$$

can also be expressed as eqn (6.41) by substituting

$$\mathbf{B} := \begin{bmatrix} \mathbf{B}_+ & \mathbf{B}_\times \end{bmatrix}; \quad \mathcal{P} := \begin{pmatrix} \mathcal{P}_+ \\ \mathcal{P}_\times \end{pmatrix}. \quad (6.45)$$

### Polarization Maps using a Network of Detectors

Finally, we may combine the previous two generalizations to estimate maps for each polarization separately using multiple baselines. We use the generalized definitions of  $\mathcal{P}$  given in eqn (6.45) containing the two polarization map vectors and signal  $\mathbf{S}$  and noise  $\mathbf{n}$  corresponding to multiple baselines given by eqn (6.42). We then generalize the definition of beam matrix  $\mathbf{B}$  even more by putting

$$\mathbf{B} := \begin{bmatrix} \mathbf{B}_+^{(1)} & \mathbf{B}_\times^{(1)} \\ \mathbf{B}_+^{(2)} & \mathbf{B}_\times^{(2)} \\ \vdots & \vdots \\ \mathbf{B}_+^{(N_b)} & \mathbf{B}_\times^{(N_b)} \end{bmatrix}, \quad (6.46)$$

which now combines the effect of each individual baseline and polarization.

### 6.6.3 Multipole moments from the directed search

The convolution equation:

$$\langle S(\hat{\Omega}) \rangle = \int_{S^2} d\hat{\Omega}' B(\hat{\Omega}, \hat{\Omega}') \mathcal{P}_{\text{true}}(\hat{\Omega}'). \quad (6.47)$$

The angular power distribution can be expanded in terms of spherical harmonics,

$$\mathcal{P}_{\text{true}}(\hat{\Omega}) = \sum_{lm} \mathcal{P}_{lm} Y_{lm}(\hat{\Omega}) \quad (6.48)$$

$$B(\hat{\Omega}, \hat{\Omega}') = \sum_{lm} B_{lm}(\hat{\Omega}) Y_{lm}(\hat{\Omega}'), \quad (6.49)$$

and substituted the above in the convolution equation:

$$\langle S(\hat{\Omega}) \rangle = \sum_{lm} \mathcal{P}_{lm} \int_{S^2} d\hat{\Omega}' B(\hat{\Omega}, \hat{\Omega}') Y_{lm}(\hat{\Omega}') = \sum_{lm} \mathcal{P}_{lm} B_{lm}^*(\hat{\Omega}). \quad (6.50)$$

The spherical harmonic transform of the convolution equation

$$\langle S_{l'm'} \rangle := \int_{S^2} d\hat{\Omega} \langle S(\hat{\Omega}) \rangle Y_{l'm'}^*(\hat{\Omega}) = \sum_{lm} \mathcal{P}_{lm} \int_{S^2} d\hat{\Omega} B_{lm}^*(\hat{\Omega}) Y_{l'm'}^*(\hat{\Omega}) = \sum_{lm} B_{lm}^{l'm'} \mathcal{P}_{lm}. \quad (6.51)$$

where the double spherical harmonic transform of the beam is<sup>3</sup>

$$B_{lm}^{l'm'} := \int_{S^2} d\hat{\Omega} Y_{l'm'}^*(\hat{\Omega}) B_{lm}^*(\hat{\Omega}) := \int_{S^2} d\hat{\Omega} Y_{l'm'}^*(\hat{\Omega}) \int_{S^2} d\hat{\Omega}' Y_{lm}(\hat{\Omega}') B(\hat{\Omega}, \hat{\Omega}'). \quad (6.52)$$

It is always possible to convert an  $lm$  index pair to a single index  $i$  using the transformation formula  $i = l^2 + l + 1 + m$ . So we can write the convolution equation as

$$\langle S_i \rangle = \sum_j B_{ij} \mathcal{P}_j \rightarrow \mathbf{S} = \mathbf{B} \cdot \mathcal{P} + \mathbf{n}, \quad (6.53)$$

where we define

$$S_{lm} \equiv S_{l^2+l+1+m}; \quad B_{lm}^{l'm'} \equiv B_{l^2+l'+1+m', l^2+l+1+m}; \quad \mathcal{P}_{lm} \equiv \mathcal{P}_{l^2+l+1+m}; \quad n_i = \text{noise}. \quad (6.54)$$

Again we have got a linear equation which can be used to obtain the Maximum Likelihood estimate of the multipole moments<sup>4</sup> as:

$$\hat{\mathcal{P}} = \boldsymbol{\Sigma} \mathbf{B}^T \mathbf{N}^{-1} \cdot \mathbf{S}; \quad \boldsymbol{\Sigma}^{-1} := \mathbf{B}^T \mathbf{N}^{-1} \mathbf{B}. \quad (6.55)$$

The difference between this approach and making a deconvolved map first and then calculating the multipole moments is that, this method gives more flexibility to discard terms (like all the higher multipoles!), which is difficult/meaningless in the context of skymap deconvolution in pixel space.

#### 6.6.4 Multipole moments from isotropic all-sky search

The true distribution of GWB power  $\mathcal{P}(\hat{\Omega})$  at different directions  $\hat{\Omega}$  can be decomposed using the standard spherical harmonic expansion

$$\mathcal{P}(\hat{\Omega}) = \sum_{lm} \mathcal{P}_{lm} Y_{lm}(\hat{\Omega}), \quad (6.56)$$

<sup>3</sup>The calculation of the double spherical harmonic  $B_{lm}^{l'm'}$  is rather straightforward and computationally efficient way. It can be expressed as a sum of products of the spherical harmonic transforms of the direction dependent overlap reduction function.

<sup>4</sup>We could also get such an equation from eqn (6.50). But this method seems more practical.

where  $\mathcal{P}_{lm}$  are the angular multipole moments we wish to measure. This problem was previously attacked using different methods [77, 78], but none of them succeeded in estimating all the spherical harmonic moments up to a certain maximum multipole, that is limited by the resolution corresponding to the baseline, using only two or three GW detectors. Here we address the problem by a straight forward extension of the ML analysis. Similar attempt has also been made for making GWB skymaps using a space based GW detector [80, 81, 82].

Consider that the above background was searched using the isotropic search filter - the observed correlation over each chunk  $\Delta S(t)$  is evaluated at all the sidereal time bins with the filter for isotropic search that involves the time independent overlap reduction function  $\gamma_{\text{iso}}(f)$  [eqn (4.92)]. However, the overlap reduction function in the source term  $\gamma_{\mathcal{P}}^{\text{true}}(t, f)$  is still time dependent; it can be expanded as

$$\gamma_{\text{true}}(t, f) = \sum_{lm} \mathcal{P}_{lm} \gamma_{lm}^*(t, f), \quad (6.57)$$

where  $\gamma_{lm}(t, f)$  are the spherical harmonic transforms of the direction dependent overlap reduction function (for a delta function like point source)  $\gamma_{\hat{\Omega}}(t, f)$  [eqn (4.98)]:

$$\gamma_{lm}(t, f) = \int_{S^2} d\hat{\Omega} e^{2\pi i f \hat{\Omega} \cdot \Delta \mathbf{x}(t)/c} \Gamma(\hat{\Omega}, t) Y_{lm}^*(\hat{\Omega}). \quad (6.58)$$

Note that, the numerical computation of  $\gamma_{lm}(t, f)$  for each set of  $l, m, t, f$  is likely to be computationally prohibitive. However, it may be possible to reduce computation cost by evaluating those quantities using a (semi)analytic method [77].

Our aim is to measure (or put upper limit on) the anisotropies of the sky from the isotropic all sky search. *We shall try to exploit the the fact that though the filter is time independent, the observed signal is not because the true sky is anisotropic.*

(Unnormalized) mean of the observed signal over each chunk:

$$\mu_{\Delta S}(t) = \Delta t \int_{-\infty}^{\infty} df H(f) \gamma_{\mathcal{P}}^{\text{true}}(t, f) \tilde{q}(t, f) \quad (6.59)$$

$$= \Delta t \sum_{lm} \mathcal{P}_{lm} \int_{-\infty}^{\infty} df \frac{H^2(f) \gamma_{\text{iso}}^*(f)}{P_1(t; |f|) P_2(t; |f|)} \gamma_{lm}^*(t, f) \quad (6.60)$$

The above equation can be transformed in to an algebraic equation. Using the definition  $\mathcal{P}_{l+l+1+m} \equiv \mathcal{P}_{lm}$  and using discrete index for sidereal time  $t$  we may write

the above equation as

$$\mu_i = \sum_j K_{ij} \mathcal{P}_j, \quad (6.61)$$

where the "kernel"

$$K_{i(l^2+l+1+m)} := \Delta t \int_{-\infty}^{\infty} df \frac{H^2(f) \gamma_{\text{iso}}^*(f)}{P_1(t_i; |f) P_2(t_i; |f)} \gamma_{lm}^*(t_i, f). \quad (6.62)$$

is a known quantity, calculable from the detectors geometries and the time series data from the detectors. Therefore we may write

$$\Delta S_i = \sum_j K_{ij} p_j + n_i \Rightarrow \Delta \mathbf{S} = \mathbf{K} \cdot \mathbf{p} + \mathbf{n}, \quad (6.63)$$

where the noise term can be expressed in terms of the detector noise  $\tilde{n}_{1,2}(t; f)$ :

$$n_i = \Delta t \int_{-\infty}^{\infty} df \tilde{n}_1^*(t_i; f) \tilde{n}_2(t_i; f) \tilde{Q}(t_i, f). \quad (6.64)$$

The Maximum Likelihood estimate for  $\mathbf{p}$  is given by

$$\hat{\mathbf{P}} = (\mathbf{K}^T \mathbf{N}^{-1} \mathbf{K})^{-1} \mathbf{K}^T \mathbf{N}^{-1} \cdot \Delta \mathbf{S}, \quad (6.65)$$

where the noise covariance matrix  $\mathbf{N} := \langle \mathbf{n} \mathbf{n}^T \rangle$ . Since the detector noise at different times are uncorrelated and time bins are much larger than the phase delay between the detector sites, this matrix should be diagonal. The diagonal elements (variance):

$$\sigma_i^2 = \frac{\Delta t}{4} \int_{-\infty}^{\infty} df P_1^*(t_i, f) P_2(t_i, f) |\tilde{Q}(t_i, f)|^2; \quad N_{ij} = \sigma_i^2 \delta_{ij}. \quad (6.66)$$

Covariance matrix for  $\hat{\mathbf{P}}$  is given by

$$\Sigma := \langle (\hat{\mathbf{P}} - \langle \hat{\mathbf{P}} \rangle) (\hat{\mathbf{P}} - \langle \hat{\mathbf{P}} \rangle)^T \rangle = (\mathbf{K}^T \mathbf{N}^{-1} \mathbf{K})^{-1}. \quad (6.67)$$

If the matrix  $\mathbf{K}$  is a square matrix, the estimated solution takes the simple form  $\hat{\mathbf{P}} = \mathbf{K}^{-1} \cdot \Delta \mathbf{S}$ . This can happen if, for example, we use 10 days' data with 60sec time bins and maximum multipole moment up to  $l = 119$ , both would then correspond to a total of  $120^2$  bins. However, we may restrict ourselves to much less number of multipoles and reduce error by solving a over-constrained linear system.

The vector  $\Delta \mathbf{S}$  is calculated for any stochastic search. However, the kernel  $\mathbf{K}$

has to be calculated, which can be computationally expensive. But, we may not want to compute it for every day, rather we may calculate this for each sidereal time bin averaged over all the days. This has to be done with  $\Delta\mathbf{S}$  also. Computationally this will be equivalent of analyzing one day's data, but with reduced error bars at each sidereal time bin.

## 6.7 Summary and Conclusions

The observed CMB and GWB anisotropy maps are convolved with experimental beam functions (point spread functions) and have additive Gaussian noise of zero mean. Deconvolution of these maps is necessary in order to estimate the true skymap. In this chapter we have described the procedure to obtain the maximum likelihood estimate the true skymap.

CMB experiments have very high resolution beams which do not vary with sky position. Our main focus was on modern anisotropy measurement experiments, e.g., WMAP, where the instrument scans the sky and at each time it points to a certain direction. So the output of the instruments is time-ordered-data. The time ordered data is a convolution of the true sky with a mapping matrix, that combines the effect of the beam function and the scanning strategy of the instrument. The noise in the observed time-ordered-data is white Gaussian.

GWB anisotropy sky is mapped using a GW radiometer described in the previous chapter. Unlike CMB, the beam of a directed GW radiometer using the ground based detectors is quite broad and vary with pointing direction. We explained the asymmetric structures of the beam using stationary phase approximation (SPA) - which suggests that those points in the sky contribute the most, whose displacement vector with respect to the pointing direction is normal to the baseline and also the cone traced out by the baseline. We also computed approximate values of the beam function along the trajectory obtained by the SPA analysis. Like CMB, the observed GWB sky is a convolution of the true sky with the beam function and has Gaussian noise of zero mean. However, the noise in different pixels in the observed map are correlated; we have computed the covariance matrix of the observed map.

In general, the observed data for CMB and GWB anisotropy map making can be expressed as a linear convolution equation - the true sky has to be estimated using the known beam function and the known properties of noise from the integral equation, or, in practice, the algebraic equation as the sky is pixelized. We briefly outline the analysis used for CMB anisotropy map making to obtain the maximum like-

likelihood estimate of skymaps. This analysis have been developed and successfully implemented for more than a decade in CMB analysis. Therefore, we considered this scheme to be quite robust and so, among several alternatives, we chose the maximum likelihood method for the estimation of the true GWB skymaps. The formal mathematics for GWB anisotropy analysis has been developed in this chapter. We also have extended the basic analysis to consider more complex problems of making separate skymap for each polarization, estimating multipole moments and using a network of detectors for better estimation. The numerical implementation of this analysis to estimate the GWB skymap is presented in the next chapter.

Though the analysis was developed for CMB map making long back, it is no longer applicable with full generality for CMB map making due to the very high resolution of modern CMB anisotropy experiments. To overcome computational difficulty, the time-ordered-data from modern CMB experiments, e.g., WMAP, is deconvolved assuming a circularly symmetric beam of infinite resolution, which introduces a bias in the estimated map and power spectrum. Attempts are being made by different groups to deconvolve the time-ordered-data using the true asymmetric beam pattern. In chapter 8 and chapter 9 we present a sub-optimal approach to correct the pseudo- $C_l$  CMB power spectrum estimator from beam asymmetry and the comparison of our predicted bias with the bias correction introduced in the recently released WMAP third year results.

## Chapter 7

# Numerical Implementation of ML Mapmaking for GWB

We have implemented the maximum likelihood estimation algorithm discussed in the previous chapter to estimate the ‘true’ GWB background sky observed with a single baseline ground based directed GW radiometer. The details of the numerical deconvolution algorithm, the simulated data and the results for simulated data are presented in this chapter. The algorithm has been implemented using the MATLAB® software package [121].

The observed map over a pixelized sky using a directed GW radiometer is a convolution of the known beam matrix and contains Gaussian noise of known statistical properties. Here we only consider a background with equal power in both polarizations. We call the observed map a “dirty map” in analogy to the nomenclature used in radio-astronomy. Following CMB analysis, we use maximum likelihood (ML) techniques to estimate the ‘true’ skymap - the “clean” map. The main computation challenges were to numerically evaluate the beam matrix and finding an estimate without introducing severe numerical errors. The details of these problems and their primary remedies have been presented in this chapter.

The method has been tested using simulated data. Detector noise is generated in the frequency domain using a Gaussian pseudo random number generator and colored with LIGO-I PSD. Modeled signal is also generated in the frequency domain and injected in the simulated noise. Dirty maps were made using the directed radiometer analysis for different types of injections - isolated point sources and diffuse backgrounds. The recovered clean maps are similar to the injected GWB backgrounds, which is a great success of this project.

The chapter is organized as follows: We first outline the generation of simulated detector output in section 7.1. The raw skymaps are then produced from the simulated data using the directed GW radiometer in section 7.2. The numerical scheme to evaluate the computationally intensive beam function is outlined in section 7.3. The strategy to estimate the true maps, the clean maps, from the dirty maps obtained from simulated data and a brief discussion on the conjugate gradient method used for deconvolution are presented in section 7.4. The numerical results and comparison between the injected and recovered maps are presented in section 7.5.

## 7.1 Preparation of Simulated Data

The data is simulated in the frequency domain for each chunk. Since the noise of ground based interferometric detectors is very high at frequencies higher than few 100 Hz and the computation cost increases with the number of frequency bins, we use an upper cut-off frequency of  $f_u = 512$  Hz and bin width of  $\Delta f = 2$  Hz for testing of the algorithm. The size of each chunk is chosen as  $\Delta t = 192$  sec and the total integration time is  $T = 86400$  sec. The sky is pixelized using the Hierarchical Equal Area isoLatitude Pixelization (HEALPix) [122] scheme, which divides the 2-sphere ( $S^2$ ) in  $12 n_{\text{side}}^2$  pixels, where  $n_{\text{side}}$  is an integer power of 2. Since the radiometer beam width is greater than  $\sim 6^\circ$ , we chose  $n_{\text{side}} = 16$ , which corresponds to a pixel width of  $\sim 3^\circ$  and a total of 3072 pixels. The HEALPix scheme also allows fast spherical harmonic transform on a sphere, which may become useful for more advanced analysis in future. Note that, the algorithm is *independent* of the pixelization scheme, other equal area pixelization schemes can also be used in the analysis.

- **Noise Generation:**

We generate the detector noise  $\tilde{n}_I(t; f)$  using a Gaussian pseudo random number generator for each chunk. The noise is colored using the (one sided) noise PSD  $P_I(t; f)$  of the corresponding detector according to the following formula [eqn (4.63)]

$$\langle |\tilde{n}_I(t; f)|^2 \rangle = \frac{1}{2} \Delta t P_I(t; |f|). \quad (7.1)$$

MATLAB® software's pseudo random number generator can generate very long sequences of random numbers, so we relied on the MATLAB® in-built function `randn` for simulating detector noise. For each of  $T/\Delta t = 86400/192 = 450$  chunks we generated a complex random sequence (that

is, two real random sequences) of  $f_u/\Delta f = 512/2 = 256$  real numbers. The total number of random numbers,  $2(T/\Delta t)(f_u/\Delta f) = 225,000$ , is much less than the period of the MATLAB® software's pseudo random number generator  $2^{1492} \gtrsim 10^{449}$  [123].

- **Signal injection:**

Signal is also generated directly in the frequency domain. However, the GW strain in each detector,  $\tilde{h}_1(t; f)$ , is not generated independently; rather the product of the strains in the detectors,  $\tilde{h}_1^*(t; f)\tilde{h}_2(t; f)$ , is generated directly using the statistical properties of the strain correlation described in subsection 4.3.2. From eqn (4.56) we know that the expected correlation between the detector strains due to a GWB sky described by  $\mathcal{P}^A(\hat{\Omega})$  may be expressed as

$$\langle \tilde{h}_1^*(t, f)\tilde{h}_2(t, f) \rangle = \Delta t H(f) \gamma_{\mathcal{P}^A}(t, f). \quad (7.2)$$

For all the cases considered in this thesis we have used flat source PSDs, i.e.,  $H(f) = \text{constant}$ . We may write the above product of the strains as a sum of its expectation value and statistical fluctuations:

$$\tilde{h}_1^*(t, f)\tilde{h}_2(t, f) = \langle \tilde{h}_1^*(t, f)\tilde{h}_2(t, f) \rangle + \text{fluctuations}. \quad (7.3)$$

Since our main aim is to generate  $\tilde{s}_1^*(t, f)\tilde{s}_2(t, f) = [\tilde{h}_1^*(t, f) + \tilde{n}_1^*(t, f)] \times [\tilde{h}_2(t, f) + \tilde{n}_2(t, f)]$  and since statistically the signal terms are much weaker than the *zero mean uncorrelated* detector noise terms, we may simply drop the signal “fluctuations” term from the signals - that is, we may approximate the product of the detector outputs using the formula<sup>1</sup>

$$\tilde{s}_1^*(t, f)\tilde{s}_2(t, f) = \langle \tilde{h}_1^*(t, f)\tilde{h}_2(t, f) \rangle + \tilde{n}_1^*(t, f)\tilde{n}_2(t, f). \quad (7.4)$$

In this analysis we assume the sky to be a collection of *uncorrelated point sources* of different strengths placed at every pixel. Moreover, the numerical analysis has been restricted to the case of equal power in each polarization. So the

---

<sup>1</sup>Note that, it is also possible to generate the correlated detector strains  $h_i(t)$  independently and construct  $\tilde{s}_i(t; f) = \tilde{h}_i(t; f) + \tilde{n}_i(t; f)$  for each detector separately using simulated colored noise  $\tilde{n}_i(t; f)$  to test the analysis. However, we chose the above method in order to reduce complications in the primary testing of the analysis presented in this thesis.

(injected) true sky is constructed by putting [eqn (6.22)]

$$\mathcal{P}_{\text{true}}(\hat{\Omega}) = \sum_k \mathcal{P}_k \delta(\hat{\Omega} - \hat{\Omega}_k), \quad (7.5)$$

where  $\mathcal{P}_k$  is the strength of the point source placed at pixel  $k$ , located in the direction  $\hat{\Omega}_k$  [In order to inject only one point source at pixel  $k_0$ , we make all the  $\mathcal{P}_k = 0$  except for  $k = k_0$ ]. In that case the expression for the overlap reduction function [eqn (4.98)] for the true GWB strain becomes

$$\gamma_{\mathcal{P}A}(t, f) = \sum_k \Gamma(\hat{\Omega}_k, t) \mathcal{P}_k e^{2\pi i f \hat{\Omega}_k \cdot \Delta \mathbf{x}(t)/c}, \quad (7.6)$$

where we use our usual notation [eqn (6.8)]

$$\Gamma(\hat{\Omega}, t) := F_1^+(\hat{\Omega}, t) F_2^+(\hat{\Omega}, t) + F_1^\times(\hat{\Omega}, t) F_2^\times(\hat{\Omega}, t). \quad (7.7)$$

We then substitute the above in eqn (7.2) and inject that simulated signal in noise using eqn (7.4) to generate products of outputs from two detectors. In order to preserve the reality of time series data, the products of signals are generated only for positive frequencies and setting the negative frequencies equal to the complex conjugates of their positive frequency counterparts, that is,  $\tilde{s}_I(t, -f) = \tilde{s}_I^*(t, f)$ .

## 7.2 Preparation of the “Dirty” Maps

The radiometer analysis is run on the simulated data to generate the raw maps - also known as the “dirty maps” in radio astronomy. It is clear from the previous two chapters that one needs to construct filters for each direction as a function of sidereal time (midpoint of each chunk) and frequency. Then the cross-correlation statistic should be computed including the filter to generate the dirty map.

The optimal filter to measure the point estimate at pixel  $k$  is the usual weighted direction dependent overlap reduction function

$$q_{\hat{\Omega}_k}(t, f) = \frac{H(f)}{P_1(t; f) P_2(t; f)} \Gamma(\hat{\Omega}_k, t) e^{2\pi i f \hat{\Omega}_k \cdot \Delta \mathbf{x}(t)/c}. \quad (7.8)$$

The details of computation of  $\Delta \mathbf{x}(t)$  and  $\Gamma(\hat{\Omega}, t)$  using Euler rotation follow from the analytical details provided in chapter 4. This filter is applied to the simulated

time-frequency cross-correlation matrix  $\widetilde{s}_1^*(t, f)\widetilde{s}_2(t, f)$  to generate the dirty map  $\mathbf{S}$ . Following eqn (4.81) and introducing finite frequency band we may write

$$S_k = 2 \left[ \Delta t \sum_{i=1}^n \|q_{\Omega_k}\|_{t_i}^2 \right]^{-1} \sum_{i=1}^n \Re \left[ \int_{f_l}^{f_u} df \widetilde{s}_1^*(t_i; f) \widetilde{s}_2(t_i; f) \widetilde{q}_{\Omega_k}(t_i, f) \right]. \quad (7.9)$$

The real part is taken from the above integral to take computational advantage of the fact that the negative frequency components are the complex conjugates of the positive frequency parts. As mentioned before, this was taken into account while simulating the detector outputs in order to preserve the reality of time series data.

The dirty maps obtained by the above analysis for different injections will be provided in the results section. The whole procedure to make dirty maps is carried out in a computationally efficient way. For clarity, the details are not presented in this section, they will be presented in the section on computation of the beam matrix, where the computation strategy plays a much more important role.

### 7.3 Computation of the Beam Matrix

The most computationally intensive part of this analysis is to numerically evaluate the beam matrix. Computation of the beam matrix is equivalent of making one dirty map for each pixel by placing a unit point source at that pixel - each row of the beam matrix describes the response function of the GW radiometer for the pointing pixel that corresponds to the row index and each column is the PSF for the direction that corresponds to the column index. We have to evaluate the dirty map for each<sup>2</sup> pixel because the radiometer beam pattern varies with pointing direction. Since we use 3072 pixels, it is equivalent of making 3072 skymaps. However, with smart application of algebra and pre-computation, we could achieve this using reasonably less computation. The details are given below.

The beam matrix  $\mathbf{B} \equiv B_{kk'}$  can be computed using the following expression

---

<sup>2</sup>If one assumes stationary noise and the observation is taken over complete days, the beam function becomes independent of pointing longitude. In that case one can make one map for each set of isoLatitude pixels, thus reducing the computation cost significantly. Though we have simulated stationary noise and used an observation time of one full day, this assumption was not used in our analysis, because testing the numerical tractability of this problem for practical applications (where these assumptions do not apply) was one of the major goals of this project.

[eqn (6.12)]

$$B_{kk'} = 2 \left[ \Delta t \sum_{i=1}^n \|q_{\hat{\Omega}_k}\|_{t_i}^2 \right]^{-1} \Delta t \sum_{i=1}^n \Re \left[ \Delta f \sum_{j=1}^{n_f} G(t_i; f_j) \Gamma(\hat{\Omega}_k, t_i) \Gamma(\hat{\Omega}_{k'}, t_i) e^{-2\pi i f_j \frac{\Delta \Omega_{kk'} \cdot \Delta \mathbf{x}(t_i)}{c}} \right], \quad (7.10)$$

where the  $n_f$  frequency bins marked by  $f_j$  cover the range  $f = f_l$  to  $f = f_u$  and, as before [eqn (6.9)], we have packed all the source and detector noise PSDs in a single function  $G(t; f) := H^2(f)/[P_1(t; |f|)P_2(t; |f|)]$ .

The key to fast computation is the structure of the quantities contained in the expression for beam. All the component in the expression are dependent on any one or two variables out of the three - direction, time and frequency. This gives us the freedom to pre-compute those quantities in advance and keep them loaded in the memory. Loading these two indexed object in memory is possible with realistic memory sizes of modern computers, while three indexed arrays would be too large. For example, we use  $N_{\text{pix}} = 3072$  pixels,  $n = 450$  sidereal time chunks and  $n_f = 256$  frequency bins. This means a three indexed double precision complex array would require  $16N_{\text{pix}}nn_f \approx 5$  GigaBytes of memory space, while any two indexed object in the expression for the beam matrix requires at most  $8N_{\text{pix}}n \approx 10$  MegaBytes of memory space. Based on this observation we plan the computation of the beam matrix as follows:

1. Pre-compute arrays (in the following order)

$$G_{ij} := G(t_i; f_j) \quad (7.11a)$$

$$\mathbf{R}_i := \mathbf{R}(-\omega_E t_i) \quad [3 \times 3 \text{ Euler-z matrices}] \quad (7.11b)$$

$$\Delta \mathbf{x}_i := \Delta \mathbf{x}(t_i) \quad (7.11c)$$

$$\Gamma_{ki} := \Gamma(\hat{\Omega}_k, t_i) \quad (7.11d)$$

$$\sigma_k := \left[ \Delta t \sum_{i=1}^n \|q_{\hat{\Omega}_k}\|_{t_i}^2 \right]^{-1/2} \quad (7.11e)$$

2. Combine the arrays

$$\mathbf{b}_{kk'} := \sum_{i=1}^n \Gamma_{ki} \Gamma_{k'i} \sum_{j=1}^{n_f} G_{ij} \cos[2\pi f_j (\hat{\Omega}_k - \hat{\Omega}_{k'}) \cdot \Delta \mathbf{x}_i / c] \quad (7.12a)$$

$$B_{kk'} = 2 \Delta t \Delta f \sigma_k^2 \mathbf{b}_{kk'} \quad (7.12b)$$

The introduction of  $\mathbf{b} \equiv b_{kk'}$  reduces the computation cost by a factor of  $\sim 2$ , as it is a symmetric matrix. Clearly the computation of  $b_{kk'}$  is very similar to evaluating the product of two matrices with one additional cosine call ( $\cos[2\pi f_j(\hat{\Omega}_k - \hat{\Omega}_{k'}) \cdot \Delta \mathbf{x}_i/c]$ ) for each pair of elements. Essentially the cosine operation consumes most of the computation, but we can neither pre-compute it as it is a three indexed object<sup>3</sup>.

The above analysis was implemented using the MATLAB® software package [121]. Utilizing the simplicity and efficiency of vectorized notations of MATLAB®, it was possible to compute the beam matrix in just 18 hours on a 2.2 GHz AMD Opteron™ processor [124]. Similar approach was also used to make the dirty maps efficiently from the (simulated) detector outputs using the radiometer analysis.

A typical beam matrix for the LIGO baseline using 192 HEALPix pixels is shown in figure 7.1. By construction  $B_{kk} = 1$  and  $B_{kk'} < 1$  for  $k \neq k'$ , hence the matrix is diagonal dominated. The “stripes” in the matrix are related to the pixelization scheme. The beam is stronger if the sources are closer to the pointing direction and it weakens as the distance between the source and pointing direction increases. So the pixels closer to a point source will have stronger contamination from the point source. However, since we have used a isoLatitude pixelization scheme, the indices of two neighboring pixels at different latitudes differ by the total number of pixels on that latitude. This fact is reflected on the plot of the beam matrix - the matrix is sparse with certain “periodic” behavior that causes the stripes in the plot. The matrix becomes even more sparse for finer resolutions as greater number of isoLatitude pixel rings pass through the core of the beam. Making a legible plot of the beam matrix for higher resolution is difficult, so the plot presented here is of lower resolution, 192 pixels instead of 3072.

Since the sparsity of the beam matrix depends on the pixelization scheme, it may be possible to make the beam matrix significantly diagonal by using a nested pixelization scheme, where the indices of the neighboring pixels are close. This possibility is being explored.

---

<sup>3</sup>It may be possible to use FFT+interpolation [79] techniques to reduce the computation cost of the cosine term also. This possibility has not been explored in this thesis, as the computational requirement for the parameters used here was far below the computing power available to us after the introduction of an appropriate efficient strategy.

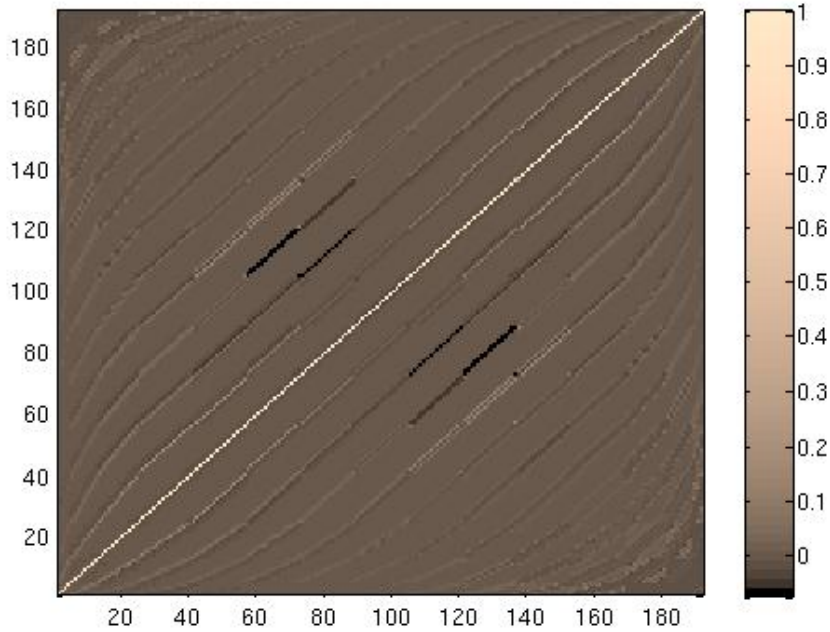


Figure 7.1: **A typical GW radiometer Beam Matrix.** Beam matrix for the LIGO baseline at a low resolution (192 pixels) has been shown. Each row of the matrix is the beam response function for the pointing direction that corresponds to the row index. The matrix is diagonal dominated as the instrument receives maximum contribution from the pointing direction. The stripes are related to the isoLatitude pixelization scheme - the indices of the neighboring pixels at different latitudes differ by the total number of pixels on that latitude. It should be noted that the possibility of reducing the sparsity of the beam matrix using a nested pixelization scheme, where the indices of the neighboring pixels are close, is being explored.

## 7.4 Deconvolution: The “Clean” Maps

The mathematical formulation to estimate the true GWB sky was developed in section 6.6. The numerical implementation scheme is presented in this section.

The Maximum Likelihood (ML estimate of the true GWB sky for a single baseline (two detectors), where the beam matrix  $\mathbf{B}$  is a square matrix, is given by eqn (6.38)

$$\hat{\mathcal{P}} = \mathbf{B}^{-1} \cdot \mathbf{S}. \quad (7.13)$$

As mentioned before, the beam matrix is a sparse matrix. Sparse matrices are easier to invert as far computational cost is concerned, however, the stability of inversion

of a sparse matrix is a numerical challenge. Therefore, we choose to solve the set of linear equations with the same number of unknowns as the number of equations (that is, the system is *not* under/over constrained)

$$\mathbf{B} \cdot \hat{\mathcal{P}} = \mathbf{S}. \quad (7.14)$$

Using the definitions used in eqn (7.12) and eqn (7.11) the kernel in the above equation can be made symmetric, which is a requirement for many linear equation solving algorithms. Thus, we may write

$$\mathbf{b} \cdot \hat{\mathcal{P}} = \mathbf{s}, \quad (7.15)$$

where

$$s_k := S_k / \sigma_k^2 = 2 \sum_{i=1}^n \Re \left[ \int_{f_l}^{f_u} df \bar{s}_1^*(t_i; f) \bar{s}_2(t_i; f) \bar{q}_{\hat{\Omega}_k}(t_i, f) \right]. \quad (7.16)$$

There are several algorithms to solve this type of linear algebraic equation. We, again, choose the method which is routinely used in CMB analysis for making skymaps - we use a Conjugate Gradient (CG) method to solve the above equation.

### Conjugate Gradient method for sparse linear systems

**Goal:** Conjugate Gradient method is used to solve sparse linear systems of the form

$$\mathbf{A} \cdot \mathbf{x} = \mathbf{b}, \quad (7.17)$$

where the matrix  $\mathbf{A}$  and the vector  $\mathbf{b}$  are known. The basic conjugate gradient method, that requires  $\mathbf{A}$  to be symmetric and positive definite, is outlined below.

**Exact Solution:** Since  $\mathbf{A}$  is positive definite, it is possible to define inner products of two vectors  $\mathbf{u}$  and  $\mathbf{v}$  in the vector space as

$$(\mathbf{u}, \mathbf{v})_{\mathbf{A}} := \mathbf{u} \cdot \mathbf{A} \cdot \mathbf{v}. \quad (7.18)$$

We call two vectors  $\mathbf{u}$  and  $\mathbf{v}$  to be  $\mathbf{A}$ -conjugate to each other if  $(\mathbf{u}, \mathbf{v})_{\mathbf{A}} = 0$ . In an  $N$  dimensional vector space, it is always possible to find  $N$  mutually  $\mathbf{A}$ -conjugate vectors  $\{\mathbf{p}^i\}$ ,  $i = 1, 2, \dots, N$ , such that  $(\mathbf{p}^i, \mathbf{p}^j)_{\mathbf{A}} = \delta_{ij} (\mathbf{p}^i, \mathbf{p}^i)_{\mathbf{A}}$ , which can be used as a basis set for the vector space.

Let  $\mathbf{x}^*$  be the exact solution of the linear equation. Then we can always

expand it in terms of the basis vectors using the components  $\alpha_i$  as

$$\mathbf{x}^* = \sum_{i=1}^N \alpha_i \mathbf{p}^i, \quad (7.19)$$

Substituting the above in the linear equation, taking “dot” products of both sides by  $\mathbf{p}^k$  and using the fact that  $(\mathbf{p}^i, \mathbf{p}^j)_A = \delta_{ij} (\mathbf{p}^i, \mathbf{p}^i)_A$  we may write

$$\mathbf{x}^* = \sum_{i=1}^N \frac{(\mathbf{p}^i \cdot \mathbf{b})}{(\mathbf{p}^i \cdot \mathbf{A} \cdot \mathbf{p}^i)} \mathbf{p}^i. \quad (7.20)$$

**Iterative Solution:** In practice, however, we need not use all the basis vectors to reach to the solution. If we choose the first few basis vectors correctly, the truncated series can provide a good approximate solution.

The main principle of the iterative scheme follows from fact that the solution of the linear equation  $\mathbf{A} \cdot \mathbf{x} = \mathbf{b}$  minimizes the function

$$f(\mathbf{x}) := \frac{1}{2} \mathbf{x} \cdot \mathbf{A} \cdot \mathbf{x} - \mathbf{b} \cdot \mathbf{x}. \quad (7.21)$$

So the aim is to reach to the minimum of the function  $f(\mathbf{x})$ ; an iterative technique (*gradient descent* method) is used to do that in the Conjugate Gradient scheme: At every iteration  $i$  an approximate solution  $\mathbf{x}_{i+1}$  is obtained by adding a correction vector  $\alpha_i \mathbf{p}_i$  to the approximate solution vector  $\mathbf{x}_i$  obtained after the previous iteration. The correction vector is *conjugate* to all the basis vectors  $\{\mathbf{p}_j\}, j = 1, 2, \dots, i$  obtained in the previous iterations and closest to the (negative) *gradient* of the function  $f(\mathbf{x})$  obtained after the previous iteration. Ideally, after  $N$  iterations, the exact solution is reached, but, in practice, lesser number of iterations are used. The residual after iteration  $i$  is

$$\mathbf{r}_i := \mathbf{b} - \mathbf{A} \cdot \mathbf{x}_i \equiv -\nabla f(\mathbf{x}_i). \quad (7.22)$$

The basis vector  $\mathbf{p}_{i+1}$  is chosen close to the residual  $\mathbf{r}_i$ , but it should be conjugate to all the previous basis vectors. It can be done by choosing

$$\mathbf{p}_{i+1} = \mathbf{r}_i - \frac{(\mathbf{r}_i, \mathbf{p}_i)_A}{(\mathbf{p}_i, \mathbf{p}_i)_A} \mathbf{p}_i. \quad (7.23)$$

The detailed algorithm can be found in, e.g., Numerical Recipes [125].

Different conjugate gradient methods can be used depending on the characteristics of the beam matrix. We use the *minimum residual* method, which efficiently utilizes the fact that  $\mathbf{b}$  is symmetric and does not require  $\mathbf{b}$  to be positive definite. The minimum residual method aims to minimize the residual  $|\mathbf{A} \cdot \mathbf{x} - \mathbf{b}|^2$  itself, instead of the quadratic form  $(1/2)\mathbf{x} \cdot \mathbf{A} \cdot \mathbf{x} - \mathbf{b} \cdot \mathbf{x}$ .

## 7.5 Results and Comparisons

The analysis was tested for different kinds of injected maps consisting of localized sources and diffuse sources. The results can be summarized using a series of figures showing different injected, dirty and clean maps as in figure 7.2. The left panels of figure 7.2 show the injected maps. The simulated data is prepared following the procedure described in section 7.1: The true GW strains in the LIGO detectors due to a given skymap are computed in the frequency domain, which is then injected into simulated Gaussian noise colored with LIGO-I PSD. The middle panels of figure 7.2 show the dirty maps obtained by applying the directed GW radiometer analysis on simulated data of one complete day. The right panels show the clean maps obtained from the dirty maps after deconvolving with the beam function for the two LIGO detectors for observation time of one full day. The deconvolution is done using the minimum residual conjugate gradient iterative technique.

Four sets of GWB maps have been shown in figure 7.2, which correspond to the following cases:

- Figure 7.2a: A 1-pixel point source near the virgo cluster
- Figure 7.2b: A 4-pixel wide source near the Virgo cluster
- Figure 7.2c: A map similar to the CMB temperature anisotropy map in galactic coordinates<sup>4</sup> measured by the WMAP satellite [96]
- Figure 7.2d: A map similar to the CMB temperature anisotropy map in barycentric coordinates generated by the Planck simulator [126]

In all the above cases each pixel of the test map is assigned a positive value between 0 to 10 with a source PSD  $H(f) = 5 \times 10^{-47}/\text{Hz}$ . Which means that, if a

<sup>4</sup>Note that, CMB maps look different, more like Figure 7.2d, in barycentric coordinates. We intentionally omit the coordinate transformation in order to get a toy equatorial diffuse source.

pixel of a test map has strength 1, the standard deviation of the Fourier transform of stochastic GW coming from that pixel is  $\sqrt{H(f)} \sim 7 \times 10^{-24} / \sqrt{\text{Hz}}$ . This standard deviation is about one third of the standard deviation of Fourier transform of noise at the most sensitive frequency band of the LIGO-I detectors which is about  $2 - 3 \times 10^{-23} / \sqrt{\text{Hz}}$ . Though the signal level is quite below the noise level, we can still detect the signal by coherently correlating outputs from the detectors for long time, which is one full day in our case. This is particularly impressive, since we are not using matched filtering usually employed to pull out a known signal buried in noise.

- **Localized sources:** Figure 7.2a and figure 7.2b have been considered as the test cases for the detection of highly localized point sources. The Virgo cluster is expected to be a strong localized source of stochastic GWB and is definitely a primary target for the targeted search. This was the reason for choosing the position of the localized sources near the virgo cluster. The dirty maps, understandably, show a broad pattern similar to the point spread function, in excess of noise, for the localized (point like) sources.

These maps were deconvolved using 20 iterations of the minimum residual algorithm. Clearly, deconvolution has accumulated power within few pixels. However, it can be seen from the figures that the recovered peak value at the injection point is considerably less than the injected value. This is possibly caused due to the inability of numerical routines to converge to a point like solution (a point source in this case). This statement can be supported by the following observation: The performance of deconvolution for a broader source in figure 7.2b is better as compared to a more pointed source in figure 7.2a. In fact, an increase in the number of iterations introduce more numerical noise than any improvement in the peak values of the clean maps for a localized source.

- **Diffuse sources:** Figure 7.2c and figure 7.2d have been used to demonstrate the cases of diffuse background (without any angular correlation). The galactic white dwarf binaries and the cosmological GWB fall in this category (of course, the cosmic GWB will additionally have angular correlations, which we have neglected in this preliminary exploratory analysis. So, we injected skymaps similar to the CMB temperature anisotropy maps with the galactic background in galactic and barycentric coordinates as toy sources. The dirty maps lose most of the detailed structures present in the injected maps. The dirty map

can even get severely distorted and provide an incorrect impression of the true map. For example, in figure 7.2c, there is no obvious similarity between the injected map and the dirty map and in figure 7.2d the dirty map takes nearly equal positive and negative peak values.

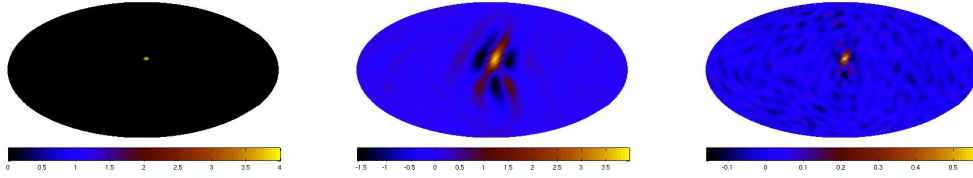
The clean maps were recovered by deconvolution using 300 iterations. Deconvolution clearly brings out almost all the structures originally present in the injected maps. The positivity of the estimated map is also vastly restored - most of the pixels in the clean map have large positive values as compared to the absolute values of the negative ones. Moreover, unlike the case of localized sources, the clean maps for diffuse background are recovered with almost similar pixel amplitude as that of the injected maps.

Although the exact quantification of the quality of deconvolution is still to be formulated, the overall performance of this first attempt to estimate simulated GWB skymaps has produced promising results and the necessity to deconvolve the dirty maps is well established.

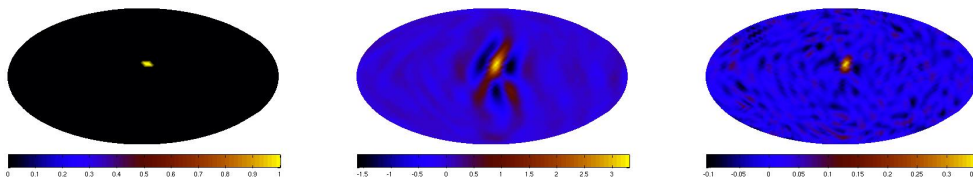
## 7.6 Summary and Conclusion

In this chapter we have numerically implemented the analytical deconvolution scheme developed in the previous chapter. A key numerical challenge was to evaluate the beam matrix using reasonable amount of computation and to obtain a clean map without introducing severe numerical errors. To accomplish these challenges, we respectively used smart pre-computation techniques and a conjugate gradient method used in the CMB analysis. This was the **first ever attempt** to estimate the true GWB skymap using the data from the recent ground based interferometric GW detectors and the success is quite remarkable - we got back nearly what we injected.

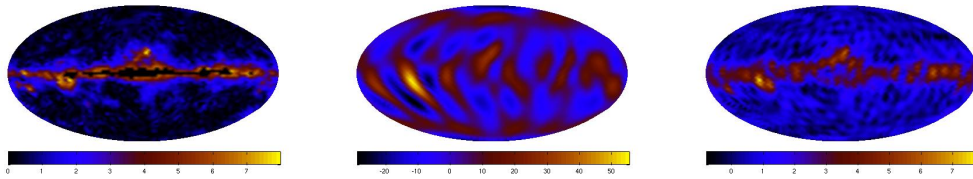
However, since this is a primary attempt, this method has scope for improvements on many fronts. Firstly, we have compared the maps just visually, a method to quantify the quality of deconvolution is necessary. To get that one needs the inverse of the beam matrix for obtaining the pixel-to-pixel noise covariance matrix of the clean map, which is a difficult task. We are currently working on it. Secondly, the ML approach used here closely follows the CMB analysis. A more customized deconvolution strategy would provide better results. Several other modifications and checks are needed before this method could finally be used for putting upper limits on the *true* stochastic GWB with enough confidence.



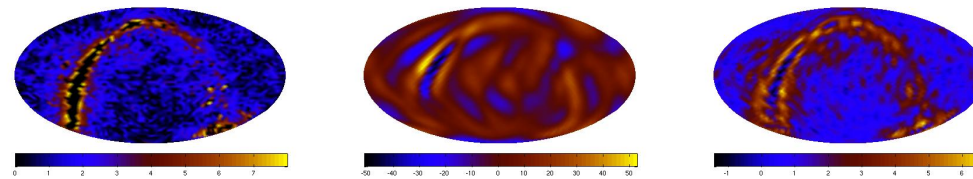
(a) A 1-pixel point source is injected near the Virgo cluster



(b) A 4-pixel broad source was injected near the Virgo cluster



(c) A map similar to the CMB temperature anisotropy map measured by the WMAP satellite [96], as seen in the Galactic coordinates, is injected as a test equatorial diffuse GWB map



(d) A modified form of the CMB temperature anisotropy map generated by the Planck simulator [126] in the barycentric coordinate is used as a toy all sky GWB map

**Figure 7.2: Deconvolved (simulated) GWB skymaps.** The four sets of images above compare the results of deconvolution of the GWB skymaps. The left panels show the maps injected to simulate strains in the LIGO Hanford and Livingston detectors with LIGO-I noise, the middle panels show the raw “dirty” maps obtained by the directed radiometer analysis and the right panels show the deconvolved “clean” maps. In each case the minimum residual Conjugate Gradient method was used for the maximum likelihood estimation with number of iterations 20 for (a) and (b) and 300 for (c) and (d). The similarity between the left and right panels illustrate the success of this first ever attempt to estimate the true GWB sky using the recent ground based GW detectors. Note that the above scales are different for the injected, dirty and clean maps.

## Chapter 8

# Non-circular Beam Correction to CMB Power Spectrum: Perturbative Analysis

A golden decade of measurements of the Cosmic Microwave Background (CMB) anisotropy has ushered in an era of precision cosmology. The theory of primary CMB anisotropy is well developed and the past decade has seen a veritable flood of data [127, 128, 129]. The measurements of the angular power spectrum of the CMB anisotropy has proved crucial to the emergence of cosmology as a precision science in recent years. In this remarkable data rich period, the limitations to precision now arise from the the inability to account for finer systematic effects in data analysis. The non-circularity of the experimental beam has become progressively important as CMB experiments strive to attain higher angular resolution and sensitivity. The optimal solution to remove this systematic effect from CMB measurements is to deconvolve the anisotropy maps accounting for the non-circularity of the beam function (as outlined in the previous chapter for the gravitational wave background skymaps). Unfortunately the full maximum likelihood estimation of a high resolution CMB map is computationally prohibitive. The CMB anisotropy maps from the high resolution instruments, like WMAP, are deconvolved assuming circularly symmetric beams of infinite resolution [96], which introduces a bias in the CMB power spectrum estimated from those maps. We have developed an analytic framework for studying the effects of a non-circular beam on the CMB power spectrum estimation [118, 130]. First we use a perturbative analysis to find the leading order correction, which will be presented in this chapter. Next, we derive a general

analytic framework to find the bias on CMB power spectrum due to the non-circular beams, where we include the effect of incomplete sky coverage in analytical calculations that was considered only numerically in the perturbative analysis. This will be presented in the chapter 9. In both the cases we consider a mildly non-circular beam, that allows us to perform a perturbative analysis and the first few orders are sufficient to account for the beam non-circularity effect for most of the recent experiments. We compute the bias in the pseudo- $C_l$  power spectrum estimator and then construct an unbiased estimator using the bias matrix. The covariance matrix of the unbiased estimator is computed for smooth, non-circular beams. Quantitative results are shown for CMB maps made by a *hypothetical* experiment with a non-circular beam comparable to our fits to the WMAP beam maps described in appendix D and uses a *toy* scan strategy. We find that significant effects on CMB power spectrum can arise due to non-circular beam on multipoles comparable to, and beyond, the inverse average beam-width where the pseudo- $C_l$  approach may be the method of choice due to computational limitations of analyzing the large datasets from current and near future CMB experiments. Recently WMAP team have corrected for the non-circular beam effect in their 3 year results. The estimated effect is in good agreement with the prediction of our method for a WMAP-like beam.

## 8.1 Pseudo- $C_l$ Approach to Non-circular Beam Correction

Increasingly sensitive, high resolution, ‘full’ sky measurements from space missions, such as, the ongoing Wilkinson Microwave Anisotropy Probe (WMAP) and, the upcoming Planck surveyor pose a stiff challenge for current analysis techniques to realize the full potential of precise determination of cosmological parameters. As experiments improve in sensitivity, the inadequacy in modeling the observational reality start to limit the returns from these experiments.

A Gaussian model of CMB anisotropy  $\Delta T(\hat{\mathbf{q}})$  is completely specified by its angular two-point correlation function. In standard cosmology, CMB anisotropy is expected to be statistically isotropic. In spherical harmonic space, where  $\Delta T(\hat{\mathbf{q}}) = \sum_{lm} a_{lm} Y_{lm}(\hat{\mathbf{q}})$ , this translates to a diagonal  $\langle a_{lm} a_{l'm'}^* \rangle = C_l \delta_{ll'} \delta_{mm'}$  where  $C_l$ , the widely used angular power spectrum of CMB anisotropy, carries a complete description of a Gaussian CMB anisotropy. Observationally, the angular power spectrum being a simple, robust point statistics is the obvious first target for cosmological observations. Theoretically, the  $C_l$  are deemed all important since the simplest inflation

models predict a Gaussian CMB anisotropy. In this case, the power spectrum provides an economical description of the CMB anisotropy allowing easy comparison to observations.

Accurate estimation of  $C_l$  is arguably the foremost concern of most CMB experiments. The extensive literature on this topic has been summarized in a recent article [131]. For Gaussian, statistically isotropic CMB sky, the  $C_l$  that correspond to covariance that maximize the multivariate Gaussian PDF of the temperature map,  $\Delta T(\hat{\mathbf{q}})$  is the Maximum Likelihood (ML) solution. Different ML estimators have been proposed and implemented on CMB data of small and modest size [132, 133, 134, 135, 136, 137]. While it is desirable to use optimal estimators of  $C_l$  that obtain (or iterate toward) the ML solution for the given data, these methods usually are limited by the computational expense of matrix inversion that scales as  $N_d^3$  with data size  $N_d$  [138, 139, 140]. Various strategies for speeding up ML estimation have been proposed, such as, exploiting the symmetries of the scan strategy [141], using hierarchical decomposition [142], iterative multi-grid method [143], etc. Variants employing linear combinations of  $\Delta T(\hat{\mathbf{q}})$  such as  $a_{lm}$  on set of rings in the sky can alleviate the computational demands in special cases [144, 145, 146]. Other promising exact power estimation methods have been recently proposed [147, 148, 149].

However there also exist computationally rapid, sub-optimal estimators of  $C_l$ . Exploiting the fast spherical harmonic transform ( $\sim N_d^{3/2}$ ), it is possible to estimate the angular power spectrum  $C_l = \langle |a_{lm}|^2 \rangle / (2l+1)$  rapidly [150, 151]. This is commonly referred to as the pseudo- $C_l$  method [152]. (Analogous approach employing fast estimation of the correlation function  $C(\hat{\mathbf{q}} \cdot \hat{\mathbf{q}}')$  have also been explored [153, 154].) It has been recently argued that the need for optimal estimators may have been over-emphasized since they are computationally prohibitive at large  $l$ . Sub-optimal estimators are computationally tractable and tend to be nearly optimal in the relevant high  $l$  regime. Moreover, already the data size of the current sensitive, high resolution, ‘full sky’ CMB experiments such as WMAP have compelled the use of sub-optimal pseudo- $C_l$  related methods [155, 156]. On the other hand, optimal ML estimators can readily incorporate and account for various systematic effects, such as non-uniform sky coverage, noise correlations and beam asymmetries.

In the years after the COBE-DMR observations [157], more sensitive measurements at higher resolution but with limited sky coverage were made by a number of experiments <sup>1</sup>. The effect of incomplete (more generally, non uniform)

<sup>1</sup>For a compendium of links to experiments refer to, e.g. <http://www.mpa-garching.mpg.de/~banday/CMB.html>

sky coverage on the sampling statistics of  $C_l$  was the dominant concern of these experiments such as the ground based experiment TOCO [158, 159], DASI [160], CBI [161], ACBAR [162], and balloon based experiments BOOMERang [163], MAXIMA [164, 165] and Archeops [166]. Comprehensive analyzes have been carried out to tackle this problem. For example, the basic semi-analytic framework developed [152] was subsequently implemented as fast, efficient scheme for the analysis of the BOOMERang experiment [167]. While the non-uniform sky coverage has been addressed in the pseudo- $C_l$  method, the other effects remain to be incorporated.

In this work, we initiate a similar line of research to address a more contemporary issue that has gained relative importance in the post WMAP [155] (and pre-Planck) era of CMB anisotropy measurement with ‘full’ sky coverage. It has been usual in CMB data analysis to assume the experimental beam response to be circularly symmetric around the pointing direction. However, any real beam response function has deviations from circular symmetry. Even the main lobe of the beam response of experiments are generically non-circular (non-axisymmetric) since detectors have to be placed off-axis on the focal plane. (Side lobes and stray light contamination add to the breakdown of this assumption). For high sensitive experiments, the systematic errors arising from the beam non-circularity become progressively more important. Recent CMB experiments such as ARCHEOPS, MAXIMA, WMAP have significantly non-circular beams. Future experiments like the Planck Surveyor are expected to be even more seriously affected by non-circular beams.

Dropping the circular beam assumption leads to major complications at every stage of the data analysis pipeline. The extent to which the non-circularity affects the step of going from the time-stream data to sky map is very sensitive to the scan-strategy. The beam now has an orientation with respect to the scan path that can potentially vary along the path. This implies that the beam function is inherently time dependent and difficult to deconvolve. Even after a sky map is made, the non-circularity of the effective beam affects the estimation of the angular power spectrum,  $C_l$ , by coupling the  $l$  modes, typically, on scales beyond the inverse angular beam-width.

Barring few exceptions (eg., [168]), the non-circularity of beam patterns in CMB experiments has been addressed in limited context. When it has not been totally ignored, one has measured with numerical simulations the biasing effect on the power spectrum of CMB anisotropies of neglecting the non-circularity of the beams

in the data analysis chain (see e.g., MAXIMA [165, 169], Archeops [166, 170]). This approach only deals with the diagonal part of the matrix relating the observed power spectrum to the underlying power spectrum, so does not fully describe the effect of the beam complexity on the CMB statistics. An integrated approach to account for the systematic effect of a non-circular beam has not yet been developed.

In this initial work we skip over the issues related to map making and focus on the CMB power spectrum estimation from a CMB sky map made with an effective beam that is non-circular. Mild deviations from circularity can be addressed by a perturbation approach [117, 171]. Besides providing an elegant analytic formalism, the approach has led to rapid methods for computing the window functions for CMB experiments [172, 173]. In this work the effect of beam non-circularity on the estimation of CMB power spectrum is studied analytically using this perturbation approach.

A brief primer on the connection between CMB power spectrum and the experimental window functions is presented in section 8.2. Though some of the basics have already been described in Chapter 5, section 8.2 is designed to keep this chapter self-contained. In section 8.2.2, the perturbation approach for computing the window functions for CMB experiments with non-circular beam [117] is briefly reviewed and also define the elliptical Gaussian beam and its spherical transform. The bias matrix accounting for the non-circularity of the beam for the pseudo- $C_l$  estimator of CMB anisotropy is derived and discussed in section 9.2. The error-covariance for the unbiased estimator is derived in section 9.2. The chapter concludes with a discussion of the results in section 8.4. An interesting exercise of fitting the WMAP beam maps with an elliptical Gaussian beam profile is presented in an appendix D. Details of the steps leading to our analytical results are given in Appendix E.

## 8.2 Window functions of CMB experiments: a brief primer

Conventionally, the CMB temperature,  $\Delta T(\hat{\mathbf{q}})$ , is expressed as a function of angular position,  $\hat{\mathbf{q}} \equiv (\theta, \phi)$ , on the sky via the spherical harmonic decomposition,

$$\Delta T(\hat{\mathbf{q}}) = \sum_{l=0}^{\infty} \sum_{m=-l}^l a_{lm} Y_{lm}(\hat{\mathbf{q}}). \quad (8.1)$$

In an idealized noise free, CMB anisotropy sky map  $\Delta T(\hat{\mathbf{q}})$  made with infinitely

high resolution, the angular power spectrum is given by

$$C_l \equiv \frac{1}{2l+1} \sum_{m=-l}^l \langle |a_{lm}|^2 \rangle, \quad (8.2)$$

where

$$a_{lm} \equiv \int d\Omega_{\hat{\mathbf{q}}} Y_{lm}^*(\hat{\mathbf{q}}) \Delta T(\hat{\mathbf{q}}) \quad (8.3)$$

are the spherical harmonic transforms of the temperature deviation field  $\Delta T(\hat{\mathbf{q}})$ . We introduce the scaled power spectrum  $C_l \equiv (l(l+1)/2\pi)C_l$ , that measures the power per logarithmic interval of angular scale,  $l$ . Eliminating  $a_{lm}$ , we may write,

$$C_l = \frac{l(l+1)}{8\pi^2} \int d\Omega_{\hat{\mathbf{q}}_1} \int d\Omega_{\hat{\mathbf{q}}_2} \langle \Delta T(\hat{\mathbf{q}}_1) \Delta T(\hat{\mathbf{q}}_2) \rangle P_l(\hat{\mathbf{q}}_1 \cdot \hat{\mathbf{q}}_2), \quad (8.4)$$

where we have made use of the expansion of Legendre Polynomials

$$P_l(\hat{\mathbf{q}}_1 \cdot \hat{\mathbf{q}}_2) = \frac{4\pi}{2l+1} \sum_{m=-l}^l Y_{lm}^*(\hat{\mathbf{q}}_1) Y_{lm}(\hat{\mathbf{q}}_2). \quad (8.5)$$

If we assume the isotropy of the CMB sky,  $\langle \Delta T(\hat{\mathbf{q}}_1) \Delta T(\hat{\mathbf{q}}_2) \rangle$  should depend only on  $\hat{\mathbf{q}}_1 \cdot \hat{\mathbf{q}}_2$ . Therefore, we can use Legendre expansion to show that,

$$\langle \Delta T(\hat{\mathbf{q}}_1) \Delta T(\hat{\mathbf{q}}_2) \rangle = \sum_{l=0}^{\infty} \frac{2l+1}{2l(l+1)} C_l P_l(\hat{\mathbf{q}}_1 \cdot \hat{\mathbf{q}}_2). \quad (8.6)$$

All CMB anisotropy experiments measure differences in CMB temperature at different locations on the sky. A step of map-making is required to derive the above temperature anisotropy map at each point on the sky. Since this is a linear operation, the correlation function of the measured quantity for a given scanning or modulation strategy can always be expressed as linear sum of ‘elementary’ correlations of the temperature given in eq. (8.6).

Typically, a CMB anisotropy experiment probes a range of angular scales characterized by a *window* function  $W_l(\hat{\mathbf{q}}, \hat{\mathbf{q}}')$ . The window depends both on the scanning strategy as well as the angular resolution and response of the experiment. However, it is neater to logically separate these two effects by expressing the window  $W_l(\hat{\mathbf{q}}, \hat{\mathbf{q}}')$  as a sum of ‘elementary’ window function of the CMB anisotropy at each point of the map [117]. In this work, we only deal with these elementary window functions. For a given scanning/modulation strategy, our results can be readily generalized

using the representation of the window function as sum over elementary window functions (see, *e.g.*, [117, 172, 173]). Although the quantitative results we present in this work refer to a scan strategy where each pixel is visited by the beam only once, this is not a limitation of our approach. If pixels are multiply visited by the beam with different orientations, the correlation function still can be expressed as a sum over appropriate elementary window functions for which all the results we describe in this work hold.

### 8.2.1 Window function for circular beams

Due to finite resolution of the instruments, the ‘measured’ temperature difference  $\widetilde{\Delta T}(\hat{\mathbf{q}})$  along the direction  $\hat{\mathbf{q}}$  in response to the CMB anisotropy signal  $\Delta T(\hat{\mathbf{q}}')$  is given by

$$\widetilde{\Delta T}(\hat{\mathbf{q}}) = \int d\Omega_{\hat{\mathbf{q}}'} B(\hat{\mathbf{q}}, \hat{\mathbf{q}}') \Delta T(\hat{\mathbf{q}}') \quad (8.7)$$

where the experimental “Beam” response function  $B(\hat{\mathbf{q}}, \hat{\mathbf{q}}')$  describes the sensitivity of the measuring instrument at different angles around the pointing direction. There is an additional contribution from instrumental noise denoted by  $n(\hat{\mathbf{q}})$  which we shall introduce later into our final results.

The two point correlation function for a statistical isotropic CMB anisotropy signal is

$$C(\hat{\mathbf{q}}, \hat{\mathbf{q}}') = \langle \widetilde{\Delta T}(\hat{\mathbf{q}}) \widetilde{\Delta T}(\hat{\mathbf{q}}') \rangle = \sum_{l=0}^{\infty} \frac{(2l+1)}{4\pi} C_l W_l(\hat{\mathbf{q}}, \hat{\mathbf{q}}'), \quad (8.8)$$

where  $C_l$  is the angular spectrum of CMB anisotropy signal and the window function

$$W_l(\hat{\mathbf{q}}_1, \hat{\mathbf{q}}_2) \equiv \int d\Omega_{\hat{\mathbf{q}}} \int d\Omega_{\hat{\mathbf{q}}'} B(\hat{\mathbf{q}}_1, \hat{\mathbf{q}}) B(\hat{\mathbf{q}}_2, \hat{\mathbf{q}}') P_l(\hat{\mathbf{q}} \cdot \hat{\mathbf{q}}'), \quad (8.9)$$

encodes the effect of finite resolution through the beam function.

For some experiments, the beam function may be assumed to be circularly symmetric about the pointing direction, *i.e.*,  $B(\hat{\mathbf{q}}, \hat{\mathbf{q}}') \equiv B(\hat{\mathbf{q}} \cdot \hat{\mathbf{q}}')$  without significantly affecting the results of the analysis. In any case, this assumption allows a great simplification since the beam function can then be represented by an expansion in Legendre polynomials as

$$B(\hat{\mathbf{q}} \cdot \hat{\mathbf{q}}') = \frac{1}{4\pi} \sum_{l=0}^{\infty} (2l+1) B_l P_l(\hat{\mathbf{q}} \cdot \hat{\mathbf{q}}'). \quad (8.10)$$

Consequently, it is straightforward to derive the well known simple expression

$$W_l(\hat{\mathbf{q}}, \hat{\mathbf{q}}') = B_l^2 P_l(\hat{\mathbf{q}} \cdot \hat{\mathbf{q}}'), \quad (8.11)$$

for a circularly symmetric beam function.

### 8.2.2 Window function for non-circular beams

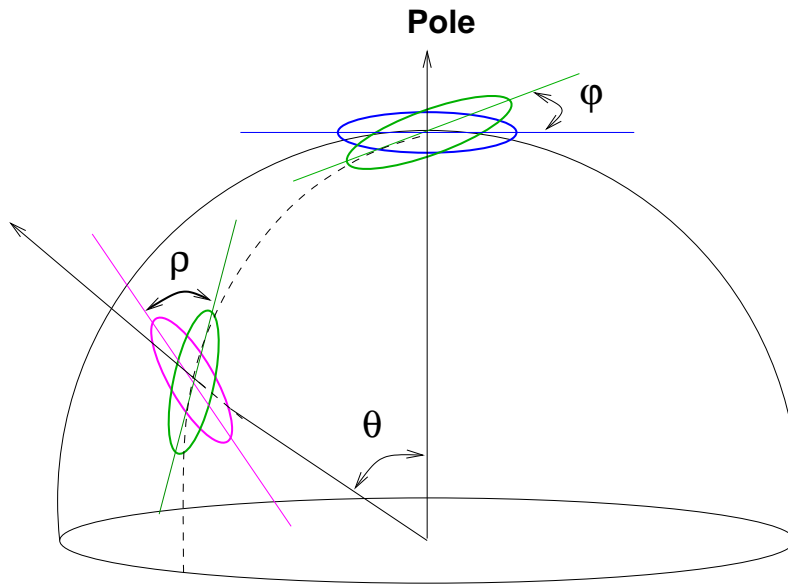


Figure 8.1: **Illustration of beam rotation.** The figure illustrates that a beam pointed in an arbitrary direction  $\hat{\mathbf{q}} = (\theta, \phi)$ , with an orientation given by the angle  $\rho(\hat{\mathbf{q}})$  can always be rotated to point along  $\hat{\mathbf{z}}$  oriented with  $\rho(\hat{\mathbf{z}}) = 0$ . The Euler angles of this rotation are clearly seen to be  $(\theta, \phi, \rho)$ . Consequently, the beam transforms are related through Wigner rotation matrices corresponding to the same rotation.

While some experiments may have circularly symmetric beam functions, most experimental beams are non-circular to some extent. The effect of non-circularity of the beam has become progressively more relevant for experiments with higher sensitivity and angular resolution. The most general beam response function can be represented as

$$B(\hat{\mathbf{z}}, \hat{\mathbf{q}}) = \sum_{l=0}^{\infty} \sum_{m=-l}^l b_{lm}(\hat{\mathbf{z}}) Y_{lm}(\hat{\mathbf{q}}) \quad (8.12)$$

by a spherical harmonic expansion when pointing along  $\hat{\mathbf{z}}$  axis (“North pole” in some given astronomical coordinate system). In case of circularly symmetric beams,

the real coefficients  $B_l = \sqrt{4\pi/(2l+1)}b_{l0}$ .

For mild deviations, the non-circularity of the beams can be parameterized by a set of *small* quantities  $\beta_{lm} \equiv b_{lm}/b_{l0}$  – the *Beam Distortion Parameters* (BDP). The smoothness of the beam response implies that at any multipole  $l$ , the coefficients  $\beta_{lm}$  decrease sufficiently rapidly with increasing  $|m|$ . In addition, for the rest of this chapter we assume<sup>2</sup> that the beam function has reflection symmetry about two orthogonal axes on the (locally flat) beam plane, which ensures that the coefficients  $b_{lm}(\hat{\mathbf{z}})$  are real and zero for *odd* values of  $m$ . An example of a non-circular beam with such symmetries is the elliptical Gaussian beam. A brief mathematical description of such beams can be found later in this section. In order to verify our analytical results, we have used the elliptical Gaussian beam as a model of non-circular beam. However, our analytic results would apply to a general form of non-circular beam (as long as  $\beta_{l1}$  is zero or sub-dominant to  $\beta_{l2}$ ).

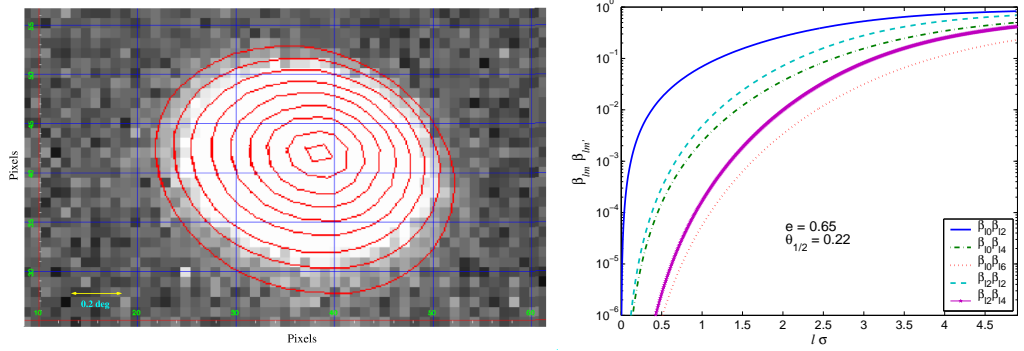


Figure 8.2: **WMAP Q1 Beam.** The left panel shows the WMAP Q1 (A side) beam map overlaid with IRAF fitted ellipses over iso-intensity contours. More details are in Appendix D. On the right panel, we plot the product of beam distortion parameters for the elliptic Gaussian fit to the WMAP-Q1 beam versus multipole corresponding to the different order of the perturbation expansion of a window function for a non-circular beam. Note that the effect kicks in at  $l\bar{\sigma} \sim 1$ .

In order to find an expression for window function in terms of the  $\beta_{lm}$  and  $B_l$ , we follow the approach in [117]. The beam transforms for an arbitrary pointing direction  $\hat{\mathbf{q}}$  may be expressed as,

$$b_{lm}(\hat{\mathbf{q}}) = \sum_{m'=-l}^l b_{lm'}(\hat{\mathbf{z}}) D_{mm'}^l(\hat{\mathbf{q}}, \rho(\hat{\mathbf{q}})), \quad (8.13)$$

<sup>2</sup>This assumption is designed for simplicity as well as due to the fact that most experimental beams are well approximated by an elliptical shape that obeys this. Our method can function perfectly without this assumption. In the next chapter we shall drop this assumption.

where  $D_{mm'}^l(\hat{\mathbf{q}}, \rho) \equiv D_{mm'}^l(\phi, \theta, \rho)$  are the Wigner- $D$  functions given in terms of the Euler angles describing the rotation that carries the pointing direction  $\hat{\mathbf{q}}$  to  $\hat{\mathbf{z}}$ -axis, as illustrated in Figure 8.1. The third angle  $\rho(\hat{\mathbf{q}})$  measures the angle by which the beam has rotated about the new pointing direction, when the pointing direction moves from  $\hat{\mathbf{z}}$  to  $\hat{\mathbf{q}}$ <sup>3</sup>. Inserting the spherical transform of the beam in eq. (8.13) into eq. (8.9) we can write the window function as

$$\begin{aligned} W_l(\hat{\mathbf{q}}_1, \hat{\mathbf{q}}_2) &= \frac{4\pi}{2l+1} \sum_{m=-l}^l b_{lm}^*(\hat{\mathbf{q}}_1) b_{lm}(\hat{\mathbf{q}}_2) \\ &= B_l^2 \sum_{m_1=-l}^l \sum_{m_2=-l}^l \beta_{lm_1}^* \beta_{lm_2} \sum_{m=-l}^l D_{mm_1}^{l*}(\hat{\mathbf{q}}_1, \rho(\hat{\mathbf{q}}_1)) D_{mm_2}^l(\hat{\mathbf{q}}_2, \rho(\hat{\mathbf{q}}_2)) \end{aligned} \quad (8.14)$$

solely in terms of the circular component of the beam function  $B_l$  and non-circular parts encoded in the BDP's,  $\beta_{lm}$ . As pointed out in [117], the window function expressed in the form of eq. (8.15) has an obvious expansion in perturbation series in  $\beta_{lm}$  retaining only the lowest values of  $|m_1|$  and  $|m_2|$ . In this chapter, we adopt this perturbation approach to evaluate the leading order correction to power spectrum estimation arising due to mild deviations of the beam from circular symmetry.

To provide a neat perturbative framework, it is advantageous to use the summation formula of Wigner- $D$  to combine the product of the two Wigner- $D$  functions in eq. (8.15) into a single one as [117]

$$W_l(\hat{\mathbf{q}}_1, \hat{\mathbf{q}}_2) = \frac{4\pi}{2l+1} \sum_{m'=-l}^l \sum_{m''=-l}^l [b_{lm'}(\hat{\mathbf{z}})]^* b_{lm''}(\hat{\mathbf{z}}) D_{m'm''}^l(\alpha - \rho_1, \gamma, \beta + \rho_2), \quad (8.15)$$

where

$$\begin{aligned} \cos\gamma &= \hat{\mathbf{q}}_1 \cdot \hat{\mathbf{q}}_2 \\ \cot\alpha &= -\cos\theta_1 \cot(\phi_1 - \phi_2) + \sin\theta_1 \cot\theta_2 \csc(\phi_1 - \phi_2) \\ \cot\beta &= -\cos\theta_2 \cot(\phi_1 - \phi_2) + \cot\theta_1 \sin\theta_2 \csc(\phi_1 - \phi_2). \end{aligned} \quad (8.16)$$

For large values of  $l$  it is computationally expensive to evaluate the entire  $m'$  and  $m''$  sum in eq. (8.15). However, for a smooth, mildly non-circular beam function, restricting the summation to a few low values of  $m'$  and  $m''$  results in a good

<sup>3</sup>Hereafter, for brevity of notation, absence of the pointing direction argument to  $b_{lm}$  or  $\beta_{lm}$  will imply a beam pointed along the  $\hat{\mathbf{z}}$  axis.

approximation. The leading order terms in the perturbation [117]

$$\begin{aligned}
W_l(\hat{\mathbf{q}}_1, \hat{\mathbf{q}}_2) &= \frac{4\pi}{2l+1} \times \\
&\left[ [b_{l0}(\hat{\mathbf{z}})]^2 d_{00}^l(\gamma) + 2b_{l0}(\hat{\mathbf{z}})b_{l2}(\hat{\mathbf{z}}) \{\cos(2(\alpha - \rho_1)) + \cos(2(\beta + \rho_2))\} d_{02}^l(\gamma) \right. \\
&+ 2 [b_{l2}(\hat{\mathbf{z}})]^2 \left[ \cos(2(\alpha + \beta + \rho_2 - \rho_1)) d_{22}^l(\gamma) \right. \\
&+ (-1)^{-l} \cos(2(\alpha - \beta - \rho_1 - \rho_2)) d_{22}^l(\pi - \gamma) \left. \right] \\
&\left. + 2b_{l0}(\hat{\mathbf{z}})b_{l4}(\hat{\mathbf{z}}) \{\cos(4(\alpha - \rho_1)) + \cos(4(\beta + \rho_2))\} d_{04}^l(\gamma) + \dots \right]. \quad (8.17)
\end{aligned}$$

can be readily evaluated using recurrence relations similar to that of Legendre function. In the above we have restricted to the common situation of beam functions with reflection symmetry ( $\beta_{lm}$  are real and  $\beta_{lm} = 0$  for odd  $m$ ) such as the elliptic Gaussian beam described next.

An elliptic Gaussian beam profile, pointed along the  $\hat{\mathbf{z}}$ -axis is expressed in terms of the spherical polar coordinates about the pointing direction as follows [117]

$$B(\hat{\mathbf{z}}, \hat{\mathbf{q}}) = \frac{1}{2\pi\sigma_1\sigma_2} \exp\left[-\frac{\theta^2}{2\sigma^2(\phi)}\right], \quad (8.18)$$

where the "beam-width"  $\sigma(\phi) \equiv [\sigma_1^2/(1 + \epsilon \sin^2 \phi)]^{1/2}$  and the "non-circularity parameter"  $\epsilon \equiv (\sigma_1^2/\sigma_2^2 - 1)$  are given in terms of  $\sigma_1$  and  $\sigma_2$  – the Gaussian widths along the semi-major and semi-minor axis, respectively. However, we characterize an elliptical beam using two different parameters: eccentricity  $e \equiv \sqrt{1 - \sigma_2^2/\sigma_1^2}$  and the size parameter  $\theta_{1/2}$ , the FWHM of a circular beam of equal "area"<sup>4</sup>.

For elliptical Gaussian beams the spherical harmonic transform is available in the closed analytical form

$$\begin{aligned}
b_{lm} &= \left[ \frac{2l+1}{4\pi} \frac{(l+m)!}{(l-m)!} \right]^{\frac{1}{2}} (l+1/2)^{-m} \times \\
&I_{m/2} \left[ \frac{(l+1/2)^2 \sigma_1^2 e^2}{4} \right] \exp \left[ -\frac{(l+1/2)^2 \sigma_1^2}{2} \left\{ 1 - \frac{e^2}{2} \right\} \right], \quad (8.19)
\end{aligned}$$

where  $I_\nu(x)$  is the modified Bessel function [117, 174]. Note, in the above equation we have used eccentricity  $e$  instead of the non-circularity parameter  $\epsilon = e^2/(1 - e^2)$

<sup>4</sup>By "area" we mean the area enclosed by the curve whose each point corresponds to the Half Maximum of the Gaussian profile. We can show that,  $\theta_{1/2}$ (in degrees) =  $(180/\pi) \sqrt{8 \ln 2} \bar{\sigma}$ , where  $\bar{\sigma}^2 \equiv \sigma_1\sigma_2$  is proportional to the area of the beam.

Table 8.1: **Definition of parameters that quantify non-circularity.** In literature, the elliptical beams have been described by several parameters which can all be expressed in terms of the Gaussian widths along the semi-major ( $\sigma_1$ ) and the semi-minor ( $\sigma_2$ ) axes of the ellipse. We have used these parameters at several places in the text.

Parameter	Symbol	Expression
Eccentricity	$e$	$\sqrt{1 - \frac{\sigma_2^2}{\sigma_1^2}}$
Non-Circularity Parameter	$\epsilon$	$\frac{\sigma_1^2}{\sigma_2^2} - 1$
Ellipticity	$\bar{\epsilon}$	$1 - \frac{\sigma_2}{\sigma_1}$

used in [117]. (See Table 8.1 for the various definitions and characterizations of elliptical beams.)

Fig 8.2 shows one of the WMAP beams as an example of a distinctly non-circular beam (see iso-contours in the left panel) that can be efficiently handled by the leading order term in the perturbation approach (see the right panel). Details of the exercise of fitting elliptical Gaussian beam profile to the WMAP beam maps is given in appendix D.

### 8.3 Bias Matrix

Given the observed temperature fluctuations  $\widetilde{\Delta T}(\hat{\mathbf{q}})$ , a naive estimator for the angular power spectrum based on eq. (8.2) is given by

$$\widetilde{C}_l \equiv \frac{l(l+1)}{2\pi} \frac{1}{2l+1} \sum_{m=-l}^l |\widetilde{a}_{lm}|^2, \quad (8.20)$$

where

$$\widetilde{a}_{lm} \equiv \int d\Omega_{\hat{\mathbf{q}}} Y_{lm}^*(\hat{\mathbf{q}}) \widetilde{\Delta T}(\hat{\mathbf{q}}) U(\hat{\mathbf{q}}) \quad (8.21)$$

are the coefficients of the spherical harmonic transform of the CMB anisotropy map [150, 151]. The weight function  $U(\hat{\mathbf{q}})$  accounts for non-uniform/incomplete sky coverage and also provides a handle to weigh the data ‘optimally’. Without the inconsequential  $l(l+1)$  scaling, this naive estimator is referred to as the pseudo- $C_l$  in recent literature [152]. The ‘pseudo’ refers to fact that the estimated  $C_l$  is

biased. Moreover, this is a sub-optimal estimator of the power spectrum. This naive power spectrum estimate has to be corrected for observational effects such as the instrumental noise contribution, beam resolution, incomplete/non-uniform sky coverage. Nevertheless, the pseudo- $C_l$  method is a computationally fast and economical approach and is currently a method of choice for the recent large CMB anisotropy datasets (at least for large  $l$  within the hybrid schemes [131]).

Faced with the computational challenges of large data sets, an approach that has been adopted is to compute the pseudo- $C_l$ 's from the CMB observations and then correct for the observational effects. The true  $C_l$  spectrum is linearly related

$$\langle \tilde{C}_l \rangle = \sum_{l'} A_{ll'} C_{l'} \quad (8.22)$$

to the pseudo- $C_l$  through a *bias* matrix  $A_{ll'}$ . Similar bias matrices arising due to the effect of non-uniform sky coverage, instrumental noise have been studied [152,167]. In this work, we compute  $A_{ll'}$  for non-circular beam and give explicit analytical results for the leading order terms for non rotating beams.

The pseudo- $C_l$  estimator in eq. (8.20) can be expressed as

$$\tilde{C}_l \equiv \frac{l(l+1)}{8\pi^2} \int d\Omega_{\hat{q}_1} \int d\Omega_{\hat{q}_2} U(\hat{q}_1)U(\hat{q}_2) \widetilde{\Delta T}(\hat{q}_1)\widetilde{\Delta T}(\hat{q}_2)P_l(\hat{q}_1 \cdot \hat{q}_2). \quad (8.23)$$

The ensemble expectation value of the pseudo- $C_l$  power spectrum estimator is

$$\begin{aligned} \langle \tilde{C}_l \rangle &= \frac{l(l+1)}{8\pi^2} \int d\Omega_{\hat{q}_1} \int d\Omega_{\hat{q}_2} U(\hat{q}_1)U(\hat{q}_2) \sum_{l'} \frac{2l'+1}{2l'(l'+1)} C_{l'} \times \\ &P_l(\hat{q}_1 \cdot \hat{q}_2) \int d\Omega_{\hat{q}} \int d\Omega_{\hat{q}'} B(\hat{q}_1, \hat{q})B(\hat{q}_2, \hat{q}')P_{l'}(\hat{q} \cdot \hat{q}'). \end{aligned} \quad (8.24)$$

Recalling the definition of a window function in eq. (8.9), the most general form of the bias matrix

$$A_{ll'} = \frac{2l'+1}{16\pi^2} \frac{l(l+1)}{l'(l'+1)} \int d\Omega_{\hat{q}_1} \int d\Omega_{\hat{q}_2} U(\hat{q}_1)U(\hat{q}_2) P_l(\hat{q}_1 \cdot \hat{q}_2)W_{l'}(\hat{q}_1, \hat{q}_2). \quad (8.25)$$

Using the expression for the window function for a non circular beam in eq. (8.15)

the bias matrix can be written as

$$A_{ll'} = \frac{B_l^2 (2l' + 1) l(l+1)}{4\pi (2l+1) l'(l'+1)} \times \quad (8.26)$$

$$\sum_{n=-l}^l \sum_{m=-l'}^{l'} \left| \sum_{m'=-l'}^{l'} \beta_{l'm'} \int d\Omega_{\hat{q}} Y_{ln}^*(\hat{q}) D_{mm'}^{l'}(\hat{q}, \rho(\hat{q})) U(\hat{q}) \right|^2.$$

The above expressions in eq. (8.25) and eq. (8.26) are valid for a completely general non-circular beam with an arbitrary orientation at each point. The scan pattern of the CMB experiment and relative orientation of the beam along it is encoded in the function  $\rho(\hat{q})$ . The weight  $U(\hat{q})$  can account for non-uniform sky coverage. Analytical progress can be made when  $U(\hat{q}) \equiv U(\theta)$  and  $\rho(\hat{q}) = \rho(\theta)$  are fixed along a given declination, but we do not discuss further it here. When the beam transform, weight function and the scan pattern are specified, the bias matrix can be evaluated numerically using eq. (8.26). However, for mild deviations from circularity, the above expression also points to a perturbation expansion in the small beam distortion parameters,  $\beta_{lm}$ .

For obtaining analytical results, in this chapter we set the weight function  $U(\hat{q}) = 1$ , corresponding to a full, uniform sky coverage and also limit attention to scans with ‘non-rotating’ beams where  $\rho(\hat{q}) = 0$ . This is presented in the next subsections.

### 8.3.1 Circular Symmetric Beam

We first consider eq. (8.26) for the simpler and well studied case of a circular beam. For clarity of presentation, we limit our discussion to full, uniform sky coverage ( $U(\hat{q}) = 1$ ). Results for non-uniform coverage with a circular beam are available in the literature [152, 167, 131].

Using the expression for the window function for circular beam eq. (8.11) into the expression for the bias in eq. (8.25) we recover

$$A_{ll'} = B_l^2 \delta_{ll'} \Rightarrow \langle \tilde{C}_l \rangle = B_l^2 C_l. \quad (8.27)$$

For a full sky measurement with a circular beam, the bias matrix is diagonal implying that there is no mixing of power between different multipoles. The true expectation value of the power spectrum can be obtained by dividing the pseudo- $C_l$  estimator by the isotropic beam transform  $B_l^2$ .

Next we account for the noise contribution and recover the well known result for a full sky observation. The pixel noise  $n(\hat{\mathbf{q}})$  adds to the observed temperature, so that the resultant observed temperature

$$\widetilde{\Delta T}'(\hat{\mathbf{q}}) = \widetilde{\Delta T}(\hat{\mathbf{q}}) + n(\hat{\mathbf{q}}) \quad (8.28)$$

and we can readily obtain

$$\langle \widetilde{C}'_l \rangle = \langle \widetilde{C}_l \rangle + C_l^N = B_l^2 C_l + C_l^N, \quad (8.29)$$

where  $C_l^N$  is the angular power spectrum of the noise  $n(\hat{\mathbf{q}})$  is a well determined quantity. The unbiased estimator for  $C_l$  obtained is

$$\widetilde{C}_l^{UB} = B_l^{-2} (\widetilde{C}'_l - C_l^N). \quad (8.30)$$

### 8.3.2 Non-circular Beam

In this chapter, we obtain analytic results for the bias matrix for a full sky observation ( $U(\hat{\mathbf{q}}) = 1$ ) with a non-circular beam that ‘does not rotate’. The phrase “non-rotating” means that the orientation of the non-circular beam does not rotate about its axis (the pointing direction) while the pointing direction scans the sky implying that

$$\rho(\hat{\mathbf{q}}) = 0. \quad (8.31)$$

For non-rotating beam, the calculation of the bias becomes simpler, which is quite useful for this first attempt to calculate and understand the bias matrix. The integral in the expression for the bias in eq. (8.26) is given by

$$\int Y_{ln}^*(\hat{\mathbf{q}}) D_{mm'}^{l'}(\hat{\mathbf{q}}, 0) d\Omega_{\hat{\mathbf{q}}} = \sqrt{(2l+1)\pi} I_{mm'}^{l'} \delta_{mn}, \quad (8.32)$$

where

$$I_{mm'}^{l'} \equiv \int_{-1}^1 d_{m0}^l(\theta) d_{mm'}^{l'}(\theta) d \cos \theta, \quad (8.33)$$

and  $d_{mm'}^l(\theta)$  are Wigner- $d$  functions related to Wigner- $D$  functions

$$D_{mm'}^l(\hat{\mathbf{q}}, \rho) = e^{-im\phi} d_{mm'}^l(\theta) e^{-im'\rho}. \quad (8.34)$$

The analytic simplicity arises from the fact that for  $\rho(\hat{\mathbf{q}}) = 0$ , the Wigner- $D$  function reduces to spherical harmonic function

$$Y_{lm}(\hat{\mathbf{q}}) = \sqrt{\frac{2l+1}{4\pi}} D_{m0}^l(\hat{\mathbf{q}}, 0). \quad (8.35)$$

We have also used the orthogonality of the phases  $\int_0^{2\pi} e^{-i(m-n)\phi} d\phi = 2\pi\delta_{mn}$  while deriving the above relations.

Substituting the expression for the integral eq. (8.32) into the expression for the bias in eq. (8.26), we obtain

$$A_{ll'} = B_{l'}^2 \left( \frac{2l'+1}{4} \right) \frac{l(l+1)}{l'(l'+1)} \sum_{m=-L}^L \left| \sum_{m'=-l'}^{l'} \beta_{l'm'} I_{mm'}^{ll'} \right|^2, \quad (8.36)$$

where  $L \equiv \min\{l, l'\}$  is the smaller between  $l$  and  $l'$ .

Further analytical progress is possible for smooth beam with mild deviations from circular symmetry through a perturbation in terms of the small beam distortion parameters,  $\beta_{lm}$ . We calculate the exact analytic expression for the leading order effect. Assuming a beam with reflection symmetry where  $\beta_{lm}$  are zero for odd  $m$ , the leading order effect comes at the second order, namely,  $\beta_{l2}\beta_{l0}$  (see eq. (8.17)). Neglecting,  $\beta_{lm}$  for  $|m| > 2$ , we obtain

$$A_{ll'} = B_{l'}^2 \left( \frac{2l'+1}{4} \right) \frac{l(l+1)}{l'(l'+1)} \sum_{m=-L}^L \left[ I_{m0}^{ll'} + \beta_{l'2}(I_{m2}^{ll'} + I_{m-2}^{ll'}) \right]^2. \quad (8.37)$$

Next we obtain analytical expression for the two integrals,  $I_{m0}^{ll'}$  and  $I_{m2}^{ll'} + I_{m-2}^{ll'}$ . The first one can be found in standard texts (e.g. [100]) given as

$$I_{m0}^{ll'} \equiv \int_{-1}^1 d_{m0}^l(\theta) d_{m0}^{l'}(\theta) d \cos \theta = \frac{2}{2l+1} \delta_{ll'}. \quad (8.38)$$

For  $m = 0$ , writing  $d_{00}^l(\theta)$  and  $d_{02}^l(\theta)$  in terms of  $P_l(\cos \theta)$  and its first derivative  $P'_l(\cos \theta)$  we have shown in Appendix-E that for odd values of  $l + l'$ ,  $I_{02}^{ll'} + I_{0-2}^{ll'} = 0$ . For even values of  $l + l'$ ,

$$I_{02}^{l'} + I_{0-2}^{l'} = \begin{cases} 8/\kappa & \text{if } l < l' \\ 0 & \text{if } l > l', \\ -(4l/\kappa)(l-1)/(2l+1) & \text{if } l = l' \end{cases} \quad (8.39)$$

where  $\kappa \equiv \sqrt{(l'-1)l'(l'+1)(l'+2)}$ .

To evaluate  $I_{m2}^{l'} + I_{m-2}^{l'}$  for non-zero  $m$  we expand  $d_{m\pm 2}^{l'}(\theta)$  in terms of  $d_{m0}^{l'}(\theta)$  using a recurrence relation of the Wigner- $D$  functions (where  $l'$  takes integer values between  $l' - 2$  to  $l' + 2$ ). The details are given in Appendix-E. We obtain that  $I_{m2}^{l'} + I_{m-2}^{l'} = 0$  for odd  $l + l'$ . For even values of  $l + l'$ , if  $L \equiv \min\{l, l'\} \geq |m| > 0$ ,

$$I_{m2}^{l'} + I_{m-2}^{l'} = \begin{cases} (4/\kappa)(|m|+1) \sqrt{\frac{(l+|m|)!(l'-|m|)!}{(l-|m|)!(l'+|m|)!}} & \text{if } l < l' \\ (4/\kappa)(|m|-1) \sqrt{\frac{(l-|m|)!(l'+|m|)!}{(l+|m|)!(l'-|m|)!}} & \text{if } l > l' \\ (4/\kappa)[|m| - (l^2 + l + 1)/(2l + 1)] & \text{if } l = l'. \end{cases} \quad (8.40)$$

The bias matrix including the leading order beam distortion (for non-rotating, reflection symmetric beams) can be summarized as

- For odd values of  $l + l'$ ,

$$A_{ll'} = 0. \quad (8.41)$$

- For even values of  $l + l'$ ,

$$A_{ll'} = \begin{cases} (B_{l'}\beta_{l'2})^2 \left( \frac{8l(l+1)(2l'+1)}{l'^2(l'+1)^2(l'-1)(l'+2)} \right) \left[ 2 + \sum_{m=1}^l \frac{(l+m)!(l'-m)!}{(l-m)!(l'+m)!} (m+1)^2 \right] & \text{if } l < l' \\ (B_{l'}\beta_{l'2})^2 \left( \frac{8l(l+1)(2l'+1)}{l'^2(l'+1)^2(l'-1)(l'+2)} \right) \left[ \sum_{m=1}^{l'} \frac{(l-m)!(l'+m)!}{(l+m)!(l'-m)!} (m-1)^2 \right] & \text{if } l > l' \\ \frac{B_l^2}{2l+1} \left[ \left\{ 1 - 2\beta_{l2} \sqrt{\frac{l(l-1)}{(l+1)(l+2)}} \right\}^2 + 2 \sum_{m=1}^l \left\{ 1 - 2\beta_{l2} \frac{(l^2+l+1)-(2l+1)m}{\sqrt{(l-1)l(l+1)(l+2)}} \right\}^2 \right] & \text{if } l = l'. \end{cases} \quad (8.42)$$

The non-zero off-diagonal terms in the bias matrix  $A_{ll'}$  imply that the non-circular beam mixes the contribution of different multipoles from the actual power

spectrum in the observed power spectrum. Off-diagonal elements in  $A_{ll'}$  that arise from non-uniform/incomplete sky coverage have been studied earlier and are routinely accounted for in CMB experiments. Non-circular beam is yet another source of off-diagonal terms in the bias matrix and should be similarly taken into account. In general, CMB experiments have both non-circular beams and non-uniform/incomplete sky coverage that could lead to interesting features in  $A_{ll'}$ .

Although the analytical result presented in this chapter is limited to mildly non-circular and non-rotating beam functions, it does bring to light certain generic features of the effect of non-circular beam functions. To be specific, we compute the elements  $A_{ll'}$  for non-rotating *elliptic Gaussian* beams (see appendix D). The non-circularity of these beams is characterized by their eccentricity  $e = \sqrt{1 - \sigma_2^2/\sigma_1^2}$ , where  $\sigma_1$  and  $\sigma_2$  are the  $1\sigma$  beam-widths along major and minor axes of the beam (see table 8.1). Many experiments have characterized their beams in terms of an elliptic Gaussian fit (e.g., [172, 173, 169, 171]). A convenient advantage of elliptical beams is that the beam transform  $b_{lm}$  (and obviously, the beam distortion parameters,  $\beta_{lm}$ ) can be expressed in a closed analytical form. The results expressed in terms of  $l\bar{\sigma}$  are broadly independent of the average beam-size [117].

Fig. 8.3 shows a density plot of the normalized bias matrix  $A_{ll'}/(B_l B_{l'})$  for a non-rotating elliptical beam. The plot illustrates the importance of off-diagonal terms that arise due to the non-circular beam relative to the diagonal terms. The absence of coupling between multipoles separated by odd integers is evident. Also evident is the fall off as one moves away from the diagonal. The left panel of Fig. 8.4 shows that the off-diagonal elements of  $A_{ll'}$  are important at  $l\bar{\sigma} \sim 1$ . The results are qualitatively independent of the average beam size  $\bar{\sigma}$ . The right panel Fig. 8.4 shows the strong dependence of the dominant off-diagonal element  $A_{ll+2}$  on the eccentricity of the beam.

The analytical results and numerical computations using eq. (8.25) were compared. The numerical and analytical results match perfectly as shown in Figure 8.4. Numerical computation involves the pixelized sky and the algorithm must ensure that this does not introduce spurious effects. We verify that  $A_{ll'}$  has numerically negligible off-diagonal elements when the beam is circularly symmetric. The numerical computation for non-circular beam are verified to be robust to the pixelization of the sky.

Next we illustrate the effect of beam-rotation and non-uniform sky coverage for a *hypothetical* experiment where  $A_{ll'}$  have been computed numerically<sup>5</sup>. The left

<sup>5</sup>The effect of beam rotation and non-uniform sky coverage has been studied *analytically* in the

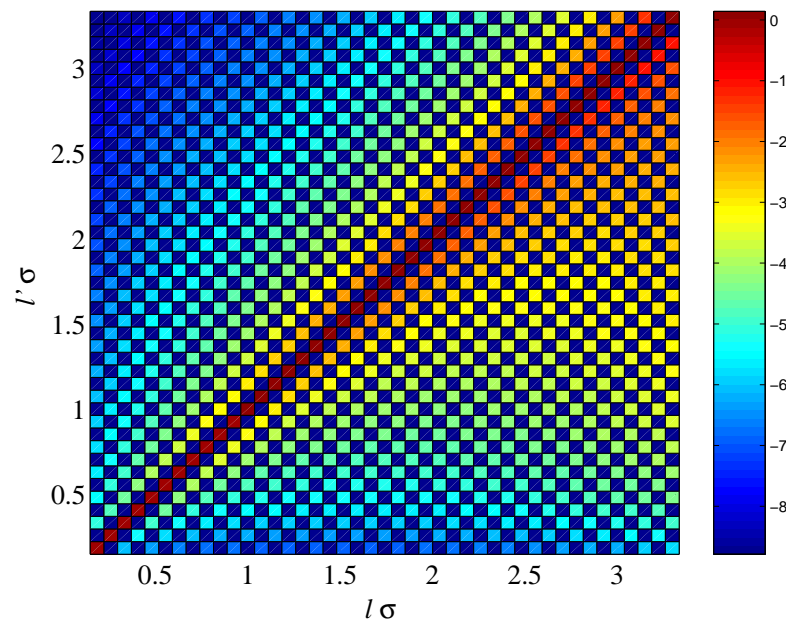


Figure 8.3: **Bias matrix without beam rotation.** The log of normalized bias matrix  $A_{ll'}/(B_l B_{l'})$  is plotted for an elliptical beam of eccentricity  $e = 0.6$  and mean beam-width  $\bar{\sigma} = 0.074$ . The normalization is carried out so that the effect of non-circularity on the bias matrix can be easily compared to that for circular beams. Beam rotation and cut-sky effects have not been considered in this figure. One notices that the off-diagonal elements of the bias matrix take significant values for  $l\bar{\sigma} \geq 1$ .

panel of Fig. 8.5 shows (in *log* scale) the normalized bias matrix arising from a  $2.5^\circ$  circular beam including a non trivial  $U(\hat{\mathbf{q}})$  in the form of a smoothed version of the galactic mask Kp2 of WMAP [155, 101]. The right panel of the figure shows the *extra* effect that a rotating non-circular beam would introduce. We assume a simple ‘toy’ beam rotation along an equal declination scan strategy, where the beam continuously ‘rotates’ by  $2\pi$  for every complete pass at a given declination which implies the simple form

$$\rho(\hat{\mathbf{q}}) \equiv \rho(\theta, \phi) = \phi. \quad (8.43)$$

The elements here have been computed numerically using eq. (8.25) retaining the leading order terms in the perturbation expansion of  $W_l$  in eq. (8.17). The off-diagonal effects at low  $l$  are dominated by the cut sky effect. The off-diagonal element  $l\bar{\sigma} \gtrsim 1$  arise solely due to non-circular beam. The numerical computation illustrates the potentially large corrections that can arise due to non-circular beam that ‘rotate’ on the sky. The numerical computations in this work pave the way for introducing realistic scan-pattern, beam-rotation and non-uniform sky coverage in a future extension to our work.

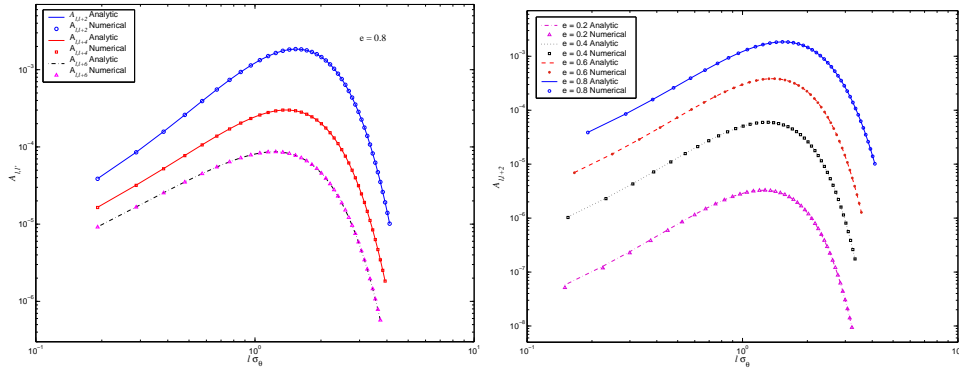


Figure 8.4: **Characteristics of the bias matrix elements (no beam rotation).** Elements of the bias matrix  $A_{l'l}$  are plotted in this figure as a function of multipole ( $l$ ). The bias matrix relates the observed  $C_l$ s to their true values. When non-circular beams are used in CMB experiments, the bias matrix can be shown to be non-diagonal, thus implying mixing of power between multipoles. On the left panel, we plot  $A_{l'l}$  for  $l' - l = 2, 4, 6$ . It is evident that the effect decreases as we move away from the diagonal and that it kicks in at  $l\bar{\sigma} \sim 1$ , for a beam of eccentricity  $e = 0.8$ . For the figure in the right panel, we plot  $A_{l,l+2}$  for several beams of the same size but different eccentricities. Clearly, the effect also depends strongly on the non-circularity of the beam.

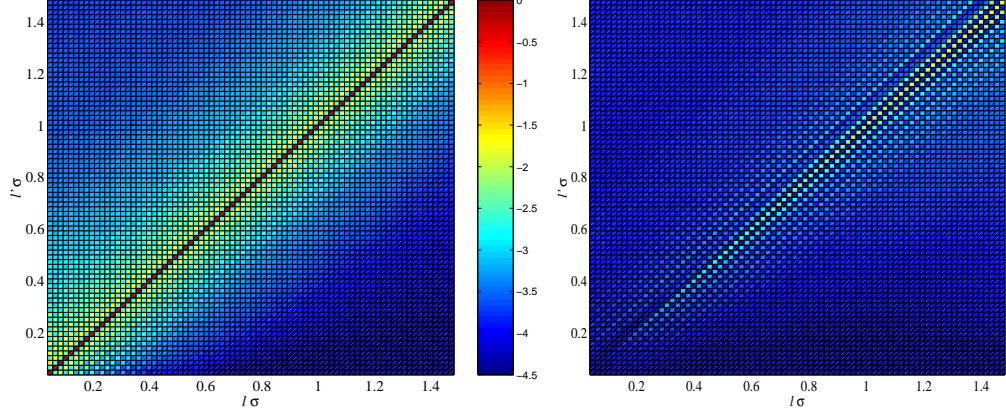


Figure 8.5: **Effect of beam rotation on bias matrix** The normalized bias matrix elements (on log scale,  $\log[A_{ll'}/(B_l B_{l'})]$ ) of a hypothetical experiment with a scan pattern (eq. 8.43) corresponding to a rotating, non circular beam ( $e = 0.6$ ) and non uniform sky coverage are studied. The left panel shows the effect of non-uniform coverage alone (circular beam approximation). The right panel isolates the additional effect that arises due to the non-circularity of the beam and its rotation. We note that significant off-diagonal elements arise at  $l\bar{\sigma} \geq 1$  from the non-circular beam comparable to that from the non-uniform coverage. The non-uniform coverage corresponds to a smoothed WMAP Kp2 galactic mask (smoothed from resolution of  $N_{side} = 512$  to 64). We use a sufficiently high resolution beam with  $\bar{\sigma} = 0.018$  ( $\theta_{1/2} = 2.5^\circ$ ) to ensure that the effects due to the galactic mask and the non-circular beam appear in distinct regions of the multipole space.

We summarize the following features of the bias matrix :

1. There is no coupling between  $\langle \widetilde{C}_l \rangle$  and  $C_{l'}$  for odd values of  $l + l'$ ,
2. Coupling decreases as  $|l - l'|$  increases,
3. Coupling increases with eccentricity for fixed beam size, and
4. Size of the beam determines the multipole  $l$  value for which coupling will be maximum ( $l\bar{\sigma} \sim 1$ ).

Figure 8.6 roughly indicates the level and nature of the effect of neglecting the non-circularity of the beam on CMB power estimation (for the conservative case of non-rotating beams). Consider the power spectrum  $\widetilde{C}_l = \sum_{l'} A_{ll'} C_{l'}$  measured using a non-circular, elliptical Gaussian beam of a given eccentricity,  $e$  and average beam-width,  $\bar{\sigma}$ . We compare the power spectrum obtained by deconvolving  $\widetilde{C}_l$  with

a circular, Gaussian beam of the beam-width,  $\bar{\sigma}$  with the true  $C_l$ . The lower panel shows that the error can be significant for multipole values beyond the inverse beam-width even for modestly non-circular comparable to the WMAP beam maps discussed in the Appendix D.

The estimation error of CMB power spectrum due to non-circular beams was recently published by the WMAP team [96]. Full scan strategy with a simple model for beam rotation was used in their calculations. Figure 8.7 is taken from the WMAP third year results paper first published in the LAMBDA website [101]. The effect of non-circular beam on CMB power spectrum from WMAP was estimated in this paper following a method similar to ours. The fractional error in power spectrum estimation error at different multipoles have been plotted in this figure. As expected, the effect is quite significant at high multipoles. The errors predicted by us for WMAP-like beams in [118] has also been overlaid on the plot. The results are quite consistent.

Once we have calculated the bias matrix, we can construct the unbiased estimator for the angular power spectrum. Invoking steps similar to the case of circular beams to account for the instrumental noise, we obtain

$$\langle \tilde{C}'_l \rangle = \langle \tilde{C}_l \rangle + C_l^N = \sum_{l'} A_{ll'} C_{l'} + C_l^N. \quad (8.44)$$

The unbiased estimator for the angular power spectrum is

$$\tilde{C}_l^{UB} = \sum_{l'} A_{ll'}^{-1} (\tilde{C}'_{l'} - C_{l'}^N). \quad (8.45)$$

## 8.4 Error-Covariance Matrix

The statistical error-covariance of the estimated angular power spectrum is defined as

$$\text{Cov}(\tilde{C}_l, \tilde{C}_{l'}) \equiv \langle (\tilde{C}_l - \langle \tilde{C}_l \rangle)(\tilde{C}_{l'} - \langle \tilde{C}_{l'} \rangle) \rangle. \quad (8.46)$$

In an idealized, noise free, CMB experiment with infinite angular resolution uniformly covering the full sky

$$\tilde{C}_l = \frac{l(l+1)}{8\pi^2} \int d\Omega_{\hat{q}_1} \int d\Omega_{\hat{q}_2} \Delta T(\hat{q}_1) \Delta T(\hat{q}_2) P_l(\hat{q}_1 \cdot \hat{q}_2). \quad (8.47)$$

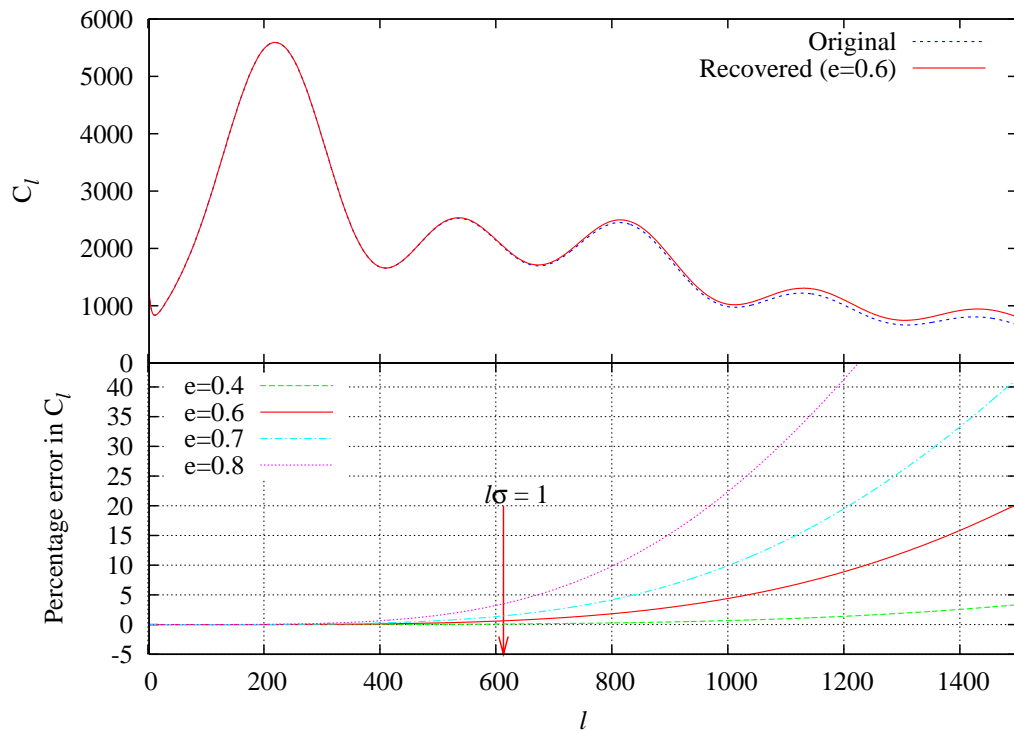


Figure 8.6:  $C_l$  estimation error due to non-circular beams. The effect of non-circular beam is studied for CMB power spectrum estimation by a CMB experiment with a WMAP-like non-circular beam. For illustration, we consider the best fit (Power law) model to be the (fiducial) true  $C_l$  of the Universe shown as the solid line in the upper panel. Let  $\tilde{C}_l$  be the power spectrum measured by using a elliptical, Gaussian beam with eccentricity,  $e = 0.6$ , and  $\bar{\sigma} = 0.0016$ . The dashed line shows the  $C_l$  that would be inferred by deconvolving  $\tilde{C}_l$  with a circular beam assumption with beam-width,  $\bar{\sigma}$ . The lower panel plots the relative error in the power spectrum recovered with a circular beam assumption for a measurements made with a non-circular beam with  $e = 0.4$  to  $0.8$ .

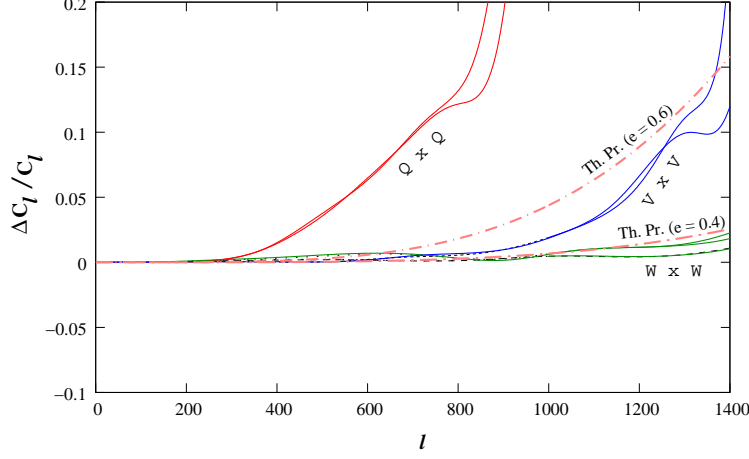


Figure 8.7:  $C_l$  estimation error published in the WMAP 3yr results [96]. The plot shows the fractional error in power spectrum estimation at different multipoles due to non-circular beams. Clearly, the error is highly significant at higher multipoles. Our prediction of estimation errors for WMAP-like beams have also been overlaid on this plot for two different values of eccentricity. The results are in very good agreement [Figure 8.6]

Using the property of Gaussian random fields that,

$$\begin{aligned}
 \langle \Delta T(\hat{\mathbf{q}}_1) \Delta T(\hat{\mathbf{q}}_2) \Delta T(\hat{\mathbf{q}}'_1) \Delta T(\hat{\mathbf{q}}'_2) \rangle &= \langle \Delta T(\hat{\mathbf{q}}_1) \Delta T(\hat{\mathbf{q}}_2) \rangle \langle \Delta T(\hat{\mathbf{q}}'_1) \Delta T(\hat{\mathbf{q}}'_2) \rangle + \\
 &\quad \langle \Delta T(\hat{\mathbf{q}}_1) \Delta T(\hat{\mathbf{q}}'_1) \rangle \langle \Delta T(\hat{\mathbf{q}}_2) \Delta T(\hat{\mathbf{q}}'_2) \rangle + \\
 &\quad \langle \Delta T(\hat{\mathbf{q}}_1) \Delta T(\hat{\mathbf{q}}'_2) \rangle \langle \Delta T(\hat{\mathbf{q}}'_1) \Delta T(\hat{\mathbf{q}}_2) \rangle
 \end{aligned}
 \tag{8.48}$$

and eq. (8.6), we recover the well known result for full sky CMB maps

$$\text{Cov}(\tilde{C}_l, \tilde{C}_{l'}) = \frac{2}{2l+1} \langle C_l \rangle^2 \delta_{ll'} = \frac{2}{2l+1} C_l^2 \delta_{ll'}, \tag{8.49}$$

corresponding to  $C_l$  being a sum of the squares of  $2l+1$  Gaussian variates, i.e.  $\chi^2_{2l+1}$  distribution. The measured power spectrum at each multipole is independent (for full sky CMB maps). The variance of the power spectrum estimator is not zero even in the ideal case. Consequently, the measurement angular power spectrum from the one available CMB sky map is inherently limited by an inevitable error the *Cosmic Variance*<sup>6</sup>.

<sup>6</sup>This is a direct consequence of the sphere being compact and, consequently, an inevitable, rigid lower bound on the uncertainty in the measurement of angular power spectrum at a given multipole  $l$ . Otherwise, the effect is the similar to the well-known sample variance of a finite data-stream

### 8.4.1 Circular Beam

For measurements made with a circular beam, the temperature is a linear transform of the actual temperature (see eq. (8.7)). So, it also represents a Gaussian random field. Hence, eq. (8.48) remains valid even for observed temperature fluctuations. Moreover, the window function takes a simple form given in eq. (8.11). Consequently, eq. (8.6) gets modified to

$$\langle \widetilde{\Delta T}(\hat{\mathbf{q}}_1) \widetilde{\Delta T}(\hat{\mathbf{q}}_2) \rangle = \sum_{l=0}^{\infty} \frac{2l+1}{2l(l+1)} B_l^2 C_l P_l(\hat{\mathbf{q}}_1 \cdot \hat{\mathbf{q}}_2). \quad (8.50)$$

The covariance matrix

$$\text{Cov}(\widetilde{C}_l, \widetilde{C}_{l'}) = \frac{2}{2l+1} \langle \widetilde{C}_l \rangle^2 \delta_{ll'} = \frac{2}{2l+1} (B_l^2 C_l)^2 \delta_{ll'}, \quad (8.51)$$

remains diagonal for circular beams, i.e., the measured power spectrum at each multipole is independent of the power measured in the other multipoles. The second equality follows from eq. (8.27).

Including the instrumental noise spectrum in the measured power spectrum  $C_l^N$ , we obtain

$$\text{Cov}(\widetilde{C}'_l, \widetilde{C}'_{l'}) = \frac{2\delta_{ll'}}{2l+1} (\langle \widetilde{C}_l \rangle + C_l^N)^2, \quad (8.52)$$

where we assume that the noise spectrum  $C_l^N$  is known much better and, in particular, does not suffer from cosmic variance. For the unbiased estimator given by eq. (8.30), the well known covariance matrix

$$\text{Cov}(\widetilde{C}_l^{UB}, \widetilde{C}_{l'}^{UB}) = B_l^{-4} \text{Cov}(\widetilde{C}'_l, \widetilde{C}'_{l'}) = \frac{2\delta_{ll'}}{2l+1} (C_l + B_l^{-2} C_l^N)^2 \quad (8.53)$$

is readily obtained from the linear transformation between  $C'_l$  and  $C_l^{UB}$  [175, 176].

### 8.4.2 Non-circular Beam

As expected, the covariance for the non-circular beam is considerably more complicated. We start with the general form of the two point correlation function. Using

eq. (8.23), the general form of the covariance matrix is

$$\begin{aligned} \text{Cov}(\widetilde{C}_l, \widetilde{C}_{l'}) &= \frac{l'(l+1)(l'+1)}{(4\pi)^4} \sum_{l_1, l_2=0}^{\infty} \frac{(2l_1+1)(2l_2+1)}{l_1 l_2 (l_1+1)(l_2+1)} C_{l_1} C_{l_2} \times \\ &\quad \int d^4\Omega U(\hat{\mathbf{q}}_1) U(\hat{\mathbf{q}}_2) U(\hat{\mathbf{q}}'_1) U(\hat{\mathbf{q}}'_2) P_l(\hat{\mathbf{q}}_1 \cdot \hat{\mathbf{q}}_2) P_{l'}(\hat{\mathbf{q}}'_1 \cdot \hat{\mathbf{q}}'_2) \times \\ &\quad [W_{l_1}(\hat{\mathbf{q}}_1, \hat{\mathbf{q}}'_1) W_{l_2}(\hat{\mathbf{q}}_2, \hat{\mathbf{q}}'_2) + W_{l_1}(\hat{\mathbf{q}}_1, \hat{\mathbf{q}}'_2) W_{l_2}(\hat{\mathbf{q}}_2, \hat{\mathbf{q}}'_1)], \end{aligned} \quad (8.54)$$

where for brevity we use  $d^4\Omega \equiv d\Omega_{\hat{\mathbf{q}}_1} d\Omega_{\hat{\mathbf{q}}_2} d\Omega_{\hat{\mathbf{q}}'_1} d\Omega_{\hat{\mathbf{q}}'_2}$ .

Noting the interchangeability of the dummy variables  $\hat{\mathbf{q}}'_1$  and  $\hat{\mathbf{q}}'_2$ , we combine the two terms in the above equation to obtain

$$\begin{aligned} \text{Cov}(\widetilde{C}_l, \widetilde{C}_{l'}) &= 2 \left[ \frac{l'(l+1)(l'+1)}{(4\pi)^4} \right] \sum_{l_1, l_2=0}^{\infty} \frac{(2l_1+1)(2l_2+1)}{l_1 l_2 (l_1+1)(l_2+1)} C_{l_1} C_{l_2} \times \\ &\quad \int d^4\Omega U(\hat{\mathbf{q}}_1) U(\hat{\mathbf{q}}_2) U(\hat{\mathbf{q}}'_1) U(\hat{\mathbf{q}}'_2) P_l(\hat{\mathbf{q}}_1 \cdot \hat{\mathbf{q}}_2) P_{l'}(\hat{\mathbf{q}}'_1 \cdot \hat{\mathbf{q}}'_2) W_{l_1}(\hat{\mathbf{q}}_1, \hat{\mathbf{q}}'_1) W_{l_2}(\hat{\mathbf{q}}_2, \hat{\mathbf{q}}'_2). \end{aligned} \quad (8.55)$$

We expand the Legendre Polynomials in terms of spherical harmonics (eq. (8.5)) and use the expression for the window function in eq. (8.15) to obtain

$$\begin{aligned} \text{Cov}(\widetilde{C}_l, \widetilde{C}_{l'}) &= \frac{l'(l+1)(l'+1)}{8\pi^2(2l+1)(2l'+1)} \sum_{l_1, l_2=0}^{\infty} \frac{(2l_1+1)(2l_2+1)}{l_1 l_2 (l_1+1)(l_2+1)} \times \\ &\quad C_{l_1} C_{l_2} B_{l_1}^2 B_{l_2}^2 \sum_{m=-l}^l \sum_{m'=-l'}^{l'} \sum_{m_1=-l_1}^{l_1} \sum_{m_2=-l_2}^{l_2} \\ &\quad \left[ \sum_{m'_1, m''_1=-l_1}^{l_1} \beta_{l_1 m'_1} \beta_{l_1 m''_1}^* \int d\Omega_{\hat{\mathbf{q}}_1} U(\hat{\mathbf{q}}_1) Y_{lm}^*(\hat{\mathbf{q}}_1) D_{m_1 m'_1}^{l_1}(\hat{\mathbf{q}}_1, \rho(\hat{\mathbf{q}}_1)) \times \right. \\ &\quad \int d\Omega_{\hat{\mathbf{q}}'_1} U(\hat{\mathbf{q}}'_1) Y_{l'm'}(\hat{\mathbf{q}}'_1) D_{m_1 m'_1}^{l_1*}(\hat{\mathbf{q}}'_1, \rho(\hat{\mathbf{q}}'_1)) \times \\ &\quad \sum_{m'_2, m''_2=-l_2}^{l_2} \beta_{l_2 m'_2}^* \beta_{l_2 m''_2} \int d\Omega_{\hat{\mathbf{q}}_2} U(\hat{\mathbf{q}}_2) Y_{lm}(\hat{\mathbf{q}}_2) D_{m_2 m'_2}^{l_2*}(\hat{\mathbf{q}}_2, \rho(\hat{\mathbf{q}}_2)) \times \\ &\quad \left. \int d\Omega_{\hat{\mathbf{q}}'_2} U(\hat{\mathbf{q}}'_2) Y_{l'm'}^*(\hat{\mathbf{q}}'_2) D_{m_2 m'_2}^{l_2}(\hat{\mathbf{q}}'_2, \rho(\hat{\mathbf{q}}'_2)) \right], \end{aligned} \quad (8.56)$$

as the general expression for error covariance for angular power spectrum for non-circular beams. Note that even for full, uniform sky observations,  $U(\hat{\mathbf{q}}) = 1$ , the

error covariance matrix is no longer diagonal.

To make further progress analytically, we restrict to the case of uniform, full sky coverage ( $U(\hat{\mathbf{q}}) = 1$ ) with no beam rotation ( $\rho(\hat{\mathbf{q}}) = 0$ ). Using the integration of eq. (8.32) and after a considerable algebra we may write the expression for covariance as

$$\text{Cov}(\tilde{C}_l, \tilde{C}_{l'}) = \frac{l'(l+1)(l'+1)}{8} \sum_{m=-L}^L \left[ \sum_{l_1=|m|}^{\infty} B_{l_1}^2 C_{l_1} \frac{(2l_1+1)}{l_1(l_1+1)} \sum_{m'_1=-l_1}^{l_1} \beta_{l_1 m'_1} I_{mm'_1}^{l l_1} \sum_{m''_1=-l_1}^{l_1} \beta_{l_1 m''_1}^* I_{mm''_1}^{l' l_1} \right]^2 \quad (8.57)$$

where  $L = \min\{l, l'\}$  is the smaller between  $l$  and  $l'$ . The integrals  $I_{mm'}^{ll'}$  are defined in §9.2 and the analytical expressions for  $m' = 0, \pm 2$  are given. It is straightforward to verify that the above equation correctly reproduces the expression for the error-covariance in the circular beam case given by eq. (8.51).

For evaluation of the covariance matrix, we note that though the summation over  $l_1$  runs from 0 to  $\infty$ , the contributions are significant only around  $l \sim 1/\bar{\sigma}$  and the summation can be truncated suitably. Further, for most beams we can confine to the leading order approximation as in eq. (8.17), by neglecting all the  $\beta_{lm}$ 's for  $m \geq 4$ . For mild deviations from circular beams, the observed power spectrum at different multipoles are weakly correlated ( $\sim \beta_{l2}\beta_{l'2}$ ). The error-covariance matrix can be diagonalized to find the independent linear combinations of estimators (eigenvectors), and the variances of these independent estimators are given by the corresponding eigenvalues. These eigenvalues are necessarily larger than the cosmic variance corresponding to a circular beam.

The inclusion of instrumental noise is similar to what was done in the circular beam case. The covariance

$$\text{Cov}(\tilde{C}'_l, \tilde{C}'_{l'}) = \text{Cov}(\tilde{C}_l, \tilde{C}_{l'}) + \frac{2\delta_{ll'}}{2l+1} \left[ 2\langle \tilde{C}_l \rangle C_l^N + (C_l^N)^2 \right] \quad (8.58)$$

clearly reproduces the result in eq. (8.51) in the limit of a circular beam. Figure 8.8 shows a density plot of the elements of the covariance matrix for a non-circular (elliptical) beam with no rotation. In contrast to the case for incomplete (cut) sky case, where the effects are at small  $l$  (see [131]), the non-circular beam affects the large multipoles region ( $l\bar{\sigma} \geq 1$ ). The pseudo- $C_l$  approach is close to optimal for large  $l$  hence it may be more important to account for non-circular beams effects

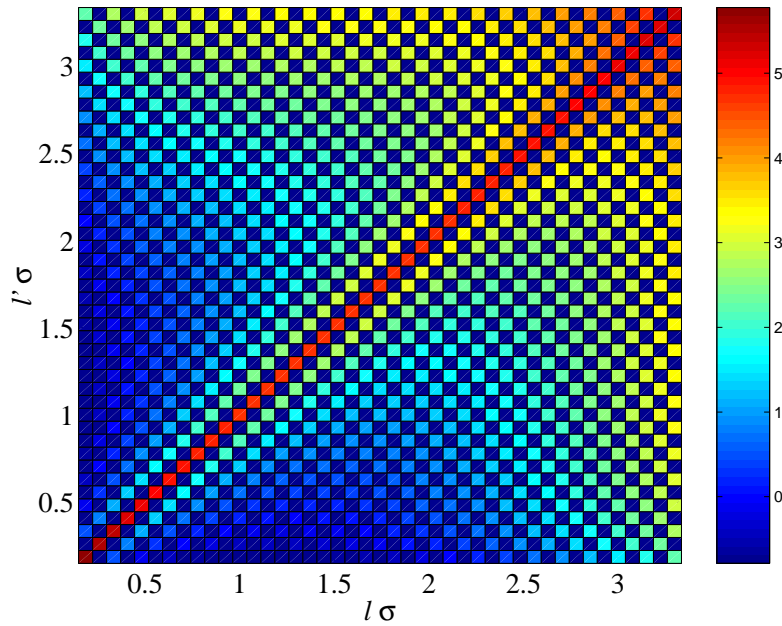


Figure 8.8: **Covariance of  $C_l$ 's due to beam non-circularity.** Log of the normalized covariance matrix  $\text{Cov}(C_l, C_{l'}) / (B_l B_{l'})^2$  [in the units of  $(\mu K)^4$ ] is plotted for an elliptical beam of eccentricity  $e = 0.6$  and mean beam-width  $\bar{\sigma} = 0.074$ . Due to the non-circularity of the beam, the error in CMB angular power spectrum estimate at different multipoles are no longer independent. We notice that the off-diagonal elements of the error covariance matrix are pronounced for  $l\bar{\sigma} \geq 1$ .

than the cut-sky, since it is possible to use maximum likelihood estimator for small  $l$ .

The error-covariance matrix for the unbiased estimator eq. (8.45) for non-circular beams is given by

$$\begin{aligned} \text{Cov}(\tilde{C}_l^{UB}, \tilde{C}_{l'}^{UB}) &= \sum_{l_1} \sum_{l_2} A_{ll_1}^{-1} A_{l'l_2}^{-1} \text{Cov}(\tilde{C}'_{l_1}, \tilde{C}'_{l_2}) \\ &= \sum_{l_1} \sum_{l_2} \frac{\alpha_{ll_1} \alpha_{l'l_2}}{(B_{l_1} B_{l_2})^2} \left[ \text{Cov}(\tilde{C}_{l_1}, \tilde{C}_{l_2}) + \frac{2\delta_{ll'}}{2l+1} \{2\langle \tilde{C}_{l_1} \rangle C_l^N + (C_l^N)^2\} \right], \end{aligned} \quad (8.59)$$

where the matrix  $\alpha_{ll'} \equiv B_{l'}^{-2} A_{ll'}^{-1}$ , being very close to identity, demonstrates that the beam-modified cosmic variance part of the covariance of unbiased estimator weakly depends on  $B_l$ 's, whereas the noise part depends on them significantly.

## 8.5 Discussion and Conclusion

We present an analytic framework for addressing the effect of non-circular experimental beam function in the estimation of the angular power spectrum  $C_l$  of CMB anisotropy. Non-circular beam effects can be modeled into the covariance functions in approaches related to maximum likelihood estimation [136, 137] and can also be included in the Harmonic ring [144, 145] and ring-torus estimators [146]. The latter is promising since it reduces the computational costs from  $N^3$  to  $N^2$ . However, all these methods are computationally prohibitive for high resolution maps and, at present, the computationally economical approach of using a pseudo- $C_l$  estimator appears to be a viable option for extracting the power spectrum at high multipoles [131]. The pseudo- $C_l$  estimates have to be corrected for the systematic biases. While considerable attention has been devoted to the effects of incomplete/non-uniform sky coverage, no comprehensive or systematic approach is available for non-circular beam. The high sensitivity, 'full' (large) sky observation from space (long duration balloon) missions have alleviated the effect of incomplete sky coverage and other systematic effects such as the one we consider here have gained more significance. Non-uniform coverage, in particular, the galactic masks affect only CMB power estimation at the low multipoles. Recently proposed hybrid scheme promotes a strategy where the power spectrum at low multipoles is estimated using optimal Maximum Likelihood methods and pseudo- $C_l$  are used for large multipoles.

We have shown that non-circular beam is an effect that dominates at large  $l$  comparable to the inverse beam width. For high resolution experiment, the

optimal maximum likelihood methods which can account for non-circular beam functions are computationally prohibitive. In implementing pseudo- $C_l$  estimation, the non-circular beam effect could dominate over the effects of more well studied effect of non-uniform sky coverage. Our work provides a convenient approach for estimating the magnitude of this effect in terms of the leading order deviations from a circular beam. The perturbation approach is very efficient. For most CMB experiments the leading few orders capture most of the effect of beam non-circularity. The perturbation approach has allowed the development of computationally rapid method of computing window functions [117]. Our work may similarly yield computationally rapid methods to estimate the error due to beam non-circularity.

We have also developed a complete analytic framework that considers the the effect of non-circular beam together with beam rotation and incomplete sky coverage. While the perturbative analysis can predict very good estimate for the bias, the complete analysis can be more accurate and has the potential to replace the computationally expensive approach of bias estimation for upcoming experiments (eg., Planck) using numerical simulation. The details has been presented in the next chapter.

The quantitative estimates of the off-diagonal matrix elements of the bias and error-covariance for ‘non-rotating’ beam graphically illustrate the general features that can be gleaned from our analytic results. They show that the beam non-circularity affects the  $C_l$  estimation on multipoles larger than the inverse beam width. A strong dependence on the eccentricity of the beam is also seen. The analytical results obtained in this chapter are limited to non-rotating beams and uniform sky coverage, these assumptions will be dropped in the next chapter. *We caution against interpreting these results as a measure of the non-circular beam effects for any real CMB experiment.* Numerical results include a scan pattern that does not belong to any known experiment. Nevertheless, our prediction of bias has been in good agreement with the recently released WMAP 3 year results [96]. Numerical calculations of the bias matrix for a ‘toy’ scanning strategy where the beam rotates on the sky indicates the possibility of significant corrections. The bias due to non-uniform sky coverage can have interesting coupling to the bias from beam non-circularity. On the other hand, it has also been shown that effects of non-circular beams can be diluted if the scan pattern is such that each point in the sky is revisited by the beam with a different orientation at different time [169]. The numerical implementation of our method can readily accommodate the case when pixels are revisited by the beam with different orientations. Evaluating the realistic

bias and error-covariance for a specific CMB experiment with non-circular beams would require numerical evaluation of the general expressions for  $A_{ll'}$  in eqs. (8.26) using real scan strategy and account for inhomogeneous noise and sky coverage. Some of these issues have been addressed analytically in the next chapter.

It is worthwhile to note in passing that the angular power  $C_l$  contains all the information of Gaussian CMB anisotropy only under the assumption of statistical isotropy. Gaussian CMB anisotropy map measured with a non-circular beam corresponds to an underlying correlation function that violates statistical isotropy. In this case, the extra information present may be measurable using, for example, the bipolar power spectrum [177, 178]. Even when the beam is circular the scanning pattern itself is expected to cause a breakdown of statistical isotropy of the measured CMB anisotropy [167]. For a non-circular beam, this effect could be much more pronounced and, perhaps, presents an interesting avenue of future study.

In addition to temperature fluctuations, the CMB photons coming from different directions have a random, linear polarization. The polarization of CMB can be decomposed into  $E$  part with even parity and  $B$  part with odd parity. Besides the angular spectrum  $C_l^{TT}$ , the CMB polarization provides three additional spectra,  $C_l^{TE}$ ,  $C_l^{EE}$  and  $C_l^{BB}$  which are invariant under parity transformations. The level of polarization of the CMB being about a tenth of the temperature fluctuation, it is only very recently that the angular power spectrum of CMB polarization field has been detected. The Degree Angular Scale Interferometer (DASI) has measured the CMB polarization spectrum over limited band of angular scales in late 2002 [179]. The WMAP mission has also detected CMB polarization [180]. The polarization maps have also been released by WMAP with the 3 year results [98, 101]. Correcting for the systematic effects of a non-circular beam for the polarization spectra is expected to become important soon. Our work is based on the perturbation approach of [117] which has been already been extended to the case of CMB polarization [171]. Extending this work to the case CMB polarization is another line of activity we plan to undertake in the near future.

In summary, we have presented a perturbation framework to compute the effect of non-circular beam function on the estimation of power spectrum of CMB anisotropy. We not only present the most general expression including non-uniform sky coverage as well as a non-circular beam that can be numerically evaluated but also provide elegant analytic results in interesting limits. In this work, we have skipped over the effect of non-circular beam functions on map-making step. In

simple scanning strategies, our results may be readily applied in this context. As CMB experiments strive to measure the angular power spectrum with increasing accuracy and resolution, the work provides a stepping stone to address a rather complicated systematic effect of non-circular beam functions.

The next chapter is a sequel to this chapter, where we evaluate the most general expression for the bias, that considers the effects of beam-rotation and incomplete sky coverage also analytically - issues which were addressed numerically in this chapter.

## Chapter 9

# Non-circular Beam Correction to CMB Power Spectrum: Complete Analysis Framework

In the previous chapter a perturbative analysis was presented to estimate the leading order effect of non-circular beams on the cosmic microwave background (CMB) power spectrum. We have extended that formalism to a complete analysis framework to consider the more general and practical scenarios in modern CMB experiments [130]. The analysis is no more limited to the leading order correction. Multipole moments of the beam function up to any order can be included in the analysis - the upper limit being set by the available computing power. Also the effect of incomplete sky coverage is automatically calculated by this new algorithm. However, as an intermediate step we have computed the final analytic results for “non-rotating” beams. We hope to include beam-rotation in near future. We have, both analytically and numerically, evaluated the leading order correction to match the results obtained with the perturbative analysis in the previous chapter as an important check of this method. Numerical evaluations also give an estimate of the computational requirement to use this method for the recent experiments. We find that wise choice of apodized mask functions (to hide the corrupt pixels) can provide significant reduction in computation cost. A possible way to construct such masks have also been explored. We conclude that this analysis has the potential to replace the computationally costly simulations currently used to determine the non-circular beam effects in the upcoming experiments like Planck.

The organization of this chapter is as follows. The full analytical details of

the new method will be presented in section 9.1. Here we also reproduce the standard analytical results in different limits, including the result of the perturbative analysis obtained in the previous chapter. The detailed calculations are given in the appendix F. An efficient algorithm for numerical implementation is given in section 9.2, which includes the possibility and demonstration of constructing apodized masks to reduce the computation cost. The detailed computational costs is also estimated in this section. Since the work presented in this chapter is a generalization to the perturbative analysis and essentially we are reproducing the results that have already appeared in the previous chapter, detailed motivation and interpretation of the results will not be repeated in this chapter - refer to the introduction and discussion sections of chapter 8 for these details. The importance and applicability of the new results will be discussed in the concluding section of this chapter.

## 9.1 Analytical Framework

The full likelihood analysis of beam non-circularity is computationally prohibitive, we use the sub-optimal pseudo- $C_l$  analysis. The basic formula for bias of the pseudo- $C_l$  estimator including the effects of the beam function and incomplete sky coverage was stated in section of the previous chapter, where the leading order correction with full sky coverage was explicitly computed. In this chapter, we derive general expression for bias including the effect of incomplete sky coverage. We start with the summary of the basic formulae provided in the previous chapters to make this chapter self-contained.

### 9.1.1 Bias in the pseudo- $C_l$ estimator

If the cosmic microwave background (CMB) temperature anisotropy field  $\Delta T(\hat{\mathbf{q}})$  over all the sky directions  $\hat{\mathbf{q}} \equiv (\theta, \phi)$  is Gaussian and statistically isotropic, the angular power spectrum,

$$C_l := \int_{S^2} d\Omega_{\hat{\mathbf{q}}_1} \int_{S^2} d\Omega_{\hat{\mathbf{q}}_2} \langle \Delta T(\hat{\mathbf{q}}_1) \Delta T(\hat{\mathbf{q}}_2) \rangle P_l(\hat{\mathbf{q}}_1 \cdot \hat{\mathbf{q}}_2) \quad (9.1)$$

provides a complete description of CMB. The angular power spectrum is related to the spherical harmonic transform of the temperature anisotropy sky,

$$a_{lm} := \int_{S^2} d\Omega_{\hat{\mathbf{q}}} \Delta T(\hat{\mathbf{q}}) Y_{lm}^*(\hat{\mathbf{q}}), \quad (9.2)$$

through the relation

$$C_l = \langle |a_{lm}|^2 \rangle = \frac{1}{2l+1} \sum_{m=-l}^l \langle |a_{lm}|^2 \rangle. \quad (9.3)$$

Following the above formulae, the pseudo- $C_l$  estimator is defined as

$$\tilde{C}_l := \frac{1}{2l+1} \sum_{m=-l}^l |\tilde{a}_{lm}|^2, \quad (9.4)$$

which can be rewritten as

$$\tilde{C}_l := \int_{S^2} d\Omega_{\hat{\mathbf{q}}_1} \int_{S^2} d\Omega_{\hat{\mathbf{q}}_2} \tilde{\Delta T}(\hat{\mathbf{q}}_1) \tilde{\Delta T}(\hat{\mathbf{q}}_2) P_l(\hat{\mathbf{q}}_1 \cdot \hat{\mathbf{q}}_2), \quad (9.5)$$

where  $\tilde{\Delta T}(\hat{\mathbf{q}})$  is temperature observed from direction  $\hat{\mathbf{q}}$  and  $P_l(x)$  is the Legendre polynomial of degree  $l$ . The observed temperature field is convolved with a beam (Point Spread) function  $B(\hat{\mathbf{q}}, \hat{\mathbf{q}}')$ , contaminated by noise  $n(\hat{\mathbf{q}})$  and partially masked by a weight function  $U(\hat{\mathbf{q}})$  to hide pixels corrupt by foreground (e.g., galactic and point) sources:

$$\tilde{\Delta T}(\hat{\mathbf{q}}) = U(\hat{\mathbf{q}}) \left[ \int_{S^2} d\Omega_{\hat{\mathbf{q}}'} B(\hat{\mathbf{q}}, \hat{\mathbf{q}}') \Delta T(\hat{\mathbf{q}}') + n(\hat{\mathbf{q}}) \right]. \quad (9.6)$$

In the circular beam and full-sky assumption the pseudo- $C_l$  estimator is trivially biased. But, in general (which is a more practical consideration), the pseudo- $C_l$  is *nontrivially biased*:

$$\langle \tilde{C}_l \rangle = \sum_{l'=0}^{\infty} A_{ll'} C_{l'} + C_N, \quad (9.7)$$

where  $A_{ll'}$  is the *bias matrix* for non-circular beams and incomplete sky coverage,

given by

$$A_{ll'} := \frac{2l'+1}{4\pi} \int_{S^2} d\Omega_{\hat{\mathbf{q}}_1} \int_{S^2} d\Omega_{\hat{\mathbf{q}}_2} U(\hat{\mathbf{q}}_1) U(\hat{\mathbf{q}}_2) P_l(\hat{\mathbf{q}}_1 \cdot \hat{\mathbf{q}}_2) \\ \times \int_{S^2} d\Omega_{\hat{\mathbf{q}}'_1} \int_{S^2} d\Omega_{\hat{\mathbf{q}}'_2} B(\hat{\mathbf{q}}_1, \hat{\mathbf{q}}'_1) B(\hat{\mathbf{q}}_2, \hat{\mathbf{q}}'_2) P_{l'}(\hat{\mathbf{q}}'_1 \cdot \hat{\mathbf{q}}'_2). \quad (9.8)$$

If the pixel to pixel noise is uncorrelated,  $\langle n(\hat{\mathbf{q}}_1) n(\hat{\mathbf{q}}_2) \rangle = \delta_{\hat{\mathbf{q}}_1 \hat{\mathbf{q}}_2} \sigma_N^2$ , where  $\sigma_N^2$  is the variance of noise at each pixel, the noise term becomes

$$C_N := \int_{S^2} d\Omega_{\hat{\mathbf{q}}_1} \int_{S^2} d\Omega_{\hat{\mathbf{q}}_2} U(\hat{\mathbf{q}}_1) U(\hat{\mathbf{q}}_2) \langle n(\hat{\mathbf{q}}_1) n(\hat{\mathbf{q}}_2) \rangle P_l(\hat{\mathbf{q}}_1 \cdot \hat{\mathbf{q}}_2) \\ = \int_{S^2} d\Omega_{\hat{\mathbf{q}}} U^2(\hat{\mathbf{q}}) \sigma_N^2(\hat{\mathbf{q}}). \quad (9.9)$$

The pixel noise variance  $\sigma_N^2$  can usually be measured with very high accuracy for CMB experiments, hence the noise term  $C_N$  is treated as a constant in our analysis.

### 9.1.2 Evaluation of the Bias Matrix

Evaluation of the bias matrix would be necessary to construct the unbiased pseudo- $C_l$  estimator

$$\tilde{C}_l^{\text{UB}} = \sum_{l'} [A^{-1}]_{ll'} (\tilde{C}_{l'} - C_N) \quad (9.10)$$

The integral expression [eqn (9.8)] for the bias matrix is computationally costly to evaluate to the desired accuracy. Unlike integration, accuracy of summations are limited by machine precision. So our aim would be to express the bias matrix as a summation. But, we shall see, that the summations often contain infinite number of terms and, hence, they have to be truncated for numerical computation. This again leads to numerical inaccuracy. However, the situation improves if we use expansions in terms of angular multipoles. Angular multipole moments give a much better geometrical picture of the system, so it becomes quite easy to identify and discard terms that have negligible contributions.

If the beam is circular, that is symmetric about the pointing direction [ $B(\hat{\mathbf{q}}, \hat{\mathbf{q}}') = B(\hat{\mathbf{q}} \cdot \hat{\mathbf{q}}')$ ], we may expand the beam function in terms of Legendre transforms  $B_l$ :

$$B(\hat{\mathbf{q}} \cdot \hat{\mathbf{q}}') = \sum_{l=0}^{\infty} \frac{2l+1}{4\pi} B_l P_l(\hat{\mathbf{q}} \cdot \hat{\mathbf{q}}'). \quad (9.11)$$

The full analysis for circular beams with incomplete sky coverage has been carried out in [167]. We shall reproduce these results in the circular beam limit as a check for our analysis. In general, the beam functions are expanded in terms of spherical harmonic moments  $b_{lm}(\hat{\mathbf{q}})$ :

$$B(\hat{\mathbf{q}}, \hat{\mathbf{q}}') = \sum_{lm} b_{lm}(\hat{\mathbf{q}}) Y_{lm}(\hat{\mathbf{q}}'). \quad (9.12)$$

Computation of the beam transforms  $b_{lm}(\hat{\mathbf{q}})$  for each direction  $\hat{\mathbf{q}}$  would be computationally prohibitive. Fortunately, the experimental beams do not change their shapes over the sky, though they can change the orientation with respect to the pointing direction as illustrated in figure 8.1. This fact was exploited in [117] to “rotate” the beam transforms evaluated at the  $\hat{\mathbf{z}}$  axis using Wigner- $D$  functions  $D_{mm'}^l(\hat{\mathbf{q}}, \rho(\hat{\mathbf{q}}))$ :

$$b_{lm}(\hat{\mathbf{q}}) = \sum_{m'=-l}^l D_{mm'}^l(\hat{\mathbf{q}}, \rho(\hat{\mathbf{q}})) b_{lm'}(\hat{\mathbf{z}}). \quad (9.13)$$

This relation made it possible to implement the analysis presented here using the available computing resources. From this point we shall drop the argument  $\hat{\mathbf{z}}$  from beam transform, i.e.  $b_{lm} \equiv b_{lm}(\hat{\mathbf{z}})$ .

Since the beams in most of the CMB experiments are mildly noncircular and circular beam approximation was used for their data analysis, in order to express the estimation error in a convenient form, we use a perturbative series to describe the deviation of the beam shape from the assumed circularity. The series is parameterized by the “beam distortion parameters” (BDP)  $\beta_{lm} := b_{lm}/b_{l0}$ . The “circularized” beam  $\mathcal{B}(\hat{\mathbf{z}} \cdot \hat{\mathbf{q}})$  is usually defined by azimuthally averaging the beam about the pointing direction:

$$\mathcal{B}(\hat{\mathbf{z}} \cdot \hat{\mathbf{q}}) = \frac{1}{2\pi} \int_0^{2\pi} d\phi B(\hat{\mathbf{z}}, \hat{\mathbf{q}}). \quad (9.14)$$

The Legendre transform of the circularized beam

$$B_l := \int_{-1}^1 d(\hat{\mathbf{z}} \cdot \hat{\mathbf{q}}) P_l(\hat{\mathbf{z}} \cdot \hat{\mathbf{q}}) \mathcal{B}(\hat{\mathbf{z}} \cdot \hat{\mathbf{q}}) \quad (9.15)$$

is related to the spherical harmonic transform of the beam by the relation

$$B_l = \sqrt{\frac{4\pi}{2l+1}} b_{l0}. \quad (9.16)$$

Which also means that the beam distortion parameters are related to the circularized beam transforms by the following equation:

$$\beta_{lm} = \sqrt{\frac{4\pi}{2l+1}} \frac{b_{lm}}{B_l}. \quad (9.17)$$

Similar to the beam function, we also expand the mask function in terms of its spherical harmonic transforms  $U_{lm}$ :

$$U(\hat{\mathbf{q}}) = \sum_{l=0}^{\infty} \sum_{m=-l}^l U_{lm} Y_{lm}(\hat{\mathbf{q}}). \quad (9.18)$$

It may be noted that roughly the beam multipoles are expected to affect the low angular scales (higher multipoles) [167] and the multipoles of mask are more significant at large angular scales (lower multipoles) [118]. However, if smaller structures are present in the mask, the higher multipole moments of the mask may get coupled with those of the beam and the overall effect of non-circular beams can significantly increase at high multipoles.

Putting everything together, we can now express the bias matrix as

$$A_{ll'} = \frac{B_{l'}^2}{4\pi} \frac{(2l'+1)}{(2l+1)} \sum_{n=-l}^l \sum_{m=-l'}^{l'} \left| \sum_{m'=-l'}^{l'} \beta_{l'm'} \sum_{l''=0}^{\infty} \sum_{m''=-l''}^{l''} U_{l''m''} J_{nm''mm'}^{ll''l'} \right|^2, \quad (9.19)$$

where the integral over two sphere  $S^2$

$$J_{nm''mm'}^{ll''l'} := \int_{S^2} d\Omega_{\hat{\mathbf{q}}} Y_{ln}(\hat{\mathbf{q}}) Y_{l''m''}(\hat{\mathbf{q}}) D_{mm'}^{l'}(\hat{\mathbf{q}}, \rho(\hat{\mathbf{q}})), \quad (9.20)$$

has to be calculated to get the general expression for the bias matrix. The details of the mathematics have been provided in appendix F.

Evaluation of the above integral is quite non-trivial. To simplify calculations, the final analytical results derived in this thesis has been restricted to “non-rotating” beams [ $\rho(\hat{\mathbf{q}}) = 0$ ]. However, this is an intermediate step and the extension of this method to include beam rotation should not be far off. We hope to include beam-rotation in the final analytical result in near future.

Two approaches have been taken in order to derive the above integral. Because of the complications inherent to the integral, we reach different forms (identical results, of course) of the final result [see appendix F for details].

First, using sinusoidal expansion of the Wigner- $D$  functions (which is motivated from [100], but we corrected the final expression given in that reference)

$$d_{mm'}^l(\theta) = i^{m+m'} \sum_{M=-l}^l \left[ (-1)^M d_{mM}^l\left(\frac{\pi}{2}\right) e^{iM\theta} d_{Mm'}^l\left(\frac{\pi}{2}\right) \right] \quad (9.21)$$

we get the following expression for the bias matrix:

$$\begin{aligned} A_{ll'} = & B_l^2 \frac{(2l'+1)}{16\pi} \sum_{n=-l}^l \sum_{m=-l'}^l \left| \sum_{l''=0}^{\infty} \sqrt{2l''+1} U_{l''(m-n)} \times \right. \\ & \sum_{M'=-l''}^{l''} d_{(m-n)M'}^{l''}\left(\frac{\pi}{2}\right) d_{M''0}^{l''}\left(\frac{\pi}{2}\right) \sum_{M=-l}^l d_{nM}^l\left(\frac{\pi}{2}\right) d_{M0}^l\left(\frac{\pi}{2}\right) \times \\ & \left. \sum_{M'=-l'}^l d_{mM'}^{l'}\left(\frac{\pi}{2}\right) \sum_{m'=-l'}^l \beta_{l'm'} d_{M'm'}^{l'}\left(\frac{\pi}{2}\right) f(m'; M+M'+M'') \right|^2, \end{aligned} \quad (9.22)$$

where the function  $f(m'; N)$  in the above expression is defined as

$$\begin{aligned} f(m'; N) & := \Re \left[ i^{m'} (-1)^N \int_0^\pi \sin \theta d\theta e^{iN\theta} \right] \\ & = \begin{cases} (-1)^{(m'\pm 1)/2} \pi/2 & \text{if } m' = \text{odd and } N = \pm 1 \\ (-1)^{m'/2} 2/(1-N^2) & \text{if both } m', N = 0 \text{ or even} \\ 0 & \text{otherwise.} \end{cases} \end{aligned} \quad (9.23)$$

Alternatively, in addition to the sinusoidal expansion of wigner- $D$  [eqn (9.21)], using the Clebsh Gordon Series [100]

$$D_{m_1 n_1}^{l_1}(\hat{\mathbf{q}}, \rho) D_{m_2 n_2}^{l_2}(\hat{\mathbf{q}}, \rho) = \sum_{l=|l_1-l_2|}^{l_1+l_2} C_{l_1 m_1 l_2 m_2}^{l(m_1+m_2)} D_{(m_1+m_2)(n_1+n_2)}^l(\hat{\mathbf{q}}, \rho) C_{l_1 n_1 l_2 n_2}^{l(n_1+n_2)}, \quad (9.24)$$

where  $C_{l_1 m_1 l_2 m_2}^{lm}$  are the Clebsh-Gordon coefficients, we get the following expression

for the bias matrix:

$$\begin{aligned}
 A_{ll'} &= B_l^2 \frac{(2l' + 1)}{16\pi} \sum_{n=-l}^l \sum_{m=-l'}^{l'} \left| \sum_{l''=0}^{\infty} \sqrt{2l'' + 1} U_{l''(m-n)} \sum_{L=|l-l''|}^{l+l''} C_{l0l''0}^{L0} C_{lm'l''(m-n)}^{Lm} \right. \\
 &\times \left. \sum_{L'=|L-l'|}^{L+l'} C_{L-ml'm}^{L'0} \sum_{N=-L'}^{L'} d_{0N}^{L'} \left( \frac{\pi}{2} \right) \sum_{m'=-l'}^{l'} \beta_{l'm'} C_{L0l'm'}^{L'm'} d_{Nm'}^{L'} \left( \frac{\pi}{2} \right) f(m'; N) \right|^2. \quad (9.25)
 \end{aligned}$$

### 9.1.3 Checking different limits

The special cases of circular beam and complete sky coverage limits are readily recovered from our general expressions.

First, we consider the simplest case of complete sky coverage  $U_{lm} = \sqrt{4\pi}\delta_{l0}$  with circular beam limit  $\beta_{lm} = \delta_{m0}$ . We show in the appendix F section F.5 that we get back the well known result

$$A_{ll'} = B_l^2 \delta_{ll'}.$$

Hivon et al. [167] formulated MASTER (Monte Carlo Apodized Spherical Transform Estimator) method for the estimation of CMB angular power spectrum from “cut” (incomplete) sky coverage for circular beams. Substituting the circular beam limit [ $\beta_{lm} = \delta_{m0}$ ] in the expression for bias matrix we recover the MASTER circular beam result in appendix F section F.6:

$$A_{ll'} = B_l^2 \frac{2l' + 1}{4\pi} \sum_{l''=|l-l'|}^{l+l'} (2l'' + 1) \begin{pmatrix} l & l' & l'' \\ 0 & 0 & 0 \end{pmatrix}^2 \mathcal{U}_{l''}, \quad (9.26)$$

where  $\mathcal{U}_{l''} := \sum_{m'=-l''}^{l''} |U_{l''m'}|^2 / (2l'' + 1)$ .

Finally, in appendix F section F.7, we recover the general formula for full sky coverage with non-circular beams presented in [118]. We substitute  $U_{lm} = \sqrt{4\pi}\delta_{l0}$  in the expression for the bias matrix and get back<sup>1</sup> eqn (38) of [118]

$$A_{ll'} = B_l^2 \frac{(2l' + 1)}{4} \sum_{m=-\min(l,l')}^{\min(l,l')} \left| \sum_{m'=-l'}^{l'} \beta_{l'm'} \int_{-1}^1 d \cos \theta d_{m0}^l(\theta) d_{mm'}^{l'}(\theta) \right|^2. \quad (9.27)$$

<sup>1</sup>Note that due to a somewhat different definition of bias matrix in [118], for  $C_l := [l(l+1)/(8\pi^2)]C_l$ , the results differ by a factor of  $[l'(l'+1)]/[l(l+1)]$ .

Unfortunately, because of the rather complicated form in the final expression for leading order correction to bias matrix presented in eqn (43) of [118], it is not possible to explicitly compare the results term by term.

## 9.2 Implementation

An important motivation for deriving the analytic results is the computationally prohibitive nature of the hierarchy of four integrals over the 2-spheres in the expression for the bias matrix. However, even the computation of the algebraic expression for the bias matrix is computationally challenging. A detailed numerical implementation has been proposed in this section.

The final analytic form of the bias matrix contains infinite summations. These summations have to be truncated using reasonable physical insights. Let us denote the  $l, m$  cut-offs for the mask and beam by  $l_{\text{mask}}, m_{\text{mask}}$  and  $l_{\text{beam}}, m_{\text{beam}}$  respectively. The choice of the numerical values for these cut-offs will be provided in the numerical results section.

Calculation of the final expression directly, using the analytic expression given by eqn (9.22), is computationally challenging. Three major innovations have been introduced in order to numerically evaluate the bias matrix for beams of reasonable size. Moreover, we also suggest the use of ‘‘apodized’’ masks in order to reduce computational cost. The details are given below:

1. We used a smart implementation of the hierarchical summations to successfully reduce the computation cost by a few orders of magnitude. To calculate three coupled loops of the form

$$S = \sum_{i=1}^N \sum_{j=1}^N \sum_{k=1}^N f(i + j + k), \quad (9.28)$$

apparently  $N^3$  operations are necessary. However, if we calculate the summation in the following order:

$$V(m) := \sum_{k=1}^N f(m + k); \quad m = 1, 2, \dots, 2N \quad (9.29a)$$

$$S = \sum_{i=1}^N \sum_{j=1}^N V(i + j) \quad (9.29b)$$

we effectively require just  $2N^2 + N^2 = 3N^2$  operations. The computational gain is  $N/3$ . For  $N = 900$ , this factor is 300. This example was for a very simple case where all the summations have the same limits, but clearly this can be extended to the case of summations with unequal limits and match our analysis [See appendix G for details].

In our analysis the summations within the modulus symbols in eqn (9.22) (that is for each pair of  $m, n$ ) are computed in three stages:

- Step I:

$$V_1(N) = \sum_{M'=-l'}^{l'} d_{mM'}^{l'} \left( \frac{\pi}{2} \right) \sum_{m'=-m_{\text{beam}}}^{m_{\text{beam}}} \beta_{l'm'} d_{M'm'}^{l'} \left( \frac{\pi}{2} \right) f(m'; M' + N) \quad (9.30a)$$

$N$  runs from  $-(l + m_{\text{mask}})$  to  $+(l + m_{\text{mask}})$

- Step II

$$V_2(M'') = \sum_{M=-l}^l d_{nM}^l \left( \frac{\pi}{2} \right) d_{M0}^l \left( \frac{\pi}{2} \right) V^1(M + M'') \quad (9.30b)$$

- Step III

$$V_3 = \sum_{l'=0}^{l_{\text{mask}}} \sqrt{2l'+1} U_{l'(m-n)} \times \sum_{M''=-m_{\text{mask}}}^{m_{\text{mask}}} d_{(m-n)M''}^{l''} \left( \frac{\pi}{2} \right) d_{M''0}^{l''} \left( \frac{\pi}{2} \right) V^2(M'') \quad (9.30c)$$

For  $l_{\text{beam}} = l_{\text{max}}$  the above algorithm reduces the computation cost from  $\sim (8/3)(2m_{\text{mask}} + 1)(2m_{\text{beam}} + 1)l_{\text{max}}^5 l_{\text{mask}}^2$  to  $\sim (4/3)(2m_{\text{mask}} + 1)(2m_{\text{beam}} + 1)l_{\text{max}}^5$ , providing a speed-up factor of  $\sim 2l_{\text{mask}}^2$ . It is important to note that, small values of  $m_{\text{beam}}$  lead to computational speed up.

Mildly non-circular beams, where the BDP  $\beta_{lm}$  at each  $l$  falls off rapidly with  $m$ , allows us to neglect  $\beta_{lm}$  for  $m > m_{\text{beam}}$ . For most real beams,  $m_{\text{beam}} \sim 4$  is a sufficiently good approximation [117] and this cuts off the summation over BDP in the bias matrix  $A_{ll'}$ .

Soft, azimuthally apodized, masks where the coefficients  $U_{lm}$  are small beyond  $m > m_{\text{mask}}$ . Moreover, it is useful to smooth the mask in  $l$ , such the  $U_{lm}$  die

off rapidly for  $l > l_{\text{mask}}$  too. More details on apodized mask will be provided below.

2. The Wigner- $d$  functions with argument  $\pi/2$  occur too frequently in the above evaluation. So one possibility to reduce computation cost is to pre-compute all the Wigner- $d$  coefficients  $d_{mm}^l(\pi/2)$  at once. But for  $l \sim 1000$  this scheme is limited by disk storage and/or program Input/Output (I/O).

However, we may observe that, in each step of computation described in eqn (9.30) only one value of  $l$  occurs in the  $d$  symbols. Hence we use an efficient recursive routine presented in [181] that generates all the  $d_{mm}^l(\pi/2)$  at once for a given value of  $l$ . This allows us to compute the Wigner- $d$  symbols efficiently and use them as constant co-efficients at each step without any significant I/O limited operations.

3. We know that the bias matrix is not far off from diagonal, because the beams are mildly non-circular. So we need not compute all the elements of the bias matrix. Rather, a diagonal band (could be of triangular shape) of average “thickness”  $\Delta l$  can be used to calculate the  $C_l$  estimation error with a fairly high accuracy. This can give an additional speed-up factor of  $\sim l/\Delta l$ .
4. As pointed out above, the computational cost is proportional to  $m_{\text{mask}}$ . Since the mask function is within our control, judicious choice of masks with low  $m_{\text{mask}}$  would reduce the computation cost. We suggest a method to construct such a mask function by smoothing over the azimuthal axis<sup>2</sup>.

We first find the spherical harmonic transforms  $U_{lm}$  of the “essential mask” (e.g., the WMAP Kp2 mask) needed to hide the foreground contaminated pixels. We smooth it using the transformation formula

$$U'_{lm} = \exp(-m * m / [\alpha m_{\text{mask}}^2]) * U_{lm}, \quad (9.31)$$

and reconstruct the new mask from the above spherical harmonic transforms  $U'_{lm}$ . Finally, in order to make sure that the contaminated points are completely blocked from the analysis, we multiply the recovered mask with the essential mask pixel by pixel. The effect of this smoothing is illustrated using figure 9.1. The left panel of figure 9.1 shows the original WMAP Kp2 mask (without the point sources) and the right panel shows the azimuthally smoothed masks.

<sup>2</sup>Recently, similar apodized masks have also been recommended in the context of CMB polarization maps [182].

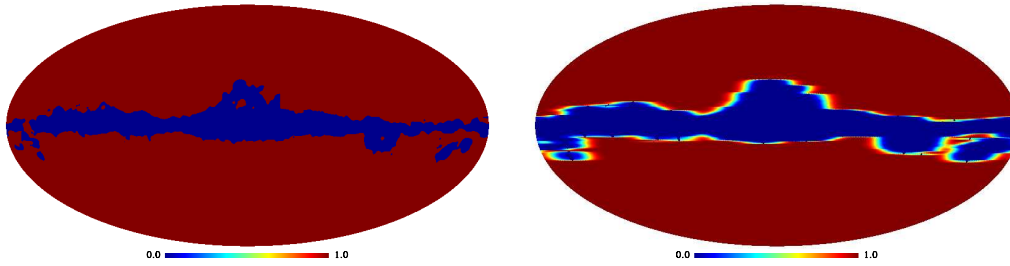


Figure 9.1: The original Kp2 mask.

The effectiveness of the smoothed mask can be readily seen by comparing the spherical harmonic transforms of the above two masks as shown in figure 9.2. The left panel shows the (real part of) the true WMAP Kp2 mask (left panel of figure 9.1) and the right panel shows the spherical harmonic transforms of the azimuthally smoothed mask (right panel of figure 9.1). Clearly, the spherical

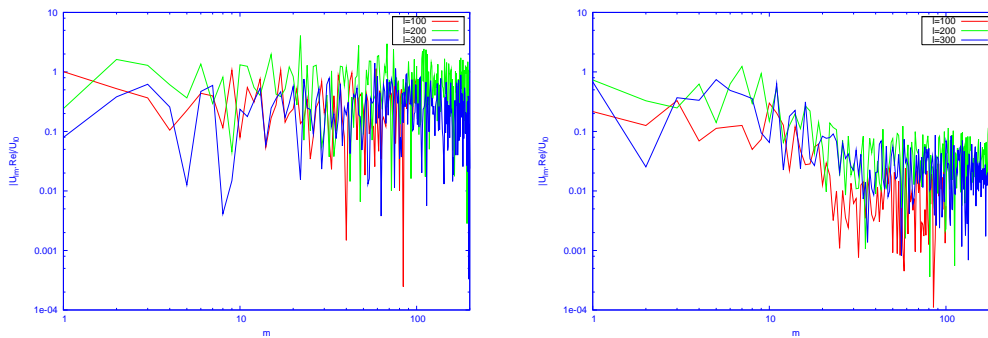


Figure 9.2: **Comparison of mask transforms.** The mask transforms for the regular WMAP Kp2 mask (left) and the azimuthally smoothed apodized mask (right) have been compared in this figure. Clearly the apodized mask has suppressed high  $m$  content, which allows an early cut off in the mask summation, leading to reduction in computation cost.

harmonic transforms of the azimuthally smoothed mask falls off by an order of magnitude after  $m \sim 20$  opening up a scope for huge computational gain, which is not accessible with the original WMAP Kp2 mask.

Apart from the above major steps we also obtained several speed-up factors utilizing the symmetries with respect to the indices.

The above scheme was numerically implemented to reproduce leading order correction to the pseudo- $C_l$  estimator presented in section . The results were consistent within numerical errors.

### 9.3 Discussions and Conclusion

The effect of non-circular beams has become progressively important as CMB experiments strive to attain higher resolution. Incorporating the non-circularity of experimental beams in the Maximum Likelihood analysis is computationally prohibitive when the number of pixels is large (say  $> 50000$ ). We present a complete analytic framework to account for the effect of non-circular beams on the pseudo- $C_l$  estimator extending to the case of incomplete sky coverage. The analytical details was presented in this section. The computation of the analytical expression is also nontrivial. Several smart innovations have been introduced in the numerical evaluation scheme for efficient computation. We also suggest azimuthally smoothed masks in order to reduce the computational cost. The leading order correction to CMB power spectrum for non-circular obtained by a perturbative analysis in our previous work has been successfully reproduced using the current analysis.

The analysis will be extremely important for the estimation of the effect of non-circular beams on CMB polarization power spectrum. It is expected that the non-circular beams would induce more leakage from E to B polarization by getting coupled to the weak gravitational lensing. Our analysis can provide a good starting point to estimate that systematic effect. Also, the work presented here can be extended to study the statistical anisotropy of the observed CMB maps induced due to the combined effect of beam non-circularity and incomplete sky coverage.



## Chapter 10

# Conclusion

The past five years have been an exciting period for the gravitational waves (GW) and cosmic microwave background (CMB) experiments. These experiments produce huge volumes of data and pose several analysis challenges. We addressed few of the important analysis issues in this thesis. We have developed and implemented techniques to efficiently extract science out of the data. Several important and relevant calculational details for GW and CMB analysis have been presented in the appendices.

GW strains in the detectors are overwhelmed by noise. Prior knowledge of the expected signal has to be used to search for GW with the present day detectors. Matched filtering is optimal where the waveform can be accurately determined. The conventional matched filtering based search for inspirals is computationally costly. Interpolation of the match function over the parameter space can reduce the number of matched filters required to search over the parameter space utilizing the statistical correlation between templates. We developed an interpolating search algorithm where we used Chebyshev interpolation for its near minimax property. We tested the algorithm for a one dimensional intrinsic parameter space using Newtonian Chirp signal from inspiraling binaries. We observed 25% reduction in the number of templates - which can lead to an order of magnitude improvement in the efficiency over a multidimensional parameter space. The Chebyshev interpolated scheme can improve the efficiencies of the conventional dense search algorithms without using any extra computation. Also, there is a possibility of using Chebyshev interpolation in the first stage of hierarchical search to improve the efficiency of the first stage, which is the most computationally costly part of the hierarchical search.

There exists a stochastic GWB generated by unresolved and unmodeled as-

trophysical sources and tensor perturbations in the early universe. This is quite similar to CMB in electro-magnetic astronomy. Since the noise in the GW detectors are independent, the best strategy to detect the GWB is by correlating outputs from different detectors. The correlation is done through a sky model dependent optimal filter. The optimal filter can be properly chosen in order to measure the all-sky averaged strength of the GWB, as well as to make map of the GWB sky by introducing a time dependent phase delay that account for the light travel time delay between the detector sites. This approach is quite similar to the earth rotation synthesis imaging used in CMB and radio astronomy, and hence named as GW radiometer.

The theory of general radiometer analysis has been presented in this thesis. In this course, we have developed the full analysis technique to estimate the true GWB skymaps, which extends to more than one baselines. The beam function (kernel of the convolution equation) has been analytically understood using Stationary Phase Approximation (SPA). We have numerically implemented the analysis on simulated data. The injected maps were successfully recovered with almost all the detailed structures, which was a great success for this first ever attempt to estimate the true GWB sky using the current ground based GW detectors.

However, this analysis relies on certain assumptions on the source - the frequency power distribution is independent of direction and the waves of polarizations are independent, these assumptions need to be removed/relaxed in order to formulate a more general analysis. The analysis should also be extended to analyze data from the space based detectors, which are more sensitive to the GWB as compared to the ground based detectors. This can be done by incorporating time delay interferometry in the radiometer framework. The radiometer analysis implemented so far considers only blind estimations - no prior knowledge of the sky was used. Construction of a model of the sky in pixel or spherical harmonic basis, e.g., by taking inputs from electro-magnetic astronomy, would improve the signal to noise ratio. Finally, different directions of the sky were assumed to be uncorrelated; this assumption does not hold for a cosmological GWB, which can be correlated at scales even greater than the beam size. The possibility of using a Legendre or spherical harmonic expansion of the angular correlation function of the GWB sky should be explored in order to generalize the GW radiometer analysis.

The observed CMB and GWB skymaps are convolved with experimental beam patterns. Estimation of the true skymap requires the deconvolution of the skymaps with the beam patterns. The maximum likelihood skymap estimation had been successfully applied to CMB analysis for more than a decade. Because of the broad

similarity between CMB and GWB map making we adapted a similar analysis strategy to estimate true GWB skymaps. The method was implemented using MATLAB® coding and test maps were deconvolved with great success - we got back nearly what we injected. So far the comparison between the injected and recovered maps has only been done visually, work is in progress to formulate a scheme to quantify the quality of deconvolution. The deconvolution technique used here closely follows CMB analysis, a more customized method would improve the quality of deconvolution.

Maximum likelihood deconvolution of CMB skymaps with non-circular beams for the present day high resolution experiments is computationally prohibitive. CMB anisotropy maps are deconvolved assuming a circular beam of infinite resolution, which introduces a bias in the skymaps and the angular power spectra. Beam correction is directly applied to debias the angular power spectrum obtained from the undeconvolved map - the pseudo- $C_l$  estimator. The effect of non-circularity of the experimental beam becomes important at high multipoles (low angular size). We have developed a general analysis technique to account for the non-circular beams including the effect of the incomplete sky coverage. The leading order correction predicted by our analysis has matched the error estimated in the WMAP third year results. We also suggest apodized masks to reduce the computational cost required to implement our analysis. The non-circular beams can introduce statistical anisotropy in the statistically isotropic true CMB anisotropy. The effect of non-circular beams will affect the CMB polarization power spectrum more severely, as this will increase the leakage of E-polarization to B-polarization by getting coupled to the weak lensing effect. We plan to estimate these effects in the near future.



## Appendix A

# Properties of the Chebyshev Polynomials

Below we list a few important properties of the Chebyshev polynomials taken from [66].

1. The  $n^{\text{th}}$  degree Chebyshev polynomial:

$$T_n(x) \equiv \cos(n \cos^{-1} x). \quad (\text{A.1})$$

2. Chebyshev polynomials  $T_n(x)$  satisfy the differential equation:

$$(1 - x^2) \frac{d^2}{dx^2} T_n(x) - x \frac{d}{dx} T_n(x) + n^2 T_n(x) = 0 \quad (\text{A.2})$$

3. Chebyshev polynomials satisfy the recursion relation:

$$T_{n+1}(x) = 2x T_n(x) - T_{n-1}(x) \quad (\text{A.3})$$

4. List of the first few  $T_n(x)$ ,  $n = 0, 1, \dots, 5$ :

$$T_0(x) = 1 \quad (\text{A.4a})$$

$$T_1(x) = x \quad (\text{A.4b})$$

$$T_2(x) = 2x^2 - 1 \quad (\text{A.4c})$$

$$T_3(x) = 4x^3 - 3x \quad (\text{A.4d})$$

$$T_4(x) = 8x^4 - 8x^2 + 1 \quad (\text{A.4e})$$

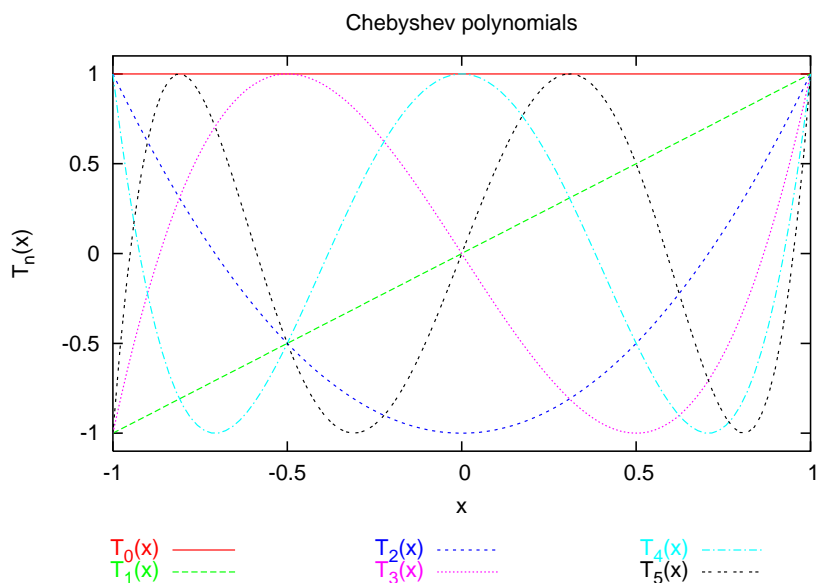


Figure A.1: Plots of the first few orders of Chebyshev polynomials

Fig. A.1 shows the plots of the above listed polynomials.

5. The zeroes ( $x_m$ ) of the  $(n + 1)^{\text{th}}$  degree Chebyshev polynomial  $T_{n+1}(x)$  are located at:

$$x_m = \cos \frac{(m - \frac{1}{2})\pi}{n + 1}, \quad m = 1, 2, \dots, n + 1. \quad (\text{A.5})$$

## Appendix B

# Directed GW Radiometer Beam: Stationary Phase Approximation

The beam function is the profile of the observed skymap using a directed GW radiometer if only one unit point source is present on the sky. The study of the beam function will enable us to analyze the properties of the convolution equation, as well as to devise a scheme for efficient pixelization of the sky. Here we attempt to develop an analytical approach to handle the beam function.

We shall find the beam function around the pointing direction  $\hat{\Omega}_0 \equiv (\theta_0, \phi_0)$ , which is equivalent of placing a unit point source at  $\hat{\Omega}_0$  and evaluating the point estimate. We may rewrite eqn (6.12) as the expectation of the observed point estimate for this case:

$$\langle S(\hat{\Omega}) \rangle = \left[ \int_0^T dt / \lambda(\hat{\Omega}, t) \right]^{-1} \int_0^T dt \Gamma(\hat{\Omega}, t) \Gamma(\hat{\Omega}_0, t) \int_{-\infty}^{\infty} df G(t; f) e^{-2\pi i f \Delta\Omega \cdot \Delta\mathbf{x}(t)/c}, \quad (\text{B.1})$$

where  $\Delta\Omega := \hat{\Omega} - \hat{\Omega}_0$ . For simplicity, in the above equation we have replaced the summation over  $i$  by an integration over sidereal time  $t$ . Our aim is to analytically extract as much as possible information from the above integral.

We shall first find an approximate beam pattern, that is, the points on the sky where the point estimates stand out. Then we shall approximately evaluate the values of the beam pattern on the trajectory.

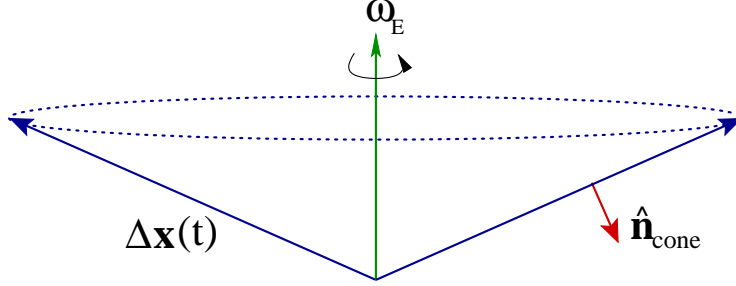


Figure B.1: **Cone traced out by a radiometer baseline.** The baseline formed by two detectors,  $\Delta \mathbf{x}(t)$  traces out a cone as the earth rotates. A schematic diagram is shown here. The vector  $\hat{\mathbf{n}}_{\text{cone}}(t)$  is normal to the baseline as we as the cone.

## B.1 Beam Pattern: SPA Trajectory

Application of Stationary Phase Approximation (SPA) can explain certain features that are present in the numerical beam function, basically the shape of the beam, which closely resembles a tear drop or the integer “8”.

The rapidly varying part in the integrand of eqn (B.1) is the phase term. Setting the first derivative of phase with respect to  $f$  and  $t$  to zero we get

$$\Delta \Omega \cdot \Delta \mathbf{x}(t) = 0, \quad (\text{B.2})$$

$$\Delta \Omega \cdot \Delta \mathbf{x}'(t) = 0, \quad (\text{B.3})$$

where  $\Delta \mathbf{x}'(t) := d\Delta \mathbf{x}(t)/dt$ . The detector separation vector  $\Delta \mathbf{x}(t)$  rotates about the earth's rotation axis (z-axis in our coordinate system) with the angular velocity  $\omega_E$ . Geometrically  $\Delta \mathbf{x}(t)$  traces out a right circular cone with z-axis as its symmetry axis [see Figure B.1].

The angle of the cone  $\Theta$  is given by [since  $0 \leq \Theta \leq \pi$ , i.e.,  $\sin \Theta$  is positive]

$$\Theta = \cos^{-1} \frac{\cos \theta_1 - \cos \theta_2}{\sqrt{2[1 - \cos \theta_1 \cos \theta_2 - \sin \theta_1 \sin \theta_2 \cos(\phi_1 - \phi_2)]}}, \quad (\text{B.4})$$

where  $(\theta_l, \phi_l)$  are the detector coordinates. If the initial phase is  $\Phi$ , we may write

$$\Delta x(t) = \Delta R \sin \Theta \cos(\omega_E t + \Phi), \quad (\text{B.5a})$$

$$\Delta y(t) = \Delta R \sin \Theta \sin(\omega_E t + \Phi), \quad (\text{B.5b})$$

$$\Delta z(t) = \Delta R \cos \Theta = \text{constant}, \quad (\text{B.5c})$$

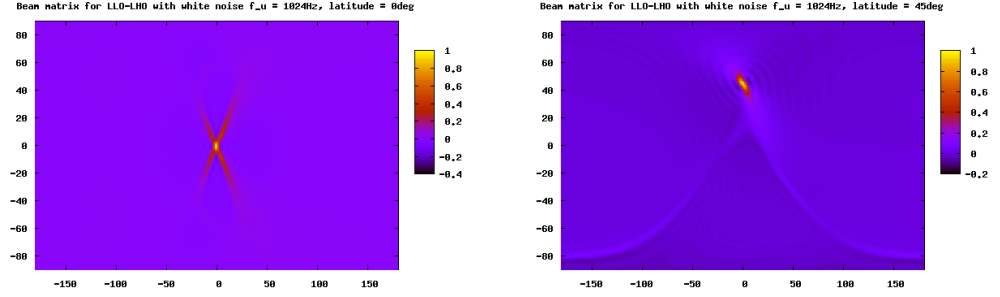


Figure B.2: **Beam functions in flat latitude-longitude grid.** The beam patterns are plotted in a flat grid of latitude and longitudes for the LIGO baseline with white noise. The upper cut off frequency is 1024Hz. Pointing directions are at latitudes  $0^\circ$  (left) and  $45^\circ$  (right). Beam functions are independent of pointing longitude because of azimuthal symmetry for observation over full day(s) with stationary noise. Note that, the slopes of the legs near the core of is  $\sim \pm 2$  in the left panel.

where  $\Delta R := |\Delta \mathbf{x}(t)|$  is the distance between the detectors and remains constant. This implies that  $\Delta \mathbf{x}(t) \cdot \Delta \mathbf{x}'(t) = 0$ . Thus  $\Delta \mathbf{x}(t)$ ,  $\Delta \mathbf{x}'(t)$  and  $\Delta \boldsymbol{\Omega}$  should form an orthogonal triad for the phase to be stationary. Therefore, for the SPA condition to exist  $\Delta \boldsymbol{\Omega}$  should be parallel to the normal  $\hat{\mathbf{n}}_{\text{cone}}(t)$  to the baseline, as well as, the cone traced out by the baseline.

We first consider the case of small  $\Delta \boldsymbol{\Omega}$  to have a feeling for the numbers. Then we derive the general solution.

### B.1.1 The case of small $\Delta \boldsymbol{\Omega}$

If the numerical beam function for a full day of observation is plotted in a plane cartesian grid of latitude and longitude, as shown in figure B.2, we can see four “legs” are coming out of the core of the beam. For equatorial pointing direction (left panel),  $\theta_0 = \pi/2$ , the legs have slopes  $\sim \pm 2$ .

Since the beam function for a full day’s observation is independent of pointing longitude, we assume the source to be at  $\phi_0 = 0$  without any loss of generality. Thus,

$$\hat{\boldsymbol{\Omega}}_0 = (\sin \theta_0, 0, \cos \theta_0). \quad (\text{B.6})$$

For small  $\Delta \boldsymbol{\Omega}$  we have  $\Delta \boldsymbol{\Omega} \cdot \hat{\boldsymbol{\Omega}}_0 = 0$ , thus  $\Delta \boldsymbol{\Omega}$  lies in a plane normal to  $\hat{\boldsymbol{\Omega}}_0$ . Writing

$\Delta\Omega = \Delta\Omega\hat{\mathbf{q}}$ , where  $\hat{\mathbf{q}}$  is a unit vector;  $q$  is parametrically given by,

$$\hat{\mathbf{q}} = (-\cos\theta_0\cos\psi, \sin\psi, \sin\theta_0\cos\psi). \quad (\text{B.7})$$

The SPA conditions are satisfied if  $\exists\phi$  and  $\psi$  such that  $\hat{\mathbf{q}}$  is normal to the cone. The set of normals to the cone is parametrically given by

$$\hat{\mathbf{n}}_{\text{cone}}(t) = (\cos\Theta\cos\phi, \cos\Theta\sin\phi, -\sin\Theta), \quad (\text{B.8})$$

where  $0 \leq \phi \leq 2\pi$  and  $\phi = \omega_E t$  [again, due to azimuthal symmetry, we have the liberty to assume  $\phi = 0$  at  $t = 0$ ]. We get three equations for  $\phi$  and  $\psi$  from eqn B.8 and eqn B.7, which must be consistent. We can solve for  $\phi$  and  $\psi$  from the  $x$  and  $z$  components:

$$\cos\psi = \pm \sin\Theta / \sin\theta_0 \quad (\text{B.9})$$

$$\cos\phi = \pm \cot\theta_0 \tan\Theta, \quad (\text{B.10})$$

which consistently matches the  $y$  component. The  $\psi$  gives the direction of the legs and the  $\phi = \omega_E t$  gives which data segment in time contributes.

Assuming source position at  $\theta_0 = \pi/2$

$$\cos\psi = \pm \sin\Theta = \cos(\Theta \pm \pi/2). \quad (\text{B.11})$$

Using

$$\sin\theta_0 \frac{\Delta\phi}{\Delta\theta} = \tan\psi \quad (\text{B.12})$$

to the first order the above equation gives

$$\frac{\Delta\theta}{\Delta\phi} = \pm \tan\Theta. \quad (\text{B.13})$$

The approximate coordinates of the LIGO detectors are given in Table B.1.1. For the LLO-LHO pair we get  $\tan\Theta = -1.98$ . The slopes of the legs of the beam, as

Detector	LLO	LHO
latitude	30.5	46.5
longitude	-90.75	-119.5

Table B.1: Coordinate of the LIGO detectors

shown in the left panel of figure B.2, are also  $\sim \pm 2$ , thus satisfying eqn (B.13).

### B.1.2 General SPA solution

The calculation for infinitesimal  $\Delta\Omega$  given above provides a comprehensive geometrical picture and the directions of the legs. It is also possible to algebraically derive a general expression for the values of  $\Delta\Omega$  for which the SPA conditions hold.

Phase part of the integrand is stationary when  $\Delta\mathbf{x}(t)$ ,  $\Delta\mathbf{x}'(t)$  and  $\Delta\Omega$  form an orthogonal triad. Since

$$\hat{\mathbf{n}}_{\text{cone}}(t) = \frac{\Delta\mathbf{x}(t) \times \Delta\mathbf{x}'(t)}{|\Delta\mathbf{x}(t) \times \Delta\mathbf{x}'(t)|'}$$

SPA condition is satisfied when  $\Delta\Omega = \Delta\Omega \hat{\mathbf{n}}_{\text{cone}}(t)$ , where  $\Delta\Omega$  can take *both positive or negative* values. Since both  $\hat{\Omega}_0$  and  $\hat{\Omega} = \hat{\Omega}_0 + \Delta\Omega$  should be of unit length

$$\hat{\Omega} \cdot \hat{\Omega} = (\hat{\Omega}_0 + \Delta\Omega) \cdot (\hat{\Omega}_0 + \Delta\Omega) \quad (\text{B.14})$$

$$\Rightarrow 1 = 1 + 2\Delta\Omega \hat{\Omega}_0 \cdot \hat{\mathbf{n}}_{\text{cone}}(t) + (\Delta\Omega)^2 \quad (\text{B.15})$$

$$\Rightarrow \Delta\Omega = -2\hat{\Omega}_0 \cdot \hat{\mathbf{n}}_{\text{cone}}(t) \quad (\text{B.16})$$

Hence we may write

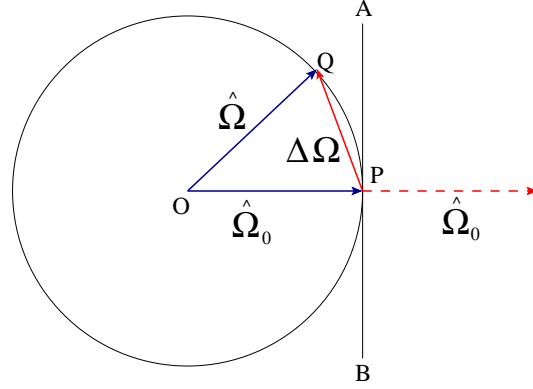
$$\Delta\Omega = -2[\hat{\Omega}_0 \cdot \hat{\mathbf{n}}_{\text{cone}}(t)] \hat{\mathbf{n}}_{\text{cone}}(t). \quad (\text{B.17})$$

Thus the set of points satisfying the SPA conditions are given in the parametric form

$$\hat{\Omega}(t) = \hat{\Omega}_0 - 2[\hat{\Omega}_0 \cdot \hat{\mathbf{n}}_{\text{cone}}(t)] \hat{\mathbf{n}}_{\text{cone}}(t). \quad (\text{B.18})$$

As a consistency check, we prove below that  $|\Delta\Omega|$  is always positive:

Note that  $\hat{\mathbf{n}}_{\text{cone}}(t)$  can have any direction. The above equation makes sure that it connects two points on a unit 2-sphere, which can be justified with the following diagram:



Here  $P(\hat{\Omega}_0)$  and  $Q(\hat{\Omega})$  are two points on the unit 2-sphere. We have drawn a plane  $AB$  tangent to the sphere at  $P$ . The figure shows a 2-D cross-section that contains both  $\hat{\Omega}$  and  $\hat{\Omega}_0$ . Clearly, since the vector  $\Delta\Omega$  starts at  $P$  and ends at another point  $Q$  on the sphere,  $\Delta\Omega$  can never cross the tangent plane. Hence the angle between  $\hat{\Omega}_0$  and  $\Delta\Omega$  is never less than  $\pi/2$ , which implies that,  $\hat{\Omega}_0 \cdot \Delta\Omega$  is always *negative*. This is consistently guaranteed by eqn (B.17), as

$$\hat{\Omega}_0 \cdot \Delta\Omega = -2 [\hat{\Omega}_0 \cdot \hat{\mathbf{n}}_{\text{cone}}(t)]^2. \quad (\text{B.19})$$

Moreover, from eqn (B.14) we could also write

$$|\Delta\Omega| = -2 \hat{\Omega}_0 \cdot \hat{\Delta\Omega}, \quad (\text{B.20})$$

where  $\hat{\Delta\Omega} := \Delta\Omega/|\Delta\Omega|$  [that is,  $\hat{\Delta\Omega} = \pm\hat{\mathbf{n}}_{\text{cone}}(t)$ ]. Since  $\hat{\Omega}_0 \cdot \Delta\Omega$  is always negative, it is guaranteed that the right hand side of eqn (B.20) is positive definite.

The above analysis tells that at each time  $t$  one direction of the sky  $\hat{\Omega}$  can satisfy the SPA condition and hence contribute significantly to the correlation. If the observation time is a day, then  $\hat{\mathbf{n}}_{\text{cone}}(t)$  completes a full rotation about the earth's rotation axis. Hence the trajectory of the stationary phase points (the set of directions  $\hat{\Omega}$  satisfying the SPA condition) becomes independent of the source azimuthal angle or the longitude.

## B.2 Evaluation of the Beam Function on SPA trajectory

We now evaluate the value of the beam function on the trajectory we have found.

## 1. Along the SPA trajectory:

Using the general solution we can now evaluate the beam function along the SPA trajectory. As we know that the integral over time contributes only when the SPA condition is satisfied, we expand  $\Delta\Omega \cdot \Delta\mathbf{x}(t)$  about  $t = t_{\text{SPA}}$  (the instant when the stationary phase condition is satisfied for a certain  $\hat{\Omega}$ ) upto second order in  $t$

$$\Delta\Omega \cdot \Delta\mathbf{x}(t) = \Delta\Omega \cdot \Delta\mathbf{x}(t_{\text{SPA}}) + \frac{1}{2}(t - t_{\text{SPA}})^2 \omega_E^2 \Delta\Omega \Delta R \cos\Theta \sin\Theta, \quad (\text{B.21})$$

which is then substituted in the expression for the the unnormalized point estimate [from eqn (B.1)]

$$\int_{-\infty}^{\infty} df \int_0^T dt \Gamma(\hat{\Omega}, t) \Gamma(\hat{\Omega}_0, t) G(t; f) e^{-2\pi i f \Delta\Omega \cdot \Delta\mathbf{x}(t)/c}. \quad (\text{B.22})$$

Assuming that  $\Gamma(\hat{\Omega}, t)$  and  $G(t; f)$  are slowly varying functions of time we may use the standard SPA prescription to evaluate the above integral:

$$\Gamma(\hat{\Omega}, t_{\text{SPA}}) \Gamma(\hat{\Omega}_0, t_{\text{SPA}}) \sqrt{\frac{2}{\omega_E^2 \Delta\Omega \Delta R |\cos\Theta \sin\Theta|/c}} \int_0^{\infty} \frac{df}{\sqrt{f}} G(t_{\text{SPA}}; f), \quad (\text{B.23})$$

where we have used the relation  $\Re[e^{i\pi/4}/\sqrt{\pm 1}] = 1/\sqrt{2}$ . Using a further simplification that all the PSDs are white (i.e.  $\Gamma(\hat{\Omega}, t) = 1$ ) within the frequency range  $f \in [f_l, f_u]$  we arrive at the final expression for the unnormalized beam function becomes

$$\Gamma(\hat{\Omega}, t_{\text{SPA}}) \Gamma(\hat{\Omega}_0, t_{\text{SPA}}) \frac{\sqrt{f_u} - \sqrt{f_l}}{\omega_E} \sqrt{\frac{8c}{\Delta\Omega \Delta R |\cos\Theta \sin\Theta|}}. \quad (\text{B.24})$$

To summarize, since only one point on the sky contribute to the stationary phase integral at one instant of time, to get the stationary phase trajectory along with the beam function evaluated at each point on the trajectory we may use the following two equations parameterized by time  $t$ :

$$\begin{aligned} \hat{\Omega}(t) &= \hat{\Omega}_0 - 2[\hat{\Omega}_0 \cdot \hat{\mathbf{n}}_{\text{cone}}(t)] \hat{\mathbf{n}}_{\text{cone}}(t) \\ \langle S(\hat{\Omega}) \rangle &\propto \Gamma(\hat{\Omega}(t), t) \Gamma(\hat{\Omega}_0, t) \frac{\sqrt{f_u} - \sqrt{f_l}}{\omega_E} \sqrt{\frac{8c}{R_E |(\cos\theta_1 - \cos\theta_2) \hat{\mathbf{z}} \cdot [\hat{\Omega}(t) - \hat{\Omega}_0]|}} \end{aligned} \quad (\text{B.25})$$

The above analysis does not produce correct result if the detectors are on the same latitude, as in that case  $\hat{\mathbf{n}}_{\text{cone}}(t) = \hat{\mathbf{z}}$ , which is always perpendicular to the base line vector  $\Delta\mathbf{x}(t)$ . So *all* the derivative of the phase vanishes at *all* the time intervals. However, we can still find the stationary phase trajectory, which is actually the image point of the source about the equatorial plane. Mathematically,

$$\hat{\Omega}(t) = \hat{\Omega}_0 - 2[\hat{\Omega}_0 \cdot \hat{\mathbf{z}}]\hat{\mathbf{z}}. \quad (\text{B.26})$$

It is easy to see that in that case the contribution to correlation coming from this point (for white PSDs) is

$$\langle S(\hat{\Omega}) \rangle \propto 2(f_u - f_l) \int_0^T dt \Gamma(\hat{\Omega}_0, t) \Gamma(\hat{\Omega}_0 - 2[\hat{\Omega}_0 \cdot \hat{\mathbf{z}}]\hat{\mathbf{z}}, t). \quad (\text{B.27})$$

2. Close to the source direction:

Right at the source direction, since  $\Delta\Omega = \mathbf{0}$ , the unnormalized correlation is

$$\int_0^T dt [\Gamma(\hat{\Omega}_0, t)]^2 \int_{-\infty}^{\infty} df G(t; f). \quad (\text{B.28})$$

For the white PSD case the above value becomes

$$2(f_u - f_l) \int_0^T dt [\Gamma(\hat{\Omega}_0, t)]^2. \quad (\text{B.29})$$

Moreover, since the phase  $2\pi i f \Delta\Omega \cdot \Delta\mathbf{x}(t)/c$  is small near the maximum of the beam function, a linear expansion  $\exp[2\pi i f \Delta\Omega \cdot \Delta\mathbf{x}(t)/c] \approx 1 + 2\pi i f \Delta\Omega \cdot \Delta\mathbf{x}(t)/c$  may be used to study the beam function near the maximum.

## Appendix C

# Cosmic Variance

The estimator for the power spectrum of Cosmic Microwave Background (CMB) has inevitable variance (error) even in case of a ideal CMB anisotropy measurement experiment, where the temperature at every direction in the sky is exactly known. This error arising due to the fact that we can observe only one observable CMB sky, it is known as cosmic variance. The well known cosmic variance for statistically isotropic Gaussian CMB is derived in this appendix for the benefit of readers from other fields.

The power spectrum estimator in a ideal CMB anisotropy experiment is given by [eqn (5.8)]

$$\tilde{C}_l := \frac{1}{2l+1} \sum_{m=-l}^l |a_{lm}|^2, \quad (\text{C.1})$$

where  $a_{lm}$  is the spherical harmonic transform of the true CMB temperature anisotropy  $\Delta T(\hat{\mathbf{q}})$  sky, where  $\hat{\mathbf{q}}$  denotes a direction on the 2-sphere [eqn (5.4)]:

$$a_{lm} := \int d\Omega_{\hat{\mathbf{q}}} \Delta T(\hat{\mathbf{q}}) Y_{lm}^*(\hat{\mathbf{q}}). \quad (\text{C.2})$$

By definition, for statistically isotropic CMB, the expectation of the estimator is the true angular power spectrum,  $\langle \tilde{C}_l \rangle = C_l$ , which follows from eqn (5.5).

The variance of the estimator, the cosmic variance, is given by

$$\text{var}(\tilde{C}_l) := \langle \tilde{C}_l^2 \rangle - \langle \tilde{C}_l \rangle^2. \quad (\text{C.3})$$

The right hand side of the above equation ( $\langle \widetilde{C}_l^2 \rangle - \langle \widetilde{C}_l \rangle^2$ ) can be written as

$$\begin{aligned} & \frac{1}{(2l+1)^2} \sum_{m=-l}^l \sum_{m'=-l}^l \int d\Omega_{\hat{q}_1} \int d\Omega_{\hat{q}_2} \int d\Omega_{\hat{q}'_1} \int d\Omega_{\hat{q}'_2} Y_{lm}^*(\hat{q}_1) Y_{lm}(\hat{q}_2) Y_{lm'}^*(\hat{q}'_1) Y_{lm'}(\hat{q}'_2) \\ & \times \left[ \langle \Delta T(\hat{q}_1) \Delta T(\hat{q}_2) \Delta T(\hat{q}'_1) \Delta T(\hat{q}'_2) \rangle - \langle \Delta T(\hat{q}_1) \Delta T(\hat{q}_2) \rangle \langle \Delta T(\hat{q}'_1) \Delta T(\hat{q}'_2) \rangle \right], \end{aligned} \quad (C.4)$$

which can be evaluated using the following relation which holds if CMB anisotropy is Gaussian

$$\begin{aligned} & \langle \Delta T(\hat{q}_1) \Delta T(\hat{q}_2) \Delta T(\hat{q}'_1) \Delta T(\hat{q}'_2) \rangle - \langle \Delta T(\hat{q}_1) \Delta T(\hat{q}_2) \rangle \langle \Delta T(\hat{q}'_1) \Delta T(\hat{q}'_2) \rangle \\ & = \langle \Delta T(\hat{q}_1) \Delta T(\hat{q}'_1) \rangle \langle \Delta T(\hat{q}_2) \Delta T(\hat{q}'_2) \rangle + \langle \Delta T(\hat{q}_1) \Delta T(\hat{q}'_2) \rangle \langle \Delta T(\hat{q}_2) \Delta T(\hat{q}'_1) \rangle. \end{aligned} \quad (C.5)$$

Moreover, if CMB anisotropy is statistically isotropic, the two point correlation functions depend only on the angular separation between two directions and, hence, can be expanded in a Fourier-Legendre series:

$$\langle \Delta T(\hat{q}_1) \Delta T(\hat{q}_2) \rangle = C(\hat{q}_1 \cdot \hat{q}_2) = \sum_{l=0}^{\infty} \frac{2l+1}{4\pi} C_l P_l(\hat{q}_1 \cdot \hat{q}_2). \quad (C.6)$$

Substituting the above in the expression for variance, using the addition theorem for spherical harmonics [eqn (5.6)],

$$\frac{4\pi}{2l+1} \sum_{m=-l}^l Y_{lm}^*(\hat{q}_1) Y_{lm}(\hat{q}_2) = P_l(\hat{q}_1 \cdot \hat{q}_2) = \frac{4\pi}{2l+1} \sum_{m=-l}^l Y_{lm}(\hat{q}_1) Y_{lm}^*(\hat{q}_2), \quad (C.7)$$

and using the orthogonality relation for spherical harmonics [eqn (5.7)],

$$\int d\Omega_{\hat{q}} Y_{lm}^*(\hat{q}) Y_{l'm'}(\hat{q}) = \delta_{ll'} \delta_{mm'}, \quad (C.8)$$

one can write final expression for cosmic variance as

$$\text{var}(\widetilde{C}_l) = \frac{2}{2l+1} C_l^2. \quad (C.9)$$

The above relation suggests that the specific error due to cosmic variance decreases with multipoles; at  $l = 2$  the fractional error is  $\sim 63\%$  and at  $l = 5$  it is  $\sim 42\%$ . This is understandable - the number of independent spherical harmonic “ $m$ ” modes increases with multipoles, which reduces the measurement uncertainty (variance).

## Appendix D

# Elliptical Gaussian fit to the WMAP beam maps

We briefly describe an exercise of characterizing non-circular beams in CMB experiments using the example of the beam maps of the WMAP mission. We analyzed the WMAP raw beam images in the Q1, V1 and W1 [101, 183] bands using two different standard software packages. We use the elliptical Gaussian fit allowed by the well known radio-astronomy software, AIPS and a more elaborate ellipse fitting routine available within the standard astronomical image/data processing software IRAF. The ELLIPSE task in the STSDAS package of IRAF, which uses the widely known ellipse fitting routines by Jedrzejewski [184], allows independent elliptical fits to the isophotes. This significant greater degree of freedom in fitting to the non-circular beam allows us to assess whether a simple elliptical Gaussian fit is sufficient. The three bands see Jupiter in the two horns (labeled A and B) as a point source. The fitting routine fits ellipses along iso-intensity contours of the beam image, parameterized by position angle (PA), ellipticity ( $\bar{\epsilon}$ ) and position of the center. Each of these parameters can be independently varied. The distance between successive ellipses can also be independently varied. The eccentricity  $e$  is related to ellipticity  $\bar{\epsilon}$  as  $e = \sqrt{1 - (1 - \bar{\epsilon})^2}$  (Please see Table 8.1).

We fit the the beams in two different ways: (a) by holding the ellipticity constant to  $\bar{\epsilon} = 0.05$  and freely varying the position angle and center and (b) fixing the center to be the pixel with the highest intensity (normalized to 1.0 at the central pixel) and varying ellipticity and position angle. In the first case, we get the closest approximation to circular beam profiles as used in WMAP data analysis. This beam has no azimuthal ( $\phi$ ) dependence. In the latter case, we get the elliptical profile of

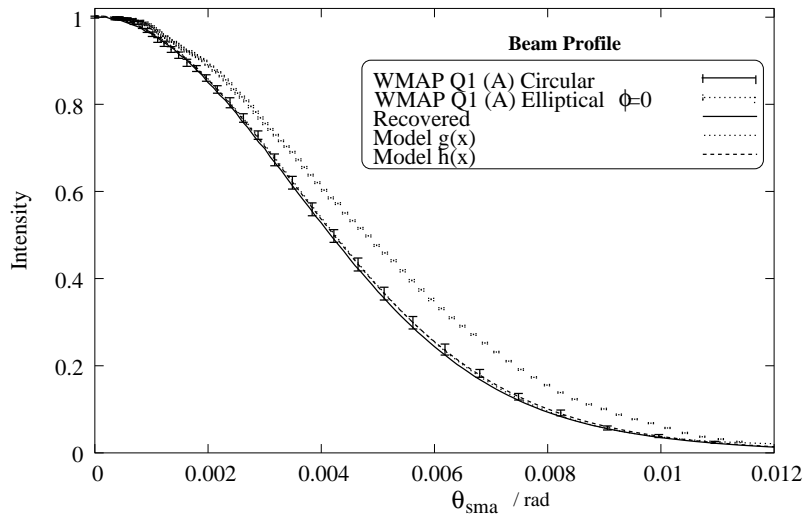


Figure D.1: **Profile of WMAP Q-beam fitted using IRAF.** The beam profile is characterized by intensity along the semi major axis (SMA). The beam in Q-band for WMAP experiment was analyzed using IRAF and fitted to both circular and elliptical profiles. We have plotted the best fit circular profile (solid error bars) and overlaid the profile recovered by inverting the WMAP beam transforms, available at LAMBDA website (solid line). Two analytical models for circular beam profile  $g(\theta)$  and  $h(\theta)$  are also considered, and the best fit profiles are overlaid. We find that these models are consistent with the IRAF and WMAP data. We have also plotted the best fit elliptical profile along SMA (broken error bar). Notice that the error bars in this case are much smaller than those for circular profile, implying a better agreement with the data.

the WMAP beam which depends on both the polar ( $\theta$ ) and azimuthal ( $\phi$ ) distance from the pointing direction. Notice that in this case it is sufficient to provide the intensity along a particular direction (usually, the semi-major axis or  $\phi = 0$ ) and the ellipticity  $\bar{\epsilon}$ .

Even a visual inspection reveals that the Q1 beam map plotted in Fig 8.2 is non-circular and the iso-intensity contours distinctly elliptical. Thus it comes as no surprise that the error bars as shown in Figure D.1 for circularized beam are larger than those for the elliptical profile. As a consistency check, we take the WMAP Q1 beam transfer function  $B_l$  from WMAP first year data archived at publicly available LAMBDA site [101] and ‘recover’ the circular beam profile  $B(\theta)$  using eq. (8.10).

From Figure D.1, it is clear that this ‘recovered’ beam profile is in good agreement with that obtained by IRAF. This allows us to make some statements about the profile fitting in CMB experiments, in the context of WMAP beams. The beam profile  $B(\theta)$  has been modeled as a Gaussian times a sum of even order Hermite

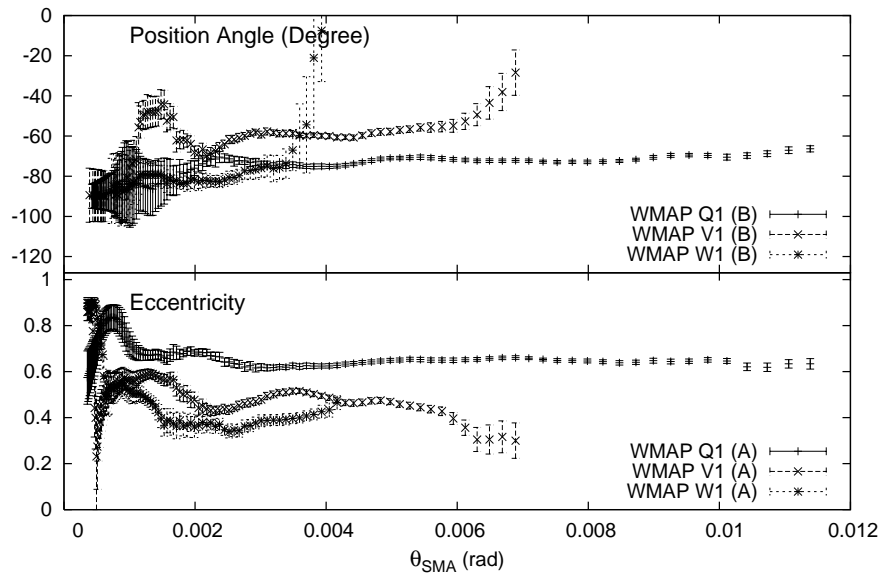


Figure D.2: **IRAF estimated parameters characterizing WMAP beams.** The beams for WMAP experiment in three bands Q, V and W for both the horns (A and B) were fitted to elliptical profiles using IRAF. The plot above shows the fitted eccentricity and position angle along the semi major axis (SMA). The presence of side-bands in the smaller beams (W band) makes it difficult for IRAF to model them sufficiently well. However, in the Q1 band, such sub-structures in the beam are not present thus allowing the IRAF ellipse fitting routine to fit reasonably good ellipses which have consistent eccentricities ( $e \sim 0.65$ ) and position angles all along the SMA. The V1 beam is smaller in extent than the Q1 beam and its eccentricity was determined to be  $e \sim 0.46$  using IRAF. The highest resolution beam in in W1 band, whose eccentricity was determined to be  $e \sim 0.40$ .

polynomials ( $H_{2n}$ ) by the WMAP team [183]. To compare, we have also modeled the beam profile with a function  $h(\theta)$  given by

$$h(\theta) = \exp\left(-\frac{1}{2} \alpha \theta^2\right) (h_0 + h_2 H_2(\theta) + h_4 H_4(\theta)), \quad (\text{D.1})$$

where  $\alpha, h_0, h_2$  and  $h_4$  are unknown parameters to be fixed by least squared method. We found that this model fits the data very well with a reduced  $\chi^2$  of about 0.7. However, on closer analysis, it is found that the chief role of the Hermite polynomials is to add a constant baseline over and above the Gaussian. To test this

hypotheses, we choose another form of the fitting function  $g(\theta)$  given by

$$g(\theta) = g_0 + g_1 \exp\left(-\frac{1}{2} g_2 \theta^2\right), \quad (\text{D.2})$$

where  $g_0, g_1$  and  $g_2$  are parameters of the model. It is very interesting to note that this model also fits the data very well with a reduced  $\chi^2$  of about 0.8 for the best fitted parameters. In all fairness,  $g(\theta)$  serves as a simpler model for the beam profile. We cannot point to the precise origin for the baseline. However, such ‘skirts’ in beam responses are not uncommon in radio-astronomy. At this point, our observation should perhaps merit a curious aside, if not as an alternative approach to beam modeling. Our best-fit models  $g(\theta)$  and  $h(\theta)$ , along with the IRAF fitted data points to the WMAP Q1 (A) beam is shown in Figure D.1.

As shown earlier in this thesis, the effects of non-circularity of the CMB experimental beams show up in the power-spectral density estimates through the off-diagonal elements of the bias matrix  $A_{ll'}$ . As shown in eq. (8.26), these in turn can be expressed in terms of the leading components of the harmonic transform of the beam. In general, the harmonic decomposition of a non-circular beam may have to be done numerically. But for the particular case of an elliptical Gaussian beam, a closed form expression given by eq. (8.19) serves as a useful test-bed for us. Thus another motivation for fitting ellipses to WMAP beams using IRAF was to get a handle on the eccentricity of these beams so as to find the harmonic transform components of an elliptical Gaussian beam of similar eccentricity. This allows us to give more realistic estimates of the effect of non-circularity of the beam on  $C_l$  estimates.

It is interesting to note how the fitted eccentricities vary as a function of the distance along the semi-major axis of the fitted ellipses for various beams. The smaller beams (V1 and W1) have sufficient sub-structure in the form of side-lobes which throws the ellipse fitting routine off course. However, where the sub-structure is less pronounced, we find that the eccentricities of the fitted ellipses takes a constant value. Toward the center of the ellipses, there are far too few pixels to average over, which in turn manifests as large error bars in the eccentricities and position angles of the ellipses. In Figure D.2, we notice that the Q1 beam has a very elliptical profile with eccentricity  $e \gtrsim 0.65$  and position angle of about  $75^\circ$ . We also fitted the Q1 (A) beam to an elliptical Gaussian model using radio astronomy standard data analysis software AIPS and got consistent numbers for the eccentricity. However the IRAF modeling gives us more freedom to vary the eccentricity and position angle as we

Table D.1: **Ellipticities of WMAP beams.** The result of ellipse fitting using IRAF on the Q1, V1 and W1 beams of the WMAP experiments. The frequency quoted is the ‘effective’ frequency of the corresponding band from Page et. al. [183]. The presence of sub-structures in the W1 band makes it difficult to fit elliptical contours to the beam.

Beam	Frequency (GHz)	Eccentricity	Position Angle (degree)
Q1 (A)	40.9	0.65	+80
Q1 (B)	40.9	0.67	-80
V1 (A)	60.3	0.48	+60
V1 (B)	60.3	0.45	-60
W1 (A)	93.5	0.40	— <sup>1</sup>

move away from the center of the ellipse and the result is that the beam is modeled more accurately.



## Appendix E

# Derivations for perturbative analysis of beam correction to pseudo- $C_l$ estimator

In the appendix we provide the details of the analytical steps involved in deriving some of the expressions used in chapter 8. This is designed to keep the thesis self contained and easy to extend. These calculations can be useful for other applications which involve Wigner- $D$  functions.

### Step I

First, we outline the steps involved in evaluating the integral

$I_{02}^{ll'} + I_{0-2}^{ll'} = 2 \int_{-1}^1 d_{00}^l(\theta) d_{02}^{l'}(\theta) d \cos \theta$  to obtain the result in eq. (8.39).

Using the expressions [117,100] for  $d_{00}^l$  and  $d_{02}^{l'}$  in terms of Legendre Polynomials and its derivatives,

$$\begin{aligned} & \int_{-1}^1 d_{00}^l(\theta) d_{02}^{l'}(\theta) d \cos \theta \\ &= -\frac{l'(l'+1)}{\kappa} \int_{-1}^1 P_l(x) P_{l'}(x) dx + \frac{2}{\kappa} \int_{-1}^1 x P_l(x) P_{l'}'(x) dx, \end{aligned} \quad (\text{E.1})$$

where,  $\kappa \equiv \sqrt{(l-1)l(l+1)(l+2)}$ . The first integral is simply the orthogonality of

Legendre polynomials

$$\int_{-1}^1 P_l(x)P_{l'}(x)dx = \frac{2\delta_{ll'}}{2l+1}. \quad (\text{E.2})$$

Further, we can show that for odd values of  $l+l'$ ,

$$\int_{-1}^1 x P_l(x) P_{l'}(x) dx = 0, \quad (\text{E.3})$$

and for even values of  $l+l'$ ,

$$\int_{-1}^1 x P_l(x) P_{l'}(x) dx = \begin{cases} 2 & \text{if } l < l' \\ 0 & \text{if } l > l' \\ 2l/(2l+1) & \text{if } l = l'. \end{cases} \quad (\text{E.4})$$

Assembling all these we can derive eq. (8.39).

## Step II

Next we evaluate the more general integral  $I_{m_2}^{ll'} + I_{m-2}^{ll'} \equiv \int_{-1}^1 d_{m_0}^l(\theta) [d_{m_2}^{l'}(\theta) + d_{m-2}^{l'}(\theta)] d \cos \theta$  to obtain the expression in eq. (8.40). The first step is to express  $d_{m\pm 2}^l(\theta)$  in terms of  $d_{m_0}^{l'}(\theta)$ . Using the recurrence relations for Wigner  $D$  functions (see eq. (4) in §4.8.1, [100]) and using the fact that

$$D_{mm'}^l(\phi, \theta, \rho) = e^{-im\phi} d_{mm'}^l(\theta) e^{-im'\rho} \quad (\text{E.5})$$

we get the recurrence relations for Wigner- $d$  functions:

$$\begin{aligned} \sin \theta d_{mm'+1}^l(\theta) &= \frac{\sqrt{(l^2 - m^2)(l + m')(l + m' + 1)}}{l(2l + 1)} d_{mm'}^{l-1}(\theta) \\ &- \frac{m \sqrt{(l - m')(l + m' + 1)}}{l(l + 1)} d_{mm'}^l(\theta) \\ &- \frac{\sqrt{[(l + 1)^2 - m^2](l - m')(l - m' + 1)}}{(l + 1)(2l + 1)} d_{mm'}^{l+1}(\theta). \end{aligned} \quad (\text{E.6})$$

Using these relations for  $d_{m_2}^l$  we may write,

$$d_{m_2}^l(\theta) = \frac{\kappa}{\sin^2(\theta)} [\kappa_0 d_{m_0}^l(\theta) + \kappa_1 d_{m_0}^{l+1}(\theta) + \kappa_{-1} d_{m_0}^{l-1}(\theta) + \kappa_2 d_{m_0}^{l+2}(\theta) + \kappa_{-2} d_{m_0}^{l-2}(\theta)], \quad (\text{E.7})$$

where

$$\begin{aligned}\kappa_0 &\equiv \frac{m^2}{l^2(l+1)^2} - \frac{l^2 - m^2}{l^2(4l^2 - 1)} - \frac{(l+1)^2 - m^2}{(l+1)^2(2l+1)(2l+3)}, \\ \kappa_1 &\equiv 2m \frac{\sqrt{(l+1)^2 - m^2}}{l(l+1)(l+2)(2l+1)}, \quad \kappa_{-1} \equiv -2m \frac{\sqrt{l^2 - m^2}}{l(l^2 - 1)(2l+1)}, \\ \kappa_2 &\equiv \frac{\sqrt{[(l+1)^2 - m^2][(l+2)^2 - m^2]}}{(l+1)(l+2)(2l+1)(2l+3)}, \quad \kappa_{-2} \equiv \frac{\sqrt{(l^2 - m^2)[(l-1)^2 - m^2]}}{l(l-1)(4l^2 - 1)}.\end{aligned}$$

Also, since  $d_{m-2}^l(\theta) = (-1)^{l+m} d_{m2}^l(\pi - \theta)$  and  $d_{m0}^l(\pi - \theta) = (-1)^{l+m} d_{m0}^l(\theta)$  we can write,

$$d_{m-2}^l(\theta) = \frac{\kappa}{\sin^2(\theta)} [\kappa_0 d_{m0}^l(\theta) - \kappa_1 d_{m0}^{l+1}(\theta) - \kappa_{-1} d_{m0}^{l-1}(\theta) + \kappa_2 d_{m0}^{l+2}(\theta) + \kappa_{-2} d_{m0}^{l-2}(\theta)]. \quad (\text{E.8})$$

Using the expression for  $d_{m\pm 2}$  we can make the following substitution

$$d_{m2}^l(\theta) + d_{m-2}^l(\theta) = 2\kappa [\kappa_0 d_{m0}^l(\theta) + \kappa_2 d_{m0}^{l+2}(\theta) + \kappa_{-2} d_{m0}^{l-2}(\theta)] / \sin^2 \theta, \quad (\text{E.9})$$

in the integral we seek to evaluate. We use the following integral for  $l \leq l'$  and  $L = \min\{l, l'\} \geq |m| > 0$ ,

$$\int_{-1}^1 d_{m0}^l(\theta) d_{m0}^{l'}(\theta) \frac{d \cos \theta}{\sin^2 \theta} = \begin{cases} \frac{1}{|m|} \sqrt{\frac{(l+|m|)!(l'-|m|)!}{(l-|m|)!(l'+|m|)!}} & \text{even } l+l' \\ 0 & \text{odd } l+l' \end{cases} \quad (\text{E.10})$$

and obviously, for  $l > l'$ ,  $l$  and  $l'$  have to be interchanged in the above expression. We then obtain  $I_{m2}^{ll'} + I_{m-2}^{ll'}$  as given in eq. (8.40).

### Step III

The integral in eq. (E.10) can also be readily derived. We use the fact that

$$d_{m0}^l(\theta) = (-1)^m \sqrt{\frac{(l-m)!}{(l+m)!}} P_l^m(\cos \theta), \quad (\text{E.11})$$

which leads to

$$\int_{-1}^1 d_{m0}^l(\theta) d_{m0}^{l'}(\theta) \frac{d \cos \theta}{\sin^2 \theta} = \sqrt{\frac{(l-m)!(l'-m)!}{(l+m)!(l'+m)!}} \int_{-1}^1 P_l^m(x) P_{l'}^m(x) \frac{dx}{1-x^2}. \quad (\text{E.12})$$

The symmetry of Associated Legendre Polynomials,  $P_l^m(-x) = (-1)^{l+m}P_l^m(x)$  dictates that the integrand is antisymmetric for odd values of  $l+l'$ , hence the integral is zero. However for even values of  $l+l'$ , we can evaluate the integral in the following manner. One of the recurrence relations for Associated Legendre Polynomials is ([185], §12.5.)

$$P_l^m(x) = P_{l-2}^m(x) + (2l-1)\sqrt{1-x^2}P_{l-1}^{m-1}(x). \quad (\text{E.13})$$

Using equation (E.13) we can write,

$$\begin{aligned} & \int_{-1}^1 P_l^m(x)P_{l'}^m(x)\frac{dx}{1-x^2} \\ &= \int_{-1}^1 P_l^m(x)P_{l'-2}^m(x)\frac{dx}{1-x^2} + (2l'-1)\int_{-1}^1 P_l^m(x)P_{l'-1}^{m-1}(x)\frac{dx}{\sqrt{1-x^2}}. \end{aligned} \quad (\text{E.14})$$

We have provided a proof that the second integral on the right is zero at the end of this section. Thus, from eq. (E.14) we have

$$\int_{-1}^1 P_l^m(x)P_{l'}^m(x)\frac{dx}{1-x^2} = \int_{-1}^1 P_l^m(x)P_{l'-2}^m(x)\frac{dx}{1-x^2}. \quad (\text{E.15})$$

In this way we can keep reducing  $l'$  by two each time until it equals with  $l$  (since  $l+l'$  is even and  $l < l'$  it will reduce to  $l$ ). Thus, we have shown that,

$$\int_{-1}^1 P_l^m(x)P_{l'}^m(x)\frac{dx}{1-x^2} = \int_{-1}^1 [P_l^m(x)]^2 \frac{dx}{1-x^2} = \frac{1}{m} \frac{(l+m)!}{(l-m)!}, \quad (\text{E.16})$$

where the second equality follows from the evaluation of a standard integral, which can be obtained, for example, from [185]. Substituting in eq. (E.12) we can evaluate the integral for  $m > 0$ . Clearly eq. (E.16) is valid for  $l = l'$ . For  $l > l'$ ,  $l$  should be replaced by  $l'$  in that equation. Moreover, using the property  $d_{-m}^l(\theta) = (-1)^m d_{m0}^l(\theta)$ , we can express the integral for any  $m \neq 0$ , as given in eq. (E.10).

## Step IV

Finally we prove the result used in simplifying eq. (E.14) that for even values of  $l+l'$  and  $l < l'$ ,

$$\int_{-1}^1 P_l^m(x)P_{l'-1}^{m-1}(x)\frac{dx}{\sqrt{1-x^2}} = 0. \quad (\text{E.17})$$

Using the recurrence relation of Legendre Polynomials in eq. (E.13), we can

write

$$\begin{aligned} & \int_{-1}^1 P_l^m(x) P_{l'-1}^{m-1}(x) \frac{dx}{\sqrt{1-x^2}} \\ &= \int_{-1}^1 P_{l-2}^m(x) P_{l'-1}^{m-1}(x) \frac{dx}{\sqrt{1-x^2}} + (2l-1) \int_{-1}^1 P_{l-1}^{m-1}(x) P_{l'-1}^{m-1}(x) dx. \end{aligned} \quad (\text{E.18})$$

Then from the orthogonality relation of associated Legendre Polynomials,

$$\int_{-1}^1 P_l^m(x) P_{l'}^m(x) dx = \frac{2}{2l+1} \frac{(l+m)!}{(l-m)!} \delta_{ll'}, \quad (\text{E.19})$$

we can see that the second integral on the right of eq. (E.18) vanishes for  $l' \neq l$ . Thus we have,

$$\int_{-1}^1 P_l^m(x) P_{l'-1}^{m-1}(x) \frac{dx}{\sqrt{1-x^2}} = \int_{-1}^1 P_{l-2}^m(x) P_{l'-1}^{m-1}(x) \frac{dx}{\sqrt{1-x^2}}. \quad (\text{E.20})$$

We can use the above equation iteratively since the lower indices of the  $P_l^{m'}$ 's will never match as  $l' > l$ . So the lower index of the first polynomial in the integration can be reduced to either  $m$  or  $m+1$  (depending on  $l-m$  is even or odd) by repeated use of the above identity. Thus we may write

$$\int_{-1}^1 P_l^m(x) P_{l'-1}^{m-1}(x) \frac{dx}{\sqrt{1-x^2}} = \begin{cases} \int_{-1}^1 P_m^m(x) P_{l'-1}^{m-1}(x) \frac{dx}{\sqrt{1-x^2}} \\ \text{or} \\ \int_{-1}^1 P_{m+1}^m(x) P_{l'-1}^{m-1}(x) \frac{dx}{\sqrt{1-x^2}}. \end{cases} \quad (\text{E.21})$$

Finally using the relations,

$$\begin{aligned} P_m^m &= (-1)^m (2m-1)!! (1-x^2)^{m/2} \\ &= (-1)(2m-1) \sqrt{1-x^2} P_{m-1}^{m-1}, \end{aligned} \quad (\text{E.22})$$

$$\begin{aligned} P_{m+1}^m &= x(2m+1) P_m^m = x(2m+1)(-1)(2m-1) \sqrt{1-x^2} P_{m-1}^{m-1} \\ &= (-1)(2m+1) \sqrt{1-x^2} P_m^{m-1} \end{aligned} \quad (\text{E.23})$$

and the orthonormality condition in eq. (E.2) we can see that in both the cases right side of eq. (E.21) is zero. This completes the proof.



## Appendix F

# Derivations for general analysis of beam correction to pseudo- $C_l$ estimator

### F.1 Useful formulae

- Important relations [eq. (1)s of §4.3, §4.17 & §5.4 and eq. (2) of §4.4 of [100]]:

$$D_{mm'}^l(\hat{\mathbf{q}}, \rho) = e^{-im\phi} d_{mm'}^l(\theta) e^{-im'\rho} \quad (\text{F.1})$$

$$Y_{lm}^*(\hat{\mathbf{q}}) = \sqrt{\frac{2l+1}{4\pi}} D_{m0}^l(\hat{\mathbf{q}}, \rho) = \sqrt{\frac{2l+1}{4\pi}} e^{-im\phi} d_{m0}^l(\theta) \quad (\text{F.2})$$

$$D_{mm'}^{l*}(\hat{\mathbf{q}}, \rho) = (-1)^{m-m'} D_{-m-m'}^l(\hat{\mathbf{q}}, \rho) \quad (\text{F.3})$$

$$Y_{lm}^*(\hat{\mathbf{q}}) = (-1)^m Y_{l-m}(\hat{\mathbf{q}}) \quad (\text{F.4})$$

Note that, unlike [118], the argument of the Wigner- $d$  function is  $\theta$  (standard definition) *not*  $\cos \theta$ .

- The Clebsch-Gordon series:

Expansion of the product of two Wigner- $D$  functions [eqn (1) of §4.6 of [100]]:

$$D_{m_1 n_1}^{l_1}(\hat{\mathbf{q}}, \rho) D_{m_2 n_2}^{l_2}(\hat{\mathbf{q}}, \rho) = \sum_{l=|l_1-l_2|}^{l_1+l_2} C_{l_1 m_1 l_2 m_2}^{l(m_1+m_2)} D_{(m_1+m_2)(n_1+n_2)}^l(\hat{\mathbf{q}}, \rho) C_{l_1 n_1 l_2 n_2}^{l(n_1+n_2)}, \quad (\text{F.5})$$

where  $C_{l_1 m_1 l_2 m_2}^{lm}$  are the Clebsch-Gordon coefficients.

The special case of spherical harmonics [eq. (9) of §5.6 of [100]]:

$$Y_{l_1 m_1}(\hat{\mathbf{q}}) Y_{l_2 m_2}(\hat{\mathbf{q}}) = \sum_{l=|l_1-l_2|}^{l_1+l_2} \sqrt{\frac{(2l_1+1)(2l_2+1)}{4\pi(2l+1)}} C_{l_1 0 l_2 0}^{l 0} C_{l_1 m_1 l_2 m_2}^{l(m_1+m_2)} Y_{l(m_1+m_2)}(\hat{\mathbf{q}}). \quad (\text{F.6})$$

In modifying the above equations (from [100]) we have used the fact that the Clebsch-Gordon coefficients  $C_{l_1 m_1 l_2 m_2}^{lm}$  vanish if  $m \neq m_1 + m_2$ .

- The integral  $\int_0^\pi d\theta \sin \theta e^{iN\theta}$  equals to:

$$\int_0^\pi d\theta \left[ \frac{e^{i(N+1)\theta} - e^{i(N-1)\theta}}{2i} \right] = \begin{cases} \pm i\pi/2 & \text{if } N = \pm 1 \\ \left[ \frac{1-e^{i(N+1)\pi}}{2(N+1)} - \frac{1-e^{i(N-1)\pi}}{2(N-1)} \right] & \text{if } N = \text{odd } (\neq \pm 1) \\ \frac{2}{1-N^2} & \text{if } N = 0, \text{ even.} \end{cases} \quad (\text{F.7})$$

The above can be used to define an useful quantity

$$f(m'; N) := \Re \left[ i^{m'} (-1)^N \int_0^\pi \sin \theta d\theta e^{iN\theta} \right] = \begin{cases} (-1)^{(m'+1)/2} \pi/2 & \text{if } m' = \text{odd and } N = \pm 1 \\ (-1)^{m'/2} 2/(1-N^2) & \text{if both } m', N = 0 \text{ or even} \\ 0 & \text{otherwise.} \end{cases} \quad (\text{F.8})$$

## F.2 Expansion of Wigner-D Function

### Motivation

This derivation is motivated from eq. (10) of §4.16 of [100]. However, the motivating equation is wrong, as it predicts  $D_{mm'}^l(\phi, \theta, \rho) = 0$  if  $m + m' = \text{odd}$ . We derive the correct formula by “reverse engineering”. We start with the second expression of

the above mentioned equation [see below for steps]:

$$\begin{aligned}
& \sum_{M_1, M_2, M_3, M_4=-l}^l \left[ D_{mM_1}^l(\phi, 0, 0) D_{M_1 M_2}^l\left(0, \frac{\pi}{2}, 0\right) D_{M_2 M_3}^l(0, \theta, 0) \right. \\
& \quad \left. D_{M_3 M_4}^l\left(0, \frac{\pi}{2}, 0\right) D_{M_4 m'}^l(0, 0, \rho) \right] \\
&= e^{-im\phi} \sum_{M_2, M_3=-l}^l \left[ D_{mM_2}^l\left(0, \frac{\pi}{2}, 0\right) D_{M_2 M_3}^l(\theta, 0, 0) D_{M_3 m'}^l\left(0, \frac{\pi}{2}, 0\right) \right] e^{-im'\rho} \\
&= e^{-im\phi} \sum_{M_2=-l}^l \left[ D_{mM_2}^l\left(0, \frac{\pi}{2}, 0\right) D_{M_2 m'}^l\left(\theta, \frac{\pi}{2}, 0\right) \right] e^{-im'\rho} \\
&= e^{-im\phi} D_{mm'}^l\left(\frac{\pi}{2}, \pi - \theta, \frac{\pi}{2}\right) e^{-im'\rho} = D_{mm'}^l\left(\frac{\pi}{2} + \phi, \pi - \theta, \frac{\pi}{2} + \rho\right) \quad (F.9)
\end{aligned}$$

## Steps

### Step I

From eq. (1) & (2) of §4.16, pg.112 of [100].

$$D_{mm'}^l(\phi, 0, 0) = e^{-im\phi} D_{mm'}^l(0, 0, 0) \quad (F.10)$$

$$D_{mm'}^l(0, 0, \rho) = D_{mm'}^l(0, 0, 0) e^{-im'\rho} \quad (F.11)$$

$$D_{mm'}^l(0, 0, 0) = \delta_{mm'}. \quad (F.12)$$

### Step II<sup>1</sup>

$$e^{-im\phi} \sum_{M_3=-l}^l \left[ D_{mM_3}^l\left(0, \frac{\pi}{2}, \theta\right) D_{M_3 m'}^l\left(0, \frac{\pi}{2}, 0\right) \right] e^{-im'\rho} \quad (F.13)$$

From the "Addition of Rotations" formula in eq. (3) of §4.7, pg.87 of [100].

$$\sum_{M=-l}^l \left[ D_{mM}^l(\phi, \theta_1, \gamma) D_{Mm'}^l(-\gamma, \theta_2, \rho) \right] = D_{mm'}^l(\phi, \theta_1 + \theta_2, \rho). \quad (F.14)$$

<sup>1</sup>Another way is to combine the first two remaining  $D$  symbols using eq. (1) of §4.16, pg.112 of [100] and then evaluate the following in Step III using the "Addition of Rotations" formula similar to the present method:

Step III

From eq. (1) of §4.7, pg.87 of [100] we may write

$$\sum_{M=-l}^l \left[ D_{mM}^l \left( 0, \frac{\pi}{2}, 0 \right) D_{Mm'}^l \left( \theta, \frac{\pi}{2}, 0 \right) \right] = D_{mm'}^l(\alpha, \beta, \gamma) \quad (\text{F.15})$$

where  $\alpha, \beta, \gamma$  are to be obtained using eq. (66)-(70) of §1.4, pg.32 of [100]. Note that the arguments of the *first*  $D$  symbol have been denoted by  $\alpha_2, \beta_2, \gamma_2$  respectively and *not* by  $\alpha_1, \beta_1, \gamma_1$ .

From eq. (66) of §1.4, pg.32 of [100], since  $0 \leq \alpha < 2\pi, 0 \leq \beta \leq \pi, 0 \leq \gamma < 2\pi$

$$\cos \alpha = 0 \Rightarrow \alpha = \frac{\pi}{2} \text{ or } \frac{3\pi}{2} \quad (\text{F.16})$$

$$\cos \beta = -\cos \theta \Rightarrow \beta = \pi - \theta \quad (\text{F.17})$$

$$\cos \gamma = 0 \Rightarrow \gamma = \frac{\pi}{2} \text{ or } \frac{3\pi}{2}. \quad (\text{F.18})$$

From eq. (67) of §1.4, pg.32 of [100]

$$\sin \alpha = \sin \gamma = \frac{\sin \theta}{\sin \theta} = 1. \quad (\text{F.19})$$

Combining the above equations we may write

$$\alpha = \frac{\pi}{2}; \quad \beta = \pi - \theta; \quad \gamma = \frac{\pi}{2}. \quad (\text{F.20})$$

### Final expression

We can modify eq. (F.9) by changing  $\phi \rightarrow \phi - \frac{\pi}{2}, \theta \rightarrow \pi - \theta, \rho \rightarrow \rho - \frac{\pi}{2}$  to reach the desired expansion:

$$D_{mm'}^l(\phi, \theta, \rho) = e^{-im(\phi-\pi/2)} e^{-im'(\rho-\pi/2)} \times \sum_{M_2, M_3=-l}^l \left[ D_{mM_2}^l \left( 0, \frac{\pi}{2}, 0 \right) D_{M_2 M_3}^l (\pi - \theta, 0, 0) D_{M_3 m'}^l \left( 0, \frac{\pi}{2}, 0 \right) \right]. \quad (\text{F.21})$$

Then using the definitions of Wigner- $d$  functions from eq. (1) of §4.3, pg.76 and eq. (1) of §4.16, pg.112 of [100], we get

$$D_{mm'}^l(\phi, \theta, \rho) = i^{m+m'} e^{-im\phi} \sum_{M=-l}^l \left[ (-1)^M d_{mM}^l \left( \frac{\pi}{2} \right) e^{iM\theta} d_{Mm'}^l \left( \frac{\pi}{2} \right) \right] e^{-im'\rho}. \quad (\text{F.22})$$

This also means

$$d_{mm'}^l(\theta) = i^{m+m'} \sum_{M=-l}^l \left[ (-1)^M d_{mM}^l\left(\frac{\pi}{2}\right) e^{iM\theta} d_{Mm'}^l\left(\frac{\pi}{2}\right) \right]. \quad (\text{F.23})$$

The coefficients  $d_{mm'}^l(\pi/2)$  can be directly calculated using eq. (5) of §4.16, pg.113 of [100]

$$d_{mm'}^l\left(\frac{\pi}{2}\right) = (-1)^{m-m'} \frac{1}{2^l} \sqrt{\frac{(l+m)!(l-m)!}{(l+m')!(l-m')!}} \times \sum_{k=\max\{0, m'-m\}}^{\max\{l+m', l-m\}} (-1)^k \binom{l+m'}{k} \binom{l-m'}{k+m-m'}. \quad (\text{F.24})$$

### F.3 Evaluation of $J_{nm''mm'}^{l''l'}$ using sinusoidal expansion of Wigner- $d$

Putting eq. (9.21) in eq. (9.20) we get

$$\begin{aligned} J_{nm''mm'}^{l''l'} &:= \int_{S^2} d\Omega_{\hat{\mathbf{q}}} Y_{ln}(\hat{\mathbf{q}}) Y_{l''m''}(\hat{\mathbf{q}}) D_{mm'}^{l'}(\hat{\mathbf{q}}, \rho(\hat{\mathbf{q}})) \quad (\text{F.25}) \\ &= \frac{\sqrt{(2l+1)(2l''+1)}}{4\pi} \int_0^{2\pi} d\phi e^{i(n+m''-m)\phi} \times \\ &\quad \int_0^\pi \sin\theta d\theta d_{n0}^l(\theta) d_{m''0}^{l''}(\theta) d_{mm'}^{l'}(\theta) e^{-im'\rho(\hat{\mathbf{q}})} \\ &= \frac{\sqrt{(2l+1)(2l''+1)}}{4\pi} i^{n+m+m'+m''} \sum_{M=-l}^l d_{nM}^l\left(\frac{\pi}{2}\right) d_{M0}^l\left(\frac{\pi}{2}\right) \times \\ &\quad \sum_{M''=-l''}^{l''} d_{m''M''}^{l''}\left(\frac{\pi}{2}\right) d_{M''0}^{l''}\left(\frac{\pi}{2}\right) \sum_{M'=-l'}^{l'} d_{mM'}^{l'}\left(\frac{\pi}{2}\right) d_{M'm'}^{l'}\left(\frac{\pi}{2}\right) \times \\ &\quad (-1)^{M+M''+M'} \int_0^{2\pi} d\phi e^{i(n+m''-m)\phi} \int_0^\pi \sin\theta d\theta e^{i(M+M'+M'')\theta} e^{-im'\rho(\hat{\mathbf{q}})}. \end{aligned}$$

To proceed further *analytically*, we need a model for  $\rho(\hat{\mathbf{q}})$ . We shall continue assuming *non-rotating* beams, i.e.  $\rho(\hat{\mathbf{q}}) = 0$ . In this case the  $\phi$  integral above is separable. Using,

$$\int_0^{2\pi} d\phi e^{i(n+m''-m)\phi} = 2\pi \delta_{m''(m-n)} \quad (\text{F.26})$$

we can get a simplified result:

$$\begin{aligned}
 J_{nm''mm'}^{l''l'} &= 2\pi \delta_{m''(m-n)} \frac{\sqrt{(2l+1)(2l''+1)}}{4\pi} \sum_{M=-l}^l d_{nM}^l \left(\frac{\pi}{2}\right) d_{M0}^l \left(\frac{\pi}{2}\right) \times \\
 &\quad \sum_{M''=-l''}^{l''} d_{m''M''}^{l''} \left(\frac{\pi}{2}\right) d_{M''0}^{l''} \left(\frac{\pi}{2}\right) \sum_{M'=-l'}^{l'} d_{mM'}^{l'} \left(\frac{\pi}{2}\right) d_{M'm'}^{l'} \left(\frac{\pi}{2}\right) \times \\
 &\quad \left[ i^{n+m+m'+m''} (-1)^{M+M'+M''} \int_0^\pi \sin \theta d\theta e^{i(M+M'+M'')\theta} \right]. \quad (\text{F.27})
 \end{aligned}$$

The above expression is real. The proof follows:

- Contribution for all of  $M, M', M'' = 0$ :

In this term (of the summation) the integral of the above expression is real. Therefore, if  $n + m + m' + m'' = \text{even}$  this term is real (because then the factor  $i^{n+m+m'+m''}$  is real). When  $n + m + m' + m'' = \text{odd}$ , which means at least one of  $n, m + m', m''$  is odd, this term does not contribute, since  $d_{m0}^l(\pi/2)d_{0m'}^l(\pi/2) = 0$  if  $m + m' = \text{odd}$  (follows from eq. (6) of §4.16 of [100]).

- Contribution for *not* all of  $M, M', M'' = 0$ :

For each set of  $M, M', M''$  in the above summation, there exists a set  $-M, -M', -M''$ , which converts the integral of the above expression to its complex conjugate. Since  $d_{mm'}^l(\pi/2) = (-1)^{l-m'} d_{-mm'}^l(\pi/2) = (-1)^{l+m} d_{m-m'}^l(\pi/2)$  [see eq. (1) of §4.4 of [100]], the Wigner- $d$  symbols give a factor of  $(-1)^{n+m+m'+m''}$ . So, if  $n + m + m' + m'' = \text{even}$ , the sum is real, as well as the factor  $i^{n+m+m'+m''}$  and both are imaginary if  $n + m + m' + m'' = \text{odd}$ .

Therefore, the full summation is always real.

Following the discussion on the reality of the expression and using eq. (F.8) we can write

$$\begin{aligned}
 J_{nm''mm'}^{l''l'} &= 2\pi \delta_{(m-n)m''} (-1)^m \frac{\sqrt{(2l+1)(2l''+1)}}{4\pi} \times \\
 &\quad \sum_{M=-l}^l d_{nM}^l \left(\frac{\pi}{2}\right) d_{M0}^l \left(\frac{\pi}{2}\right) \sum_{M''=-l''}^{l''} d_{(m-n)M''}^{l''} \left(\frac{\pi}{2}\right) d_{M''0}^{l''} \left(\frac{\pi}{2}\right) \times \\
 &\quad \sum_{M'=-l'}^{l'} d_{mM'}^{l'} \left(\frac{\pi}{2}\right) d_{M'm'}^{l'} \left(\frac{\pi}{2}\right) f(m'; M + M' + M''). \quad (\text{F.28})
 \end{aligned}$$

Moreover, since for "symmetric" beams  $\beta_{lm} = 0$  for  $m = \text{odd}$ , in the final expression terms with  $m' = \text{odd}$  shall not contribute, that means, for symmetric beams,  $f(m'; N)$  contributes *only* when both  $m', N = 0$  or *even*.

To make the final expression more simple, we can write the bias matrix for non-rotating beam with incomplete sky coverage as:

$$\begin{aligned}
 A_{ll'} &= B_l^2 \frac{(2l'+1)}{16\pi} \sum_{n=-l}^l \sum_{m=-l'}^{l'} \left| \sum_{l''=0}^{\infty} \sqrt{2l''+1} U_{l''(m-n)} \times \right. \\
 &\quad \sum_{M'=-l''}^{l''} d_{(m-n)M'}^{l''} \left(\frac{\pi}{2}\right) d_{M''0}^{l''} \left(\frac{\pi}{2}\right) \sum_{M=-l}^l d_{nM}^l \left(\frac{\pi}{2}\right) d_{M0}^l \left(\frac{\pi}{2}\right) \times \\
 &\quad \left. \sum_{M'=-l'}^{l'} d_{mM'}^{l'} \left(\frac{\pi}{2}\right) \sum_{m'=-l'}^{l'} \beta_{l'm'} d_{M'm'}^{l'} \left(\frac{\pi}{2}\right) f(m'; M + M' + M'') \right|^2. \tag{F.29}
 \end{aligned}$$

This form could be useful for numerical evaluation.

#### F.4 Evaluation of $J_{nm''mm'}^{l''l'}$ using Clebsch-Gordon series and sinusoidal expansion of Wigner- $d$

Putting eqn (F.6), (F.4), (F.2), (F.5) & (9.21) in eqn (9.19) we get

$$\begin{aligned}
 J_{nm''mm'}^{l''l'} &\equiv \int_{S^2} d\Omega_{\hat{\mathbf{q}}} Y_{ln}(\hat{\mathbf{q}}) Y_{l''m''}(\hat{\mathbf{q}}) D_{mm'}^{l'}(\hat{\mathbf{q}}, \rho(\hat{\mathbf{q}})) \tag{F.30} \\
 &= \sum_{L=|l-l''|}^{l+l''} \sqrt{\frac{(2l+1)(2l''+1)}{4\pi(2L+1)}} C_{l0l''0}^{L0} C_{lnl''m''}^{L(n+m'')} \times \\
 &\quad \int_{S^2} d\Omega_{\hat{\mathbf{q}}} Y_{L(n+m'')}(\hat{\mathbf{q}}) D_{mm'}^{l'}(\hat{\mathbf{q}}, \rho(\hat{\mathbf{q}})) \\
 &= (-1)^{n+m''} \frac{\sqrt{(2l+1)(2l''+1)}}{4\pi} \times \\
 &\quad \sum_{L=|l-l''|}^{l+l''} C_{l0l''0}^{L0} C_{lnl''m''}^{L(n+m'')} \int_{S^2} d\Omega_{\hat{\mathbf{q}}} D_{(-n-m'')0}^L(\hat{\mathbf{q}}, \rho(\hat{\mathbf{q}})) D_{mm'}^{l'}(\hat{\mathbf{q}}, \rho(\hat{\mathbf{q}})) \\
 &= (-1)^{n+m''} \frac{\sqrt{(2l+1)(2l''+1)}}{4\pi} \sum_{L=|l-l''|}^{l+l''} C_{l0l''0}^{L0} C_{lnl''m''}^{L(n+m'')} \times \\
 &\quad \sum_{L'=|L-l'|}^{L+l'} C_{L(-n-m'')l'm}^{L'(m-n-m'')} C_{L0l'm'}^{L'l'm'} \int_{S^2} d\Omega_{\hat{\mathbf{q}}} D_{(m-n-m'')m'}^{L'}(\hat{\mathbf{q}}, \rho(\hat{\mathbf{q}})).
 \end{aligned}$$

Now using eq. (9.21) one can write integrals of the above form as ( $m - n - m'' \rightarrow M'$  &  $m' \rightarrow M''$ ):

$$\int_{S^2} d\Omega_{\hat{\mathbf{q}}} D_{M'M''}^{L'}(\hat{\mathbf{q}}, \rho(\hat{\mathbf{q}})) = \quad (F.31)$$

$$i^{M'+M''} \sum_{N=-L'}^{L'} (-1)^N d_{M'N}^{L'}\left(\frac{\pi}{2}\right) d_{NM''}^{L'}\left(\frac{\pi}{2}\right) \int_{S^2} d\Omega_{\hat{\mathbf{q}}} e^{-iM'\phi} e^{iN\theta} e^{-iM''\rho(\hat{\mathbf{q}})}.$$

To proceed further *analytically*, we need a model for  $\rho(\hat{\mathbf{q}})$ . We shall continue assuming *non-rotating* beams, i.e.  $\rho(\hat{\mathbf{q}}) = 0$ . In this case the  $\phi$  integral above is separable. Then, putting eq. (F.26) we get

$$\int_{S^2} d\Omega_{\hat{\mathbf{q}}} D_{M'M''}^{L'}(\hat{\mathbf{q}}, 0) = \quad (F.32)$$

$$2\pi \delta_{M'0} i^{M''} \sum_{N=-L'}^{L'} (-1)^N d_{0N}^{L'}\left(\frac{\pi}{2}\right) d_{NM''}^{L'}\left(\frac{\pi}{2}\right) \int_0^\pi \sin \theta d\theta e^{iN\theta}.$$

This integral is real. This becomes clear if we write the right hand side of the above equation as

$$2\pi \delta_{M'0} i^{M''} \left[ 2 d_{00}^{L'}\left(\frac{\pi}{2}\right) d_{0M''}^{L'}\left(\frac{\pi}{2}\right) + \sum_{N=1}^{L'} (-1)^N d_{0N}^{L'}\left(\frac{\pi}{2}\right) d_{NM''}^{L'}\left(\frac{\pi}{2}\right) \int_0^\pi \sin \theta d\theta \{e^{iN\theta} + (-1)^{M''} e^{-iN\theta}\} \right]. \quad (F.33)$$

When  $M'' = \text{even}$  both  $i^{M''}$  and the integrand are real, and when  $M'' = \text{odd}$  both  $i^{M''}$  and the integrand are imaginary. The first term inside the square bracket does not contribute when  $M'' = \text{odd}$  (since  $d_{00}^{L'}(\pi/2)d_{0M''}^{L'}(\pi/2)$  vanishes in that case). Therefore irrespective of the value of  $M''$  the above expression is real. Thus,

$$\int_{S^2} d\Omega_{\hat{\mathbf{q}}} D_{M'M''}^{L'}(\hat{\mathbf{q}}, 0) = \quad (F.34)$$

$$2\pi \delta_{M'0} \sum_{N=-L'}^{L'} d_{0N}^{L'}\left(\frac{\pi}{2}\right) d_{NM''}^{L'}\left(\frac{\pi}{2}\right) \Re \left[ i^{M''} (-1)^N \int_0^\pi \sin \theta d\theta e^{iN\theta} \right].$$

Now we can use the above results and combine with eq. (F.8) to get

$$\begin{aligned}
J_{mm'mm'}^{ll'l'} &= (-1)^{n+m''} \delta_{m''(m-n)} \frac{\sqrt{(2l+1)(2l''+1)}}{2} \times \\
&\sum_{L=|l-l''|}^{l+l''} C_{l0l''0}^{L0} C_{lnl''m''}^{L(n+m'')} \sum_{L'=|L-l'|}^{L+l'} C_{L(-n-m'')l'm}^{L'(m-n-m'')} C_{L0l'm'}^{L'm'} \times \\
&\sum_{N=-L'}^{L'} d_{0N}^{L'} \left(\frac{\pi}{2}\right) d_{Nm'}^{L'} \left(\frac{\pi}{2}\right) f(m'; N). \tag{F.35}
\end{aligned}$$

The final form of the bias matrix for non-rotating beam with incomplete sky coverage can now be written as (after replacing  $m''$  by  $m-n$ , pulling out few factors outside the modulus and squaring):

$$\begin{aligned}
A_{ll'} &= B_l^2 \frac{(2l'+1)}{16\pi} \sum_{n=-l}^l \sum_{m=-l'}^{l'} \left| \sum_{l''=0}^{\infty} \sqrt{2l''+1} U_{l''(m-n)} \times \right. \\
&\sum_{L=|l-l''|}^{l+l''} C_{l0l''0}^{L0} C_{lnl''(m-n)}^{Lm} \sum_{L'=|L-l'|}^{L+l'} C_{L-ml'm}^{L'0} \sum_{N=-L'}^{L'} d_{0N}^{L'} \left(\frac{\pi}{2}\right) \times \\
&\left. \sum_{m'=-l'}^{l'} \beta_{l'm'} C_{L0l'm'}^{L'm'} d_{Nm'}^{L'} \left(\frac{\pi}{2}\right) f(m'; N) \right|^2. \tag{F.36}
\end{aligned}$$

## F.5 The full sky and circular beam limit

Here we recover the special case of circular beam and complete sky coverage limit. From Eq. F.36, the full sky limit [ $U_{lm} = \sqrt{4\pi}\delta_{l0}$ ] is obtained by replacing  $U_{l''(m-n)}$  with  $\sqrt{4\pi}\delta_{l''0}\delta_{mn}$ ; and for the circular beam, we replace the BDP  $\beta_{l'm'}$  with  $\delta_{m'0}$ . So,

$$\begin{aligned}
A_{ll'} &= B_l^2 \frac{2l'+1}{4} \sum_{n=-\min(l,l')}^{\min(l,l')} \left| C_{l000}^{l0} C_{ln00}^{ln} \sum_{L'=|l-l'|}^{l+l'} C_{l-nl'n}^{L'0} C_{l0l'0}^{L'0} \times \right. \\
&\left. \sum_{N=-L'}^{L'} d_{0N}^{L'} \left(\frac{\pi}{2}\right) d_{N0}^{L'} \left(\frac{\pi}{2}\right) f(0; N) \right|^2. \tag{F.37}
\end{aligned}$$

## Chapter F. Derivations for general analysis of beam correction to pseudo- $C_l$ estimator

From the relation  $C_{a\alpha 00}^{c\gamma} = \delta_{ac}\delta_{\alpha\gamma}$  (Eq. (2) in §8.5.1 of [100]), we can reduce  $C_{l00}^{l0}$  and  $C_{lm00}^{ln}$  to unity, and get:

$$A_{ll'} = B_l^2 \frac{2l'+1}{4} \sum_{n=-\min(l,l')}^{\min(l,l')} \left| \sum_{L'=|l-l'|}^{l+l'} C_{l-nl'n}^{L'0} C_{l0l'0}^{L'0} \sum_{N=-L'}^{L'} d_{0N}^{L'}\left(\frac{\pi}{2}\right) d_{N0}^{L'}\left(\frac{\pi}{2}\right) f(0;N) \right|^2. \quad (\text{F.38})$$

To get the value of  $\sum_{N=-L'}^{L'} d_{0N}^{L'}\left(\frac{\pi}{2}\right) d_{N0}^{L'}\left(\frac{\pi}{2}\right) f(0;N)$ , we have to start a step back.

$$\begin{aligned} Y_{lm}^*(\hat{q}) &= \sqrt{\frac{2l+1}{4\pi}} D_{mm'}^l(\hat{q}, 0) \\ &= \sqrt{\frac{2l+1}{4\pi}} i^m e^{-im\phi} \sum_{N=-l}^l (-1)^N d_{mN}^l\left(\frac{\pi}{2}\right) d_{N0}^l\left(\frac{\pi}{2}\right) e^{iN\theta} \end{aligned} \quad (\text{F.39})$$

From the relation

$$\int_{S^2} Y_{lm}^*(\hat{q}) d\Omega_{\hat{q}} = \sqrt{4\pi} \delta_{l0} \delta_{m0}$$

it follows that

$$\begin{aligned} &\sqrt{\frac{2l+1}{4\pi}} i^m \sum_{N=-l}^l (-1)^N d_{mN}^l\left(\frac{\pi}{2}\right) d_{N0}^l\left(\frac{\pi}{2}\right) \int e^{iN\theta} \sin\theta d\theta \int e^{-im\phi} d\phi \\ &= \sqrt{4\pi} \delta_{l0} \delta_{m0}. \end{aligned} \quad (\text{F.40})$$

The last integral (i.e.,  $\int e^{-im\phi} d\phi$ ) gives  $2\pi\delta_{m0}$ . So, equating out both sides and rearranging, we have

$$i^m \sum_{N=-l}^l (-1)^N d_{mN}^l\left(\frac{\pi}{2}\right) d_{N0}^l\left(\frac{\pi}{2}\right) \int e^{iN\theta} \sin\theta d\theta \int e^{-im\phi} d\phi = \frac{2}{\sqrt{2l+1}} \delta_{l0}. \quad (\text{F.41})$$

The l.h.s. is identified with the relation  $\sum_{N=-L'}^{L'} d_{0N}^{L'} \left(\frac{\pi}{2}\right) d_{N0}^{L'} \left(\frac{\pi}{2}\right) f(0; N)$ , and hence Eq.(F.38) reduces to

$$\begin{aligned} A_{ll'} &= B_l^2 \frac{2l'+1}{4} \sum_{n=\max(-l, -l')}^{\min(l, l')} \left| \sum_{L'=|l-l'|}^{l+l'} C_{l-nl'n}^{L'0} C_{l0l'0}^{L'0} \frac{2}{\sqrt{2L'+1}} \delta_{L'0} \right|^2 \\ &= B_l^2 (2l'+1) \sum_{n=\max(-l, -l')}^{\min(l, l')} |C_{l-nl'n}^{00} C_{l0l'0}^{00}|^2. \end{aligned} \quad (\text{F.42})$$

We know from Eq. (1) of §8.5.1 of [100]

$$C_{a\alpha b\beta}^{00} = (-1)^{a-\alpha} \frac{\delta_{ab} \delta_{\alpha, -\beta}}{\sqrt{2a+1}}.$$

Hence,  $A_{ll'}$  finally reduces to the desired result

$$A_{ll'} = B_l^2 \delta_{ll'}.$$

## F.6 The circular beam limit with cut sky

We will show in this section that our formulation reduces to the analytic limit of the MASTER method of Hivon et al. [167] for the incomplete sky coverage taking circular beams. Following the procedure mentioned in section F.5, we proceed as:

$$\begin{aligned} A_{ll'} &= B_l^2 \frac{2l'+1}{16\pi} \sum_{n=-l}^l \sum_{m=-l'}^{l'} \left| \sum_{l''=0}^{\infty} \sqrt{2l''+1} U_{l''(m-n)} \sum_{L=|l-l''|}^{l+l''} C_{l0l''0}^{L0} C_{lm'l''(m-n)}^{Lm} \right. \\ &\quad \left. \times \sum_{L'=|L-l'|}^{L+l'} C_{L-m'l'm}^{L'0} C_{L0l'0}^{L'0} \sum_{N=-L'}^{L'} d_{0N}^{L'} \left(\frac{\pi}{2}\right) d_{N0}^{L'} \left(\frac{\pi}{2}\right) f(0; N) \right|^2 \end{aligned} \quad (\text{F.43})$$

Using Eq. (F.41), we get

$$\begin{aligned}
 A_{ll'} &= B_l^2 \frac{2l'+1}{4\pi} \sum_{n=-l}^l \sum_{m=-l'}^{l'} \\
 & \left| \sum_{l''=0}^{\infty} \sqrt{2l''+1} U_{l''(m-n)} \sum_{L=|l-l''|}^{l+l''} C_{10l''0}^{L0} C_{lnl''(m-n)}^{Lm} C_{L(-m)l'm}^{00} C_{L0l'0}^{00} \right|^2 \\
 &= \frac{B_l^2}{4\pi} \sum_{n=-l}^l \sum_{m=-l'}^{l'} \left| \sum_{l''=0}^{\infty} \sqrt{2l''+1} U_{l''(m-n)} \sum_{L=|l-l''|}^{l+l''} C_{10l''0}^{L0} C_{lnl''(m-n)}^{Lm} \right|^2
 \end{aligned}$$

To arrive at Eq. A31 of Hivon et al. [167], we first replace (m-n) by  $m''$  and then open up the modulus square. The symbol  $C_{lnl''m''}^{l'm}$  contributes only when  $m''$  is equal to (m-n) and also  $l''$  satisfies the triangle inequality.

$$\begin{aligned}
 A_{ll'} &= \frac{B_l^2}{4\pi(2l'+1)} \sum_{n=-l}^l \sum_{m=-l'}^{l'} \left| \sum_{l''=0}^{\infty} \sqrt{2l''+1} \sum_{m''=-l''}^{l''} U_{l''m''} C_{10l''0}^{l'0} C_{lnl''m''}^{l'm} \right|^2 \\
 &= \frac{B_l^2}{4\pi(2l'+1)} \sum_{n=-l}^l \sum_{m=-l'}^{l'} \left[ \sum_{l''_1=0}^{\infty} \sqrt{2l''_1+1} C_{10l''_1 0}^{l'0} \sum_{l''_2=0}^{\infty} \sqrt{2l''_2+1} C_{10l''_2 0}^{l'0} \right. \\
 & \quad \left. \sum_{m''_2=-l''_2}^{l''_2} \sum_{m''_1=-l''_1}^{l''_1} U_{l''_1 m''_1} U_{l''_2 m''_2}^* C_{lnl''_1 m''_1}^{l'm} C_{lnl''_2 m''_2}^{l'm} \right] \\
 &= \frac{B_l^2}{4\pi(2l'+1)} \sum_{l''_1=0}^{\infty} \sum_{l''_2=0}^{\infty} \sqrt{2l''_1+1} \sqrt{2l''_2+1} C_{10l''_1 0}^{l'0} C_{10l''_2 0}^{l'0} \\
 & \quad \sum_{m''_2=-l''_2}^{l''_2} \sum_{m''_1=-l''_1}^{l''_1} U_{l''_1 m''_1} U_{l''_2 m''_2}^* \sum_{n=-l}^l \sum_{m=-l'}^{l'} C_{lnl''_1 m''_1}^{l'm} C_{lnl''_2 m''_2}^{l'm} \tag{F.44}
 \end{aligned}$$

The last summation  $\sum_{n=-l}^l \sum_{m=-l'}^{l'} C_{lnl''_1 m''_1}^{l'm} C_{lnl''_2 m''_2}^{l'm}$  simplifies to  $(2l'+1)/(2l''_1+1) \delta_{l''_1 l''_2} \delta_{m''_1 m''_2}$  by Eq. (5) of § 8.7.2 of [100]. So, we have

$$\begin{aligned}
 A_{ll'} &= \frac{B_l^2}{4\pi} \sum_{l''=|l-l'|}^{l+l'} (C_{10l''0}^{l'0})^2 \sum_{m''=-l''}^{l''} |U_{l''m''}|^2 \\
 &= B_l^2 \frac{2l'+1}{4\pi} \sum_{l''=|l-l'|}^{l+l'} (2l''+1) \begin{pmatrix} l & l' & l'' \\ 0 & 0 & 0 \end{pmatrix}^2 \mathcal{U}_{l''}, \tag{F.45}
 \end{aligned}$$

where  $\mathcal{U}_{l'} := \sum_{m''=-l'}^{l'} |U_{l'm''}|^2 / (2l' + 1)$ . This matches the final expression of [167] [See eqn (A31)].

## F.7 The full sky limit with non-circular beam

The full sky limit to the final expression should reproduce the result obtained in [118]. We substitute  $U_{lm} = \sqrt{4\pi}\delta_{l0}$  [ $\Rightarrow U_{l'(m-n)} = \sqrt{4\pi}\delta_{l'0}\delta_{mn}$ ] in eqn (9.25) and get

$$A_{l'} = B_l^2 \frac{(2l' + 1)}{4} \sum_{m=-\min(l,l')}^{\min(l,l')} \left| C_{l000}^{l0} C_{lm00}^{lm} \sum_{L=|l-l'|}^{l+l'} C_{l-m'l'm}^{L0} \times \sum_{N=-L}^L d_{0N}^L \left( \frac{\pi}{2} \right) \sum_{m'=-l'}^{l'} \beta_{l'm'} C_{l0l'm'}^{Lm'} d_{Nm'}^L \left( \frac{\pi}{2} \right) f(m'; N) \right|^2. \quad (\text{F.46})$$

Using the relation  $C_{aa00}^{c\gamma} = \delta_{ac}\delta_{a\gamma}$  [Eq. (2) in §8.5.1 of [100]] we may write  $C_{l000}^{l0} = C_{lm00}^{lm} = 1$ . Then rearranging terms, we may write

$$A_{l'} = B_l^2 \frac{(2l' + 1)}{4} \sum_{m=-\min(l,l')}^{\min(l,l')} \left| \sum_{m'=-l'}^{l'} \beta_{l'm'} \sum_{L=|l-l'|}^{l+l'} C_{l-m'l'm}^{L0} C_{l0l'm'}^{Lm'} \times \sum_{N=-L}^L d_{0N}^L \left( \frac{\pi}{2} \right) d_{Nm'}^L \left( \frac{\pi}{2} \right) f(m'; N) \right|^2. \quad (\text{F.47})$$

Using the definition of  $f(m'; N)$  [eqn (9.24)] and the expansion formula for Wigner- $d$  [eqn (9.21)] we may write

$$\sum_{N=-L}^L d_{0N}^L \left( \frac{\pi}{2} \right) d_{Nm'}^L \left( \frac{\pi}{2} \right) f(m'; N) = \int_{-1}^1 d \cos \theta d_{0m'}^L(\theta). \quad (\text{F.48})$$

Then, using the Clebsch-Gordan series [eqn (F.5)] we get

$$\sum_{L=|l-l'|}^{l+l'} C_{l-m'l'm}^{L0} d_{0m'}^L(\theta) C_{l0l'm'}^{Lm'} = (-1)^m d_{m0}^l(\theta) d_{mm'}^l(\theta). \quad (\text{F.49})$$

## Chapter F. Derivations for general analysis of beam correction to pseudo- $C_l$ estimator

Finally, putting everything together, we get the expression for the bias matrix in the full sky limit with non-circular beam as

$$A_{ll'} = B_l^2 \frac{(2l' + 1)}{4} \sum_{m=-\min(l,l')}^{\min(l,l')} \left| \sum_{m'=-l'}^{l'} \beta_{l'm'} \int_{-1}^1 d \cos \theta d_{m0}^l(\theta) d_{mm'}^{l'}(\theta) \right|^2, \quad (\text{F.50})$$

which matches eqn (38) of [118].

## Appendix G

# Fast computation of non-circular beam correction to CMB power spectrum

The general analytical results obtained in chapter 9 to estimate the bias in CMB power spectrum due to noncircular beams including the effect of incomplete sky coverage will be important only if the evaluation time is much faster than carrying full blown simulations. The fast evaluation of the analytical results is, however, not straight forward. Smart innovations are necessary for the numerical implementation of the analysis. The basic principle of the fast implementation algorithm have been outlined in section 9.2, the detailed calculations are presented in this appendix.

The full expression for the bias matrix with no rotation:

$$\begin{aligned}
 A_{ll'} = & B_l^2 \frac{2l'+1}{16\pi} \sum_{n=-l}^l \sum_{m=-l'}^{l'} \left| \sum_{l''=0}^{\infty} \sqrt{2l''+1} U_{l''(m-n)} \times \right. \\
 & \sum_{M''=-l''}^{l''} d_{(m-n)M''}^{l''} \left( \frac{\pi}{2} \right) d_{M''0}^{l''} \left( \frac{\pi}{2} \right) \sum_{M=-l}^l d_{nM}^l \left( \frac{\pi}{2} \right) d_{M0}^l \left( \frac{\pi}{2} \right) \times \\
 & \left. \sum_{M'=-l'}^{l'} d_{mM'}^{l'} \left( \frac{\pi}{2} \right) \sum_{m'=-l'}^{l'} \beta_{l'm'} d_{M'm'}^{l'} \left( \frac{\pi}{2} \right) f(m'; M + M' + M'') \right|^2. \tag{G.1}
 \end{aligned}$$

The following way of calculation requires less computation cost.  $V^{1,2,3}$  have been used as intermediate arrays. This prescription is only for the loops inside the modulus, so for each  $m, n$  pair all the three steps have to be performed.

- Step I:

$$V_1(N) = \sum_{M'=-l'}^{l'} d_{mM'}^{l'} \left(\frac{\pi}{2}\right) \sum_{m'=-l'}^{l'} \beta_{l'm'} d_{M'm'}^{l'} \left(\frac{\pi}{2}\right) f(m'; M' + N), \quad (\text{G.2})$$

$N$  runs from  $-(l + l''_{\max})$  to  $+(l + l''_{\max})$ .

- Step II

$$V_2(M'') = \sum_{M=-l}^l d_{nM}^l \left(\frac{\pi}{2}\right) d_{M0}^l \left(\frac{\pi}{2}\right) V_{l'}^1[M + M''; m]. \quad (\text{G.3})$$

- Step III

$$V_3 = \sum_{l''=0}^{l''_{\max}} \sqrt{2l'' + 1} U_{l''(m-n)} \sum_{M''=-l''}^{l''} d_{(m-n)M''}^{l''} \left(\frac{\pi}{2}\right) d_{M''0}^{l''} \left(\frac{\pi}{2}\right) V_{l'}^2[M''; n]. \quad (\text{G.4})$$

Required number of cycles to compute  $V^3$  for each pair  $m, n$  for  $l_{\max} \gg l''_{\max}$  and the cut off for the  $m'$  summation at  $m'_{\max} = m_{\text{beam}}$  is:

$$\left[ \{2(l + l''_{\max}) + 1\}(2l' + 1)(2m_{\text{beam}} + 1) + (2l''_{\max} + 1)(2l + 1) + \sum_{l''=0}^{l''_{\max}} (2l'' + 1) \right] \quad (\text{G.5})$$

As mentioned earlier we are interested in the total number of computation cycles in the limit  $l_{\max} \gg l''_{\max}$ . Before proceeding further we note that  $U_{l''m''} = U_{l''m-n}$  is limited to only  $m_{\text{mask}}$  modes for each  $l''$ . Here  $m_{\text{mask}} > 0$ . Thus means that  $N$  varies from  $-(l + m_{\text{mask}})$  to  $(l + m_{\text{mask}})$  in Step I. Moreover, the condition for non-negligible values of  $U_{l''m-n}$  becomes  $|m - n| < m_{\text{mask}}$ . This in turn implies that  $m - n < m_{\text{mask}}$  when  $m - n > 0$ , and  $-m + n < m_{\text{mask}}$  when  $m - n < 0$ . Then we see that for each  $n, m$  can run only from  $n - m_{\text{mask}}$  to  $n + m_{\text{mask}}$  for a total of  $2m_{\text{mask}} + 1$  values so that  $U_{l''m-n}$ 's are non zero.

Thus considering two outer loops over  $m, n$  total computation cycles becomes

$$\begin{aligned}
& \sum_{l=2}^{l_{\max}} \sum_{l'=2}^{l_{\max}} (2l+1)(2m_{\text{mask}}+1) \left[ \{2(l+l''_{\max})+1\}(2l'+1)(2m_{\text{beam}}+1)+ \right. \\
& \left. (2l''_{\max}+1)(2l+1) + \sum_{l''=0}^{l''_{\max}} (2l''+1) \right] \\
= & (2m_{\text{mask}}+1) \sum_{l=2}^{l_{\max}} \sum_{l'=2}^{l_{\max}} (2l+1) \left[ \{2(l+l''_{\max})+1\}(2l'+1)(2m_{\text{beam}}+1)+ \right. \\
& \left. (2l''_{\max}+1)(2l+1) + \sum_{l''=0}^{l''_{\max}} (2l''+1) \right] \\
= & (2m_{\text{mask}}+1) \sum_{l=2}^{l_{\max}} \sum_{l'=2}^{l_{\max}} (2l+1) \left[ 2l''_{\max}(2l'+1)(2m_{\text{beam}}+1)+ \right. \\
& \left. (2l+1)(2l'+1)(2m_{\text{beam}}+1) + (2l''_{\max}+1)(2l+1) + \sum_{l''=0}^{l''_{\max}} (2l''+1) \right]
\end{aligned}$$

The computation cycles will be decided by the maximum power of the largest term in the above expression. Clearly the second term in the bracket will give the maximum contribution as it contains highest powers combined from  $l, l'$ . Hence the total number of cycles is

$$\begin{aligned}
& (2m_{\text{mask}}+1) \sum_{l=2}^{l_{\max}} 4l^2 \sum_{l'=2}^{l_{\max}} (2l')(2m_{\text{beam}}+1) = (2m_{\text{mask}}+1)(2m_{\text{beam}}+1) \times \\
& 8 \left[ \frac{l_{\max}(l_{\max}+1)(2l_{\max}+1)}{6} - 1 \right] \left[ \frac{l_{\max}(l_{\max}+1)}{2} - 1 \right] \quad (\text{G.6})
\end{aligned}$$

For  $l_{\max} \gg 1$  the computation cost scales as  $(4/3)(2m_{\text{mask}}+1)(2m_{\text{beam}}+1)l_{\max}^5$ .



# Bibliography

- [1] L. D. Landau and E. M. Lifshitz, *Classical Theory of Fields*, vol. 2 of *Course of Theoretical Physics*. Pergamon Press, Oxford, UK, 1980.
- [2] C. W. Misner, K. S. Thorne, and J. A. Wheeler, *Gravitation*. Freeman, New York, USA, 1973.
- [3] S. Weinberg, *Gravitation and Cosmology: Principles and applications of the general theory of relativity*. Wiley, New York, USA, 1972.
- [4] B. F. Schutz, *A first course in general relativity*. Cambridge University Press, Cambridge, UK, 1995.
- [5] K. S. Thorne, "Gravitational radiation", in *300 Years of Gravitation*. Cambridge University Press, Cambridge, UK, 1987.
- [6] É. É. Flanagan and S. A. Hughes *New Journal of Physics* **7** (2005) 204, [gr-qc/0501041](#).
- [7] J. Hough and S. Rowan *Living Reviews in Relativity* **3** (2000), no. 3,.
- [8] "LISA images".  
<http://www.srl.caltech.edu/lisa/graphics/master.html>.
- [9] R. A. Hulse and J. H. Taylor *Astrophys. J. Lett.* **195** (1975) L51.
- [10] J. M. Weisberg and J. H. Taylor, "The Relativistic Binary Pulsar B1913+16:Thirty Years of Observations and Analysis", in *ASP Conf. Ser. 328: Binary Radio Pulsars*, F. A. Rasio and I. H. Stairs, eds., p. 25. 2005.  
[astro-ph/0407149](#).
- [11] J. Weber *Phys. Rev. Lett.* **20** (1968) 1307.

- [12] "ALLEGRO Resonant Bar Detector".  
<http://sam.phys.lsu.edu/ALLEGRO/allegro.html>.
- [13] "The NAUTILUS Gravitational Wave Antenna".  
<http://www.roma1.infn.it/rog/nautilus/>.
- [14] "AURIGA Home Page". <http://www.auriga.lnl.infn.it/>.
- [15] "The EXPLORER Gravitational Wave Antenna".  
<http://www.roma1.infn.it/rog/explorer/explorer.html>.
- [16] "MiniGRAIL, the first spherical gravitational wave detector".  
<http://www.minigrail.nl/>.
- [17] "IGA Mult-Axis Resonant Mass Detector".  
<http://sam.phys.lsu.edu/TIGA/tiga.html>.
- [18] "ALLEGRO Archive Photos". <http://sam.phys.lsu.edu/ImageSets/ImageSets.php?whichpage=../ALLEGRO%20Archive%20Photos>.
- [19] "LIGO Press & Media Kit: LIGO photos".  
[http://www.ligo.caltech.edu/LIGO\\_web/PR/scripts/photos.html](http://www.ligo.caltech.edu/LIGO_web/PR/scripts/photos.html).
- [20] "LIGO Laboratory Home Page". <http://www.ligo.caltech.edu/>.
- [21] D. Sigg Internal working note LIGO-P980007-00, Laser Interferometer Gravitational Wave Observatory (LIGO), 1998.
- [22] "TAMA300: The 300m Laser Interferometer Gravitational Wave Antenna".  
<http://tamago.mtk.nao.ac.jp/>.
- [23] M. Ando *et al.* *Phys. Rev. Lett.* **86** (2001) 3950.
- [24] "GEO 600 Home Page (Hannover)".  
<http://www.geo600.uni-hannover.de/>.
- [25] "GEO 600 - Technical Reports".  
<http://www.geo600.uni-hannover.de/geo600/technical/index.html>.
- [26] "Virgo". <http://www.virgo.infn.it/>.
- [27] "Virgo Description". <http://www.ego-gw.it/virgodescription/>.

- [28] “Australian Consortium for Interferometric Gravitational Astronomy (ACIGA)”. <http://www.anu.edu.au/Physics/ACIGA/>.
- [29] “Australian International Gravitational Observatory (AIGO)”. [http://www.gravity.uwa.edu.au/docs/aigo\\_prospectus.pdf](http://www.gravity.uwa.edu.au/docs/aigo_prospectus.pdf).
- [30] “LCGT Project: Large Scale Gravitational Wave Telescope”. <http://www.icrr.u-tokyo.ac.jp/gr/gre.html>.
- [31] K. Kuroda *et al.* *Int. J. Mod. Phys.* **D8** (2000) 557.
- [32] “LIGO Sensitivity”. [http://www.ligo.caltech.edu/~jzweizig/distribution/LSC\\_Data/](http://www.ligo.caltech.edu/~jzweizig/distribution/LSC_Data/).
- [33] “Laser Interferometric Space Antenna”. <http://lisa.jpl.nasa.gov/>.
- [34] “What Is LISA?”. <http://lisa.jpl.nasa.gov/WHATIS/intro.html>.
- [35] “LISA System and Technology Study Report”. [http://www.srl.caltech.edu/lisa/documents/sts\\_1.05.pdf](http://www.srl.caltech.edu/lisa/documents/sts_1.05.pdf), 2000.
- [36] S. Kawamura *et al.* *Class. Quant. Grav.* **23** (2006) S125.
- [37] S. V. Dhurandhar and M. Tinto *Living Reviews in Relativity* **8** (2005), no. 4,.
- [38] “Big Bang Observer”. <http://universe.nasa.gov/technology/vision.html#big%20bang%20observer>.
- [39] S. Phinney *et al.*, “The Big Bang Observer: Direct detection of gravitational waves from the birth of the Universe to the Present”, *NASA Mission Concept Study* (2004).
- [40] “Beyond Einstein: The Program”. <http://universe.nasa.gov/program.html>.
- [41] T. Damour, B. R. Iyer, and B. S. Sathyaprakash *Phys. Rev.* **D66** (2002) 027502.
- [42] “Einstein@Home”. <http://einstein.phys.uwm.edu/>.
- [43] “SETI@home”. <http://setiathome.berkeley.edu/>.
- [44] S. Mitra, S. V. Dhurandhar, and L. S. Finn *Phys. Rev.* **D72** (2005) 102001, [gr-qc/0507011](http://arxiv.org/abs/gr-qc/0507011).

- [45] G. H. Sanders, "Gravitational-wave detection", in *Proceedings of the SPIE*, M. Cruise and P. Saulson, eds., vol. 4856, pp. 247–257. 2003.
- [46] **LIGO Scientific** Collaboration, B. Abbott *et al.* *Phys. Rev.* **D69** (2004) 122004.
- [47] M. Ando and K. Tsubono, "Gravitational waves", in *proceedings of the Third Edoardo Amaldi Conference*, S. Meshkov, ed., no. 523 in AIP Conference Proceedings. American Institute of Physics, Melville, New York, 2000.
- [48] F. Acernese *et al.* *Class. Quant. Grav.* **20** (2003) S609.
- [49] L. Blanchet, T. Damour, and B. R. Iyer *Phys. Rev.* **D51** (1995) 5360.
- [50] T. Damour, B. R. Iyer, and B. S. Sathyaprakash *Phys. Rev.* **D63** (2001) 044023.
- [51] A. Lazzarini and R. Weiss Internal working note LIGO-E950018-02-E, Laser Interferometer Gravitational Wave Observatory, 1995.
- [52] L. S. Finn and D. F. Chernoff *Phys. Rev.* **D47** (1993) 2198.
- [53] L. S. Finn *Phys. Rev.* **D46** (1992) 5236.
- [54] B. S. Sathyaprakash and S. V. Dhurandhar *Phys. Rev.* **D44** (1991) 3819.
- [55] S. V. Dhurandhar and B. F. Schutz *Phys. Rev.* **D50** (1994) 2390.
- [56] B. J. Owen *Phys. Rev.* **D53** (1996) 6749.
- [57] **LIGO Scientific** Collaboration, B. Abbott *et al.* *Phys. Rev.* **D69** (2004), no. 12, 122001.
- [58] C. W. Helstrom, *Statistical Theory of Signal Detection*. Pergamon Press, London, England, 2nd ed., 1968.
- [59] B. Schutz, "Introduction to the analysis of low-frequency gravitational wave data", in *ESA SP-420: Fundamental Physics in Space*, A. Wilson, ed., p. 265. 1997.
- [60] A. Buonanno, Y. Chen, and M. Vallisneri *Phys. Rev.* **D67** (2003) 104025.
- [61] S. D. Mohanty and S. V. Dhurandhar *Phys. Rev.* **D54** (1996) 7108.
- [62] A. S. Sengupta, S. Dhurandhar, and A. Lazzarini *Phys. Rev.* **D67** (2003) 082004.

- [63] R. P. Croce, T. Demma, V. Pierro, I. M. Pinto, D. Churches, and B. S. Sathyaprakash *Phys. Rev.* **D62** (2000), no. 12, 121101.
- [64] R. P. Croce, T. Demma, V. Pierro, I. M. Pinto, and F. Postiglione *Phys. Rev.* **D62** (2000) 124020.
- [65] C. E. Shannon *Proc. Inst. Radio Eng.* **37** (1949) 10.
- [66] J. C. Mason and D. C. Handscomb, *Chebyshev polynomials*. Chapman & Hall/CRC, Boca Raton, FL, USA, 2003.
- [67] M. J. D. Powell *The Computer J.* **9** (1967) 404.
- [68] R. C. Li *IEEE Trans. Comp.* **53** (2004) 678.
- [69] M. Matsumoto and T. Nishimura *ACM Trans. on Modeling and Computer Simulation* **8** (1998) 3.
- [70] A. Buonanno, Y. Chen, Y. Pan, and M. Vallisneri *Phys. Rev.* **D70** (2004) 104003.
- [71] S. D. Mohanty *Phys. Rev.* **D57** (1998) 630.
- [72] R. P. Croce, T. Demma, M. Longo, S. Marano, V. Matta, V. Pierro, and I. M. Pinto *Phys. Rev.* **D70** (2004) 122001.
- [73] R. P. Croce, T. Demma, M. Longo, S. Marano, V. Matta, V. Pierro, and I. M. Pinto *Class. Quant. Grav.* **21** (2004) 4955.
- [74] N. Christensen *Phys. Rev.* **D46** (1992) 5250.
- [75] E. E. Flanagan *Phys. Rev.* **D48** (1993) 2389.
- [76] B. Allen and J. D. Romano *Phys. Rev.* **D59** (2001) 102001, [gr-qc/9710117](#).
- [77] B. Allen and A. C. Ottewill *Phys. Rev.* **D56** (1997) 545.
- [78] N. J. Cornish *Class. Quant. Grav.* **18** (2001) 4277.
- [79] S. W. Ballmer *Class. Quant. Grav.* **23** (2006) S179, [gr-qc/0510096](#).
- [80] H. Kudoh and A. Taruya *Phys. Rev.* **D71** (2005) 024025, [gr-qc/0411017](#).
- [81] H. Kudoh and A. Taruya *Phys. Rev.* **D72** (2006) 104015, [gr-qc/0507114](#).
- [82] A. Taruya *Phys. Rev.* **D74** (2006) 104022, [gr-qc/0607080](#).

- [83] **LIGO Scientific** Collaboration, B. Abbott *et al.* *Phys. Rev. Lett.* **95** (2005) 221101, [astro-ph/0507254](#).
- [84] **LIGO Scientific** Collaboration, B. Abbott *et al.* [astro-ph/0608606](#).
- [85] S. Ballmer August LSC Presentation LIGOG060431-00-0, LIGO Scientific Collaboration (LSC), 2006.
- [86] D. Baskaran, L. P. Grishchuk, and A. G. Polnarev *Phys. Rev.* **D74** (2006) 083008, [gr-qc/0605100](#).
- [87] D. Coward and T. Regimbau *New Astron. Rev.* **50** (2006) 461, [astro-ph/0607043](#).
- [88] J. Bock, S. Church, M. Devlin, G. Hinshaw, A. Lange, A. Lee, L. Page, B. Partridge, J. Ruhl, M. Tegmark, P. Timbie, R. Weiss, B. Winstein, and M. Zaldarriaga, "Task force on cosmic microwave background research", [astro-ph/0604101](#).
- [89] A. Lazzarini and R. Weiss Internal working note LIGO-T040140-00-Z, Laser Interferometer Gravitational Wave Observatory (LIGO), 2004.
- [90] "Big Bang - Wikipedia". [http://en.wikipedia.org/wiki/Big\\_bang\\_theory](http://en.wikipedia.org/wiki/Big_bang_theory).
- [91] S. Dodelson, *Modern Cosmology*. Academic Press, Oxford, UK, 2003.
- [92] "Cosmic microwave background radiation - Wikipedia". [http://en.wikipedia.org/wiki/Cosmic\\_microwave\\_background\\_radiation](http://en.wikipedia.org/wiki/Cosmic_microwave_background_radiation).
- [93] "Wilkinson Microwave Anisotropy Probe". <http://map.gsfc.nasa.gov/>.
- [94] J. C. Mather *et al.* *Astrophys. J. Lett.* **354** (1990) L37.
- [95] "Cosmic Background Explorer". <http://lambda.gsfc.nasa.gov/product/cobe/>.
- [96] G. Hinshaw *et al.* [astro-ph/0603451](#).
- [97] N. Jarosik *et al.* [astro-ph/0603452](#).
- [98] L. Page *et al.* [astro-ph/0603450](#).
- [99] W. Hu and M. White *New Astron.* **2** (1997) 323, [astro-ph/9706147](#).

- [100] D. A. Varshalovich, A. N. Moskalev, and V. K. Khersonskii, *Quantum theory of angular momentum*. World Scientific, Singapore, 1988.
- [101] “Legacy Archive for Microwave Background Data Analysis (LAMBDA)”.  
<http://lambda.gsfc.nasa.gov/>.
- [102] G. Smoot *et al.* *Astrophys. J.* **360** (1990) 685.
- [103] G. F. Smoot *et al.* *Astrophys. J. Lett.* **396** (1992) L1.
- [104] “Degree Angular Scale Interferometer”.  
<http://astro.uchicago.edu/dasi/>.
- [105] J. Kovac, E. M. Leitch, C. Pryke, J. E. Carlstrom, N. W. Halverson, and W. L. Holzapfel *Nature* **420** (2002) 772.
- [106] “Planck Surveyor”.  
<http://www.rssd.esa.int/index.php?project=PLANCK>.
- [107] “CMBPol Experiment Proposal”.  
[http://www.mssl.ucl.ac.uk/www\\_astro/submm/CMBpol1.html](http://www.mssl.ucl.ac.uk/www_astro/submm/CMBpol1.html).
- [108] “Boomerang”. <http://boom.caltech.edu/>.
- [109] “CMB Resources”. <http://www.mpa-garching.mpg.de/~banday/CMB.html>.
- [110] “CMB Experiments”.  
[http://lambda.gsfc.nasa.gov/links/experimental\\_sites.cfm](http://lambda.gsfc.nasa.gov/links/experimental_sites.cfm).
- [111] “Timeline of cosmic microwave background astronomy - Wikipedia”.  
[http://en.wikipedia.org/wiki/Timeline\\_of\\_cosmic\\_microwave\\_background\\_astronomy](http://en.wikipedia.org/wiki/Timeline_of_cosmic_microwave_background_astronomy).
- [112] D. F. Morrison, *Multivariate Statistical Methods*. McGraw-Hill, New York, USA, third ed., 1990.
- [113] W. Feller, *An Introduction to Probability theory and its applications*, vol. II. Wiley, New York, USA, 1965.
- [114] E. L. Wright, “Scanning and Mapping Strategies for CMB Experiments”,  
[astro-ph/9612006](http://astro-ph/9612006).
- [115] J. Borrill [astro-ph/9911389](http://astro-ph/9911389).

- [116] "Microwave Anisotropy Dataset Computational Analysis Package (MADCAP)". <http://crd.lbl.gov/~borrill/cmb/madcap/>.
- [117] T. Souradeep and B. Ratra *Astrophys. J.* **560** (2001) 28.
- [118] S. Mitra, A. S. Sengupta, and T. Souradeep *Phys. Rev.* **D70** (2004) 103002, [astro-ph/0405406](http://arxiv.org/abs/astro-ph/0405406).
- [119] C. Burigana and D. Saez *Astron. & Astrophys.* **409** (2003).
- [120] C. Armitage and B. D. Wandelt *Phys. Rev.* **D70** (2004) 123007.
- [121] "MATLAB® Matrix Laboratory". <http://www.mathworks.com/>.
- [122] "Hierarchical Equal Area isoLatitude Pixelization". <http://healpix.jpl.nasa.gov/>.
- [123] "MATLAB® function reference: rand". <http://www.mathworks.com/access/helpdesk/help/techdoc/ref/rand.html>.
- [124] "AMD Opteron™". <http://www.amd.com/opteron>.
- [125] W. H. Press, S. A. Teukolsky, W. T. Vetterling, and B. P. Flannery, *Numerical Recipes in C*. Cambridge University Press, New York, USA, second ed., 1992.
- [126] "The Planck Simulator". <http://www.g-v.o.org/planck/>.
- [127] W. Hu and S. Dodelson *Ann. Rev. of Astron. and Astrophys.* **40** (2002) 171.
- [128] J. R. Bond, C. R. Contaldi, and D. Pogosyan *Phil. Trans. Roy. Soc. Lond.* **A361** (2003) 2435.
- [129] F. Bouchet in *Proceedings of "Where Cosmology and Fundamental Physics Meet" 23-26 June, 2003*. 2004. [astro-ph/0401108](http://arxiv.org/abs/astro-ph/0401108).
- [130] T. Souradeep, S. Mitra, A. S. Sengupta, S. Ray, and R. Saha in *Proceedings of the "Fundamental Physics With CMB workshop" March 23-25, 2006, New Astron. Rev.*, vol. 50, p. 1030. 2006. [astro-ph/0608505](http://arxiv.org/abs/astro-ph/0608505).
- [131] G. Efstathiou *Mon. Not. Roy. Astron. Soc.* **349** (2004) 603.
- [132] K. M. Gorski *Astrophys. J. Lett.* **430** (1994) L85.
- [133] K. M. Gorski *et al.* *Astrophys. J. Lett.* **430** (1994) L89.

- [134] K. M. Gorski *et al.* *Astrophys. J. Lett.* **464** (1996) L11.
- [135] K. M. Gorski in *the Proceedings of the XXXIst Recontres de Moriond, 'Microwave Background Anisotropies'*. 1997. [astro-ph/9701191](#).
- [136] M. Tegmark *Phys. Rev.* **D55** (1997) 5895.
- [137] J. R. Bond, A. H. Jaffe, and L. Knox *Phys. Rev.* **D57** (1998) 2117.
- [138] J. Borrill *Phys. Rev.* **D59** (1999) 27302.
- [139] J. Borrill in *Proceedings of the 5th European SGI/Cray MPP Workshop*. 1999. [astro-ph/9911389](#).
- [140] J. R. Bond, R. G. Crittenden, A. H. Jaffe, and L. Knox *Comput.Sci.Eng.* **1** (1999) 21.
- [141] S. P. Oh, D. N. Spergel, and G. Hinshaw *Astrophys. J.* **510** (1999) 551.
- [142] O. Dore, L. Knox, and A. Peel *Phys. Rev.* **D64** (2001) 3001.
- [143] U. L. Pen *Mon. Not. Roy. Astron. Soc.* **346** (2001) 619.
- [144] A. D. Challinor *et al.* *Mon. Not. Roy. Astron. Soc.* **331** (2002) 994.
- [145] F. van Leeuwen *et al.* *Mon. Not. Roy. Astron. Soc.* **331** (2002) 975.
- [146] B. D. Wandelt and F. Hansen *Phys. Rev.* **D67** (2003) 23001.
- [147] B. D. Wandelt, D. L. Larson, and A. Lakshminarayanan *Phys. Rev.* **D70** (2004) 083511, [astro-ph/0310080](#).
- [148] B. D. Wandelt 2004. [astro-ph/0401623](#).
- [149] J. Jewell, S. Levin, and C. H. Anderson *Astrophys. J.* **609** (2004) 1, [astro-ph/0209560](#).
- [150] J. T. Yu and P. J. E. Peebles *Astrophys. J.* **158** (1969) 103.
- [151] P. J. E. Peebles *Astrophys. J.* **185** (1974) 431.
- [152] B. Wandelt, E. Hivon, and K. M. Gorski *Phys. Rev.* **D64** (2003) 083003.
- [153] I. Szapudi, S. Prunet, D. Pogosyan, A. Szalay, and J. R. Bond *Astrophys. J.* **548** (2001) L115.

- [154] I. Szapudi, S. Prunet, and S. Colombi *Astrophys. J.* **561** (2001) L11.
- [155] C. L. Bennett *et al.* *Astrophys. J. Suppl.* **148** (2003) 1.
- [156] G. Hinshaw *et al.* *Astrophys. J. Suppl.* **148** (2003) 135.
- [157] G. F. Smoot *et al.* *Astrophys. J. Lett.* **396** (1992) L1.
- [158] E. Torbet *et al.* *Astrophys. J.* **521** (1999) L79.
- [159] A. D. Miller *et al.* *Astrophys. J.* **524** (1999) L1.
- [160] S. Padin *et al.* *Astrophys. J. Lett.* **549** (2001) L1.
- [161] T. J. Pearson *et al.* *Astrophys. J.* **591** (2003) 556.
- [162] C. L. Kuo *et al.* *Astrophys. J.* **600** (2004) 32.
- [163] P. de Bernardis *et al.* *Nature* **404** (2000) 955.
- [164] S. Hanany *et al.* *Astrophys. J. Lett.* **545** (2000) L5.
- [165] A. T. Lee *et al.* *Astrophys. J.* **561** (2001) L1.
- [166] A. Benoit *et al.* *Astron. & Astrophys.* **399** (2003) L19.
- [167] E. Hivon, K. M. Gorski, C. B. Netterfield, B. P. Crill, S. Prunet, and F. Hansen *Astrophys. J.* **567** (2002) 2.
- [168] B. D. Wandelt and K. M. Gorski *Phys. Rev.* **D63** (2001) 123002.
- [169] J. H. P. Whu *et al.* *Astrophys. J. Suppl.* **132** (2001) 1.
- [170] M. Tristram, J. C. Hamilton, J. F. Macias-Perez, and C. Renault *Phys. Rev.* **D69** (2004) 123008, [astro-ph/0310260](#).
- [171] P. Fosalba, O. Dore, and F. R. Bouchet *Phys. Rev.* **D65** (2002) 063003.
- [172] K. Coble *et al.* *Astrophys. J.* **584** (2003) 585.
- [173] P. Mukherjee *et al.* *Astrophys. J.* **592** (2003) 692.
- [174] A. Challinor, 2001. Private communication.
- [175] L. Knox *Phys. Rev.* **D52** (1995) 4307.

- [176] J. R. Bond, "Theory and observations of the cosmic background radiation", in *Cosmology and Large Scale Structure Les Houches Session LX, August 1993*, R. Schaeffer, ed. Elsevier Science Press, 1996.
- [177] A. Hajian and T. Souradeep *Astrophys. J.* **597** (2003) L5.
- [178] A. Hajian, T. Souradeep, and N. Cornish *Astrophys. J. Lett.* **618** (2004) L63, [astro-ph/0406354](#).
- [179] J. M. Kovac *et al.* *Nature* **420** (2002) 772.
- [180] A. Kogut *et al.* *Astrophys. J. Suppl.* **148** (2003) 161.
- [181] T. Risbo *Journal of Geodesy* **70** (1996).
- [182] G. Efstathiou *Mon. Not. Roy. Astron. Soc.* **370** (2006).
- [183] L. Page *et al.* *Astrophys. J. Suppl.* **148** (2003) 39.
- [184] R. I. Jedrzejewski *Mon. Not. Roy. Astron. Soc.* **226** (1987) 747.
- [185] G. B. Arfken and H. J. Weber, *Mathematical Methods for Physicists*. Academic Press, San Diego, CA, USA, 2001.
- [186] A. S. Sengupta, "Cosmic Microwave Background Power Spectrum Estimation using Non-circular Beams", internal working note, Inter-University Centre for Astronomy and Astrophysics, 2001.